UNIVERSITÉ BORDEAUX 1
Sciences Technologies

N° d'ordre: 2135
CENBG 9913

THÈSE

présentée à

L' UNIVERSITÉ BORDEAUX I

École Doctorale de
Sciences Physiques et de l'Ingénieur

par

Vassilis VLACHOUDIS

pour obtenir le grade de

DOCTEUR

Spécialité: PHYSIQUE

TAUX DE CAPTURE ET DE FISSION DU ^{232}Th, ^{238}U, ^{237}Np ET ^{239}Pu
PAR DES NEUTRONS DE SPALLATION DANS UN GRAND MASSIF DE PLOMB

Soutenue le 11 Janvier 2000

Après avis de:	M. P. Assimakopoulos	Rapporteurs
	Mme S. Leray	

Devant la Commission d'Examen formée de:

M. P. Quentin	Professeur, Université Bordeaux I	Président du Jury
M. P. Aguer	Directeur de Recherche, CENBG	
M. S. Andriamonje	Chargé de Recherche, CENBG	
M. P. Assimakopoulos	Professeur, Université Ioannina	
M. G. Goggi	Professeur, Université de Pavia et CERN Genève	
Mme. S. Leray	Physicien, CEA Saclay	
M. P. Pavlopoulos	Professeur, Université Bâle et CERN Genève	

Centre d' Études Nucléaires de Bordeaux - Gradignan

Acknowledgments

With pleasure I have stayed for the past three years at the European Organization for Nuclear Research (CERN) preparing my PhD work in the TARC experiment. I would like to thank Prof. Panagiotis Pavlopoulos, my daily supervisor, for providing me with the opportunity to work with him in this interesting field of physics, with the many advices and stimulating discussions.

The leader of the TARC Collaboration, Prof. Carlo Rubbia, has continuously supported me with many good pieces of advice and ispiring ideas.

I am deeply thankful to my thesis supervisor, Prof. Samuel Andriamonje, for being an excellent supervisor and for his help and encouragement during this research. I especially like to thank Dr. Christos Eleftheriadis for his help and useful discussions.

I would like to thank Prof. P. Assimakopoulos and Mme. S. Leray for their accurate reading of the manuscript. I want to thank also Prof. P. Aguer, Prof. G. Goggi, Prof. P. Quentin for accepting to be members of my jury.

Of the many people who have made the realization of this thesis possible I want to mention especially E.Savidis, G.Kitis, J.P.Revol, E.Radermacher, F.Carminati, A.Tzima, V.Lacoste, Y.Kadi, J.Galvez, I.Papadopoulos, and all the members of the TARC collaboration for their great help and assistance.

I owe a special gratitude to my wife Vivian Syntetta for being there when ever I needed her. Thanks for your endless patience and infinite love. Finally, I want to thank my parents who have been a source of encouragement with their support and the interest they have shown in my activities.

Contents

Chapter 1

Introduction

The present concern about a sustainable energy supply is characterized by a considerable uncertainty. The green house effect and foreseeable limits in fossil fuel resources call for a nuclear revival, which is of concern due to the environmental impact of present technology of nuclear fission energy and to the long term fusion research. This uncertainty has led to the consideration of a variety of innovative strategies for the nuclear fuel cycle and related nuclear energy systems. The present concern of the research is concentrated on the extension of the life span of presently operating reactors, the increase of the fuel burn up, the plutonium recycling (in particular the incineration of actinides and long-lived fission products), the accelerator driven nuclear energy systems like the *Energy Amplifier* [1], and the possible use of the Thorium cycle. The detailed feasibility study and safety assessment of these strategies requires the accurate knowledge of nuclear data of neutron induced reactions. Both, higher fuel burn up and especially waste incineration options require improved and partly new data, in particular on minor actinides and long-lived fission products.

Regarding the incineration of the radioactive waste, nuclear data mainly for capture and fission reactions, are required for the nuclides, which are important in the ^{232}Th- ^{233}U fuel cycle and in the burning of ^{239}Pu, as well as for the higher actinides present in fission reactor waste, that would be incinerated in such new devices.

The (n,γ) and (n,f) reactions play the most important role in incineration devices, since they allow to transform long-lived radioactive isotopes into short-lived ones. Charged particle producing reactions such as (n,p) and (n,α) have generally much lower cross sections, usually below 100 $mbarns$, being therefore, of less importance in an Accelerator Driven System (ADS). However, (n,n') and (n,xn) have cross sections which can attain several barns and are of great interest in the conception of ADS projects using fast neutron spectra, since they govern the neutron fluence and a large part of the energy flux.

As shown by C. Rubbia et al, in the concept of *Energy Amplifier* [1], fast neutron ADS using the Thorium cycle is a very promising solution. It has been shown that it reduces radiotoxicity released by the fuel preprocessing, by large factors, compared to present solutions or to the uranium based cycle. Moreover, in the *Energy Amplifier* the minimal production of ^{239}Pu is preventive for nuclear weapons. The total discharge of Neptunium and Plutonium is of the order of 4 - 5 kilograms after a long burn-up (5 years of operation) of a typical *Energy Amplifier*. Hence, in order to accumulate the amount of explosive to reach a single critical mass, the full discharges of many decades of operation, and the result of re processing of hundreds of tons of spent fuel must be used. In a different scenario, actinides Pu and other heavy elements are recycled in fast neutron reactors (critical or ADS reactors). In this case, the heavy element component of the waste is used as fissile material. In another scenario, a new generation of

PWR reactors is operated, coupled to fast neutron reactors (fully or partially based on ADS) in order to burn and to reduce significantly the amount of waste to be put in repository. Thermal ADS reactors using molten salt fuel are also proposed to reduce the Plutonium inventory [2].

The *Energy Amplifier* system is based on a convection driven molten Lead swimming pool, where lead plays the role of the coolant medium at a maximum temperature of 600 - 700^oC. In view of the high boiling temperature of Lead (1743^oC at n.p.t.) and the negative void coefficient of the *Energy Amplifier*, even higher temperatures may be considered. The lead isotopes have a large mass and also a very low capture cross-section to neutrons. Thus, an energetic neutron will lose energy by elastic collisions in a very large number of small decrements. The fuel is made of mixed oxides, where the choice of the chemical composition of the fuel is strongly related to the one of the fuel reprocessing. The preferred fertile material is therefore the ^{232}Th, although applications based on other Actinides are of interest for burning Plutonium, depleted Uranium and similar surpluses. Neutron capture in the fertile element lead to production of fissile material.

The importance of the innovative concept of the thorium cycle is two-fold: as an alternative fuel, it is the basis for safe and sustainable energy generation through accelerator assisted systems, as well as the design and development of nuclear waste incinerators, based on the Th-U fuel. In both cases the knowledge of total, capture and (n,xn) reaction Nuclear Data, including the resonance parameters, for the elements present to the Th-cycle are crucial.

The main chain of events for ^{232}Th is then

$$^{232}\mathrm{Th} \xrightarrow{(n,\gamma)} {}^{233}\mathrm{Th} \xrightarrow{\beta^-} {}^{233}\mathrm{Pa} \xrightarrow{\beta^-} {}^{233}\mathrm{U}$$

In steady neutron flux conditions, the chain will tend to an equilibrium, namely in a situation in which each fissioned ^{233}U nucleus is replaced by a newly bred fuel nucleus.

$$N(^{232}\mathrm{Th})\,\sigma_\gamma(^{232}\mathrm{Th})\,\Phi = N(^{233}\mathrm{Pa}) \,/\, \tau(^{233}\mathrm{Pa} \rightarrow ^{233}\mathrm{U}) = N(^{233}\mathrm{U})\,(\sigma_{fiss} + \sigma_\gamma)\,(^{233}\mathrm{U})\,\Phi$$

where, $\sigma_\gamma, \sigma_{fiss}$ is the capture and fission cross section averaged over the neutron spectrum of integrated flux Φ, $\tau(x)$ is the half life of the decay x, and $N(y)$ is the atomic density of the isotope y. Such a "breeding" equilibrium is naturally attained with a specific value of the fuel/breeder concentration ratio determined solely by the ratio of cross section ψ

$$\psi = \frac{N(^{233}\mathrm{U})}{N(^{232}\mathrm{Th})} = \frac{\sigma_\gamma(^{232}\mathrm{Th})}{\sigma_{fiss+\gamma}(^{233}\mathrm{U})}$$

This equation assumes no alternatives besides the main chain, justified as long as the rate of neutron captures by ^{233}Pa competing with natural decay is kept negligible with a sufficiently low neutron flux. This is the "decay dominated" regime in contrast with the high flux, "capture dominated" regime investigated by BOWMAN et al [2], where the ^{233}Pa must be quickly extracted to avoid capture.

In the Uranium cycle (^{238}U-^{239}Pu) the main fissile element is ^{239}Pu, and the regeneration process of the fissile element is

$$^{238}\mathrm{U} \xrightarrow{(n,\gamma)} {}^{239}\mathrm{U} \xrightarrow{\beta^-} {}^{239}\mathrm{Np} \xrightarrow{\beta^-} {}^{239}\mathrm{Pu}$$

In 1994, the former *TARC* collaboration has proved experimentally[3] the principle of the *Energy Amplifier*. The amount of energy produced, when neutrons originating from spallation by a proton beam are further multipled by fission in a subcritical assembly of fissile material and moderator, is much larger than the energy that would be necessary to power the proton

accelerator if a dedicated installation were built for that purpose. In the same spirit of testing physics properties on which new devices with important practical applications can be based, the *TARC* experiment was proposed to study the behavior of neutrons as they migrate in a large lead volume.

While the consepts of the *Energy Amplifier* appears realistic in the computer simulation, it was needed to be tested experimentally, since they are sensitive to rather subtle properties such as the resonant captures in the lead medium itself and its possible impurities. Thus the direct measurements in an approximated ADS device such as the TARC experiment, with the corresponding energy spectrum are very instructive in estimating:

- the production rates of the fissile ^{233}U element, from the fertile ^{232}Th;
- the production of the strategic ^{239}Pu from depleted Uranium, as well the production rate of the fissile ^{239}Pu in the Uranium cycle;
- the incineration rate for ^{237}Np, ^{235}U, ^{239}Pu, as well as the integrated fission rate of ^{232}Th.

1.1 Transmutation of Long Lived Fission Products LLFP

Apart from the prospect of safe nuclear energy production with minimised radioactive by-products, Thorium based systems may offer the solution to a serius present-day problem, related to the use of conventional PWR reactors. Given the contribution of nuclear energy, even in its existing state, to the overall European energy policy, there remains the problem of radioactive waste management and final disposal and radio-toxicity in general.

1.1.1 Current Approach to Fission Products

It is well known that fission produces fragments of intermediate mass which are radioactive and constitute an unwanted and radio toxic waste. The large majority of these are short-lived and will naturally decay to stable elements. Among those few elements which after a few years are still of concern because of their remaining radioactivity, we can distinguish two cases:

- The large majority of the toxicity is carried out by isotopes such as ^{90}Sr and ^{137}Cs with half-lives of the order of 30 years.
- A few products however have much larger half-lives. The most abundant of these are ^{135}Cs ($2.3\ 10^6$ years), ^{99}Tc ($2.1\ 10^5$ years) and ^{129}I ($1.6\ 10^7$ years).

The current approach to deal with these waste products, including also the actinide elements, is to store them in secure locations for a long period of time, with the intent of finding a permanent disposal in a secure geological repository. Institutional storage (for a few centuries) seems a valid approach for the first group. However, there is less consensus that geological predictions are reliable enough to ensure over millennia that the long-lived fraction can be permanently contained. These chemical elements are all highly soluble in water, and could therefore drift back to the biosphere, thus enhancing their toxic impact on the environment. This is in contrast to actinide elements for which there is evidence that they do not migrate appreciably over geological times.

1.1.2 The Transmutation Approach

From the preceding, it is easy to see why the possibility of destroying the most offending Long Lived Fission Products by transmutation has received a lot of attention. In fact, by capturing one neutron, all these nuclei can be transformed to stable elements (sometimes through an intermediate very short-lived one). The integrated cross-section for thermal neutrons per energy bin, is generally smaller than the corresponding at the resonance region. This is why one needs a very high neutron flux to destroy them. This has been attempted both with reactors and also with high fluxes that can be generated by Accelerator Driven Systems, such as the ATW concept[2] proposed by the Los Alamos group. Incineration of Fission Products does not produce energy (in contrast to the incineration of Actinides which generally occurs by fission) so that it will inevitably cause an increase in the cost of electricity. The conclusion is that transmutation, (even though it is technically possible to achieve it also for the medium-lived elements) should preferably be reserved for the LLFP. In addition, one is bound to devise the most effective possible ways of using the neutrons for that purpose. One of them is the ARC concept.

1.2 Adiabatic Resonance Crossing (ARC)

An Accelerator Driven System (ADS) has the potential to destroy actinide elements by fission. Long term ($\geq$ 500 years) radiotoxicity of the waste is dominated by long-lived fission fragments ($LLFF$), which can be destroyed by nuclear decay following neutron capture.

In both cases, it is important to optimize the efficiency of the neutron induced process. The specific reaction rate R,

$$R = \int \sigma(E)\, \Phi(E,t)\, dE \tag{1.1}$$

can be enhanced by maximizing each of the relevant factors:

a. *neutron flux* $\Phi(E,t)$, choosing a dense neutron "storage" medium (Lead, Beryllium, Carbon), with high neutron elastic cross section and high neutron transparency (small capture cross section). With these materials we are increasing the neutron flux by increasing the neutron path-length. We are operating them in a regime, where the medium has the largest possible transparency.

b. *reaction cross section* $\sigma(E)$ of the element to be transmuted, by an efficient use of resonances, made possible because of the very small lethargic steps of neutrons slowing down.

The purpose of $TARC$ (*Transmutation by Adiabatic Resonance Crossing*), was to test directly the concept of ARC to enhance significantly the neutron capture efficiency for Long Lived Fission Products $LLFP$. Indeed, neutrons have a peculiar behavior in lead;

a. a small average lethargy ξ due to the high atomic mass of lead:

$$\xi = 1 + \frac{a}{1-a}\ln(a) \approx 9.6\ 10^{-3} \quad \text{where} \quad a = \frac{(m_{Pb} - m_n)^2}{(m_{Pb} + m_n)^2} \approx 0.98 \tag{1.2}$$

b. a high and nearly energy independent elastic scattering cross section.

c. a long "storage" time, because below the capture resonances ($E_n \leq 1\ keV$) and down to epithermal energies, the elastic scattering process is nearly isotropic and the transparency to neutrons is very high[1].

[1] it takes about 3 ms, 1800 scatterings and a path in lead of 60 meters to thermalize a 1 MeV neutron.

As a consequence, neutrons produced by spallation at relatively high energy ($E_n \approx$ few MeV), after having been quickly moderated by (n,n') or $(n,2n)$ reactions down to energies of a few keV, will slow down quasi adiabatically with small isolethargic steps and will reach the capture resonance energy of an element to be transmuted where it will have high probability to be captured. The resonance width Γ is usually larger than the average lethargic step in lead. This is the case, for instance, of ^{99}Tc which has a strong neutron capture resonance at 5.6 eV (4000 $barns$) covering four average lethargy steps. The resonance integral of ^{99}Tc is 310 $barns$ while cross section at thermal/epithermal neutron energies ($E_n \leq 1$ eV) is only of the order of 20 $barns$. Neutron capture on ^{99}Tc ($t_{1/2} = 211\,100$ yr) produces ^{100}Tc ($t_{1/2} = 15.8$ s) which then decays to ^{100}Ru, a stable element. Thus, the radiotoxicity can be eliminated by neutron capture. *ARC* should be most efficient for elements with strong capture resonances, such as ^{99}Tc and ^{129}I (which represent 95% of the total *LLFF* radiotoxicity inventory).

In medicine, radioactive elements are increasingly used for diagnostic, therapy and pain relieving. These elements can be produced through neutron capture on stable elements in an ADS, as an alternative to production from nuclear reactor [4], using the inverse process invoked for the destruction of *LLFP*.

1.3 Experimental Program

The main purpose of *TARC* is to demonstrate the possibility of using Adiabatic Resonance Crossing to destroy efficiently Long-Lived Fission Fragments (*LLFP*) in Accelerator Driven Systems and to validate a new simulation developed in the framework of the Energy Amplifier program. For this purpose, an experimental set-up was installed at *CERN*. This set-up was consisted of a large lead block ($3.3 \times 3.3 \times 3$ m^3) where the proton beam from *PS* was producing neutrons by spallation.

Several detectors/techniques have been used in *TARC* to measure the neutron fluence Fig. 5.17 on page 77. For the low energy part ($E_n \leq 50$ keV), two of the detectors were using the Energy-Time relation, the ^{6}Li/^{233}U silicon detectors and ^{3}He scintillation counter. The rest were based on activation techniques, using Thermoluminescence for integral measurements, and the Activation foils (Triple Foils), for measuring the fluence at specific energies. In the High energy domain (10 $keV \leq E_n \leq 2$ MeV), ^{3}He ionization counters were used, integral measurements with activation methods (fission measurements in ^{232}Th, and the threshold reactions ^{12}C$(n,2n)$,^{11}C ($E_n > 22$ MeV), and ^{12}C$(n,3n)^{10}$C ($E_n > 34$ MeV)). Finally, a pneumatic system were used for measuring the transmutation rates of LLFF of ^{99}Tc and ^{129}I were the half lives of the transmutation products are short.

For the capture rate measurements of ^{232}Th and ^{238}U, thin foils of these elements were used. The foils were placed inside the lead volume at various positions. After the irradtion the foils were analysed by means of gamma-spectroscopy with the use of a Ge-detector. The fission measurements were performed with the use of lexan foils mounted on the fissionable material. When a fission fragment passes through a lexan foil it leaves a track which is visible after the proper appropriate treatment. By counting the number of tracks the number of fissions can be estimated.

TARC has shown that this phenomenology of spallation neutrons can open new possibilities for the incineration of the present radioactive waste, even as pre-treatment before being placed in repository, for the energy production with the absence of radioactive waste. Moreover, the production of radioactive isotopes, as an alternative to nuclear reactors, in particular for medical applications [4].

1.4 Monte Carlo Simulation and Computing

The *Monte Carlo* method has the advantage over other methods that in principle it provides a very realistic evolution of the system. However, the computing time is long and the results are affected by statistical errors. Therefore, a special effort was made to develop an innovative simulation, both for the transport of the neutrons generated in the spallation process and for the evolution of material composition under combined effects of neutron activation and nuclear decay. In this effort, we paid special attention in optimizing as much as possible the program code, since the *Monte Carlo* technique is a time consuming method of solving problems. The spallation process itself, was simulated with FLUKA [5], one of the best Monte Carlo simulation for hadronic interactions at intermediate energies. In particular, the complex structures of cross sections in the resonance region require careful treatment to describe correctly self-shielding effects. These computational tools, indispensable for the analysis and understanding of the data were developed and validated.

Both the energy and space distributions and the absolute magnitude of the neutron fluence, throughout the entire lead volume are well described by the simulation. We find that about 70% of the spallation neutrons survive the lead capture resonances. The ratio of fluences (between 0.1 eV and 10 keV) measured at two proton momenta is found to be 1.52 ± 0.1 consistent with the expectation from the simulation 1.57 ± 0.01, which is essentially the ratio of kinetic energies of the beams.

The global uncertainty in the Monte Carlo prediction comes mainly from the uncertainties in the spallation process 10% and in the neutron transport in Lead (mainly the uncertainty on the Lead cross section of 10%) and amounts to a total of 15%. It is important that the lead material is free from impurities, since the ARC effect is very sensitive to the resonances of the impurities. For example, a fraction of Silver (ppm) in the lead volume would modify the neutron spectrum considerably and in particular below the main Silver resonance at 5.2 eV. The impurity content was small enough, with well-measured concentrations, so that the corresponding uncertainty on the neutron fluence is negligible.

The excellent agreement with the entire *TARC* data set validates in detail our innovative simulation. It confirms, in particular, that the spallation process is correctly predicted within the errors mentioned above. Typically, we expect 93 neutrons per 3.5 GeV/c proton (FLUKA neutrons with transport down to 19.6 MeV). The dependence of the neutron fluence on energy and space, validates the neutron transport code and tests the reliability of the lead cross sections[2]. The correct prediction of integral and differential transmutation rates for ^{99}Tc and ^{129}I validate the efficiency of the *TARC* method to transmute *LLFF*.

[2]when simulating the transport of neutrons in an infinite medium (dimensions greater than one diffusion length), only the interaction cross sections of neutrons with the medium are important.

Chapter 2

Fundamentals of Neutron Physics

2.1 Cross Sections and Mean Free Path

The interactions between neutrons and nuclei depend on the neutron energy and the element involved. At the same neutron energy there may be more than one reaction that can occur, but it is possible to consider various energy ranges where one type of mechanism tends to be more probable than the others. The numerical measure of the probability of interaction is the *cross section* σ, giving the effective target area for each atom. The dimensions of σ are those of area and it is measured in *barns* ($1\ barn = 10^{-24}\, cm^2$).

Scattering and absorption cross sections are usually distinguished from one another (σ_s, σ_a, respectively); each of these cross sections is composed of partial cross sections such as *elastic* and *inelastic scattering*, *radiative capture*, *fission* etc. The sum of all partial cross sections is called *total* cross section; thus

$$\sigma_t = \sigma_s + \sigma_a \tag{2.1}$$

Frequently, use is made of the quantity

$$\sigma N = \Sigma \tag{2.2}$$

called *macroscopic* cross section. It specifies the cross section per cm^3. It can also be considered as the probability that the neutron interacts in a path $1\, cm$ long. The number of atoms N in one cm^3 of a substance is obtained from

$$N = \frac{density}{atomic\ weight} \times \text{AVOGADRO'S } number \tag{2.3}$$

The probability of transmission through the sample is given by

$$\frac{I(x)}{I(0)} = e^{-\sigma_t N x} \tag{2.4}$$

where $I(x)$ is the neutron beam intensity at distance x.

The average penetration of the neutron beam into the sample $\overline{x}$ is given by

$$\begin{aligned} \overline{x} &= \int_0^\infty x e^{-\sigma_t N x} N \sigma_t \, dx \\ &= \frac{1}{\sigma_t N} \\ &= \lambda \end{aligned} \tag{2.5}$$

λ is known as the *mean free path* of the neutron in the material, which equals the reciprocal of the macroscopic cross section Σ. We distinguish between the mean free path for *scattering* λ_s and for absorption λ_a. Thus

$$\frac{1}{\lambda} = \Sigma_t = \frac{1}{\lambda_s} + \frac{1}{\lambda_a} \tag{2.6}$$

The subscript s stands for scattering cross section, t for total, and a for absorption cross section. The mean free path is usually expressed in cm.

Fig. 2.1 shows the three most important cross sections for natural lead (Pb) where we can see that the scattering cross section σ_s is constant at low energies up to the resonance region, where σ_s varies rapidly with energy in the vicinity of each resonance, while in between resonances, σ_s is constant. Taking an average value of $\sigma_s = 11\,barns$ we have

$$\Sigma_s = 0.362\ cm^{-1} \qquad \text{and} \qquad \lambda_s = 2.76\ cm \tag{2.7}$$

The transport of neutrons, inside a *Lead* moderator, from low energies up to several keV is dominated from the elastic cross section, which results in an isolethargic distribution of neutrons.

2.2 Elastic Scattering and Moderation

The *elastic scattering* is one of the most important processes of the neutron slowing down in energy towards to thermalization. The scattering cross section, σ_s, falls into the following three categories according to the mass number A of the nucleus:

1. *Light and some magic nuclei.* With these nuclei, σ_s is constant from low energies up to about the MeV region, where a number of fairly wide ($\Gamma \approx keV$) scattering resonances are observed. Above the resonance region, σ_s becomes smooth, and broad resonances are found at the same energies as for total cross section σ_t.

2. *Heavy nuclei.* Here, σ_s is again constant at low energies, although the data in this region are frequently rather inaccurate. In the resonance region, σ_s varies rapidly with energy in the vicinity of each resonance, while in between resonances, σ_s is constant.

3. *Intermediate nuclei.* The elastic cross sections of these nuclei, as expected, exhibit a behavior intermediate between those of the light and heavy nuclei.

For neutron energies in the range up to several MeV, the elastic collision of a neutron with a nucleus with mass number A is described by classical mechanics. The energy of the neutron after the scattering, is strongly dependent on the mass number A of the nucleus it struck onto, as it is shown on the following formula

$$\frac{E_2}{E_1} = \frac{A^2 + 2A\cos\varphi + 1}{(A+1)^2} \tag{2.8}$$

where E_2 is the energy of the neutron after the collision, E_1 its energy before the collision, and φ is the scattering angle in the *CMS* (center of mass system). The scattering angle ϑ in the Lab system is (see Fig. 2.2)

$$\cos\vartheta = \frac{A\cos\varphi + 1}{\sqrt{A^2 + 2A\cos\varphi + 1}} \tag{2.9}$$

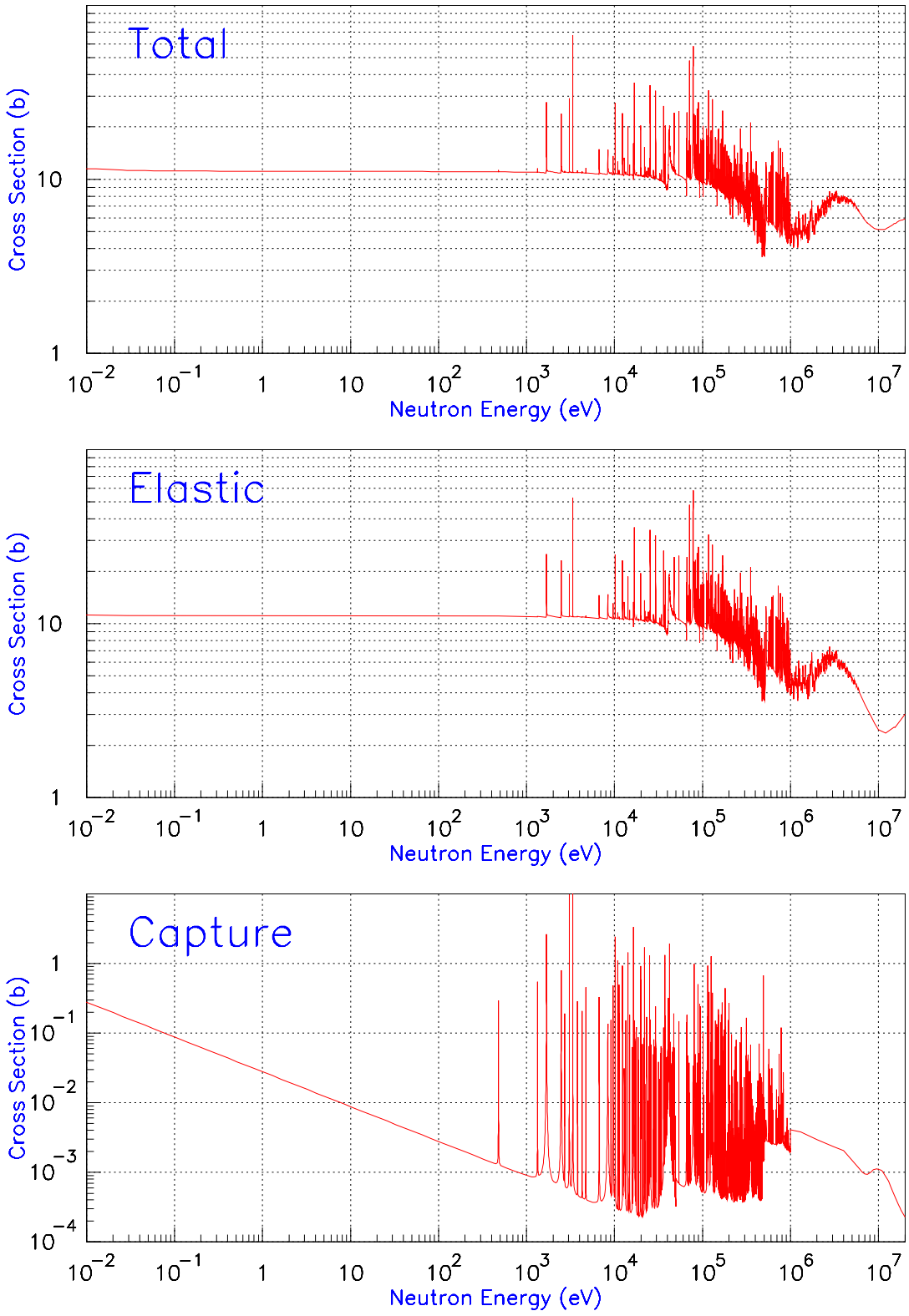

Figure 2.1: Natural **Pb**, Total, Elastic and Capture cross sections, from *JENDL-3.2*

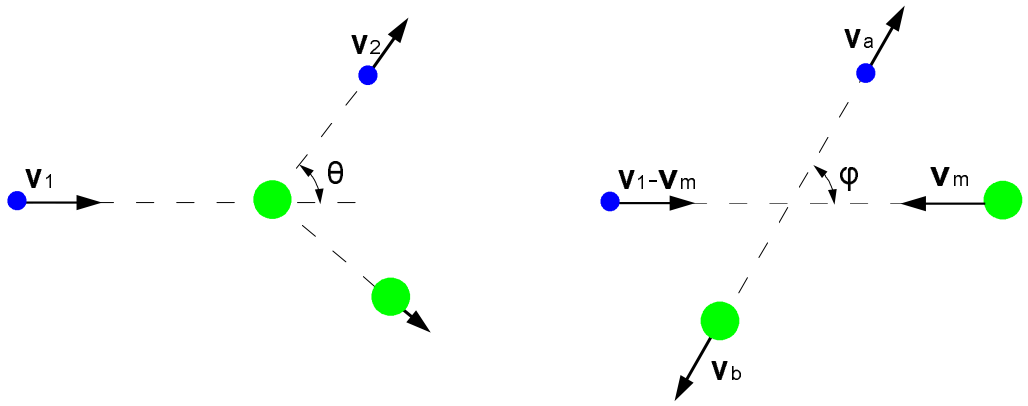

Figure 2.2: Kinematics in the Lab(left) and CMS(right) system.

For most of the transport problems, only the mean cosine of the scattering angle, $\overline{\cos\vartheta}$, is of interest; for isotropic scattering in the CMS this is

$$\overline{\cos\vartheta} = \frac{2}{3\,A} \tag{2.10}$$

The forward direction is more strongly preferred the lighter the struck nucleus is. For heavy nuclei, $\overline{\cos\vartheta} = 2/3A \approx 0$, so the scattering in the laboratory system is nearly isotropic. For higher energies, the scattering becomes anisotropic and the angular correlation becomes an important factor.

2.3 The Average Logarithmic Energy Decrement

The average energy loss ΔE of a neutron per collision with a moderator nuclei, is given by

$$\overline{\Delta E} = \overline{E_1 - E_2} = E_1\,\frac{1-a}{2} \tag{2.11}$$

where, E_2 is the energy of the neutron after the collision, E_1 its energy before the collision, and

$$a = \left(\frac{A-1}{A+1}\right)^2 \tag{2.12}$$

since, a is a constant value, depending only on the moderator material, the neutrons loses (on average), in each elastic collision, a constant fraction of its energy. So, the average *logarithmic* energy loss ξ is

$$\xi = \ln E_1 - \overline{\ln E_2} = \overline{\ln\left(\frac{E_1}{E_2}\right)} = 1 + \frac{a}{1-a}\ln a \tag{2.13}$$

which is an energy independent constant. For light nuclei, ξ takes large values, ie. ξ is equal to 1 for hydrogen, and for large A can be quite well approximated by (Table 2.1)

$$\xi \approx \frac{2}{A+\frac{2}{3}} \tag{2.14}$$

	H	D	He	Li	Be	C	O	Pb	U
A	1	2	4	7	8	12	16	207	238
a	0	0.111	0.360	0.562	0.640	0.716	0.778	0.981	0.983
ξ	1.0	0.725	0.425	0.268	0.209	0.158	0.120	0.00963	0.00838
n	18	25	43	67	86	114	150	1888	2172

Table 2.1: Slowing down parameters of various substances, for moderation from $2\,MeV \rightarrow 0.0253\,eV$.

The quantity of ξ, makes it possible for us, to estimate the average number n of collisions, necessary to moderate a neutron with an initial energy E_Q to the energy E

$$n\xi = \ln \frac{E_Q}{E}; \qquad n = \frac{\ln(E_Q/E)}{\xi} \tag{2.15}$$

Table 2.1 contains a, ξ, and n (for the moderation from 2 MeV to 0.0253 eV) for several nuclei. The values of n obtained from Eq. 2.15 are only approximate, since thermalization effects at low energies and non-isotropic scattering at high energies have not been taken into account. For an accurate calculation of the number of collisions, the energy distribution of the neutrons during the slowing-down process must be taken into account [6].

Frequently, the slowing-down process is described with the help of a logarithmic energy scale. The use of such a scale is suggested by the constancy of the average logarithmic energy loss per collision. We use as a variable the so-called *lethargy* defined by

$$u = ln\left(\frac{E_Q}{E}\right) \tag{2.16}$$

Here E_Q, is an arbitrary reference energy; in most practical applications, E_Q is taken to be the highest energy appearing in the source spectrum. Then, $u = 0$ at the beginning of the slowing-down process and during moderation it increases continuously.

2.4 Neutron Fluence and Density

Let us consider a volume element $dV = dx\,dy\,dz$ of the scattering medium with the position vector $\mathbf{r}$. Let $n(\mathbf{r}, \mathbf{\Omega}, E)\,dV\,d\Omega\,dE$ be the number of neutrons in this volume element whose flight direction, characterized by the unit vector $\mathbf{\Omega}$, lies in the differential solid angle $d\Omega$ around $\mathbf{\Omega}$, and whose kinetic energy lies between E and $E+dE$. $n(\mathbf{r}, \mathbf{\Omega}, E)\,dV\,d\Omega\,dE$ $(cm^{-3}\,steradian^{-1}\,eV^{-1})$ is thus the number per cm^3, i.e., the density, of neutrons with energies in a unit interval at E and flight directions in a unit solid angle around $\mathbf{\Omega}$. Specifying this *differential density*, which can also depend on time, is sufficient to describe a neutron field. The total number of neutrons with a given direction, is obtained by integration over all energies:

$$n(\mathbf{r}, \mathbf{\Omega})dVd\Omega = \int_0^\infty n(\mathbf{r}, \mathbf{\Omega}, E)\,dV\,d\Omega\,dE \tag{2.17}$$

$n(\mathbf{r}, \mathbf{\Omega})$ is called the *vector density*. It replaces $n(\mathbf{r}, \mathbf{\Omega}, E)$ when we are dealing with a neutron field of constant energy. If we now integrate over all flight directions as well, we obtain the total

number of neutrons in the volume element dV at the point $\mathbf{r}$:

$$\begin{aligned} n(\mathbf{r})\,dV &= \int_{4\pi} n(\mathbf{r},\mathbf{\Omega})\,dV d\Omega \\ &= \int_{4\pi}\int_0^\infty n(\mathbf{r},\mathbf{\Omega},E)\,dV d\Omega dE \end{aligned} \tag{2.18}$$

$n(\mathbf{r})$ is the *density* of neutrons at the point $\mathbf{r}$.

Next, we introduce the *differential neutron fluence*, defined by

$$F(\mathbf{r},\mathbf{\Omega},E)\,d\Omega dE = n(\mathbf{r},\mathbf{\Omega},E)\,v\,d\Omega dE \tag{2.19}$$

where $v = \sqrt{2E/m}$ is the neutron velocity. It is the number of neutrons at the point $\mathbf{r}$ with energies between E and $E + dE$ and flight directions in the differential solid angle $d\Omega$ around $\mathbf{\Omega}$ which penetrate a surface of area $1\,cm^2$ perpendicular to the direction $\mathbf{\Omega}$ in one second. By integration of the differential fluence $F(\mathbf{r},\mathbf{\Omega},E)$ $(cm^{-2}sec^{-1}steradian^{-1}eV^{-1})$ over energy, we obtain the *vector fluence* $F(\mathbf{r},\mathbf{\Omega})$, which is the number of neutrons that penetrate the $1\,cm^2$ surface perpendicular to the direction $\mathbf{\Omega}$ through the differential solid angle $d\Omega$ per second. Finally,

$$\Phi(\mathbf{r}) \;=\; \int_{4\pi} F(\mathbf{r},\mathbf{\Omega})\,d\Omega \;=\; n(\mathbf{r})\,v \tag{2.20}$$

is called the *fluence* of neutrons[1]. In practice, the fluence $\Phi(cm^{-2}sec^{-1})$ is the datum most frequently used for describing neutron fields, and for this reason, it is important to make its physical significance clear.

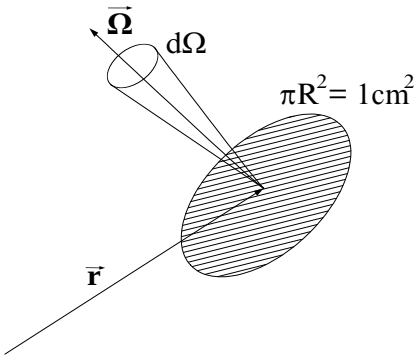

Figure 2.3: Definition of *vector fluence* and *fluence*.

Let us consider a circular disc with a surface area $\pi R^2 = 1\,cm^2$ whose center is rigidly fixed to the point $\mathbf{r}$ (Fig. 2.3). $F(\mathbf{r},\mathbf{\Omega})\,d\Omega$ is the number of neutrons which penetrate the disc through the solid angle element $d\Omega$ around the direction of its normal $\mathbf{\Omega}$ per *sec*. In this picture, the integration by which the fluence is formed can be represented by rotation of the disc in all directions keeping the center fixed. In such a rotation, the disc describes a sphere of cross section $\pi R^2 = 1\,cm^2$ and of surface $4\pi R^2 = 4\,cm^2$. Thus, the fluence Φ is the number of neutrons which penetrate this sphere per second from all sides. It follows from this fact, that in an isotropic neutron field, i.e., a field in which all flight directions are equally represented, $\Phi/2$ neutrons penetrate a $1\,cm^2$ surface per second. For an isotropic field equally many neutrons pass through each surface element of the sphere introduced above. Since altogether 2Φ neutrons pass through $4\,cm^2$ per second (each neutron passes once from the outside to the inside and once from the inside to the outside), $\Phi/2$ neutrons go through the $1\,cm^2$ per second. This conclusion also holds for weakly anisotropic neutron fields.

In most cases, F can be represented as a function of only one angle ϑ that is measured from the "distribution axis" with respect to which the field is considered to be rotationally symmetric. In such a case, we can always expand the quantity $F(\mathbf{r},\mathbf{\Omega})$ in Legendre polynomials, as a rule

[1] In a mono-energetic neutron field, v is simply the velocity; but in a polyenergetic field, v is the average of the velocity over the energy spectrum of the density.

with considerable advantage insofar as the mathematical treatment of the problem is concerned:

$$F(\mathbf{r},\mathbf{\Omega}) = \frac{1}{4\pi}\sum_{l=0}^{\infty}(2l+1)F_l(r)P_l(\cos\vartheta) \tag{2.21}$$

The first four Legendre polynomials are:

$$P_0 = 1 \qquad P_1 = \cos\vartheta$$
$$P_2 = \frac{1}{2}(3\cos^2\vartheta - 1) \qquad P_3 = \frac{1}{2}(5\cos^3\vartheta - 3\cos^2\vartheta)$$

The equation

$$\mathbf{F_l}(\mathbf{r}) = 2\pi\int_0^{\pi} F(\mathbf{r},\mathbf{\Omega})P_l(\cos\vartheta)\sin\vartheta\, d\vartheta \tag{2.22}$$

holds for the quantities $\mathbf{F_l}(\mathbf{r})$. In particular,

$$\mathbf{F_0}(\mathbf{r}) = 2\pi\int_0^{\pi} F(\mathbf{r},\mathbf{\Omega})\sin\vartheta\, d\vartheta = \int_{4\pi} F(\mathbf{r},\mathbf{\Omega})\, d\Omega = \Phi(\mathbf{r}) \tag{2.23}$$

The second expansion coefficient has also a physical significance. In order to see this, lets introduce an important new quantity, the *current density* J in the direction of the distribution axis. The magnitude of this vector is the net number of neutrons which penetrate a $1\,cm^2$ surface perpendicular to the distribution axis per second. Thus

$$\mathbf{J}(\mathbf{r}) = \int_{4\pi} F(\mathbf{r},\mathbf{\Omega})\cos\vartheta d\Omega = 2\pi\int_0^{\pi} F(\mathbf{r},\mathbf{\Omega})\cos\vartheta\sin\vartheta\, d\vartheta \tag{2.24}$$

By comparison with (Eq. 2.22) it follows that $\mathbf{J}(\mathbf{r}) = \mathbf{F_1}(\mathbf{r})$. Thus, the first two terms of the expansion (Eq. 2.21) can be written:

$$F(\mathbf{r},\mathbf{\Omega}) = \frac{1}{4\pi}\Phi(\mathbf{r}) + \frac{3}{4\pi}\mathbf{J}(\mathbf{r})\cos\vartheta \tag{2.25}$$

and it will turn out that in many cases the vector fluence $F(\mathbf{r},\mathbf{\Omega})$ can be approximated by these two terms with adequate accuracy.

2.4.1 Iso-lethargic Fluence

While the correct mathematical representation of the fluence is done by using the differential fluence

$$\Phi(E) = \frac{d\,\text{neutrons}}{dE} \tag{2.26}$$

with units $cm^{-2}\,sec^{-1}\,eV^{-1}$, $\Phi(E)\,dE$ gives the number of neutrons with energies between E and $E + dE$. In the epithermal energy range, where the spectrum is predominantly determined by the neutrons being slowed down, by elastic collision with the nuclei of the moderator substance, frequent use is done of the quantity called *isolethargic fluence* Φ_{iso} or *epithermal fluence* Φ_{epi} defined as

$$\Phi(E)\,dE = \frac{\Phi_{iso}}{E}\,dE = \Phi_{iso}\,d\ln E \tag{2.27}$$

which is the number of neutrons per logarithmic unit of energy or per lethargy unit, giving thus a better understanding of the number of neutrons for each energy. An easier way of reading these isolethargic plots is to assume that it gives you the number of neutrons in a certain energy E, for an energy range $\Delta E = E$ equal with that energy. Since the lethargy of a moderator is constant, except in the thermal energy region, we expect that the neutron spectrum for most of the materials without large absorption cross section to be flat if plotted per lethargy unit, hence following the $1/E$ rule.

2.4.2 Computing the Neutron Fluence

There are several ways to compute the neutron fluence, from the experiment or from the *Monte Carlo* calculation. In *TARC* experiment and also in the simulations we have used the following:

- dN/dS_{perp} is calculated as the number of neutrons crossing a small surface element dS, when the surface element is rotated, keeping its center fixed, in such a way that it is perpendicular to the direction of the neutron velocity considered. $dS_{perp} = dS \times \cos\theta$, there θ is the angle between the proton direction and the normal to the surface element.
- It is more practical in Monte Carlo calculations to compute the average in a volume element dV as dl/dV, where dl is the total track length of neutrons in the volume element dV. If the space distribution of neutrons does not change too abruptly, this allows, by selecting appropriate volume elements, to obtain better statistics. It is clear that the larger the region, the larger the systematic uncertainty on the flux. In *TARC*, we have tested several volumes (inside the lead block, sphere with diameter equal to the diameter of one hole, cylinder of length 15 cm with the same diameter as the hole, etc.) and found that the difference was negligible compared to usual statistical errors.
- In the data we usually record the number of interactions in a detector, therefore, we compute the quantity $(1/\Sigma) \times dN/dV$, where dN is the number of interactions in volume element dV.

Of course, the above three methods are equivalent, with the assumption that the detector it self, does not alter the neutron flux, either because of it's small size or of the small cross section of the detector material.

2.5 Activation and the Neutron Fluence

Let us consider a monoenergetic neutron field. Let the vector fluence be represented by a series of Legendre polynomials in $\cos\vartheta$, where ϑ is the angle to the field axis:

$$F(\mathbf{r},\mathbf{\Omega}) = \frac{1}{4\pi}\sum_{l=0}^{\infty}(2l+1)F_l(r)P_l(\cos\vartheta) \tag{2.28}$$

Let ψ be the angle between the field axis and the normal to the foil Fig. 2.4. Then, in a system of polar coordinates around the normal to the foil, we have

$$\begin{aligned}\mathbf{F}(\mathbf{r},\mathbf{\Omega}^*) = \ & \tfrac{1}{4\pi} \sum_{l=0}^{\infty}(2l+1)\mathbf{F}_l(\mathbf{r})[P_l(\cos\vartheta^*)P_l(\cos\psi) + \\ & + \ 2\sum_{m=1}^{l}\frac{(l-m)!}{(l+m)!}P_l^m(\cos\theta^*)P_l^m(\cos\psi)\cos^m\phi^*]\end{aligned} \tag{2.29}$$

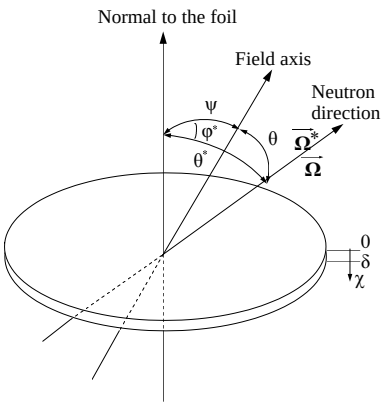

We assume that the $F_l(\mathbf{r})$ do not change appreciable along the foil surface, with the result that we can henceforth omit the argument $\mathbf{r}$. Furthermore, we assume that (a) no scattering occurs in the foil ($\mu_t = \mu_\alpha$), and (b) no neutrons enter the foil through its edges (or, in other words, the radius of the foil is very large compared to its thickness).

Where μ_x is the coefficient for the reaction x given by $\mu_x = \Sigma_x/\rho$ (cm^2/g), ρ is the foil density, δ (g/cm^2) the foil thickness. The subscript α means the sum of all the reactions leading to the absorption of the neutron (capture, (n,p), (n,a) etc.), t is for the total cross section, s for scattering and act for the activation reaction that we will finally observe.

The number of neutrons that are absorbed per cm^2 per sec at depths between x and $x + dx$ is then

$$\begin{aligned} P_A(x)dx &= [\int_0^{\pi/2}\int_0^{2\pi} \mathbf{F}(\mathbf{\Omega}^*) e^{-\frac{\mu_\alpha(\delta-x)}{\cos\vartheta^*}} \sin\vartheta^* d\vartheta^* d\phi^*]\mu_\alpha dx + \\ &+ [\int_{\pi/2}^{\pi}\int_0^{2\pi} \mathbf{F}(\mathbf{\Omega}^*) e^{-\frac{\mu_\alpha x}{|\cos\vartheta^*|}} \sin\vartheta^* d\vartheta^* d\phi^*]\mu_\alpha dx \end{aligned} \quad (2.30)$$

The first term on the right-hand side describes the contribution to the absorption of the neutrons incident "from below", the second term the contribution of those incident "from above". If we substitute the value of $\mathbf{F}(\mathbf{\Omega}^*)$, the terms containing the associated Legendre polynomials vanish upon integration over ϕ^* and we obtain

$$P_A(x) = \frac{1}{2}\sum_{l=0}^{\infty}(2l+1)F_l g_l(\mu_\alpha, x, \delta)P_l(\cos\psi) \quad (2.31)$$

with

$$\begin{aligned} g_l(\mu_\alpha, x, \delta) = \mu_\alpha &[\int_0^{\pi/2} e^{-\frac{\mu_\alpha(\delta-x)}{\cos\vartheta^*}} P_l(\cos\vartheta^*)\sin\vartheta^* d\vartheta^* + \\ &+ \int_{\pi/2}^{\pi} e^{-\frac{\mu_\alpha x}{|\cos\vartheta^*|}} P_l(\cos\vartheta^*)\sin\vartheta^* d\vartheta^*] \end{aligned} \quad (2.32)$$

In particular, if $\cos\vartheta^* = t$

$$\begin{aligned} g_0(\mu_\alpha, x, \delta) &= \mu_\alpha \int_0^1 [e^{-\frac{\mu_\alpha(\delta-x)}{t}} + e^{-\frac{\mu_\alpha x}{t}}]dt \\ &= \mu_\alpha[E_2(\mu_\alpha(\delta-x)) + E_2(\mu_\alpha x)] \quad (2.33) \\ g_1(\mu_\alpha, x, \delta) &= \mu_\alpha \int_0^1 [te^{-\frac{\mu_\alpha(\delta-x)}{t}} - e^{-\frac{\mu_\alpha x}{t}}]dt \\ &= \mu_\alpha[E_3(\mu_\alpha(\delta-x)) + E_3(\mu_\alpha x)] \quad (2.34) \\ g_2(\mu_\alpha, x, \delta) &= \mu_\alpha \int_0^1 \frac{1}{2}(3t^2-1)[e^{-\frac{\mu_\alpha(\delta-x)}{t}} - e^{-\frac{\mu_\alpha x}{t}}]dt \quad (2.35) \\ &= \mu_\alpha[3E_4(\mu_\alpha(\delta-x)) + 3E_4(\mu_\alpha x) - E_2(\mu_\alpha(\delta-x)) - E_2(\mu_\alpha x)] \end{aligned}$$

Where $E_n(x)$ are the functions:

$$E_n(x) = \int_1^\infty \frac{e^{-ux}}{u^n}du = \int_0^1 t^{n-2}e^{-\frac{x}{t}}dt \quad (2.36)$$

The activation C is obtained from $P_A(x)$ by multiplication with μ_{act}/μ_α and integration over the foil thickness:

$$\begin{aligned} C &= \frac{\mu_{act}}{\mu_\alpha}\int_0^\delta P_A(x)dx \\ &= \frac{\mu_{act}}{\mu_\alpha}\sum_{l=0}^{\infty}(2l+1)F_l\phi_l(\mu_\alpha\delta)P_l(\cos\psi) \quad (2.37) \end{aligned}$$

Here

$$\phi_l(\mu_\alpha\delta) = \int_0^\delta g_l(\mu_\alpha, x, \delta)dx \tag{2.38}$$

$$= \mu_\alpha \int_0^\delta [\int_0^{\pi/2} e^{-\frac{\mu_\alpha(\delta-x)}{\cos\vartheta^*}} P_l(\cos\vartheta^*)\sin\vartheta^* d\vartheta^* +$$

$$+ \int_{\pi/2}^{\pi} e^{-\frac{\mu_\alpha x}{|\cos\vartheta^*|}} P_l(\cos\vartheta^*)\sin\vartheta^* d\vartheta^*] \tag{2.39}$$

We can see immediately that all the $\phi_l(\mu_\alpha\delta)$ with odd l vanish. For even l on the other hand,

$$\phi_l(\mu_\alpha\delta) = 2\int_0^1 P_l(t)(1 - e^{-\frac{\mu_\alpha\delta}{t}})tdt \tag{2.40}$$

where $\cos\vartheta^* = t$. In particular

$$\phi_0(\mu_\alpha\delta) = 1 - 2E_3(\mu_\alpha\delta), \tag{2.41}$$

$$\phi_2(\mu_\alpha\delta) = \frac{1}{4} + E_3(\mu_\alpha\delta) - 3E_5(\mu_\alpha\delta). \tag{2.42}$$

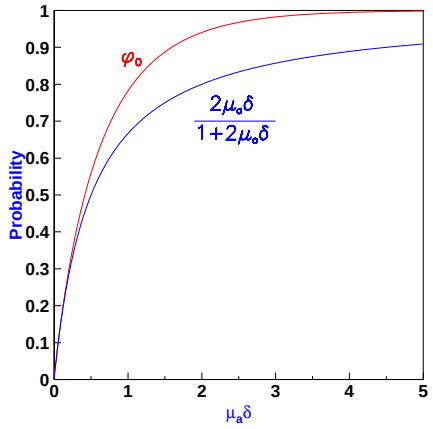

Figure 2.5: The absorption probability $\phi_0(\mu_\alpha\delta)$.

In the following, we shall limit ourselves to neutron fields whose vector fluence is described by only the first two terms in the expansion in Legendre polynomials. Then, simply,

$$C = \frac{\mu_{act}}{\mu_\alpha}\frac{\Phi(\mathbf{r})}{2}\phi_0, \tag{2.43}$$

ie. the activation is independent of the foil orientation and proportional to the fluence. The current term affects the local distribution of the activation in the foil but not the total activation integrated over the foil thickness.

Since $\mathbf{\Phi(r)/2}$ is the number of neutrons falling on both sides of the foil per cm^2, $\phi_0(\mu_\alpha\delta)$ can obviously be identified as the absorption probability of the foil in an isotropic neutron field. For an extremely thick foil ($\mu_\alpha\delta \gg 1$) we have $\phi_0(\mu_\alpha\delta) = 1$; thus $C = \frac{\mu_{act}}{\mu_\alpha}\frac{\Phi(\mathbf{r})}{2}$. On the other hand, for an extremely thin foil, $\phi_0(\mu_\alpha\delta) = 2\mu_\alpha\delta$ and

$$C = \frac{\mu_{act}}{\mu_\alpha}\frac{\Phi(\mathbf{r})}{2}2\mu_\alpha\delta = \mu_{act}\delta\Phi(\mathbf{r}) = \Sigma_{act}d\Phi(\mathbf{r}) \tag{2.44}$$

Fig. 2.5 shows $\phi_0(\mu_\alpha\delta)$ and the simple approximation $2\mu_\alpha\delta/(1+2\mu_\alpha\delta)$ to it.

Let us consider a foil in a homogeneous neutron field whose energy distribution is given by

$$\Phi(E)dE = \Phi_{epi}(E)\frac{dE}{E}$$

and let $\Phi_{epi}(E)$ vary slowly with energy. If we neglect scattering in the foil, the activation (disregarding the foil perturbation) is given by

$$C = \frac{1}{2}\int_{E_C}^{E_{max}} \Phi_{epi}(E)\frac{\mu_{act}(E)}{\mu_\alpha(E)}\phi_0(\mu_\alpha(E)\delta)\frac{dE}{E} \tag{2.45}$$

Where E_C is the lower cut-off energy in resonance integrals the energy E_{max} is the highest energy appearing in the spectrum and can frequently be taken as infinite without appreciable error. In general, the energy integral is difficult to carry out exactly, but it can be numerically evaluated with the help of the neutron cross section databases.

2.6 Neutron Diffusion

Consider a small volume $dV = dx\,dy\,dz$ Fig. 2.6 in a large transparent to neutrons moderating medium. The net outflow of neutrons from the system, in the z direction, is given by Taylor's theorem

$$(J_{z+dz} - J_z)\,dx\,dy = -D\frac{\partial^2\Phi}{\partial z^2}\,dx\,dy\,dz \tag{2.46}$$

Where D is the *diffusion coefficient* given by $D = \lambda_s/3$ [2]. (For anisotropic scattering, a correction must be introduced, $D = \lambda_s/3(1-\mu)$ where $\mu = \overline{\cos\vartheta}$). Thus, the total outflow per unit volume per second is written as $-D\,\nabla^2\Phi$, and the balance in the number of neutrons per unit volume is

$$\frac{\partial\Phi(\mathbf{r})}{\partial t} = \text{production rate} - \text{outflow rate} - \text{absorption rate} \tag{2.47}$$

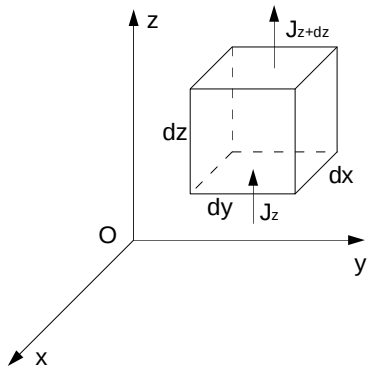

Figure 2.6: The net outflow of neutrons from the volume dV.

If $S(\mathbf{r})$ represents the production rate of neutrons per unit volume, then

$$\frac{\partial\Phi(\mathbf{r})}{\partial t} = S(\mathbf{r}) + D\nabla^2\Phi(\mathbf{r}) - \Sigma_a\Phi(\mathbf{r}) \tag{2.48}$$

In the case that the source, is point-like located at the center, and for a steady state, FICK'S law leads to the differential equation

$$\frac{S(\mathbf{r})}{D} + \nabla^2\Phi(\mathbf{r}) - \frac{\Sigma_a}{D}\Phi(\mathbf{r}) = 0 \tag{2.49}$$

If we now introduce the *diffusion length*

$$L = \sqrt{D/\Sigma_a} = \sqrt{\frac{1}{3\Sigma_a\,(\Sigma_t r + \Sigma_a)}} \tag{2.50}$$

we have

$$\frac{S(\mathbf{r})}{D} + \nabla^2\Phi(\mathbf{r}) - \frac{1}{L^2}\Phi(\mathbf{r}) = 0 \tag{2.51}$$

The diffusion length specifies within a numerical factor, the average distance between the place where a neutron is produced and the place where it is absorbed.

Considering an isotropic point source in an infinite medium, by solving the diffusion equation Eq. 2.51 at large distances from the source, leads to the asymptotic solution which because of the spherical symmetry has the form

$$\Phi(r) \approx S_o\frac{e^{-\kappa\,r}}{4\pi Dr} \tag{2.52}$$

where S_o is the rate of neutrons from the source per unit of time (n/sec) and κ is given by

$$1 = \frac{\Sigma_s}{2\kappa}\ \ln\frac{1+\kappa\Sigma_t}{1-\kappa\Sigma_t} \tag{2.53}$$

When the elastic scattering is large and the absorption cross section very small, D is a small number (cm), while $1/\kappa$ is large (m). By expanding the logarithm, one then obtains

$$\kappa^2 = 3\,\Sigma_a\,\Sigma_t\left(1 - \frac{4}{5}\frac{\Sigma_a}{\Sigma_t}\right) \tag{2.54}$$

[2] A complete discussion about the diffusion theory can be found in Ref. [7, 8].

which becomes

$$\kappa = \sqrt{3\,\Sigma_a\,\Sigma_t} \tag{2.55}$$

For a region close to the source $\kappa\, r \ll 1$, the neutron fluence is given by $\Phi(r) \approx S_o/4\pi Dr$, namely is considerably enhanced with respect to the fluence in absence of a moderator $\Phi_o(r) \approx S_o/4\pi r^2$ by the factor $F = \Phi(r)/\Phi_o(r) = r/D$, ie. at a sample distance of $r = 30\,cm$, the enhancement factor is very substantial in the case of Carbon where $F = 30/0.86 = 34.88$ and for Lead where $F = 30/1.01 = 29.7$. The diffusing medium is acting as a powerful fluence enhancer, due to multiple traversals.

2.7 Neutron Capture as a Transmutation Method

Neutron capture ${}^{A}_{Z}E + n \rightarrow {}^{A+1}_{Z} E^*$ provides one of the most effective ways of element transmutation [4], when we operate in an energy regime of high neutron fluence. Capture reactions can be further enhanced, in the energy regions where the capture cross section is high, *ie.* at the resonance regions of the "father" element. This can be easily achieved, if the initial "father" isotope ${}^{A}_{Z}E$, is embedded in a diffusing medium which is highly transparent to neutrons and has the appropriate physical properties as to enhance the occurrence of the capture process. The produced "daughter" nucleus ${}^{A+1}_{Z}E^*$, depending on the application, can either be used directly or in turn allowed for instance to beta decay, ${}^{A+1}_{Z}E^* \xrightarrow{\beta-decay} {}^{A+1}_{Z+1} X^*$, or more generally, to undergo an adequate spontaneous nuclear transformation into another radio-active isotope.

This transmutation method relies on a vastly increased neutron capture efficiency[3], achieved with the effective use of the resonances of the actived element and the geometry of the medium surrounding the source and in which a small amount of the material to be activated is introduced in a diffused way:

1. The medium is highly transparent[4], but highly diffusive; the succession of many, closely occurring elastic scattering[5] events gives a random walk nature to the neutron propagation. The fluence is enhanced because of long resulting, tortuous, random paths that neutrons perform before being eventually captured or exiting the large volume of the transparent medium. Using an optical analogy, the target-moderator sphere is chosen to be diffusive, but highly transparent to neutrons. Doping it with small amount of additional material makes it "cloudy". As a consequence, most of the neutrons are captured by the absorbing impurities.

2. In addition, the large peek values of capture cross section of the sample, in correspondence to the nuclear resonances, may be exploited using a diffusing medium as of (1), but of large atomic number A. In such medium, the neutron energy is slightly reduced at each (elastic) scattering, thus "scanning" in very tiny energy steps through the resonance spectrum of the sample during the smooth, otherwise unperturbed, energy slow-down of the initially high energy (MeV) neutrons of the source.

The choice of the diffusing medium depends on the most appropriate energy at which neutron captures must occur. If neutrons are to be thermalized, i.e. captures have to occur at thermal

[3] Neutron capture efficiency is defined as capture probability in the sample for one initial neutron and unit mass of father element.

[4] Transparency is meant as property of the medium in which neutrons undergo mostly elastic scattering

[5] Scatterings are generally isotropic

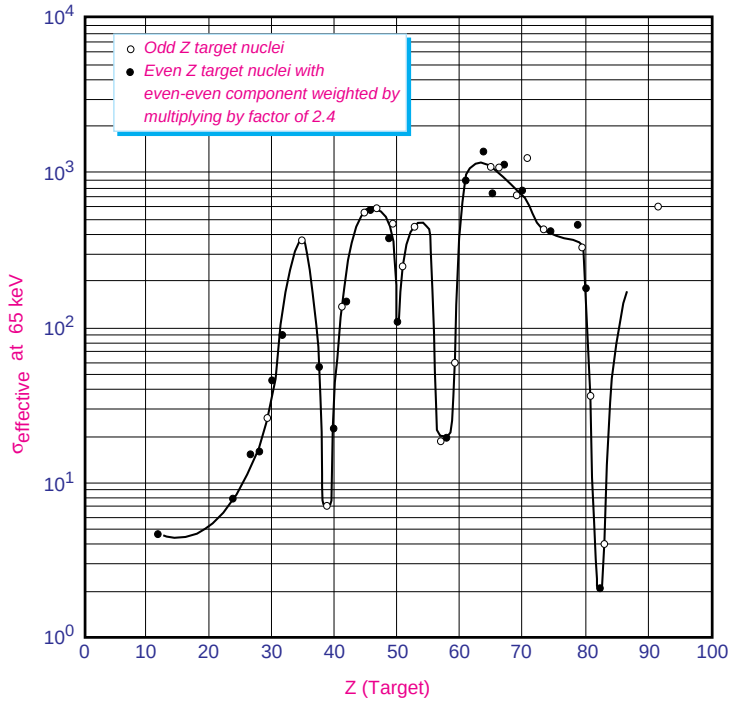

Figure 2.7: Capture cross section at 65 keV as a function of the atomic number Z for various elements.

energies ($0.025\,eV$), only the previously mentioned feature (1) is used and a low A (atomic number) medium but very transparent to neutrons is to be used, like for instance reactor purity grade graphite or D_2O (deuterated water). If instead neutron capture has to be performed with father elements which have large values of capture cross section in correspondence with resonances, both features (1) and (2) are used and the best elements for the diffusing medium are *Lead* or *Bismuth* (eventually mixed), (Fig. 2.7), which have simultaneously a small[6] neutron capture cross section and a very small "lethargy", ξ. While ^{209}Bi is a single isotope, natural *Lead* is made of ^{204}Pb (1.4 %), ^{206}Pb (24.1 %), ^{207}Pb (22.1 %) and ^{208}Pb (52.4 %), which have quite different cross sections Fig. 2.8.

2.7.1 Energy Tuning

In order to maximize the capture of neutrons from the element to be transmuted, the energy spectrum of neutrons must be matched to the largest values of the capture cross section of the relevant isotope. The energy spectrum of a bare source is not optimal because its energy is generally too high to produce an effective capture rate Fig. 2.9. Therefore, an energy matching (moderation) must be performed before utilization, from the resonance escape probability we expect to have the maximum profit in transmutation with the use of a highly transparent, diffusing material which must have in addition a large atomic number. This is because the energy of neutrons is progressively shifted in a multitude of small steps by a large number of

[6] According to the Shell Nuclear model, built in analogy to atomic electrons, "magic" numbers occur in correspondence of "closed" neutron or proton shells. $Z = 82$ is magic, so is the number of neutrons in correspondence of ^{208}Pb. Magic number elements, in the nuclear sense, have a behavior similar to the one of Noble Elements in the atomic scale. Therefore, the neutron transparency is the consequence of a specific nuclear property, analogue to the one for electrons in noble gases.

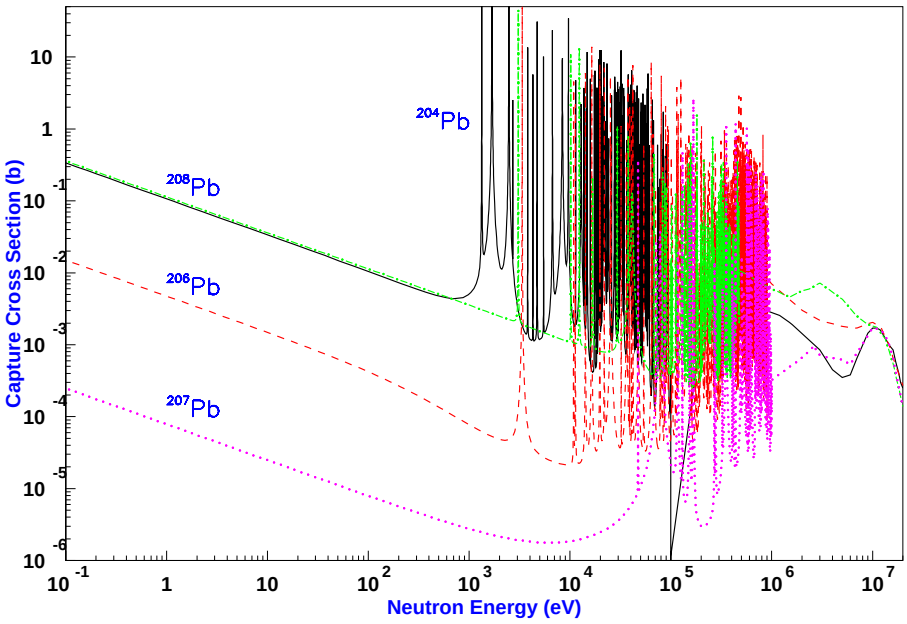

Figure 2.8: Capture cross section of lead isotopes ^{204}Pb, ^{206}Pb, ^{207}Pb and ^{208}Pb.

multiple, elastic collisions[7]. Eq. 2.13 on page 10 suggest that large A minimize the energy loss of the neutron in each scattering. Thus, for large A, isotropic scattering is an excellent approximation.

The logarithmic energy decrement for *Lead* is very small $\xi = 9.54 \cdot 10^{-3}$. The average number of collisions for instance to slow down from $0.5\,MeV$ to $0.025\,eV$ (thermal energies) is $n_{coll} = \ln(0.5\,MeV/0.025\,eV)/\xi = 1.76\,10^3$. The elastic cross section, away from the resonances is almost constant down to thermal energies and large ($\sigma_s = 11\,barn$). The total path length λ_{coll} to accumulate n_{coll} is then the enormous path of 53.4 meters. The actual displacement is of course much shorter, since the process is diffusive. As a consequence of the property that neutrons loose at each step a constant fraction of their energy, the energy spectrum generated by a high-energy neutron injected in the moderator is flat when plotted as a function of the variable $dE/E = d\ln(E)$. Neutrons scan progressively the full energy interval down to thermal energies, "seeking" for large values of the capture cross section of the added impurities due to strong resonances. This method is evidently profitable, provided that the added impurities experience strong resonances in the intermediate energy region. It is a fortunate circumstance, that this is the case for several of the isotopes of practical interest.

2.8 Resonance Escape Probability

If in a moderating medium, consisting of an infinite homogeneous mixture of a non-absorbing moderator (ie *Carbon, Lead*), we introduce a small amount of impurity with an appreciable absorption cross section; we can define the neutron survival probability $P_{surv}(E_1, E_2)$, as the probability that the neutron moderated through the energy interval $E_1 \to E_2$ is not capture by the nuclei of the impurity. The probability that the neutron does *not* get captured while in the

[7] Below a few hundred keV and in a transparent medium, the only dominant process is elastic scattering.

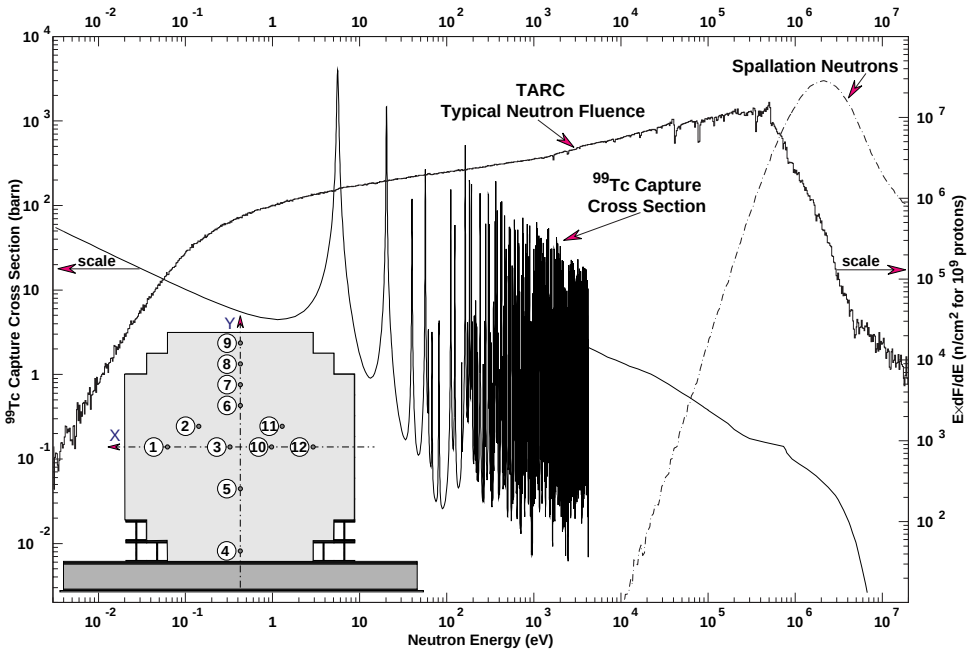

Figure 2.9: ^{99}Tc neutron capture cross section (*JENDL-3.2* data base), as a function of neutron energy (left-hand side scale); Typical neutron fluence energy distribution in *TARC*, as a function of neutron energy in isolethargic bins, for 3.57 GeV/c protons (right-hand side scale); Energy distribution of spallation neutrons as they were born in Lead in arbitrary units. About 14% of these neutrons are above 20 MeV. Instrumentation hole positions are shown in a sketch of the detector seen along the bean line (Z axis).

energy interval between E and $E + dE$ is

$$P_{surv}(E, E+dE) = 1 - \frac{\Sigma_a}{\Sigma_a + \Sigma_s}\frac{dE}{\xi E} \tag{2.56}$$

Combining the probabilities that it survives capture in each of the infinitesimal intervals, $P_{surv}(E_1, E_2)$ is equal to the product over the energy range

$$\begin{aligned} P_{surv}(E_1, E_2) &\cong \prod_{E_1}^{E_2}\left(1 - \frac{\Sigma_a}{\Sigma_a + \Sigma_s}\frac{dE}{\xi E}\right) \\ &= \exp\left[-\frac{1}{\xi}\int_{E_2}^{E_1}\frac{\Sigma_a}{\Sigma_a + \Sigma_s}\frac{dE}{E}\right] \\ &\approx \exp\left[-\frac{1}{\sigma_s^{mod}\xi}\left(\frac{N_{imp}}{N_{mod}}I_{eff}^{imp}(E_1, E_2) + I_{eff}^{mod}(E_1, E_2)\right)\right] \end{aligned} \tag{2.57}$$

where N_{imp} and N_{mod} are the number of nuclei per unit volume for the impurity and the moderator, with the approximation that the elastic scattering on the moderator is dominant and approximately constant, namely $\Sigma_s \approx \sigma_s^{mod} N_{mod} = const \gg \Sigma_a$. The *effective resonance integrals* for the moderator and the added impurity are defined as

$$I_{eff}(E_1, E_2) = \int_{E_2}^{E_1}\sigma_a\frac{dE}{E} \tag{2.58}$$

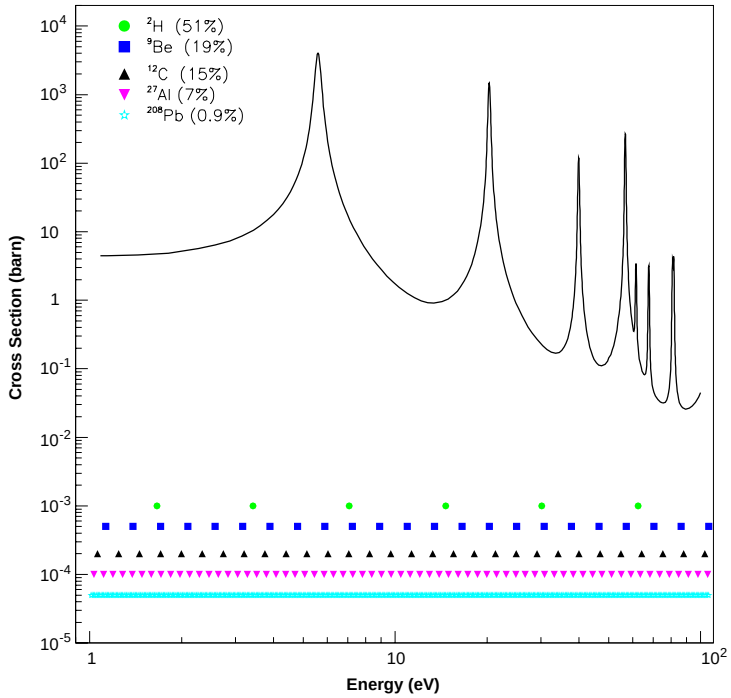

Figure 2.10: Capture cross section of ^{99}Tc and the lethargic steps for various moderators. In parenthesis is reported the average logarithmic energy loss in each elastic collision.

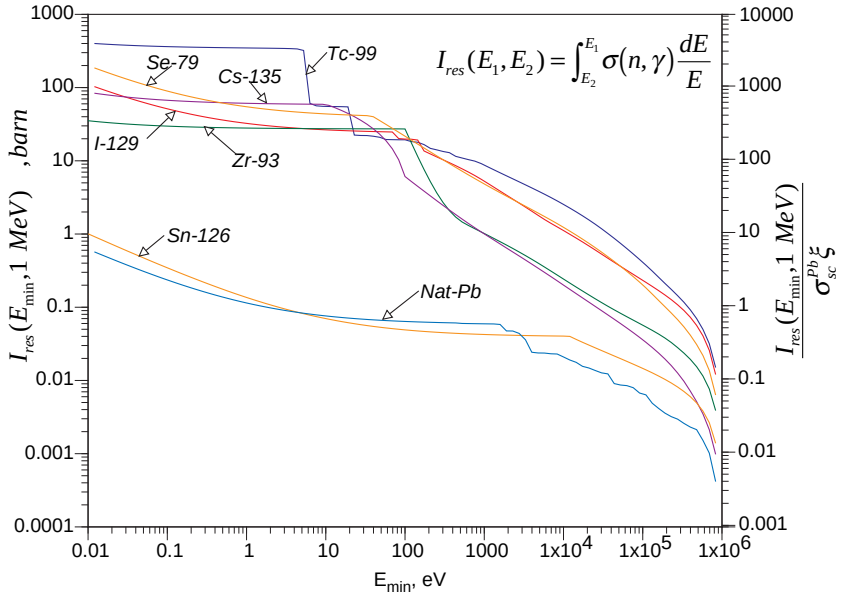

Figure 2.11: Resonance integral $I_{eff}(E, 1\,MeV)$ for various elements. The figure explicates as well the values of $I_{res}(E_{min}, 1\,MeV)/\sigma_s^{mod}\xi$ a dimensionless quantity (see Eq. 2.59) which gives the capture probability once multiplied by N_{imp}/N_{mod}. The value for any energy interval can be easily worked out by the formula $I_{eff}^{imp}(E_1, E_2) = I_{eff}^{imp}(E_1, 1\,MeV) - I_{eff}^{imp}(E_2, 1\,MeV)$

The probability of absorption in the same energy interval is given by

$$\begin{aligned} P_{abs}(E_1, E_2) &= 1 - P_{surv}(E_1, E_2) \\ &\approx \frac{1}{\sigma_s^{mod}\xi}\left(\frac{N_{imp}}{N_{mod}} I_{eff}^{imp}(E_1, E_2) + I_{eff}^{mod}(E_1, E_2)\right) \end{aligned} \tag{2.59}$$

Fig. 2.10 shows the steps in energy done by a neutron inside various moderators, during the slowing down process and the main resonances of ^{99}Tc. It is obvious, that as the energy steps are getting smaller for heavier moderators, the probability of capture from a resonance due to the increased time spent from the neutron inside the resonance, is increased. Fig. 2.11 shows the resonance integral $I_{eff}(E, 1\,MeV)$ for various elements.

2.9 Energy-Time Relation

During the neutron moderation in the epithermal energy region, the increase in lethargy u, that a neutron of velocity v experiences in one second remains practically constant. Since the number of collisions per second is $v\Sigma_s$ and the average increase in lethargy per collision is ξ, the increase rate of the neutron lethargy u will be

$$\frac{du}{dt} = \xi\Sigma_s v \tag{2.60}$$

and because $v = v_o\, e^{-u/2}$, we have

$$\frac{dv}{dt} = -\frac{\xi\Sigma_s}{2}v^2 \tag{2.61}$$

Integrating, it follows that

$$t = \frac{2}{\xi\Sigma_s}\int_v^{v_o}\frac{dv}{v^2} = \frac{2}{\xi\Sigma_s}\left(\frac{1}{v} - \frac{1}{v_o}\right) \tag{2.62}$$

If $v \ll v_o$, then

$$v(t) = \frac{2}{\xi\Sigma_s t} \tag{2.63}$$

By replacing the velocity in the formula of the kinetic energy $E = m_n/2v(t)^2$ we have

$$E = \frac{2m_n}{\xi^2\Sigma_s^2 t^2}v(t) = \frac{2}{\xi\Sigma_s t} \tag{2.64}$$

The derivation of this equation presupposes that the neutrons have a definite energy at every time, which is only valid for very large A, where the average lethargic decrement ξ is very small.

From the Eq. 2.63 we can extract the relationship between the energy of the neutron that is being moderated and its time, for $A \gg 1$ the mean energy at a fixed time t is given by

$$\overline{E}(t) = \frac{m}{2}\frac{A(A+2)}{(\Sigma_s t)^2} \cong \frac{mA^2}{2(\Sigma_s t)^2} = \frac{A^2}{(\Sigma_s t)^2}\,0.522\mu\,sec^2\,cm^{-2}\,eV \tag{2.65}$$

and its dispersion is given by

$$\overline{\left(\frac{\Delta E}{E}\right)^2} = \frac{\overline{E^2} - \overline{E}^2}{\overline{E}^2} \cong \frac{8}{3\,A} \tag{2.66}$$

This equation shows that the energy spectrum during moderation in heavy substances is always very sharp. This sharpness is a result of the nearly continuous nature of the slowing-down

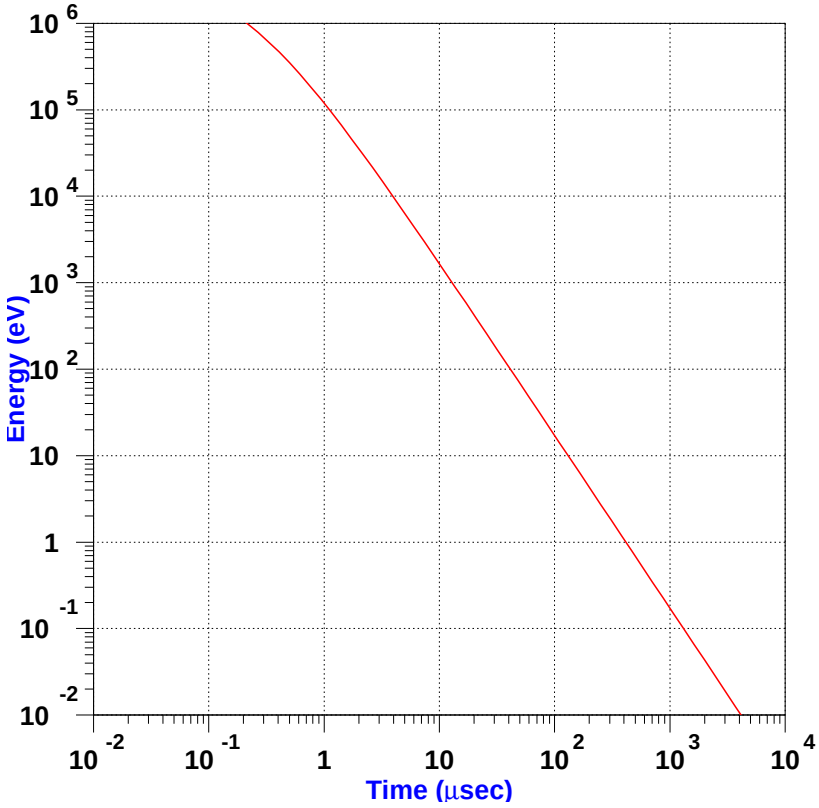

Figure 2.12: Energy-Time relation for *Lead* moderator

process. For lead $(A = 207)$, for example, $\sqrt{\overline{(\Delta E/E)^2}} = 11.4\%$. A more accurate calculation of the Energy-Time relation is done by R.E.Slovacek et al. [9] giving the formula (Fig. 2.12)

$$E = \frac{K}{(t + t_o)^2} \tag{2.67}$$

where the parameters K and t_o depend on the initial energy of the neutron and the moderator involved.

$$K = \frac{m\lambda_s^2(1-a)^2}{2\,a^2} \quad \text{and} \quad t_o = (1-a)\frac{\lambda_s}{a}\sqrt{\frac{m}{2E_o}} \tag{2.68}$$

where a is given by Eq. 2.12 on page 10.

An important quantity that we can extract from Eq. 2.63, is by multiplying the velocity $v(t)$ with the neutron time t. This gives us a constant number λ with units of meters.

$$\lambda = v(t)\,t = \frac{2}{\xi\,\Sigma_s} \tag{2.69}$$

and the uncertainty $d\lambda$

$$\frac{\Delta E}{E} = 2\frac{\Delta\lambda}{\lambda} = 2\frac{\Delta t}{t} \tag{2.70}$$

For the case of lead $\lambda = 5.7 \pm 0.327m$, Fig. 2.13 shows the distribution of λ as a function of the neutrons energy. This unit, λ, is frequently used in neutron TOF facilities to describe the resolution of the device. Instead of describing the uncertainty in energy from the energy-time

relation, is more convenient to assume that the error in time is zero (no moderator material exists) and all the neutrons are born at a distance $\lambda \pm \Delta\lambda$, with initial energy equal to the energy when the neutron exits. Since this quantity is not so strongly correlated with the energy (for energies below several keV), it provides a good measure of the resolution of the TOF facility.

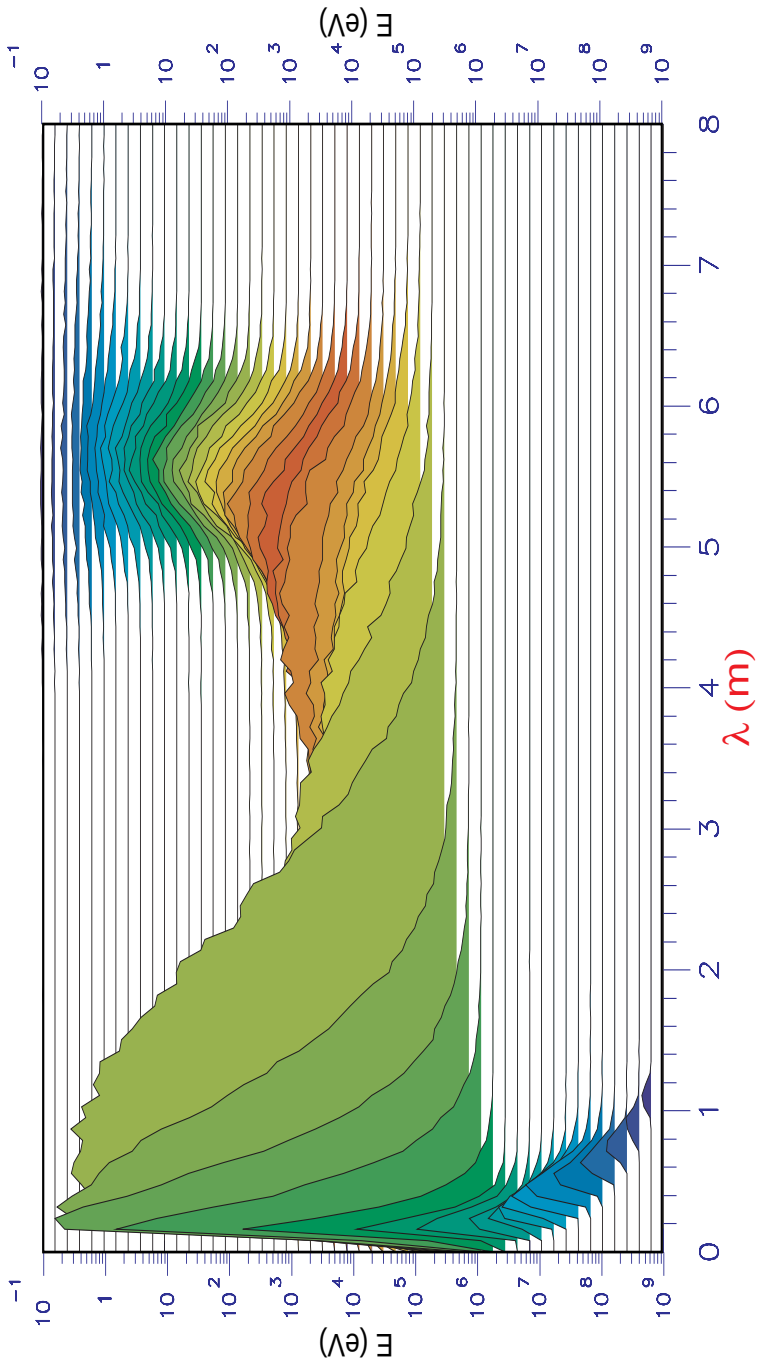

Figure 2.13: Montecarlo distribution of the equivalent neutron path inside the moderator, evaluated at the energy of observation. The narrow clustering for energies $\leq 10^4\,eV$ is evident. For higher energies, the isolethargic model breaks down due to the emergence of inelastic channels and the distribution broadens up. At higher energies, it narrows again.

2.10 Neutron Production Mechanisms

The hadronic mechanisms responsible for the production of primary and secondary neutrons are the following:

Spallation Is the initial phase for the neutron production, consisting of a series of interactions particle-nucleons (intra-nuclear cascades [10]). The spallation neutrons from lead have a constant behavior, for proton energies above 1 GeV giving on average 30 $n/p/GeV$. Fig. 2.14 gives the neutron yields, as a function of the kinetic energy of the proton beam, from Lead and Beryllium infinite moderators. The generated neutrons are described by the evaporation model.

Evaporation For neutron energies above a few MeV, the inelastic reactions reactions like (n, n'), (n, xn), can produce secondary neutrons. The secondary neutrons from (n, xn) inelastic reactions are described by the evaporation model, giving an isotropic distribution of velocities, with a peak around the MeV region.

Fission Is the most well known neutron production mechanism, used in all nuclear reactors. When a nucleus reaches the critical energy needed for fission, it splits up into two or more fission fragments and some secondary neutrons. This critical energy can be reached in a variety of ways. Two are the most important (a) absorption of a neutron (n,f) reaction, and (b) the absorption of a γ-radiation, photo-fission. A more analytic description of the evaporation model and the fission, as well the implementation inside the *Monte Carlo* code can be found in § 3.8.7 on page 45.

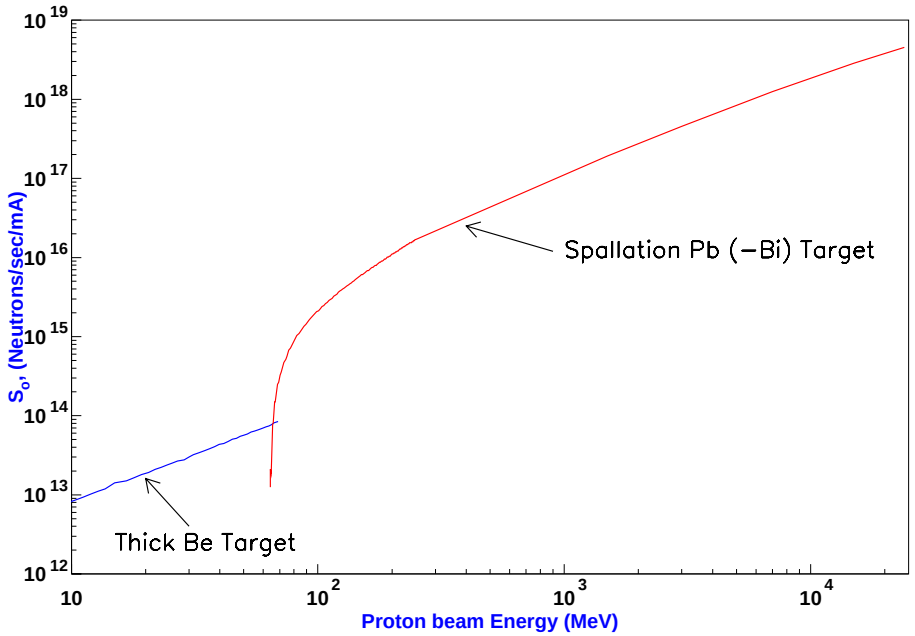

Figure 2.14: Neutron yield S_o for 1 mA proton current, as a function of the kinetic energy of the proton beam, for an infinite moderator of Lead and a thick Beryllium target.

Chapter 3

Computer Simulation

The sequence of phenomena ranging from a high-energy proton induced cascade in lead, to the production of neutrons that subsequently interact until they are finally absorbed or escaped from the system, is rather complex. For a correct simulation of the *Energy Amplifier* [1] it is essential to understand the fine details of the physics related to all these phenomena. This is one of the main purposes of the *TARC* experiment aimed at the study of the spallation neutron phenomenology in a large lead volume.

A complete understanding of this phenomenology can only be achieved if it is possible to predict correctly the observed behavior of the entire system. In order to do so, an innovative simulation was developed for the *Energy Amplifier*, using *Monte Carlo* techniques, initially by C. Rubbia. This code allows the description of complicated geometries and material compositions. A special attention was devoted to the development of techniques (for kinematic calculation, cross section evaluation, etc.) to minimize the computer time in order to provide sufficient statistics. In the case of the *TARC* simulation, a computing time of 20 μs/neutron per single process per processor, was achieved on the CONVEX supercomputer of type SPP 1200 with 8 parallel processors.

Since the simulation represents a new approach and is highly complex, it needs to be validated. In this respect, *TARC* is an ideal benchmark not only for *TARC* simulation code but also for any *ADS* simulation, since it provides many different measurements generally more precise than previously available simulation predictions.

3.1 The Choice of the Simulation Strategy

The study of accelerator driven fission machines, and similarly of an experiment such as *TARC* where the neutron source, is the result from the high-energy proton beam, calls for a new approach to the well-established problem, of neutron transport in nuclear reactors. Computer programs used for this, and in general for all neutron multiplying devices fall in two broad categories:

- *Deterministic codes*
- *Monte Carlo codes*

3.1.1 Deterministic Codes

Deterministic algorithms are based on the solution of the neutron transport equations. To make the problem amenable to a computer solution, a discretisation is used both in space and in

energy. These codes operate on a spatial grid and on a fixed number of energy *groups*. While this approach has shown its viability in many applications[1], it suffers from some drawbacks, which become important in the case of a sub-critical device coupled to a particle accelerator.

The neutron source is usually given in terms of a neutron energy spectrum, which has then to be converted into an energy-space grid, introducing an approximation.

Variations in the neutron energy are described by a transition matrix among different energy groups called scattering matrix. Non-fission multiplying processes of the kind (n,Xn) are poorly handled by this formalism, when not totally ignored.

The fine interplay of the interaction probability peaks (resonances) is of great importance, particularly for fast hybrid systems, and when interaction probabilities are averaged in the energy groups some effects may be lost or badly modeled.

Deterministic codes usually describe the working conditions of the "associate critical device", which is a good approximation if the system under study is close to criticality, but may be very distant from reality when the system is sub-critical.

The spatial resolution is limited, as space is discretised by a grid. Most of these codes are bi-dimensional, while the few available three-dimensional codes usually require a large amount of computing resources, leading to large computation times.

Activation can be handled only "off-line", using the calculated neutron fluence, but again through some averaging in space and energy due to the group structure, which necessarily introduces approximations which may be difficult to control.

The fuel composition does not change during the transport, and so the evolution of the fuel can only be described by several runs alternated with "off-line" material evolution runs, where again the spectral and spatial effects are poorly modeled.

In summary deterministic models are well adapted to the simulation of the relatively well known critical systems, but they cannot be easily used in their present form to explore the new domain of the sub-critical accelerator driven systems.

3.1.2 Monte Carlo Codes

The second major approach to the simulation of fissioning systems is the *Monte Carlo* method, which can be used to simulate theoretically a statistical process, and it is particularly useful for complex problems that cannot be modeled by computer codes using deterministic methods. The individual probabilistic events that comprise a process are simulated sequentially. The probability distributions governing these events are statistically sampled to describe the total phenomenon. The sampling process is based on the selection of random numbers. In particle transport, the *Monte Carlo* technique is pre-eminently realistic (a theoretical experiment). It consist of actually following each of many particles from a source throughout their life, from birth to death. Probability distributions are randomly sampled using transport data to determine the outcome at each step of the particles life. When point-like cross sections are used, the *Monte Carlo* is free from almost all the drawbacks of the deterministic codes, but its precision varies inversely with the square root of the number of events processed. This represents a potentially large problem of CPU time, particularly when several simulations are required at several moments in the life time of a power producing system.

In particular, the sampling of the interaction length, which takes place at every propagation of a neutron, requires a computer time that grows linearly with the number of elements.

[1] it is widely used to simulate critical reactors

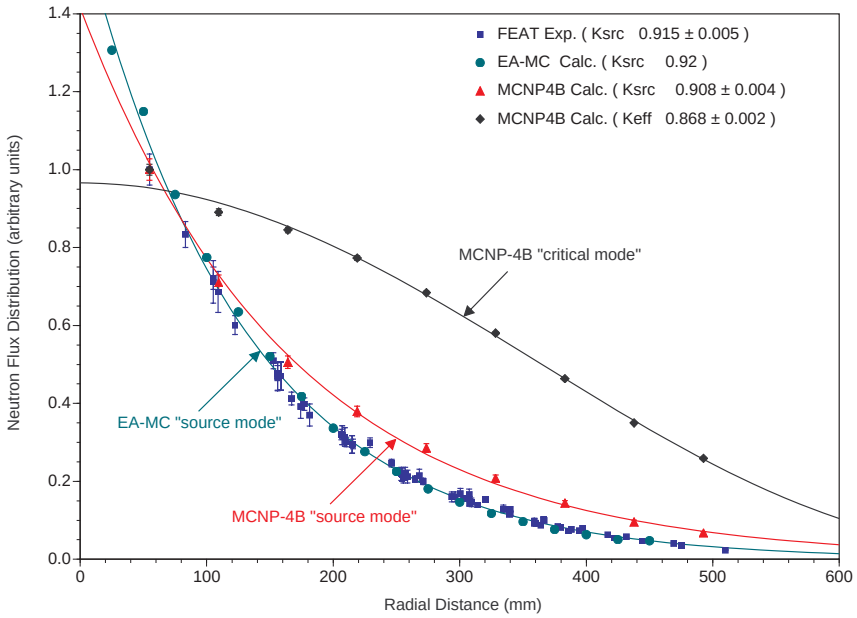

Figure 3.1: Comparison of the neutron flux radial distribution between experimental data and *Monte Carlo* calculations in the 'source mode' with the EA-MC and MCNP-4B codes, and in the 'reactor mode' with MCNP-4B.

3.2 Theroretical Considerations

One reason why the simulation tools developed for nuclear reactors cannot be applied directly to external driven systems and to the *Energy Amplifier* in particular [11], is that the spatial distribution of the neutron flux is expected to be radically different in the two cases. While in a critical reactor the flux distribution inside the volume is determined essentially by the boundary conditions, in an *Energy Amplifier* the effect of the initial high-energy cascade is dominant.

In such arrangement the neutron flux along any radial direction starting from the beam axis must fall off in an approximately exponential manner. The corrections to the exponential behavior depend primarily on the shape of the source and are important in the region close to it.

In addition, one cannot use the 'critical reactor' formalism in order to describe a system, since all 'modes' of the neutron fluence distribution must be evaluated. Using only the principal mode results in underestimating k (the neutron multiplication factor) since the escape probability is enhanced by the 'cosine-like' distribution of the fundamental mode while the real distribution is exponential-like.

This point has been proven experimentally by the FEAT [3] experiment at CERN, with a $k \approx 0.91$ system. In particular, Fig. 3.1 shows that *Monte Carlo* calculations give an excellent agreement with experimental data (FEAT experiment, $k \approx 0.915$), while the same calculations in the 'reactor mode' with MCNP-4B [12] give large disagreements with the measurements ($k \approx 0.868$).

3.3 Building Blocks of the Monte Carlo

The *Monte Carlo* code developed at CERN, was aiming to the following requirements:

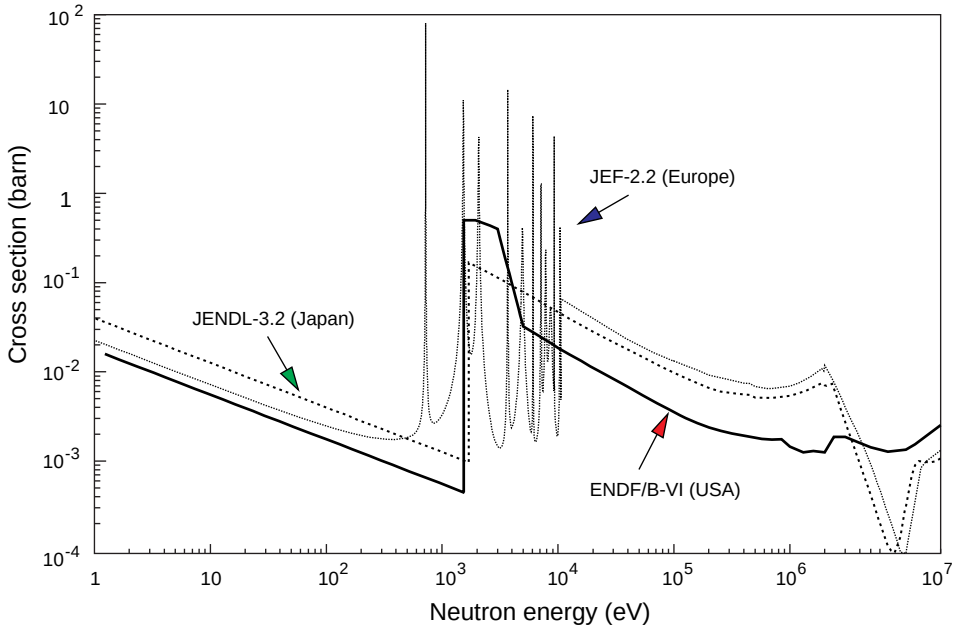

Figure 3.2: Comparison of the ^{137}Cs capture cross section in the different databases available.

- Modelisation of the high energy cascade and neutron production via spallation;
- Transport of low ($E \leq 20\ MeV$) energy neutrons;
- Description of the changes in chemical composition (structural material, fuel) due to neutron fluence and the high energy cascade and subsequent nuclear decay.

In the development of a neutron transport code the neutron cross section data have a special importance, as the physics is not expressed with models but rather in term of tabulations.

3.3.1 Neutron Cross Sections

The neutron cross section data files are taken from the latest compilations available [13]: *ENDF-B/VI* (USA), *JENDL-3.2* (Japan), *JEF-2.2* (Europe), *EAF-4.2* (Europe), *CENDL-2.1* (China), *EFF-2.4* (Europe) and *BROND-2* (Russia). The input to the *Energy Amplifier* Monte Carlo code is taken from the original data files. This has given us the possibility to generate any nuclide at any temperature and to upgrade our cross section database whenever a new version of the original files is available.

For each nuclide, the *TARC* group selected one evaluation out of those available based on a systematic comparison [14]. In practice, the selection was done isotope per isotope according to the evaluation of the resonances and the number of reaction cross sections. Fig. 3.2 shows the capture cross section of ^{137}Cs from the different databases available. The one chosen for the case of *Energy Amplifier Monte Carlo* corresponds to the European Database *JEF-2.2*. When both the resonance region and the number of cross sections evaluated are similar, then the most recently evaluated cross section was selected. This resulted in a database of 800 nuclides with neutron reaction cross sections. For all nuclides, the corresponding information on isomeric state exists, and isomer dependent reactions are treated correctly whenever they are available.

Activation/Transmutation data for unstable nuclides are taken from the *EAF-4.2* compilation that we have converted to ENDF format [15], including (MF) files: 8 (Radioactive decay

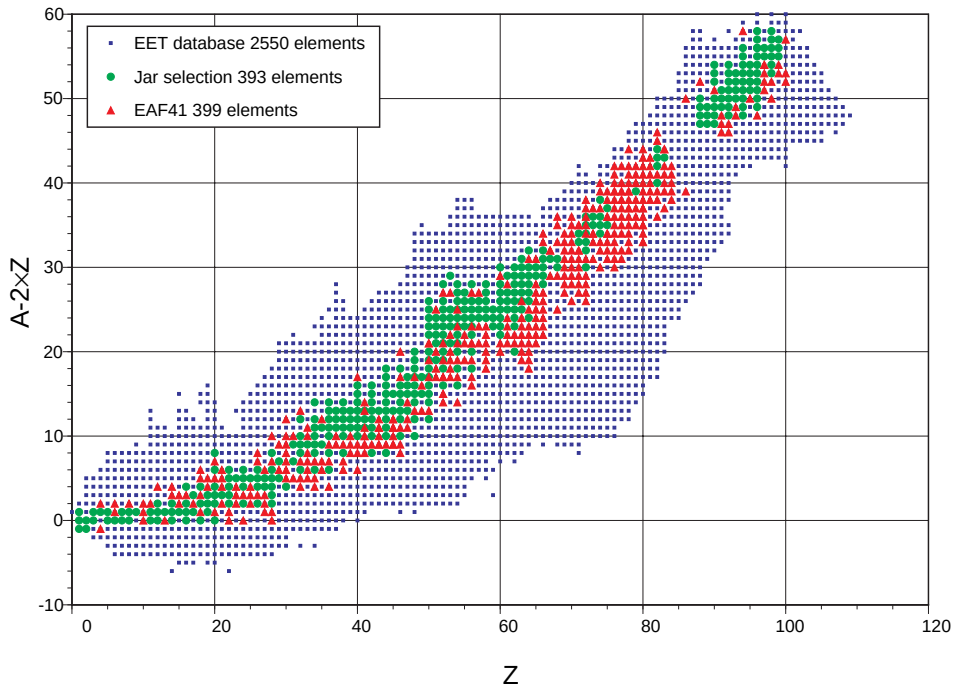

Figure 3.3: Summary of the element content in the EET Nuclear Database, illustrated by a plot of A-2Z versus Z, showing the larger extent of the EET Database.

and fission product yield data), 9 (Multiplicities for production of radioactive elements), and 10 (Cross sections for production of radioactive nuclides).

All cross section files have been processed and checked for inconsistencies with the standard PREPRO-96 [16] code suite (LINEAR, RECENT, SIGMA1 and FIXUP) including *EAF-4.2*.

All cross section files produced by PREPRO-96 have been subsequently processed with the code package PROCESS [17] to create a direct access library containing: neutron cross sections, cumulative secondary neutron energy distributions and cumulative neutron angular distributions.

The Evaluated Nuclear Data Files contain not only energy-dependent interaction probabilities, but also a wealth of other information concerning neutron transport. Auxiliary routines [18] have been developed to sample several quantities of interest during transport: the products of a reaction, including the isomeric state of the residual nuclei; the mass-correlated fission fragments in case of fission, the energy-dependent number of neutrons emitted in a fission and the angular and energy distributions of secondary neutrons emitted in non-fission reactions. The retrieval of all these quantities has been carefully optimized in order not to penalize the execution time of the program.

Cross section data Doppler broadened at different temperatures can be present at the same time in memory for the same isotope.

3.3.2 Nuclear Data

For nuclear transmutation studies accurate mass, and decay tables are needed. Here again the *TARC* group decided to go to the source of the data and to create a nuclear database from the most updated compilations available: the Brookhaven nuclear database, the NUBASE by AUDI et al. [19], the National Radiological Protection Broad (UK) database, the International

Committee for Radiation Protection databases, and the informations contained in the ENDF data files. The data base contains detailed information on the mass levels, the half lives and the decay channels, including the probability of decaying into an isomeric level of the daughter nucleus, and the latest compilation of ingestive and inhalation toxicity. This database is probably the most extensive and effective summary of nuclear data available at this time (Fig. 3.3).

3.3.3 Visualization

The large amount of work needed to select a consistent set of cross section data made it necessary to develop appropriate visualization tools [20] to help explore the databases. It happened that simple visual inspection of a given cross section was enough to detect technical problems such as the mismatch between energy ranges.

3.4 Structure of the Program

In the *Energy Amplifier* system the geometrical description is first automatically translated into the *FLUKA* combinatorial geometry. Then the *FLUKA* simulation is performed. Neutrons are transported down to 20 MeV and then handed over to the *Energy Amplifier Monte Carlo* that continues the transport. Neutrons are transported in time steps that vary in an adaptive way, each one including a given number of protons.

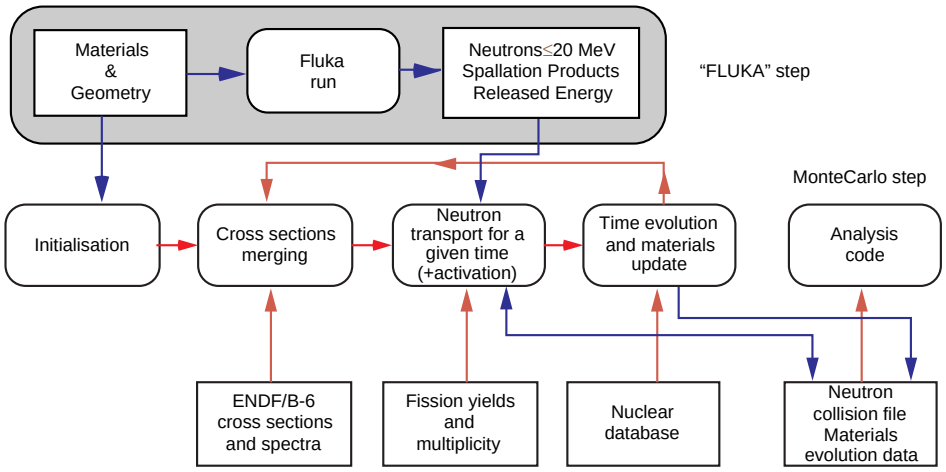

Figure 3.4: General architecture of the *Energy Amplifier* simulation program.

The general architecture of the *Energy Amplifier Monte Carlo* program is shown in Fig. 3.4. The material composition is updated based on the neutron interactions simulated in every zone. Material composition evolution due to nuclear decay is performed between transport steps. High energy spallation products generated by *FLUKA* are added to the material composition on each transport step. The contribution of all fission, spallation, decay and activation products is considered during neutron transport, no "lumped" fission products are used in our code. Every material can have a different temperature that will be the same of all the species produced there. New temperatures can be generated during the run either by Doppler broadening or by linear interpolation of existing evaluations.

The cross sections are used directly, without any averaging. This poses an enormous challenge to execution time. For instance the (n,γ) cross section of ^{232}Th alone contains more than

60000 points. To be able to contain the execution time, the sampling of the reactions has been optimized. A clever algorithm allows a fast evaluation of the next interaction point, independently from the number of elements in the material. Once the interaction point has been determined, a careful dynamic allocation of the internal pointers allows a fast sampling of the target nuclide and of the reaction channel.

All samplings of the energy and angle of produced neutrons are done from tables, with one single random number per extraction. The routine for elastic scattering has been particularly optimized and it can perform a scattering with thermal motion of the target nucleus in few μs. At the end of every transport phase, all materials are evolved during the time step. The underlying assumption is that the material composition changes very little during the time step. As the gradient of change depends on the burn up phase, the time step changes during burn up. To avoid all approximations in the concentration evolution, a complete solution to the Bateman equations involving thousands of elements is computed. A combination of storage techniques and decay chain algorithms allows to evolve all materials in few seconds. No time stepping is used, the solution is analytically correct within the assumptions made. Different smoothing techniques have been developed in case of very short lived elements or strong concentration gradients. The algorithm has been checked for stability against different time steps.

3.5 The Parallel Environment

One of the main problems of *Monte Carlo* codes, is the control of the statistical fluctuation intrinsic to the sampling method. The usual solution is to run several *Monte Carlo* runs and to evaluate the dispersion and the average of the results. The limitation of this technique is the time taken for the different runs. To improve the performance of the code, the programs was adapted to run, on a parallel machine, Convex SPP 2000 with 16 processors. One of the parallel versions developed was based on the so called "*shared memory*" approach Fig. 3.5. Several processors share part of the storage and the access to the shared resources is synchronized. While this version showed a substantial performance improvement, its performance did not behave linearly with the number of processors, hindering the full exploitation of the power of our machine.

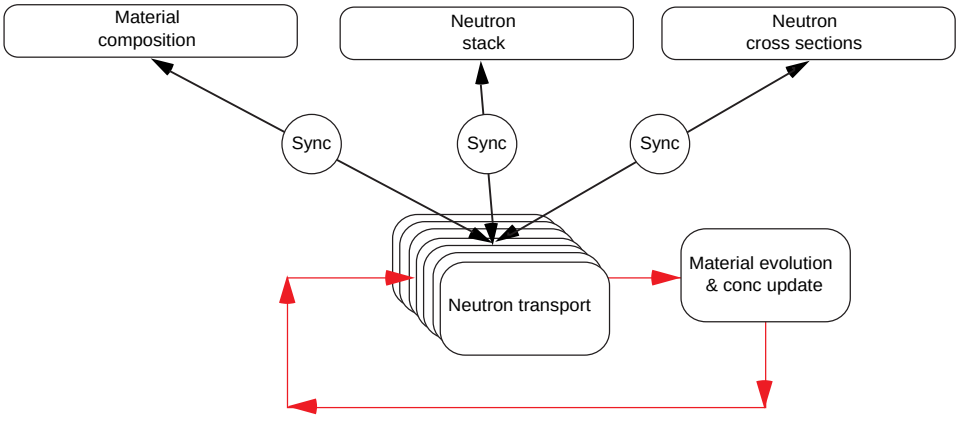

Figure 3.5: Structure of the parallel version of the *Energy Amplifier* program using the Shared memory approach.

Thus, a second parallel version of the code Fig. 3.6 was developed, in which several copies of the program are run in parallel and each one writes it's own summary file. Separate programs

(also parallel) can be run to analyze the data and compute the dispersion around the average, while the production is running. Each processor initializes its random number generator to a different, independent sequence. The parameters of the run are broadcast to all the processors, then there is no further interaction between the processors.

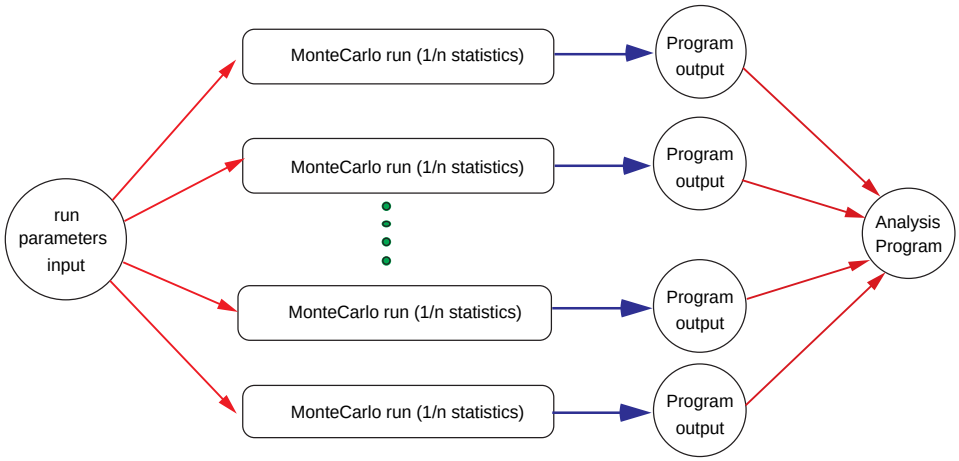

Figure 3.6: Structure of the parallel version of the *Energy Amplifier* program using the distributed memory approach.

This second approach is more versatile and its effectiveness augments linearly with the number of processors. More over the code is more easily adaptable to other different types of operating systems. The only drawback of this method is the memory required since each process needs to load separately all the cross sections necessary.

3.6 Fluka - High Energy Transport

In practice, the spallation neutron source distribution is generated by FLUKA-96 [5]. Neutrons are transported by FLUKA down to an energy of 19.6 MeV and then are written into a history file. 19.6 MeV is selected for neutrons as being just below the upper limit (20 MeV) of neutron cross section data sets, thereby easing the transition to fast neutron transport codes.

In the energy range, from the pion production threshold ($\approx$ 290 MeV for a free nucleon, down to 200 MeV for nucleons in nuclei because of the Fermi motion) to high energies, IntraNuclear Cascade (INC) models are practically the only available tools, to model hadron-nucleus interactions. At lower energies, a variety of pre-equilibrium models can do a very good job, with physics foundations that become more robust than INC codes, as the energy decreases.

It is important to note that in principle, IntraNuclear Cascade (INC) codes like FLUKA are able to compute reaction cross sections by themselves. Indeed, the reaction cross section is given by the product of the geometrical cross section by the probability of interaction.

The basic assumption in calculations of intra-nuclear cascades is that nuclear reactions involving incident particles of high energy can be described in terms of hadron-nucleon collisions within the nucleus. Therefore, a description mainly phenomenological, of hadron-nucleon interactions is essential in understanding the following more complex treatment of nuclear interactions. A typical INC code usually adopts the following logic:

- target nucleus description, typically realized through a few concentric spheres of different density and Fermi energy;

- geometrical cross section, corresponding to the nuclear radius or to the maximum possible impact parameter;
- impact parameter selection with a constant probability over the geometrical cross section area. More than one selection can be required if the particle crosses the nucleus without interacting;
- interaction point selection and projectile tracking through the nucleus, according to Fermi motion averaged hadron-nucleon cross sections and possibly to the nuclear mean field, including the Coulomb field;
- target nucleon selection according to hadron-pion and hadron-nucleon cross sections and local Fermi energy;
- interaction simulation according to free hN interactions, local Fermi energy and Pauli blocking;
- secondary tracking into the nucleus, until interaction, escape, or energy cut-off;
- pre-equilibrium stage, whenever all excited nucleons are below a given energy threshold (typically a few tens of MeV). This stage is included only in the most recent developments;
- evaporation stage whenever the pre-equilibrium stage is finished, or all particles are below a given threshold (usually of the order of the binding energy), and the system can be assumed to be equilibrated;
- final deexcitation stage when the excitation energy is below the threshold for particle emission and it is spent through photon emission. A more detailed description of the physics involved in all stages can be found in Ref. [10].

3.7 Low-Energy Neutron Transport

Transport of neutrons below 19.6 MeV is performed with the *Energy Amplifier Monte Carlo* code:

- neutron transport is done in time steps which vary adaptively according to the burn up phase, each step corresponding to a given number of incoming protons (typically a few hundreds);
- the material composition is updated according to the neutron interactions simulated in every material zone;
- material evolution is performed between transport steps;
- high-energy spallation products coming from FLUKA are added to the material composition on a proton by proton basis;
- the contribution of all fission, spallation, decay and activation products is considered explicitly during neutron transport, no lumped fission product is used;
- every material can have a different temperature, new elements generated in that material will have their own temperature. New temperatures can be generated during the run either by Doppler broadening or by linear interpolation of existing ones.

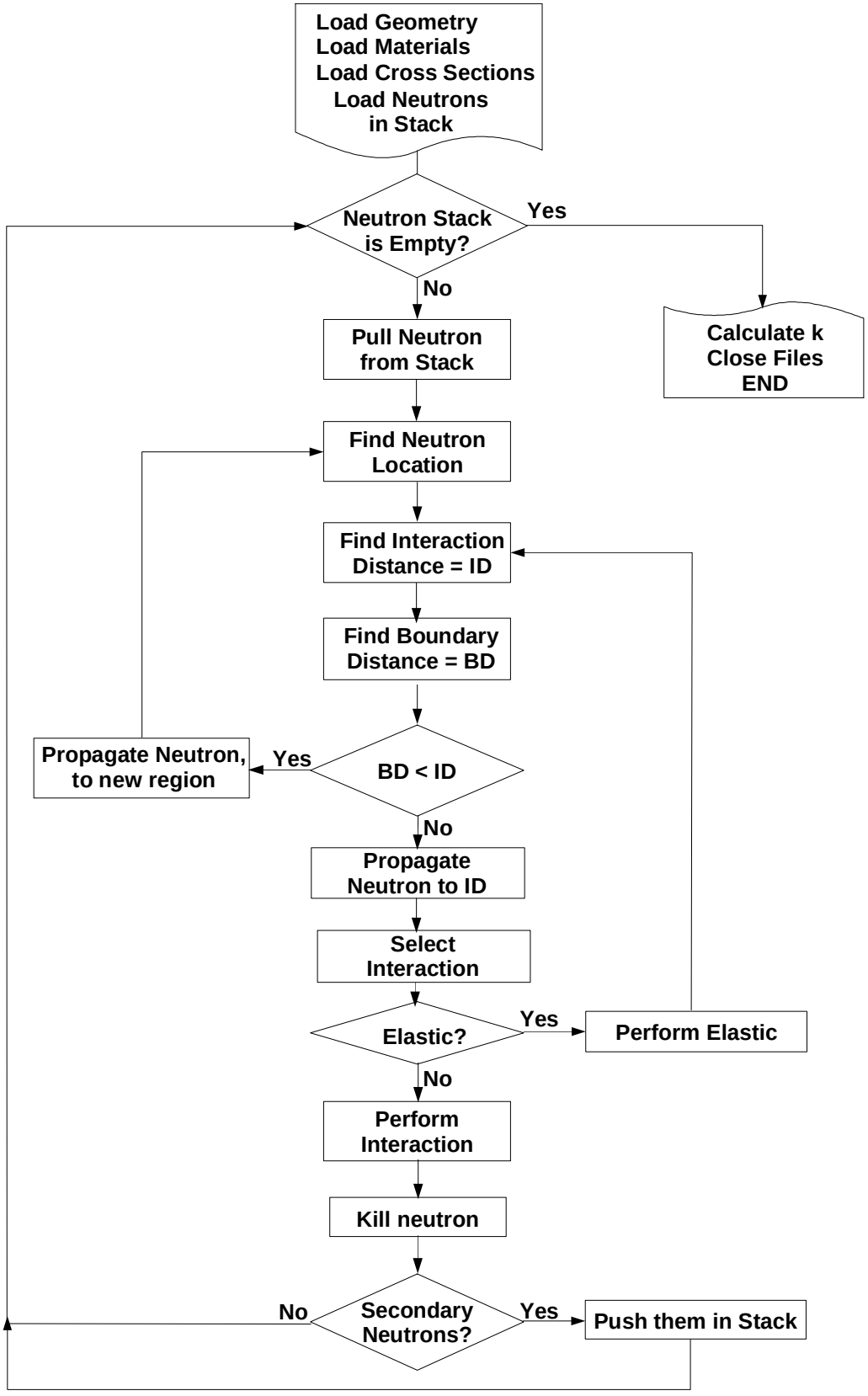

Figure 3.7: Flow chart of the *TARC Monte Carlo* program.

3.8 Monte Carlo Program

The *Monte Carlo* code used to simulate the *TARC* experiment is a version of the *Energy Amplifier Monte Carlo* where the time evolution has been switched off [21]. The program is able to transport neutrons with energies below 20 MeV where neutron nuclear data are available. The Fig. 3.7 shows the general flow chart of the *Monte Carlo* program. In the initialization process, the program loads all the necessary informations about the geometry and the initial source of neutrons. After the initialization, the program continues with the main loop where, one by one, all the neutrons are transported until they are finally absorbed or escape from the system. The program terminates, when no more neutrons are left to process. In the next sections follows, a more analytic description of all the parts of the program.

3.8.1 Initialization

In the initialization process, the program reads the input file with the definition of several parameters (temperature, track length, detectors, etc.) and the associated files (geometry, materials, elements, cross sections, and neutron source). The initial neutron source can be either FLUKA neutrons[2], or neutrons collected in a Data Summary Tape (DST), or from a previous run of the *Monte Carlo* program.

The geometry of the detector to be simulated is described with the use of simple primitives[3]. The current version of the program supports only sphere, cylinder, box, and cone. The geometry follows a tree like scheme, with the head object being the father, which contains all the sub-volumes (branches). With the restriction that logical operations (union, intersection, subtraction) are not allowed between the volumes. Therefore complex geometries are rather difficult to be simulated. Each region is defined as the subtraction of all the daughter objects from the father volume. For each region, a material can be assigned, from the materials file.

The material file defines compounds, mixtures or simple elements. A unique identity number and a name define each material, followed by the density, and all the isotopes that consists the material and their relative mass fraction. The *Monte Carlo* has been optimized to use lead as the main material, where the neutrons will spend most of their life. Because of this special treatment, lead material must always be placed in the first position of the file, having also a definition that is slightly different from the rest of the materials. The user must assign a value of 1 as a mass fraction of the natural lead element, and the *ppm* values of all the impurities (see § 4.2 on page 53). The program will later re-normalize the mass fraction of lead.

The *TARC Monte Carlo* is using point-wise cross sections, which are loaded from a pre-processed file, and stored in binary format for faster access. For each nuclide we have selected one evaluation for each neutron cross section, which seemed more reliable (§ 3.3.1 on page 32). All these selected evaluations where processed with the standard suite of programs (PREPRO-96) for several temperatures, namely 0^oK, 293^oK, 723^oK, 900^oK, and 1300^oK. The pairs (energy, cross section) were selected such as to allow an error of less than 1% for the energies which are interpolated linearly. The lead neutron cross sections with the impurities are loaded from a separated file (*Tubro.dat*) containing, in a common energy grid the total macroscopic cross section, elastic cross section in lead, and the inverse path length.

[2]By FLUKA neutrons we refer to the output of a FLUKA run. These neutrons are those, which are after their transport they have reached the threshold value of 20 MeV.

[3]basic geometrical objects like sphere, box etc.

3.8.2 Main Loop

The main loop is the heart of the *TARC Monte Carlo* program, where all the neutrons are followed (transported) until their death (absorption or exiting from the system). The program starts by pulling one by one the neutrons from the neutron stack and decides for its fate based on probability distributions depending on the position and energy of the neutron.

When a neutron starts from a source (fluka neutrons or from previous *Monte Carlo* runs) a particle track is created. The program loops until all the particle tracks are terminated (when no more neutrons are left in the stack). Reactions like (n, xn) and fission can produce more neutron tracks, that are again pushed in the neutron stack for further processing.

In order to increase the statistics, the initial neutrons can be propagated by the program a number of times, with the use of different random numbers in each run. This method is valid, since after a few elastic collisions with lead, the neutrons are completely randomized, following a completely different track from the one of the previous runs.

In the main loop, the user can extract information by assigning estimators[4] either to specific regions, or to the complete assembly. Among the various output mechanisms, the most useful are the track length, energy deposition, surface crossing, and reaction estimators.

The track length estimators are used for calculating the neutron fluence. The flux is given as the ratio between the total path length of all the particles that crossed the region, and the volume of the region.

$$\Phi(E, E+\Delta E) = \frac{\sum_{i=1}^{N} l_i(E, E+\Delta E)}{V} \tag{3.1}$$

where $\Phi(E, E+\Delta E)$ is the neutron flux in the energy region from E to $E+\Delta E$, $l_i(E, E+\Delta E)$ the track length of a neutron crossing the specified region with energies between E and $E+\Delta E$, and V is the volume of the region. This method is correct, as long as, the region is small enough, and the neutron flux is uniform in all the volume.

Surface crossing estimators are also used for calculating the neutron fluence, or better the neutron current.

Energy deposition estimators, are storing in a PAW [22] *n-tuple*, the position of a reaction and the deposited energy. These kinds of estimators are useful for creating 3D maps of the deposited energy.

Reaction estimators are storing the position, the energy of the neutron and the reaction type. With this way, we can create histograms to visualize the reactions as a function of the neutron energy. This procedure it can be applied to all kind of reactions, except the elastic scattering (Due to the huge number of elastic reactions, the storage capacity of the program is insufficient).

3.8.3 Geometry

Since no *Monte Carlo* is more precise than the three-dimensional geometrical description of the system simulated, a large effort has been devoted to the development of computable geometrical models. Different libraries of 3-Dimension geometrical modeling routines have been constructed for different configurations of the Energy Amplifier, the lead volume of *TARC* experiment [21] and the various detectors. Particular attention has been paid to efficiency: typical execution times have been kept around a few μs per routine call.

In all cases two geometrical procedures have been provided. The first one determines the volume in which a point is located, and hence its material. A careful hierarchical organization

[4] *Estimator* is a computer term, defining the various "scoring" mechanisms used in the *Monte Carlo* codes for creating histograms, or logging information about specific type of events. In some other Monte Carlo codes, they are also called *tallies*.

of the volumes and the exploitation of the symmetries of the system allow this routine to be particularly fast (typical call times are between one and three microseconds). Once the information on the location of the point is collected, the distance to the next boundary along the fly-path is returned by another routine. Particular attention has been devoted to treat the limiting cases such as trajectories tangent to a cylinder or parallel to a plane, to avoid arithmetical errors and always provide a meaningful and conservative answer.

A difficult problem has been the handling of boundary crossing during transport. When the geometrical step is chosen, i.e. the particle proceeds un-collided to a boundary, the step length is artificially increased. This increase is done by a quantity comparable with the computer's precision in order to avoid rounding errors and "oscillations" on the boundary that could slow down transport or lead to the loss of particles. Special cases like lattices of bars have been treated by reduction to a plane and local rotations to maximize computing speed.

Voxels optimization

In the case of the *TARC* experiment, since there were many and completely different detectors, I have followed a different approach, to ensure the versatility of input files and to have a routine fast enough. The technique used, was the voxels algorithm [23], a selective search algorithm by dividing the space in voxels.

In the initialization, the most complex objects are divided into a grid, for example $10\times10\times10$ of voxels. For each voxel of the grid that overlaps with another object either fully or partially, the volume information is stored in a 3D cache array.

When the distance routine is called, the program finds the initial voxel, where the neutron is positioned and the direction of its flight path. A simple and fast loop, using only one addition and a few *IF* statements, can determine the voxels that fall inside the neutron path. Hence, boundary checks are only performed with the specific volumes, which are overlapping with the voxels in the neutron trajectory. The process exits from the loop when an intersection is found, or when the voxel distance is larger than the interaction distance returned by the *fate* routine.

This approach can result in a speed-up, independent of the complexity of the geometry, because with the voxel algorithm the program is always searching for an intersection with only a specific number of volumes, those which are falling along the neutron trajectory. In the classical approach the increase in the computation time is linear, to the number of objects present in the geometry. Improvement in speed by factors up to 5 are easily achievable for moderate complexity geometries.

3.8.4 Interaction Distance

Within a given region of fixed composition, the method of sampling a collision along the track is determined using the following theory. The probability of a first collision for a particle between l and $l+dl$ along its line of flight is given by

$$p(l)dl = e^{-\Sigma_t l}\Sigma_t dl \tag{3.2}$$

where Σ_t is the macroscopic total cross section of the medium and is interpreted as the probability per unit length of a collision. Setting r the random number in the unit interval $[0,1)$, to be

$$r = \int_0^l e^{-\Sigma_t s}\Sigma_t ds = 1 - e^{-\Sigma_t l} \tag{3.3}$$

it follows that

$$l = -\frac{1}{\Sigma_t}\ln(1-r) \tag{3.4}$$

But, because $1-r$ is distributed in the same manner as r, and hence may be replaced by r, we can obtained the following expression for the distance to collision

$$l = -\frac{1}{\Sigma_t}\ln(r) \tag{3.5}$$

The total cross section is obtained by binary searching from the array containing the pairs (energy, cross section) for all the isotopes present in the material. The binary search for 2^n items, has to perform an average number of searches of

$$< \text{depth} >= \frac{\sum_{i=1}^{n} i2^{i-1}}{2^n} \tag{3.6}$$

ie. around 15 steps, are needed for an isotope with a cross section, which contains around 100,000 points. This number of steps increases proportional, to the number of isotopes in each material.

To speed up calculation, given the small lethargic loss of neutrons in elastic collisions with lead, the last upper boundary of the energy bin is recorded as well as the inverse of the width of the energy bin. If the neutron is still in the same energy bin, the binary search is skipped. If the neutron has an energy smaller than the previous upper limit, which is always the case, apart from up-scatterings and new neutrons, a sequential search is done for the next three lower bins. If the bin is not found, then the full binary search is started using, if possible, the previous upper bin. In the end, the new upper bin and the inverse of the width of the energy bin are stored.

As the number of elements in the lead is very high, the above process can be very slow. Noting that the large majority of reactions are elastic scatterings on lead, a faster approach has been introduced [24]. A separate program calculates once and for all four tables:

- the path length (inverse of the total macroscopic cross section);
- the fraction of the total macroscopic cross section due to non elastic scattering on lead;
- the fraction due to non elastic scattering on impurities;
- the fraction due to elastic scattering on impurities.

This is then written onto a file that is read by the *TARC Monte Carlo* program at initialization. These quantities share the same energy grid, so only one binary search is needed. Again the previous upper bin is kept to speed up search time. Sampling among these four main categories is done without having to construct at every interaction the macroscopic cross section. If the result is an elastic cross section on lead, then no further sampling is required, otherwise the remaining samplings are performed. This has enabled a gain of 15 in calculation time when compared with the previous routine.

If there are n different isotopes forming the material, in which the collision occurs, then the routine chose randomly the collision nuclide k, with the following probability

$$\sum_{i=1}^{k-1}\Sigma_{ti} < r\sum_{i=1}^{n}\Sigma_{ti} \leq \sum_{i=1}^{k}\Sigma_{ti} \tag{3.7}$$

where r is a random number in the interval $[0,1)$, Σ_{ti} is the macroscopic total cross section of nuclide i.

With the same way as for the selection of the nuclide, is also determined, the reaction r (elastic, inelastic, fission, absorption) that the neutron will perform on the selected isotope.

$$\sum_{r=1}^{r-1} \sigma_i < r\sigma_t \leq \sum_{i=1}^{r} \sigma_i \tag{3.8}$$

where r is the random number, r is the reaction to be performed, from all the possible exit channels (interactions, in our case this number is limited to 35), and σ_t is the total microscopic cross section.

90% of the computing time is spent into the routines *fate* and *distance*, so we gave special attention to optimize the code such as: a) redundant calls in the random generator routine are done only in one call, where the routine fills an array of random numbers. b) Most of the sub-functions like the binary searching, were inlined in the routines to avoid the overhead of calling a new routine. Usually such kinds of optimizations are the source of errors, and this was an extra reason for running a lot of test cases to ensure the robustness of the routines.

3.8.5 Elastic Scattering

The elastic scattering of neutrons with nuclei, is the most important process, because the elastic cross section is almost flat for most of the isotopes, with a large value of about 10 *barns*, compared to the other reactions[5]. For the elastic scattering, we have developed two routines. The first one uses isotropic scattering in the CMS system. This routine is used as a fast alternative, for the isotopes with small concentration (mostly impurities in lead), where the effect of the angular dependence can be neglected. The second routine takes into account the angular distribution, information that is available in the ENDF files. This routine, is used for a more accurate treatment of the neutrons with energies above the MeV region, where the elastic collisions are mostly forward peaked. The only disadvantage of this approach is the computation time. Tests we have done showed a delay up to 30% when we enabled the angular distribution for lead.

Since the thermal motion of the atom affects the collisions of a neutron with an atom, the thermal motion has been added in the treatment of the elastic scattering. In the *TARC Monte Carlo*, we use the free gas approximation, to take into account the effects of the thermal motion.

Even though the free gas approximation, assumes that the medium is a free gas, it gives accurate results even for solids (see SAMMY [25] manual). The free gas treatment consists of adjusting the elastic cross section, by taking into account the velocity of the target nucleus, when the kinematics of a collision are calculated. Note that the Doppler broadening of the cross sections has already been done in the processing of the cross section libraries.

During the calculation of the kinematics of a collision, the routine takes into account the velocity of the target nucleus. The velocity of the target nucleus, is sampled using a Maxwell-Boltzmann distribution, from a pre-normalized table, with an isotropic random orientation in the laboratory system (LAB). Then, the kinematics of the the collision are calculated in the Center of Mass System (CMS) (see § 2.2 on page 8).

In the CMS system, the first routine chose an isotropic random direction of the scattered neutron, where the second implementation of the elastic collision routine, samples the neutron direction from the angular distribution tables, based on the incident neutron energy. More specific, the cosine of the angle between the incident and exiting particle directions, μ, is sampled from the distribution tables that are available in the ENDF library, while the azimuthal angle is sampled randomly in the interval $[0, 2\pi)$. In the ENDF library, there are two ways of describing

[5] a neutron in an infinite lead moderator, can undergo $\sim$ 1800 elastic scatterings before it is captured.

the distribution (a) with the use of Legendre coefficients, and (b) with tabulated distributions [27]. In the initialization process, the program loads these informations from the associated *ENDF-B/VI* files and creates normalized tabulated distributions consisting of 101 equiprobable cosine bins. A random number r in the interval $[0, 1)$ is then used to select the cosine bin so as $i = 101 * r + 1$. The value of μ is then computed as

$$\mu = \mu_i + (101 \times r - i)(\mu_{i+1} - \mu_i) \tag{3.9}$$

which is then, interpolated linearly within the selected cosine bin. After the selection of the direction of the exiting neutron and the target velocity, we apply the two-body kinematics (see § 2.2 on page 8). At the end, the new neutron velocity is transformed back to the Laboratory System (LAB).

3.8.6 Inelastic Reactions

In the inelastic reactions, we include all the reactions that have at least one neutron in the exiting channels. These reactions, are generally defined as (n, xn), such as (n, n'), $(n, 2n)$, (n, f) etc. The treatment of inelastic scattering depends upon the particular inelastic reaction chosen.

In the inelastic reactions the initial incident neutron is always killed, while the new neutrons are pushed in the neutron stack. For many reactions, like $(n, 2n), (n, f)$, more than one neutron, can be emitted from every incident neutron. The energy and direction of the exiting particles, is governed by various scattering laws [27], that are sampled independently from the cross section files. Because the emerging energy, angle and products are sampled independently for each particle, there is no correlation between them. Hence, energy is not conserved for all the reactions while for the fission reaction, also the mass and the charge are not conserved. For example, a 10 MeV neutron can generate through a $(n, 2n)$ reaction two neutrons with 8 MeV. Because, there is no biasing in the histories of the different particles, the routine, in average gives the correct amount of energy (mass and charge) of the emitted particles.

For all the inelastic reactions except fission, the program is using two emission laws for sampling the energy:

- The first uses a tabulated distribution of the exiting neutron energy, which is normalized in the pre-processing of the neutron databases, into equiprobable energy bins. These are stored as two dimensional tables. There are NRANG values of incoming neutron energy and for each of them there are NPERC+1 values of energy of the outgoing neutron such that the probability for the neutron to have energy between one value and the next is 1/NPERC. A random number is sampled between 1 and NPERC+1 and this gives the interval. The value of the energy is chosen in this interval via a linear interpolation between the upper and lower energies of the sampled bin, using the fractional remainder of the random number. The final value, is then given from the interpolation, as a function of the incoming neutron energy. The values of NRANG and NPERC, are defined into the pre-processing code, and in the beginning in our case we have used a small value of 25 bins. This small number of the number of isoprobable bins, has introduced some problems, since the last bin was extending from 5.5 MeV up to 20 MeV. This was producing a small discontinuity of the flux in the MeV region, especially in the lower boundary of the last bin. The only solution was to re-process the neutron libraries, with a larger number of bins, increasing significantly the size of the cross section library. With the 25 bins, the size was 46MB. With 100 bins it reached the 51MB, and still the last bin was extending from 7.5MeV up to 20MeV (Fig. 3.8).

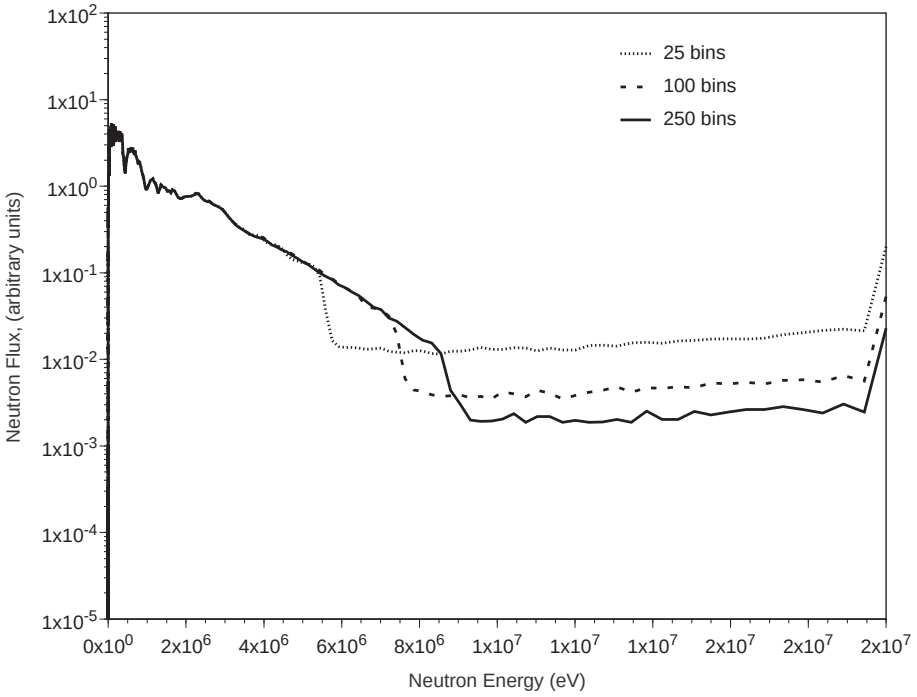

Figure 3.8: Neutron fluence versus energy for a different number of isoprobable bins, for the exiting neutron energy in inelastic reactions Ref.[26].

- When no tabulated information exists in the cross section files, the program is using the Evaporation spectrum.

$$f(E_{in} \rightarrow E_{out}) = \frac{E_{out}}{I}\, e^{-E_{out}/\Theta(E_{in})} \tag{3.10}$$

where the nuclear temperature $\Theta(E_{in})$ is a tabulated function of the incident energy. The normalization constant I, is given by

$$I = \Theta^2 \left[1 - e^{-(E_{in}-U)/\Theta}(1 + E_{in} - U)/\Theta)\right] \tag{3.11}$$

The energy U, is a constant introduced to define the proper upper limit for the final particle, so that E_{out} is limited by $0 \leq E_{out} \leq E_{in} - U$. The density function is sampled by

$$E_{out} = -T(E_{in}) \ln(r_1 r_2) \tag{3.12}$$

where, r_1 and r_2 are random numbers in the unit interval, which are rejected if $E_{out} > E_{in} - U$

After defining the neutron energy of the exiting particles, their direction is chosen randomly in an isotropic manner in the LAB system. After the processing, the existing neutrons are pushed into the neutron stack to be later handled by the transport code.

3.8.7 Fission

Since the number of exiting neutrons from fission is not constant, fission has a special treatment compared to the rest of the inelastic channels. For every fission reaction with an isotope, the

program selects the average fission neutron multiplicity $\bar{\nu}(E_{in})$, as a function of the incident neutron energy. This information is either, a tabulated function of energy, or a polynomial function of energy. After selecting the $\bar{\nu}(E_{in})$, the routine chooses randomly from a Poisson distribution the number of exiting neutrons. For each one of the exiting neutrons, the energy and direction are chosen with the same way as in the Inelastic scattering, provided that the information in the cross section file is stored as a tabulated distribution of energies, or as Evaporation spectrum. In the case of Fission the ENDF files use also another emission law, the energy dependent Watt Spectrum [27].

The probability $f(E_{in} \rightarrow E_{out})$, for selecting the outgoing energy E_{out}, from an initial neutron energy E_{in}, with the Watt Spectrum is given by

$$f(E_{in} \rightarrow E_{out}) = \frac{e^{-E_{out}/a(E_{in})}}{I} \sinh \sqrt{b(E_{in})E_{out}} \tag{3.13}$$

where, the constants a and b are energy depended tabulated functions of the incident energy and U is a constant from the library. The normalization constant I is given by

$$\begin{aligned} I &= \frac{1}{2}\sqrt{\frac{\pi a^3 b}{4}}\, e^{ab/4} \left[\mathrm{erf}\left(\sqrt{\frac{E_{in}-U}{a}} - \sqrt{\frac{ab}{r}} \right) + \mathrm{erf}\left(\sqrt{\frac{E_{in}-U}{a}} + \sqrt{\frac{ab}{r}} \right) \right] \\ &- a \exp\left[-\frac{E_{in}-U}{a} \right] \sinh \sqrt{b(E_{in}-U)} \end{aligned}$$

where, the constant U limits the range of the outgoing energy so that $0 \leq E_{out} \leq E_{in} - U$. This density function is sampled as follows.

$$f = \sqrt{\left(1 + \frac{ab}{8}\right)^2 - 1} + \left(1 + \frac{ab}{8}\right) \tag{3.14}$$

Then $E_{out} = af \ln r_1$. E_{out} is rejected if

$$[(1-f)(1 - \ln r_1) - \ln r_2]^2 > b\ E_{out} \tag{3.15}$$

where, r_1 and r_2 are random numbers in the unit interval. A more detailed description of the Watt and Evaporation spectra can be found in the ENDF manual [27].

Finally, the program gives a random isotropic direction for all the emitted neutrons, which are subsequently pushed into the neutron stack, for further processing.

3.8.8 Absorption

All the reactions that do not produce any secondary neutrons are considered as absorption. Since in the *TARC Monte Carlo*, only neutrons are transported, the program kills the incident neutron, and stores in a PAW [22] n-tuple all the relevant information including place of death, time, energy and the type of the reaction.

3.8.9 Finalization

When all the neutrons have been processed, the program terminates by closing all the opened files and updating all the necessary information for the estimators, histograms and n-tuples. Also, the program calculates the multiplication factor k as

$$k = 1 - \frac{N_s}{N_t} \tag{3.16}$$

where N_s are the source neutrons, and N_t are the total number of neutrons, processed by the program. The total number of neutrons includes the neutrons produced by inelastic reactions, and fission. The program has also the ability to create data summary tapes (DST) for specific regions defined by the user. These DST's can be used as an entry point for further processing, emulating the biasing technique.

3.8.10 Precision of Monte Carlo

The *Monte Carlo* error is usually something very difficult to evaluate, since it contains both the systematic and statistical errors. The only way of estimating the statistical fluctuations is by running many times the same problem with different initial random seeds. Hence, the *Monte Carlo* results are represented as the average of the contributions from the histories sampled during the simulation of the problem. The precision of the simulation is caused by the statistical fluctuations of the result that we are interested in. The estimation of the statistical fluctuations is calculated as the standard deviation of the population. This quantity gives the confidence interval of the behavior of the system, but it doesn't give any information about the accuracy of the result. It is possible to simulate a very precise result, which is far from truth, because the relevant physical processes are not modeled correctly.

The precision of the simulation is something that can be improved with the following ways [28]:

- by using more appropriate estimators;
- by factorizing the problem;
- by increasing the statistics of the program (ie. running more histories to improve the precision). Because the precision is proportional to $1/\sqrt{N}$, running more particles is often more costly in computer time.

The accuracy is affected by the errors in the modeling of the code, the uncertainty in the cross sections from reaction databases and by the incorrect modeling of the problem.

In the *TARC Monte Carlo*, the fate routine (that selects the interaction distance and the interaction type) for each neutron energy uses the mean value of the cross section, which is found in the ENDF database (E, σ). Thus, the program does not take into account the uncertainty in the estimation of the cross section, but rather assumes that the cross section for the specific energy is accurate, underestimating the final uncertainty of the results. A more "accurate" treatment would be for each energy from the cross section σ and the error $\delta\sigma$, to sample a new cross section, using a random distribution, from the mean and the error values given by the library. This way the uncertainty of the cross sections will be used by the *Monte Carlo* program and the error estimation will be more precise. Unfortunately in neutron reaction databases (ENDF) there are MF-files that contain the covariance data for the cross sections. But the relevant correlation matrix is not present, due to the huge amount of space that needs. The correlation matrix is important in order to estimate the error in the cross section at each energy.

Chapter 4

TARC Experimental Setup

At the end of the *FEAT* experiment (see App. B on page 159), after the experimental proof of the "*Energy Amplifier*" principle (see App. A on page 153), the formerly *FEAT* collaboration submitted for funding, the *TARC* proposal [29] in March 1995, to the relevant Committee of the European Union. The main purpose, of the proposed experiment was "*the study of the neutrons produced by spallation inside a large Lead volume and their slowing down from the energies of production (crossing in particular the Lead absorption resonance region) towards the* $5\,eV$ *region where resonant transmutation of* ^{99}Tc *takes place*". The goal of the experiment was to exploit the physics involved in the neutron moderation inside a large *Lead* block, which can lead to the better understanding and development of an *Energy Amplifier*, using fast rather than thermal neutrons called the "Fast Energy Amplifier". This could have a higher energy gain and increased safety characteristics. Furthermore, this could lead in a neutron efficient incineration method of some of the most offending Long-Lived Fission Products. This involves the resonant behavior of the cross sections for neutron capture.

4.1 Lead Volume

The shape and the dimensions of the Lead volume was chosen in such a way as to approach the behavior of an infinite Lead volume. Thus, the neutrons reaching the surface of the Lead block have a very small probability to travel back to the place of birth. This distance is given from the diffusion length of the moderating material. In our case, lead has a diffusing length of about $1.5\,m$. The dimensions, we have chosen for the *TARC* lead assembly, tend to have a cylindrical symmetry with a diameter of $3.3\,m$ and a length of $3\,m$ Fig. 4.1. In such a large lead block only 25% of the neutrons are escaping, while the rest remain enclosed for quite some time.

A main consideration for the design of the experimental area was to minimize neutron reflections from the surrounding concrete walls, ceiling and floor. As a result, the roof was raised to about $1.9\,m$ above the lead volume, and the side walls were $1.1\,m$ away from the vertical sides of the lead assembly, figures 4.2, and 4.3. Monte Carlo calculations showed that the average penetration of the albedo neutrons is of the order of a few centimeters.

Simulations have showed, that a large number of reflected neutrons were coming from the concrete of the floor, due to the fact, that the Lead was in contact with the floor. The solution was to put a material with high capture cross section, to absorb all the neutrons that were exiting from the bottom of the lead. Several test cases were simulated. In these cases the room was considered empty, to focus only on the effect of the neutrons exiting from the lower surface of TARC block. The lead block was placed on top of steel I-beams, and in between was a

layer of embeco. In the Monte Carlo calculation, we were monitoring the neutrons that were absorbed, and reflected by the materials of the Lead base (embeco, I-beams, concrete floor). Several cases were simulated, 1) with no embeco layer, only I-Beams. 2) the I-beams filled with Boron-polyethylene pellets, 3) a plain embeco layer, 4) embeco layer enriched with ^{10}B 10%, and finally different thickness of the embeco layer. Table 4.1 shows the results of the absorbed, and reflected neutrons as a function of the ^{10}B concentration. A fit performed using these values, gave the following results:

$$\text{Absorbed}(\%) = 78.062 - 70.07e^{-0.767\ c} \tag{4.1}$$

and

$$\text{Reflected}(\%) = 15.572 + 55.84e^{-0.723\ c} \tag{4.2}$$

where, c is the ^{10}B concentration.

B_4C (%)	^{10}B (%)	Absorbed (%)	Reflected (%)
0	0	5.1±0.7	75.6±0.6
5	0.77	46.1±0.5	42.5±0.3
10	1.53	57.6±0.5	33.5±0.4
12.8	1.96	61.0±0.4	30.8±0.3
15	2.30	63.7±0.4	28.6±0.3
30	4.60	73.5±0.4	21.4±0.3
65.2	10.0	81.8±0.3	12.6±0.2

Table 4.1: Neutrons absorbed and reflected as a function of the ^{10}B concentration in the embeco layer. The uncertainties are only the statistical ones.

Finally the lead assembly was placed on a steel platform formed from I-beams covered by a 3 cm, embeco [30] layer enriched 20 % in B_4C, since ^{10}B has a high capture cross section in the thermal region.

The Lead ingots had to be transformed into carefully machined blocks, in order to construct the assembly with the required geometry. A machining process was devised with the goal of avoiding introducing impurities.

The Lead assembly was mounted with three different building blocks of Lead (dimensions of $15 \times 30 \times 60\ cm^3$ and $30 \times 30 \times 60\ cm^3$). Each piece of lead (weighting 300 and $600\,kg$ respectively) was placed with a special suction device, taking care to avoid any kind of deformation and positioning them precisely. The Lead Assembly was placed in the *T7* area of the *CERN-PS* East Hall Fig. 4.2.

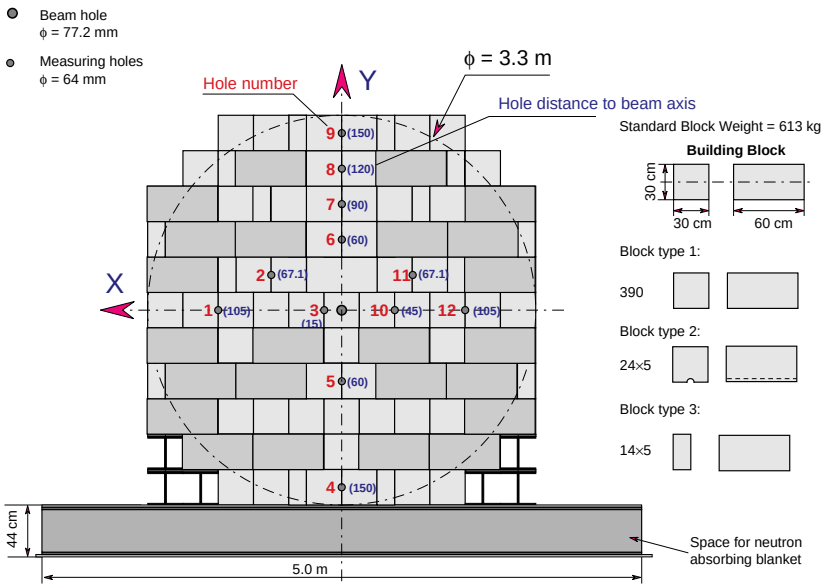

Figure 4.1: The Lead Assembly

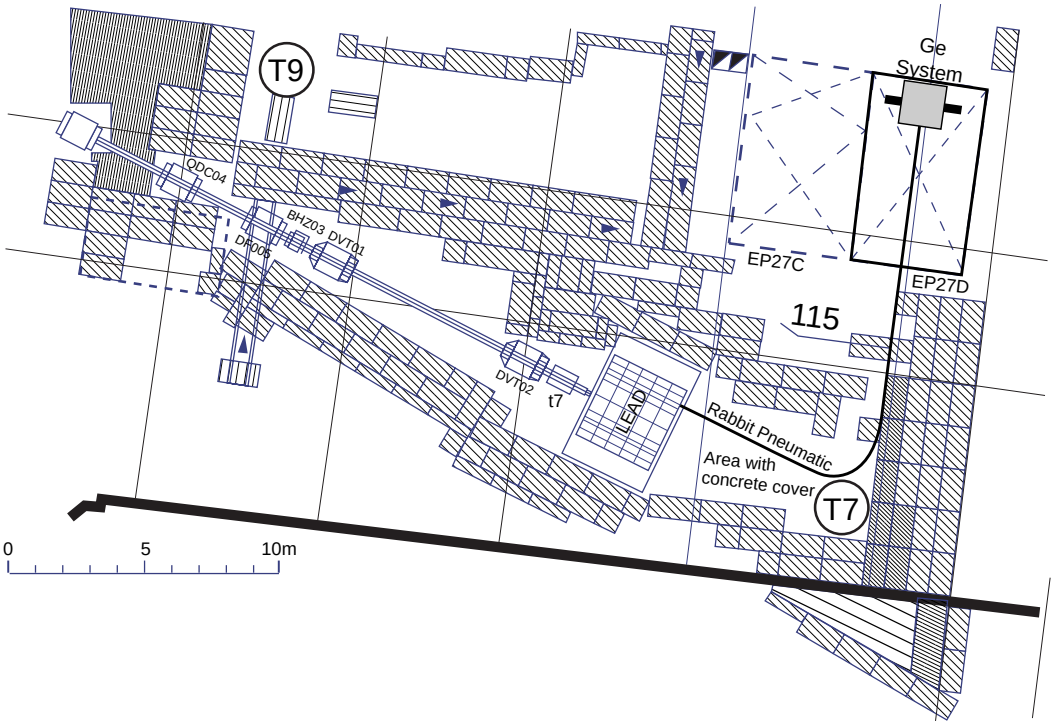

Figure 4.2: The experimental area.

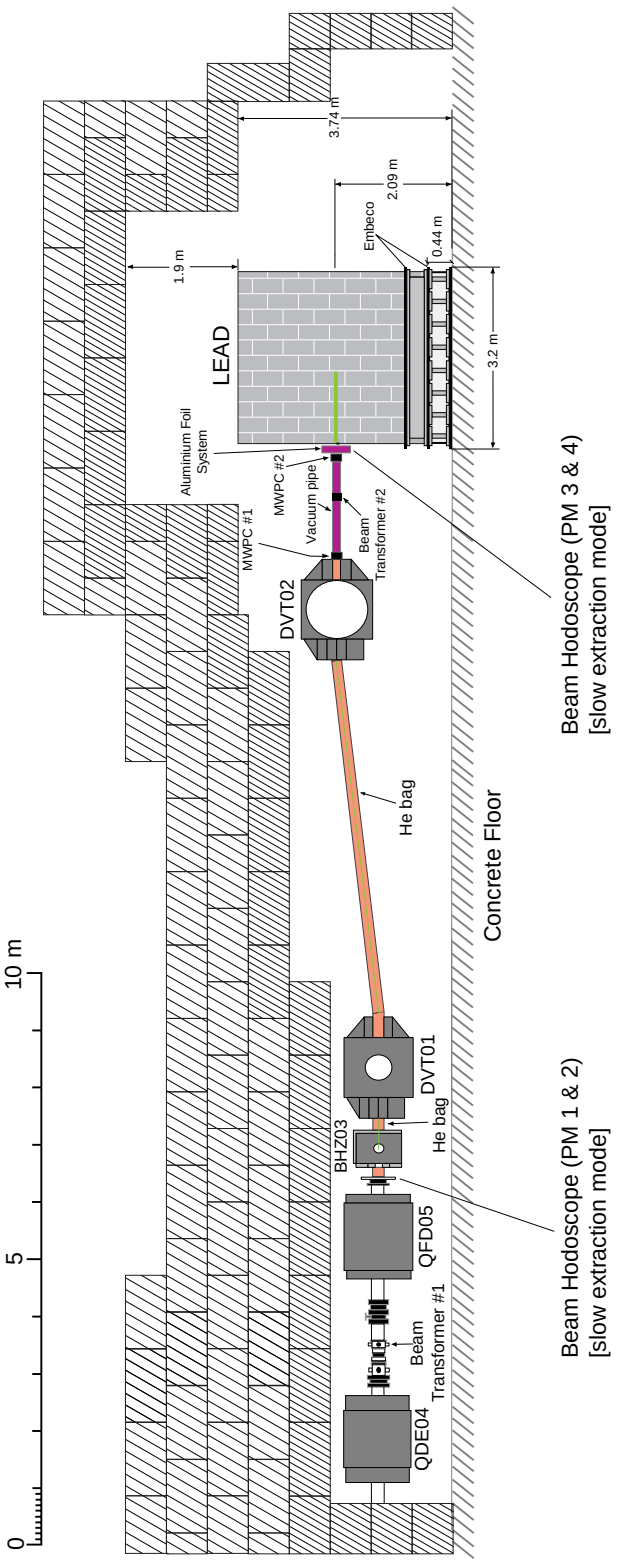

Figure 4.3: Side view of Lead Assembly

4.2 Impurity Analysis of Lead

The experiment calls for high purity Lead devoid of such known impurities as Silver, Antimony and Cadmium. The *4N* quality Lead offered by *Britannia Refined Metals (UK)* [31] was subject to thorough chemical analyses as samples were sent to several independent laboratories world-wide. All the measurements were combined to obtain the best estimates of the impurity concentration of our lead.

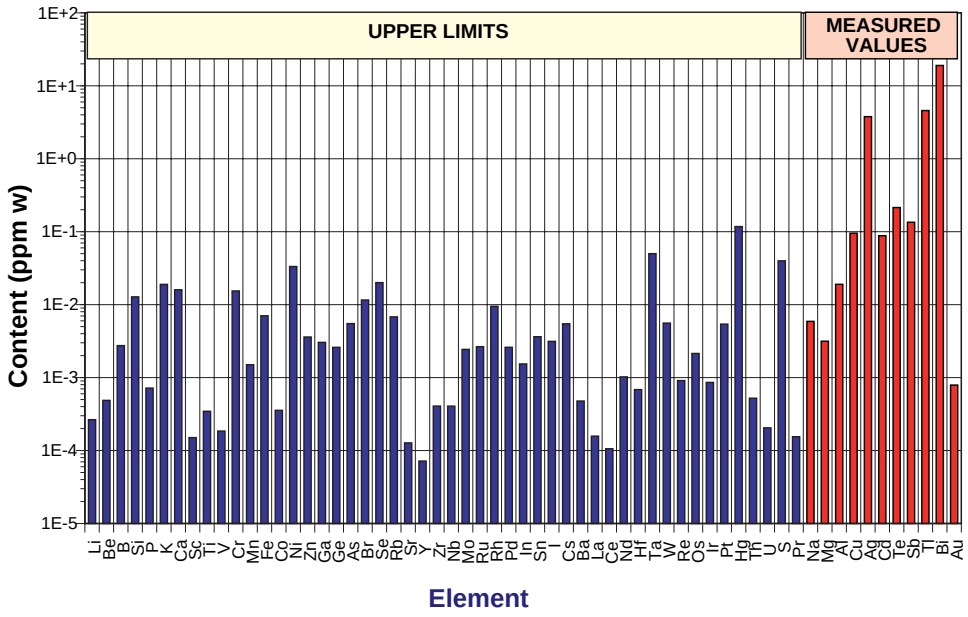

Figure 4.4: Impurity contents (ppm by weight) in the *TARC* Lead blocks.

Information was obtained on the concentration level for 60 elements (Fig. 4.4).

- measured values for 11 elements: Na, Mg, Al, Cu, Ag, Cd, Sb, Te, Tl, Au and Bi
- upper limits for 50 other elements

The main elements that could affect the behavior of the process are *Silver*, *Cadmium* and *Antimony*. We have demonstrated (see § 5.3.1 on page 73) that *4N* quality commercial Lead is adequate for that use and have identified a process whereby that purity can survive manufacturing of blocks (Table 4.2) [32].

4.3 PS Complex

For the experiment we have used the proton beam from the *CERN-PS* Complex [33]. The *PS* Complex consists of nine interleaved machines, delivering beams of protons, anti-protons, electrons, positrons and lead ions of various energies and intensities. The $200\,m$ diameter combined function *PS* machine remains the heart of the *PS* Complex (Fig. 4.5). With 3 RF systems (9.5, 114 and 200 MHz), 4 injection and 4 extraction channels, it routinely process five types of particles ($p^+, \overline{p}, e^+, e^-, {}^{53+}\mathrm{Pb}$) at momenta ranging from $2.5\,10^{13}$ particles per pulse (ppp).
The rest of the complex consists of:

Element	Concentration (ppmw)	Error Spread (ppmw)	Syst. Error (ppmw)	Total Error (ppmw)
Na*	0.00059	0.0074	0.00012	0.0074
Mg*	0.00315	0.0048	0.00063	0.0048
Al*	0.019	0.0099	0.0038	0.011
Cu	0.095	0.205	0.0125	0.21
Ag	3.65	0.59	0.074	0.595
Cd	0.088	0.044	0.0065	0.044
Te	0.215	0.086	0.025	0.089
Sb	0.135	0.14	0.0057	0.14
Tl	4.6	1.3	0.29	1.36
Bi	19.0	2.8	0.23	2.8
Au	0.00088	0.00025	0.000343	0.0004

* *Some upper limits are included*

Table 4.2: Summary of the concentration levels, for manufactured Lead blocks, with the error contributions.

- *Linac 2*, producing protons from a duo-plasmatron source followed by a $750\,keV$ RFQ and 3 Alvarez tanks operating at $200\,MHz$. Proton pulses are delivered at $50\,MeV$ every $1.2\,s$, with a length from 10 to $150\,\mu s$ and an intensity of up to $180\,mA$.
- *Linac 3* which uses one $101\,MHz$ RFQ accelerating $^{27+}$Pb up to $250\,keV/u$.
- The *PS Booster* (PSB), an assembly of four vertically stacked synchrotrons of $50\,m$ diameter, which accelerate the linac beams respectively up to $1.69\,GeV/c$ for protons and $0.43\,GeV/c/u$ for $^{53+}$Pb.

In the *proton* mode of operation the PSB is able to supply up to $3\,10^{13}\,ppp$ in 20 bunches at $1\,GeV$ every $1.2\,s$. The PS machine accelerates these beams and tailors their longitudinal characteristics to the specific needs of every user. A large variety of proton beams is routinely available:

- debunched and slow extracted ($\sim 400\,ms$ spills) at up to $24\,GeV/c$,
- bunched at $200\,MHz$ and "continuously ejected" over 5 turns at $14\,GeV/c$ to SPS,
- compressed into 1/4 of a turn (5 bunches) at $26\,GeV/c$.

4.4 The Proton Beam and its Calibration

The proton beam line was set-up in collaboration with the *CERN-PS* staff. It was capable, as required, to supply beam in two modes: (a) the fast extraction mode, used for activation experiments (high intensities, up to 10^{10} protons per PS shot) and for the measurements of neutron fluences relying on the energy-time relation; (b) the slow extraction mode, which was used for the operation of the ^{3}He ionization chambers, for which a very low beam intensity was needed (1 000 protons per PS extraction).

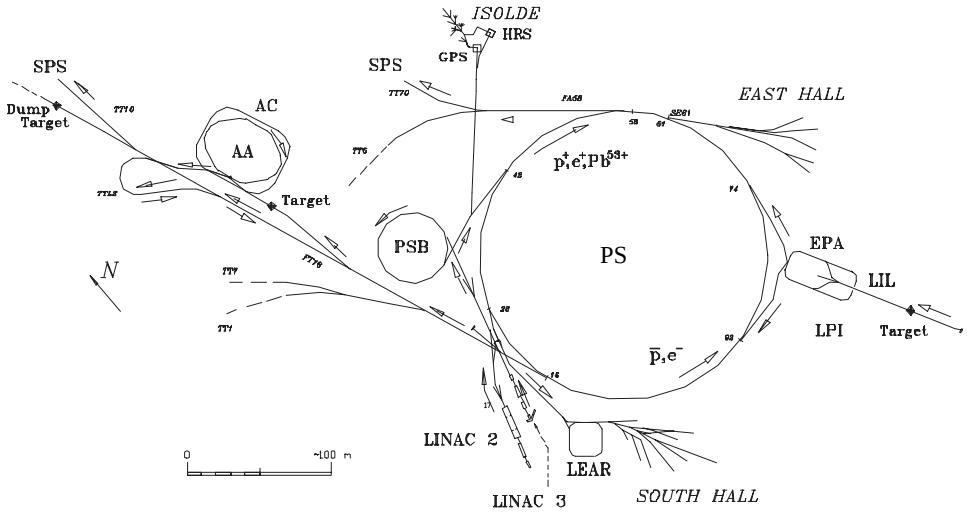

Figure 4.5: General map of the *PS* Complex

4.4.1 Fast Extraction

The beam was extracted all at once, by the fast rise of a magnetic kicker. In this mode, the structure of the beam in the PS machine was preserved, namely bunches $20-30\ ns$ wide recurring every 14.4 seconds. We were able to obtain, at the end of the T7 beam line, intensities ranging from 3 10^7 to 2 10^{10} protons per shot. Of special concern was the accurate measurement of the intensity of the beam. Two beam transformers were used to measure the number of protons, from the signal induced by the beam charge in a coil mounted around a vacuum pipe. One beam transformer was situated at 13.4 m from the lead assembly. The other one was situated immediately in front of the lead assembly, which was an improved version developed for our purpose by industry [34]. A new design of the induction loop, through which calibrated charges simulating the beam were injected, allowed a more linear behavior of the calibration system [35]. The readout scheme is shown in Fig. 4.6. The beam transformers measure the beam intensity of each PS shot (Fig. 4.7) providing the detailed history of the experimental runs.

Since the beam intensity measurement was the key to the ultimate accuracy of the experiment, it was important to cross check measurements. This was done by comparing the results of the two beam transformers that, according to beam simulation, should record the same beam intensity, since particle losses between them were expected to be negligible, under normal circumstances. In fact, the two measurements usually agree very well, within 1 to 2% and were used as diagnostic for beam quality.

It was also important to check the linearity of the device. This was done by performing two types of calibration: (i) bombarding Aluminum foils with protons and counting the ^{24}Na produced, and (ii) through the injection of calibrated charge pulses, through a wire simulating the beam.

The calibration of the beam transformers was done, with the irradiation of Aluminum foils. This is a classical technique, involving the formation of ^{24}Na by the reaction $^{27}\mathrm{Al}\,(p,3pn)\,^{24}\mathrm{Na}$, ^{24}Na being detected via its $1368.45\,keV$ gamma ray emission. The method is affected by a systematic error of 6.9%, of which the largest component is due to the lack of knowledge of the ^{24}Na production cross section of the order of 4%. Fig. 4.8 represents the absolute calibration of the proton beam transformer using Al foils.

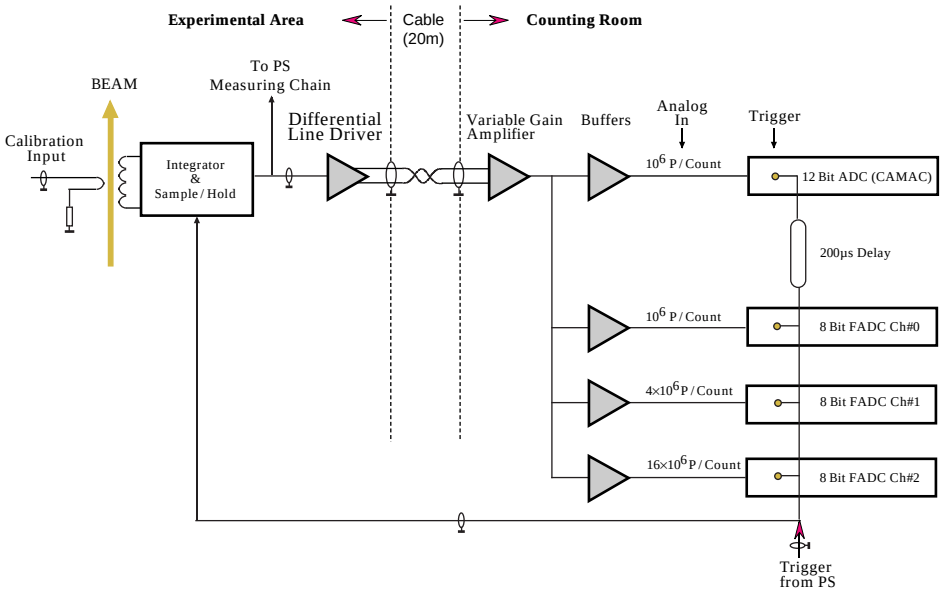

Figure 4.6: Beam Transformer Read-out and Calibration Block diagram.

4.4.2 Slow Extraction

The ^{3}He ionization chambers required a very low beam intensity of $\sim$ 10 ^{3} protons ($\approx$ 5 10^3 particles) per PS ejection which could not be obtained with a fast extraction, due to the impossibility to control such a low intensity beam in the PS accelerator system. Therefore, a low intensity beam was prepared by collecting secondary particles produced by 24 GeV/c primary protons hitting a target (usually Al), allowing beam intensities down to about 5 10^3 particles. Primary protons were extracted progressively, by resonant extraction, over a 350 ms period, every 14.4 seconds. However, the secondary beam contains a mixture of pions, protons, electrons, muons, etc. (of the same momentum) which need to be distinguished. Fig. 4.9 shows a calculation of the proton and pion content, for a $T7$ beam line configuration not too different from the one we used. A time of flight hodoscope was built using 4 Photo multipliers, which could separate protons and heavier particles from pions, muons, etc. from the difference in time of flight over a distance of 13.4 m. The time resolution was about 0.5 ns, and this forced us to select a low enough beam momentum of 2.5 GeV/c, to have $\sim$ 6 standard deviations between proton and pion time distributions (Fig. 4.10, 4.11). At this momentum, the beam contains about 20% of protons, and the time difference between protons and pions was 3 ns.

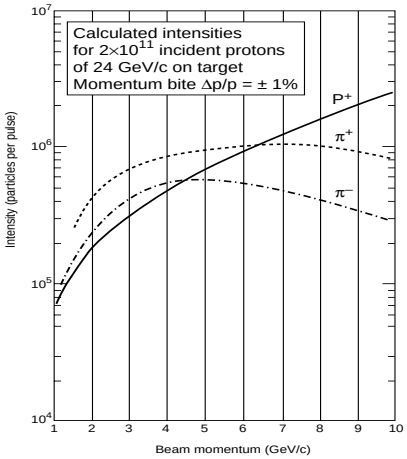

Figure 4.9: Proton, π^+ and π^- beam content as a function of momentum, for 2 10^{11} GeV/c proton beam.

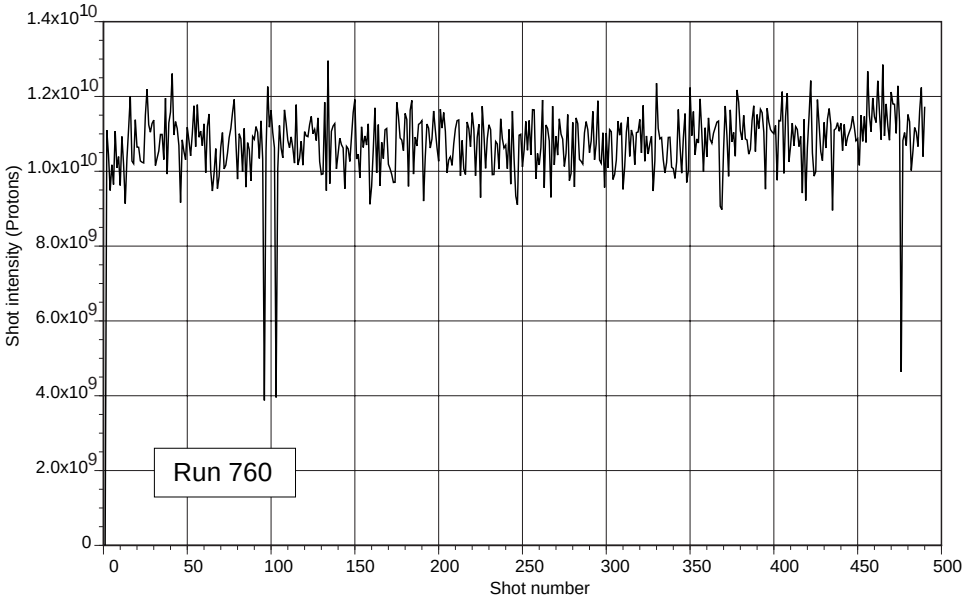

Figure 4.7: Example of the measurement of the beam intensity (run 760), showing the number of protons for each PS shot.

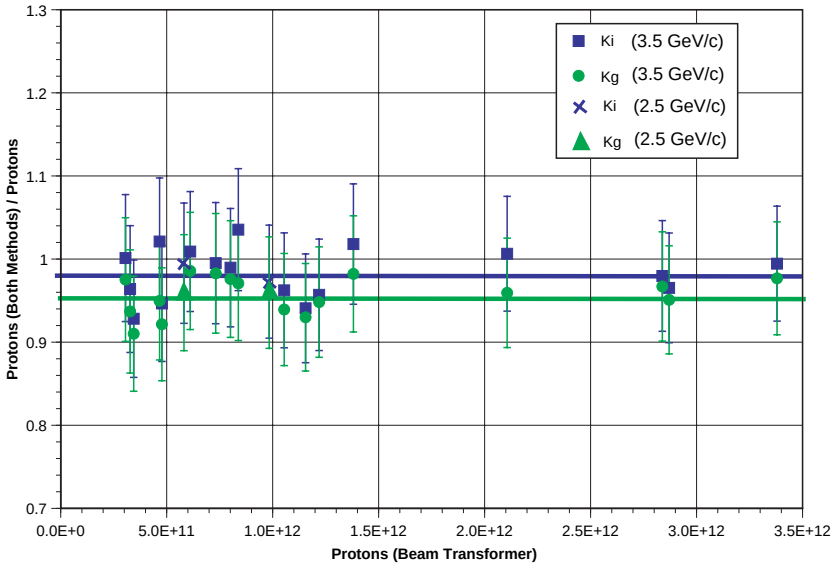

Figure 4.8: Absolute calibration of proton beam transformer using Al foils activation for global (g) and individual (i) methods.

4.5 Data AcQuisition System

The *TARC* DAQ [36] system was designed as a network of VME crates, controlled by a UNIX workstation. Fig. 4.12 shows a scheme of the system. Each VME crate includes a Motorola 68040 CPU 25 MHz in a $FIC8234$ module running the *OS9* operating system. The DAQ software for *TARC* was developed using the CASCADE package provided by CERN [37]. In the CASCADE model the DAQ was a distributed system with a unified central Run Control.

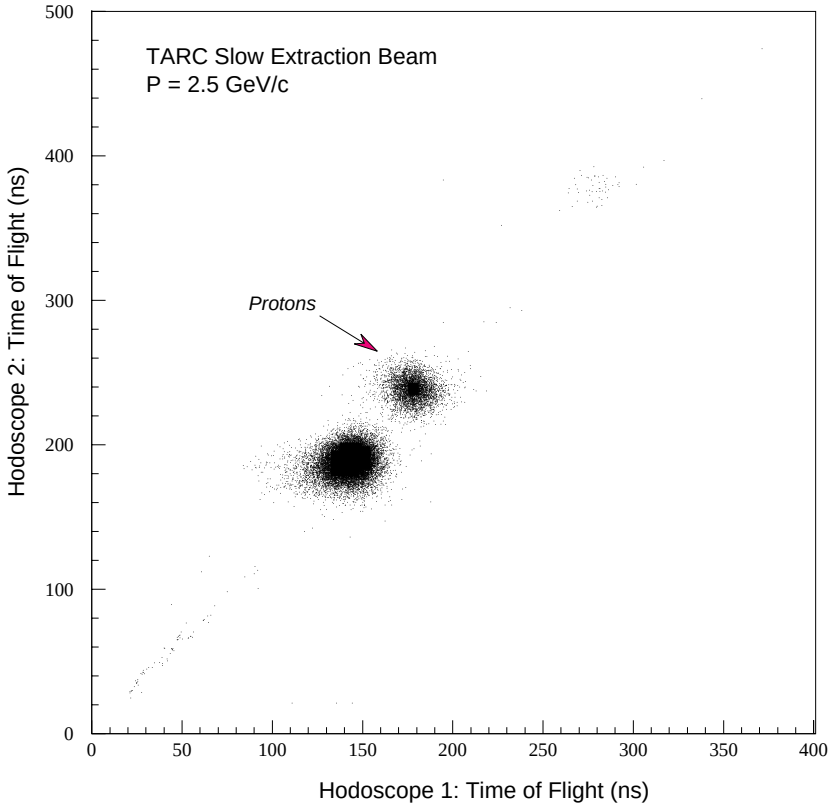

Figure 4.10: Time differences measured by hodoscope 1 (PM 1 & 3) versus hodoscope 2 (PM 2 & 4), showing the 6 standard deviation separation between protons and lighter particles.

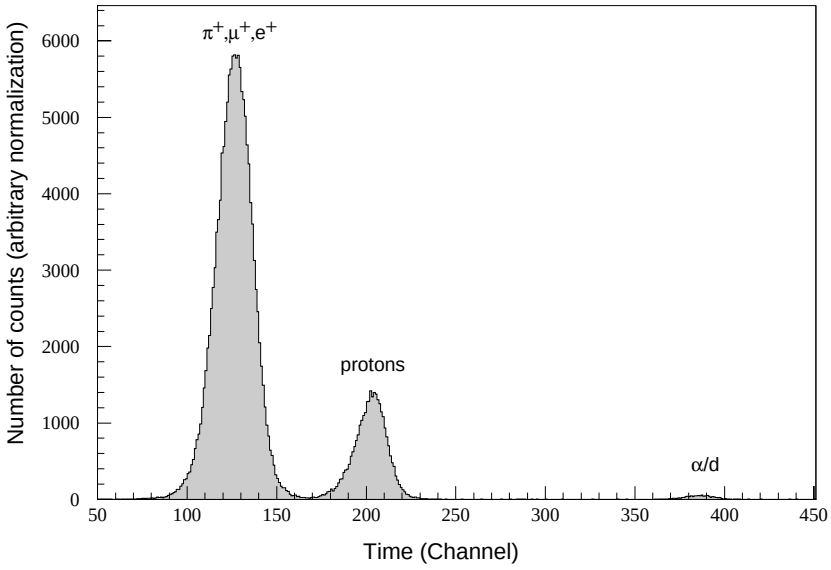

Figure 4.11: Separation of protons from other particles, by time of flight, using scintillators 1 & 4, at a beam momentum of 1.866 GeV/c

The software was subdivided in pieces, called stages, some of them running on the VME CPUs and others running in the RUN CONTROL and monitoring Unix workstations.

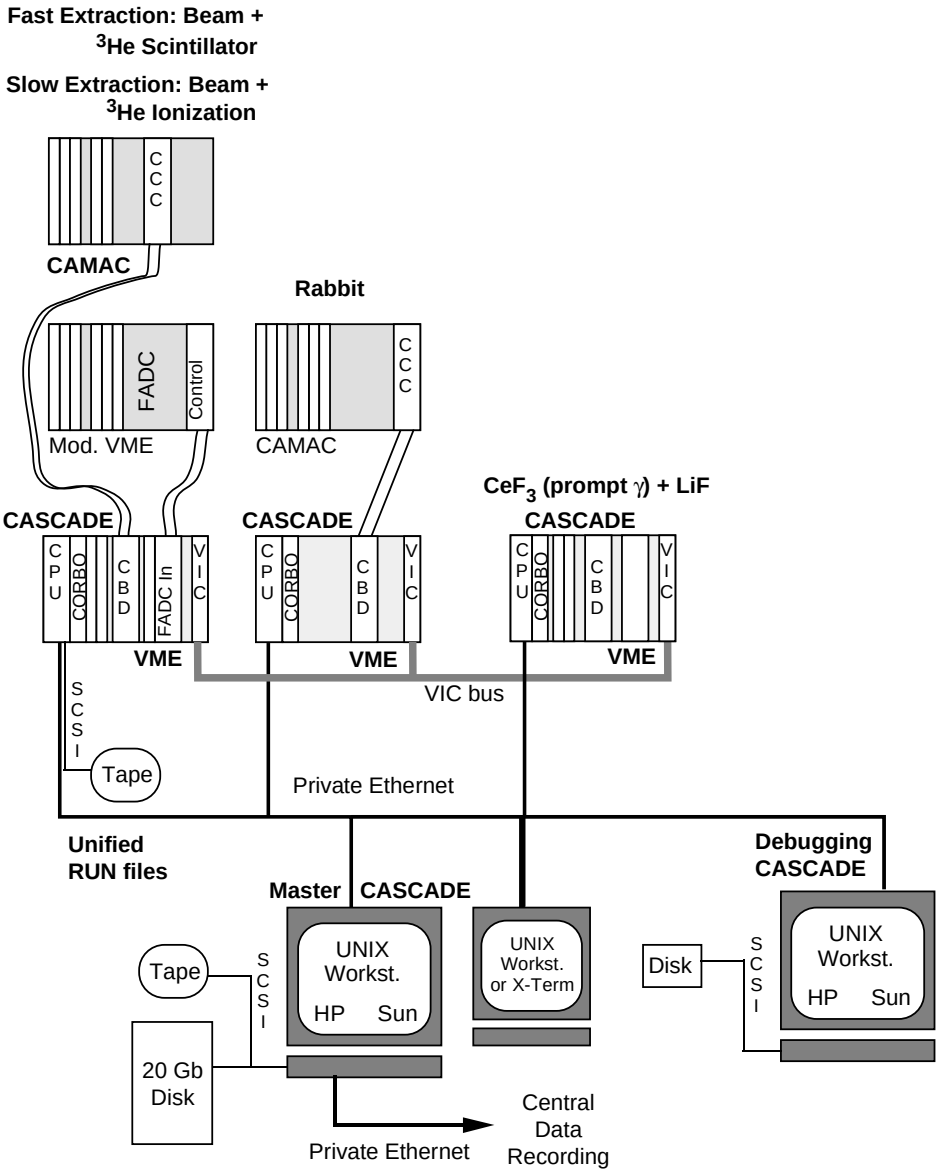

Figure 4.12: Architecture of the *TARC* Data Acquisition System.

All the data from *TARC* were collected in the VME crates, by means of ADC modules and other I/O devices, either installed directly in the VME bus or using AMAC, modified-VME buses and RS-232 interfaces. The front-end hardware readout and the manager of the event buffer were the main, but not the only, stages running on the VME modules. Several trigger signals were used by the DAQ system and in some sub-detectors, as the RABBIT and the ^{3}He ionization chamber, where organized in two levels of triggers. These trigger signals were collected in a CORBO unit at each VME crate and handled by the specific drivers included in the CASCADE system. The VME crates were linked together by a VIC bus and at the same time use a TCP/IP network, in a private Ethernet segment, to communicate with the UNIX workstations. Even when it was possible to use stand-alone VME crates with disk and other

mass storage units, in *TARC*, the VME crates were disk-less. These crates used the BOOTP protocol to load the operating system from the UNIX workstation disks. Once booted they use NFS to access the remote workstation file system as their main file system, however a specific client-server protocol was used to send the data from the VME crates to the workstation disks.

4.5.1 Data Flow

The data from the *TARC* experiment were collected, from the ADC and other front-end electronic modules, by the readout stage, through the VME bus, in some cases using CAMAC or other interfaces. On each VME crate, there was a single readout stage that collects all the data from the crate and handles all the triggers reaching the crate. All the sub-detectors in one VME crate must be operated within the same DAQ system at any time. However each individual VME crate can be connected or disconnected to different DAQ system instances, that can run concurrently, by simple software instruction on a run by run basis.

The events that were collected were temporarily stored in a memory buffer. Depending on the instructions given at the beginning of each RUN, the events were then sent directly to one UNIX workstation data recording server or to another VME crate, behaving as event builder. The event builder can join events from several VME crates at different levels of integration. In *TARC*, the events from the different sub-detectors included in one RUN of the same instance of the DAQ, and corresponding to the same beam trigger, were grouped together and sent orderly to the UNIX workstation data recording server. This one will write them coherently in the same intermediate unified data file in the workstation disks, in the FZ ZEBRA format. Once the RUN has finished, the unified data file was sent to the Central Data Recording, CDR [38], server in the CERN computing center using a specific client-server protocol. At the CDR, the data were archived in DLT tapes. An automatic service allows requesting for any RUN data file to be restored into a cache disk file, accessible for analysis through AFS.

4.5.2 Data and Detector Status Monitoring

The data were stored, for different periods of time, in three locations: the VME RAM memory, the intermediate data files in the UNIX workstation and the CDR tapes. Data monitoring was possible, and has been performed during the *TARC* experiment runs, from these three locations. A dedicated server running on each VME crate provided pure on-line data monitoring. When a monitoring client, normally running on a UNIX workstation, requests an event of a given type, the server provides the most recent data available. In this way the data, from all the subsystems with small event sizes, were available and analyzed only a few milliseconds after collection. For the subsystems with very large event sizes (^{3}He ionization), the monitoring analysis program reads the data directly from the intermediate data file corresponding to the current RUN. Because of that, there was a small delay (several seconds to 1 minute) between the data being analyzed and the last data recorded. On the other hand, the data traffic in the private Ethernet line, between the VME and the UNIX workstation, was substantially reduced, avoiding unnecessary dead time to the DAQ.

Independently of the data source, the monitoring analysis program produces an HBOOK [39] direct access file with a set of histograms, and in special cases *n-tuples*, that include information on the last event collected, the history of data collection during the run, some accumulated histograms and specific histograms displaying the detector status and performance during the last event. These HBOOK files were visualized at the *TARC* counting room, and in several other remote locations simultaneously, using PAW [22]. A panel-based interface was build to simplify

the access to the different informations available from each monitor. The data monitoring was an essential tool for beam and detector tuning after any change of the *TARC* experimental conditions.

4.5.3 The Run Control

All the elements involved in the DAQ, were centrally controlled from the RUN CONTROL, running on the UNIX workstation. The Run Control was used to start or stop a RUN, to define which VME crates takes part in the run, the configuration for each VME crate, the data path and the data destination. The RUN CONTROL, also takes care of synchronizing and monitoring the different stages involved in one RUN. The set of the RUN CONTROL parameters defining one RUN was managed in a database with a public domain relational database system called mSQL [40]. The Run Control involves two processes running on a UNIX workstation: the run control engine (NRC) and the human interface (XHI). The communication, between NRC and the DAQ units, was based in the TCP/IP protocol trough the Ethernet link.

Chapter 5

Neutron Flux Measurements

5.1 TARC Lead Volume Simulation

In order to reduce the computing time needed to simulate the *TARC* experiment; it has been decided to factorize the problem into a number of transport steps. In the first step, the neutrons generated by the high-energy proton beam are described by the FLUKA program. They are followed in the lead block without any detectors, until they escape the block or they are captured. During this transport, a Data Summary Tape is produced. This is a condensed description of the neutrons escaping from the system or crossing internal boundaries providing secondary source terms for further calculations. Creating such a tape has the advantage of allowing repeated and various analyses with the same neutron source data.

All crossings of the same neutron in and out of a block are recorded. In successive transport steps the effect of the surrounding lead can thus be neglected, all incoming neutrons can be used as independent source neutrons and neutrons exiting the block must be discarded. This simplifies the problem of the simulation of specific detectors. This approximation is correct only if the perturbation introduced by the detector is negligible.

While simulating a detector in a single instrumented block, the same neutron sample is run more than once, which introduces some correlation in the events. However, when the neutron sample is large enough, to represent a consistent fraction of the neutron population, the error should be negligible. Therefore, the neutron histories will be different because of different random numbers.

The size of 15 cm around the instrumentation hole has been chosen to be large enough to allow the randomization of the neutron flux due to scattering in lead and to minimize the perturbations due to the presence of detectors.

All the neutrons escaping the lead assembly are recorded. These neutrons are used as independent source neutrons in subsequent Monte Carlo calculations where they are propagated through the area surrounding the lead assembly (here on called cave). Those scattered back onto the lead assembly are recorded on a special history tape and used to re-compute the detector response and evaluate the effect of background coming from neutron reflections on the surrounding concrete walls of the cave.

5.1.1 TARC Geometry Description

The 12 instrumentation holes and the beam hole have been included in the simulation. A virtual box of $15 \times 15 cm^2$ in cross section and 300 cm in length is placed around each instrumented hole. This box is further subdivided in 20 slices along z, each one 15 cm long. The center of

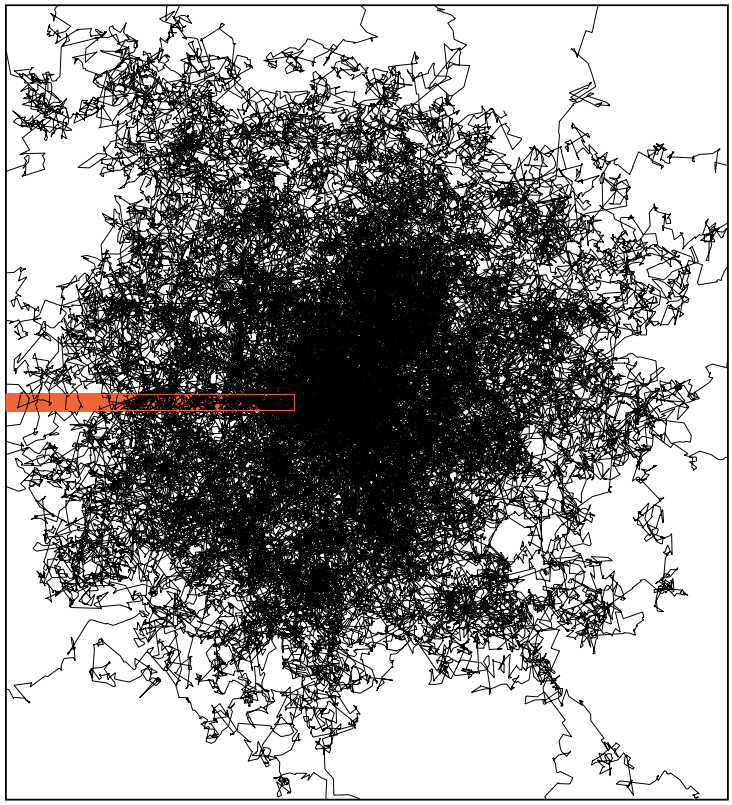

Figure 5.1: A complete simulation of the secondary neutron shower produced by a single 3.5 GeV/c proton.

the reference system is in the geometrical center of the block and the beam is along the positive z-axis. The y-axis is along the vertical direction. The general layout of the assembly is shown in Fig. 5.2 The co-ordinates of the centers of the Monte Carlo blocks are listed in Table 5.1.

5.1.2 Data Handling for TARC Simulation

For every neutron crossing a surface of an instrumented block ($15 \times 15 \times 15 cm^3$), all the relevant information is written in a file, packed in 160 bits. The surface crossing points are given in the local reference frame of the block for the instrumented blocks. A reference system, having the axes parallel to the main system, but with the origin in the corner of the instrumented block. In the case of neutrons escaping from the lead assembly, the reference system is still with the axes parallel to the main one, but its origin is such that the coordinates are always positive. To achieve the maximum compression in the DST file, boundary crossings are written only once to the file.

The code is portable on different machines. To simulate a detector inside an instrumented block, the following steps had to be taken:

- add the necessary nuclides in the material routine;
- add the material definition; material 1 is always defined as the lead with all the impurities;
- modify the routine that returns the region in which the particle is located given its position to take into account the presence of the detector;

Hole no.	x (m)	y (m)	Hole no.	x (m)	y (m)
1	1.05	0.00	2	0.60	0.30
3	0.15	0.00	4	0.00	1.50
5	0.00	0.60	6	0.00	0.60
7	0.00	0.90	8	0.00	1.20
9	0.00	1.50	10	0.45	0.00
11	0.60	0.30	12	1.05	0.00

Table 5.1: Summary of the co-ordinates of the centers of the twelve instrumented holes contained in the 334 ton lead assembly unit. The beam is introduced through a 77.2 mm diameter blind hole, 1.2 m long.

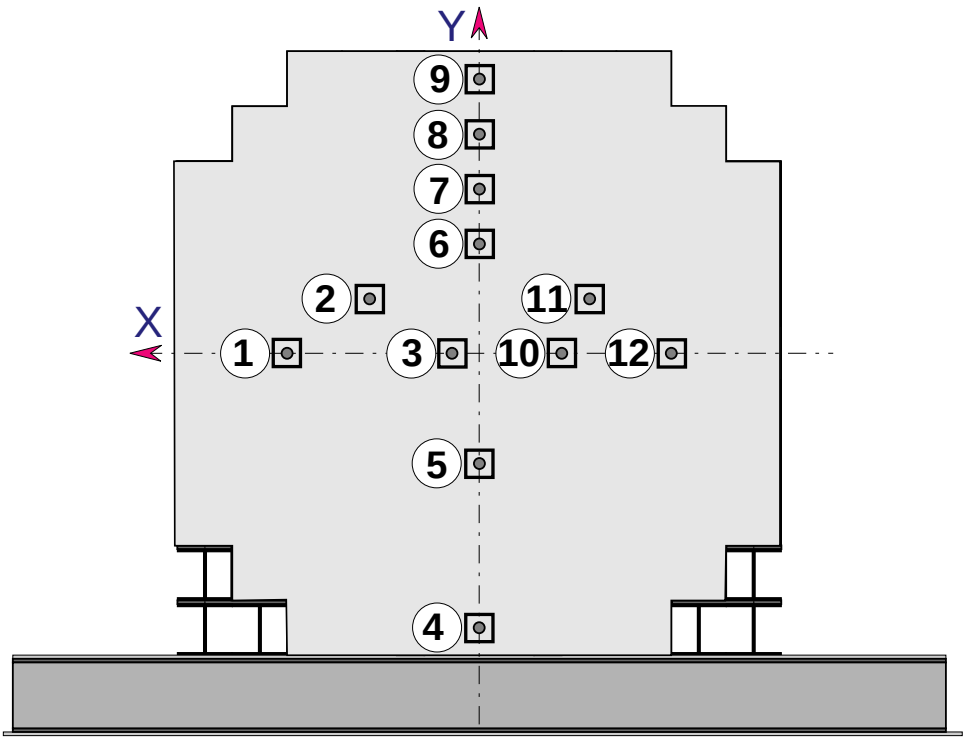

Figure 5.2: Schematic view of the simulated lead assembly. The z-axis is along the beam direction.

- modify the routine that returns the distance that the neutron can travel before changing material to take into account the detector;

- select a particular instrumented block in which to perform the transport. This is done by extracting from the full DST a mini DST containing only the neutrons entering the block of interest;

- select the number of neutrons to be processed. All the information concerning the neutrons entering the block of interest is contained in the mini DST. This DST file is used as an entry point for later processing.

5.2 Energy-Time Relation in Lead

The quantity that describes the neutron field, and the whole *TARC* experiment, is the neutron flux. Thus, it is of primary importance to know the exact neutron distribution in the lead volume, as a function of the primary proton source and the neutron energy. Neutron energy, is a quantity which cannot be measured directly, most of the neutron flux detectors where counting the number of events as a function of a time channel. From the time, with the use of the Energy-Time relation, we can extract the energy of the event. Thus, the first step of the measurements is the calibration of the Energy-Time relation. This relation was calculated with *Monte Carlo* simulation and experimentally verified with the measurements performed by the Grenoble group of the *TARC* collaboration.

5.2.1 Calibration

As it is already mentioned in § 2.9 on page 23, through the elastic slowing down of neutrons inside an infinite block of lead a strong correlation develops between the time at which a neutron is observed and its kinetic energy, (Eq. 2.67 on page 24). This correlation, already noted by Feinberg [41] in 1944, has been used to measure neutron energies in so-called slowing down spectrometers [42].

$$E = \frac{K}{(t + t_o)^2}$$

In *TARC*, two of the neutron fluence detectors (^6Li and ^{233}U detectors & ^3He scintillation counters) used this technique to obtain neutron energies from measurements of interaction times. The Energy-Time relation, as we have already seen in § 2.9 on page 23 is valid in the energy domain $E_{th} \leq E \leq 50\ keV$ with an accuracy, of about 11.4%.

The actual value of the K parameter, determined by simulation verifying the theoretical predictions. Moreover, it was experimentally determined (see § 5.2.3 on the facing page) by the Grenoble group, giving result in good agreement with the simulation. The quantity t_o, can be considered as a time correction, due to the fact, that the initial neutron is not created at infinite energy, but at certain energy E_o. In practice, all spallation neutrons are not created at the same energy, nor at the same place and nor exactly at the same time. Moreover, for neutron with energies above MeV the slowing down process is determined by inelastic scattering. Therefore t_o is a phenomenological constant, which has to be estimated experimentally, and in our case, it was checked using our simulation code.

5.2.2 Simulation

A dedicated *Monte Carlo* run was performed using the complete Lead Volume geometry, in order to extract the Energy-Time distribution from the simulation. The *TARC Monte Carlo* program was slightly modified, in a way, to write in a file the energy and the corresponding time of all the neutron collisions. Since, for every initial proton we have around 100 spallation neutrons, and each neutron makes on average $\sim$ 1800 collisions before it is being absorbed, a run of only a few protons was sufficient, for obtaining a complete image of the slowing down process. Fig. 5.3, 5.4 shows the output of this run, where each point, corresponds to one neutron collision. In Fig. 5.4 is visible the Gaussian shape of the slices in energy, with a typical spread $\sigma_E/E = 0.13$, between 3 eV and 1 keV. The same Gaussian distributions we can get if we make a cut in time.

Performing a fit on the simulated data, with the Energy-Time relation, we have extracted the following values

$$\begin{aligned} K_{sim} &= 173 \pm 3 \; KeV \; \mu s^2 \\ t_o &= 0.37 \pm 0.2 \; \mu s \end{aligned}$$

which are in good agreement with the theoretical predictions.

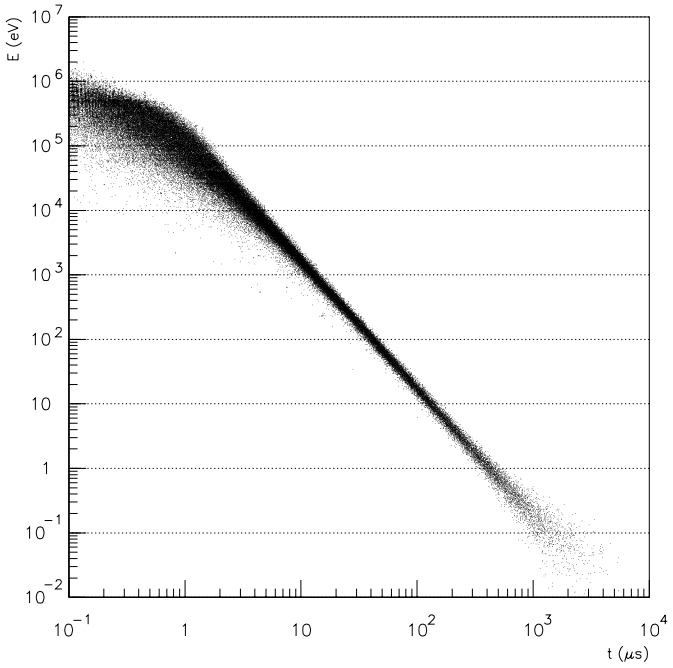

Figure 5.3: Simulation of Energy vs. Time using the *Monte Carlo* code developed for *TARC*.

5.2.3 Experimental Parameters of the Energy-Time Relation

The Grenoble group, used a CeF_3 scintillator mounted in front of a special quartz photomultiplier (Fig. 5.5) to record the prompt gammas, associated with the radiative capture of a neutron on selected target elements, as a function of the time delay after the arrival of a proton pulse. The Energy-Time relation was verified by using calibration elements with known resonances (Table 5.2).

Isotope	Resonance energy (eV)	Time (μs)	Width (μs)	Position Hole	Z (cm)	K value $keV \times \mu s^2$
^{181}Ta	4.28	199.5 ± 1	16 ± 2.7	10	7.5	171 ± 1.8
^{197}Au	4.906	187.1 ± 1	17.5 ± 2.8	5	82.5	172.4 ± 1.8
^{109}Ag	5.19	180.7 ± 1	13.1 ± 2.1	12	7.5	170.2 ± 1.8
^{99}Tc	5.584	175.2 ± 0.9	14.7 ± 2.8	10	7.5	172.2 ± 1.8
^{115}In	9.07	136.9 ± 0.7	8.84 ± 1.1	5	82.5	170.9 ± 1.9
^{107}Ag	16.3	102.3 ± 0.6	6.0 ± 0.7	12	7.5	171.9 ± 2
^{55}Mn	337	22.4 ± 0.3	1.9 ± 0.4	5	82.5	174.4 ± 5

Table 5.2: Experimental parameters for determination of the energy-time correlation function, including the position at which the measurement was performed.

The photomultiplier (PM) allows good detection only for times larger than 1 μs, therefore, we do not have a very accurate determination of t_o. However, this does not matter so much, because in most of the range, where we actually use this Energy-Time relation to measure neutron energies, the effect of t_o can be neglected. Hence, we fixed the value of t_o parameter at 0.37 μs, the value given by the *Monte Carlo* simulation.

From all K determinations, using the analysis of the various resonances mentioned above, the final experimental value of K was (Fig. 5.6)

$$K = 172 \pm 2 \; KeV \; \mu s^2$$
$$t_o = 0.37 \pm 0.2 \; \mu s$$

It should be noted that the universality of the K constant was verified, which was found to vary

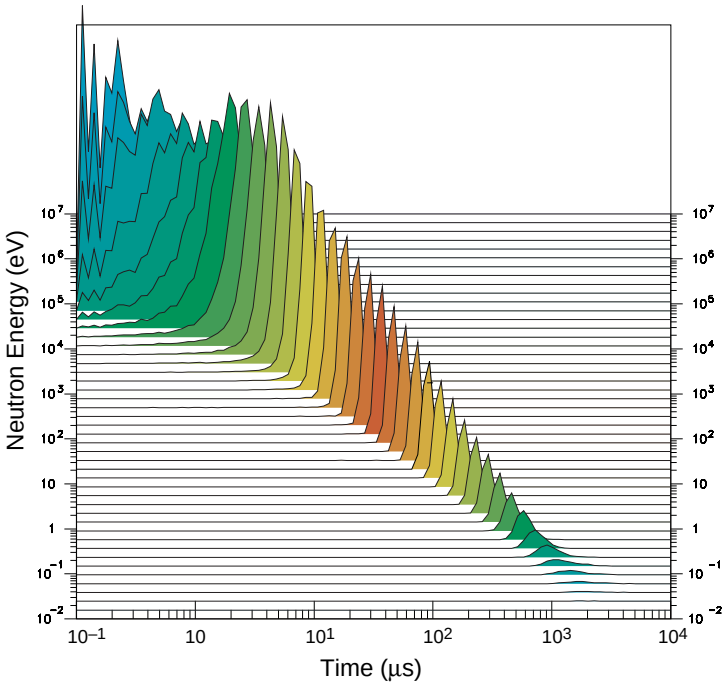

Figure 5.4: Evolution of the width of the correlation function shown as a function of time (time distribution for various energy slices).

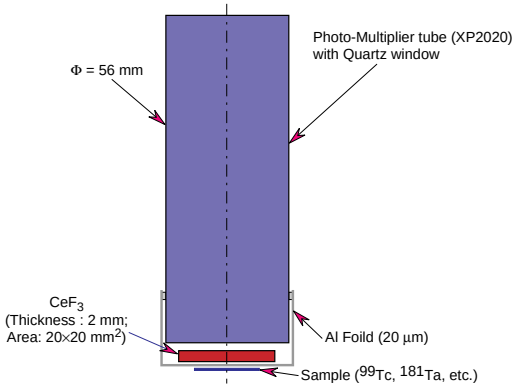

Figure 5.5: Schematics of CeF_3 scintillator set up for prompt gamma measurements.

by less than 1% over the Lead volume (Fig. 5.7). Also, no significant change of K was found with the value of the resonance energy (Fig. 5.8).

In summary, the time distribution of the intensity of capture gammas γ_c gives us the energy variation of the quantity $\Phi(E)\sigma_c(E)$, where σ_c is the capture cross section of the activated element.

Data have also been obtained for other nuclei (^{181}Ta, Ag, In, ^{238}U, ^{55}Mn, etc.) at several positions in the Lead volume, and consequently at different distances from the centroid of the spallation source. Thus, reliable data can, be obtained with a relatively small amount of material (50 to 10 mg). Above 10 keV, the measurements become impossible as they correspond to times too close to the beam pulse and background subtraction becomes impossible. In the resonance region, self-screening effects are observed. To study these in detail, in the case of ^{99}Tc, samples of different thickness have been studied.

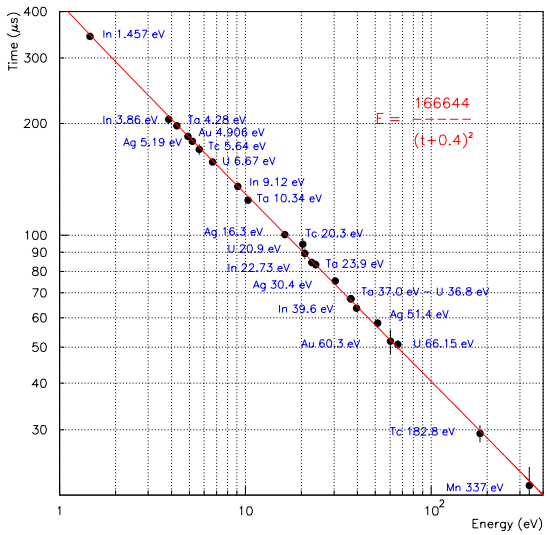

Figure 5.6: Calibration of the Time vs. Energy relationship using elements with known resonances.

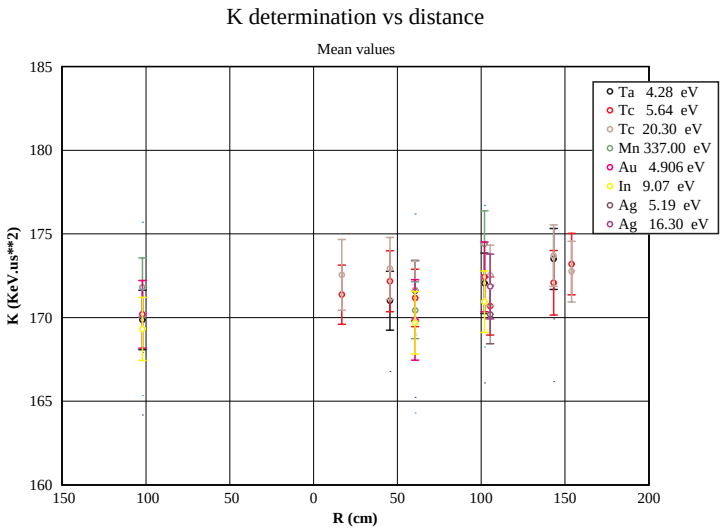

Figure 5.7: K parameter as a function of the distance from the center of the lead block.

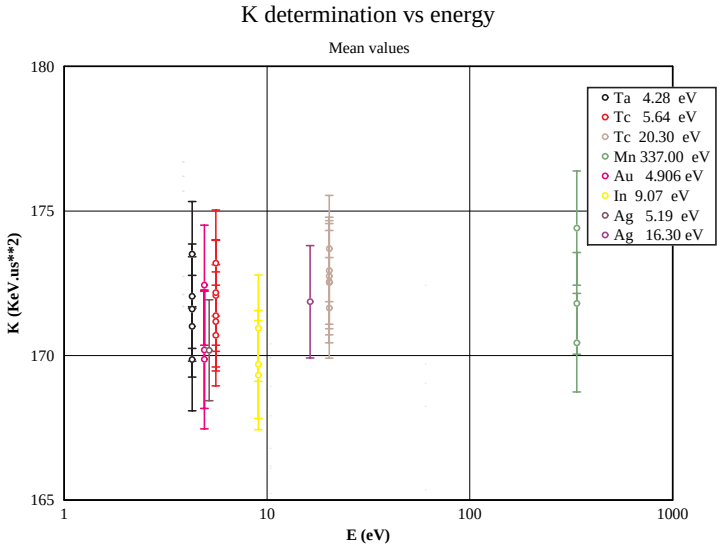

Figure 5.8: K parameter as a function of the resonance energy.

5.2.4 Spread of the Energy-Time

As we can see from Fig. 5.3 on page 67, for energies below 0.1 eV and above 3 keV, the spread is becoming larger. In the thermal region the broadening of the Energy-Time relation is due to the destruction of the isolethargic motion (§ 2.3 on page 10), caused from the thermal motion of the moderator nuclei. When a neutron, at thermal energies, makes an elastic collision with a nucleus, there is a probability that the kinetic energy of the neutron is increased, extracting some energy from the nucleus. Neutrons are forced to remain in this energy region, and their kinetic energy distribution follows a Maxwellian spectrum. In the thermal region, the error is given by [42]

$$\frac{\Delta E}{E} = 11.55\% \sqrt{1 + \frac{1.89}{E}} \tag{5.1}$$

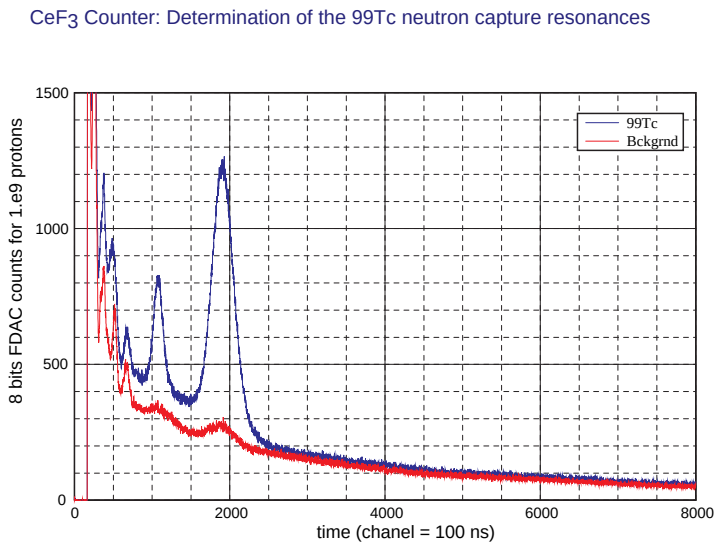

Figure 5.9: Determination of the ^{99}Tc capture resonances.

With the use of CeF_3 detector, the error in the thermal region was found to be

$$\frac{\Delta E}{E} = 12.11\% \sqrt{1 + \frac{1.70}{E}} \tag{5.2}$$

For neutron energies above 3 keV, the Energy-Time relation also spreads up because of the emerge of neutrons from inelastic $(n,2n),(n,3n)$ reactions on the Lead atoms. For the remaining energy domain, where true isolethargic moderation occurs, the error is given theoretically from 2.66 on page 23, where in the case of Lead is equal to 11.4%.

5.2.5 Conclusions

The Energy-Time correlation function has been simulated and experimentally determined for a number of neutron energies and positions in the lead volume. Experimental results are in very good agreement with the simulation, and the theoretical predictions. Recalling that the time width of the neutron source is very small (20 ns), this systematic study shows that the actual lead block is a very efficient neutron spectrometer. With a precisely determined Energy-Time correlation function, that can be well reproduced by Monte Carlo simulation.

5.3 Monte Carlo Flux Calculation

The *TARC* flux measurements have to be compared to the prediction of the EET Monte Carlo chain: *FLUKA* for the spallation followed by the TARC Monte Carlo for neutron transport below 19.6 MeV and finally by the same program simulating a small region around the detector. This detailed comparison is an important prerequisite step for the understanding of Adiabatic Resonance Crossing. It is therefore crucial to assess precisely the degree of agreement (or disagreement) between the data and the prediction. This requires not-only technical checks of the Monte Carlo calculation, insuring that the whole chain, from FLUKA to the detector simulation is handled in a consistent way, but also an evaluation of the systematic errors.

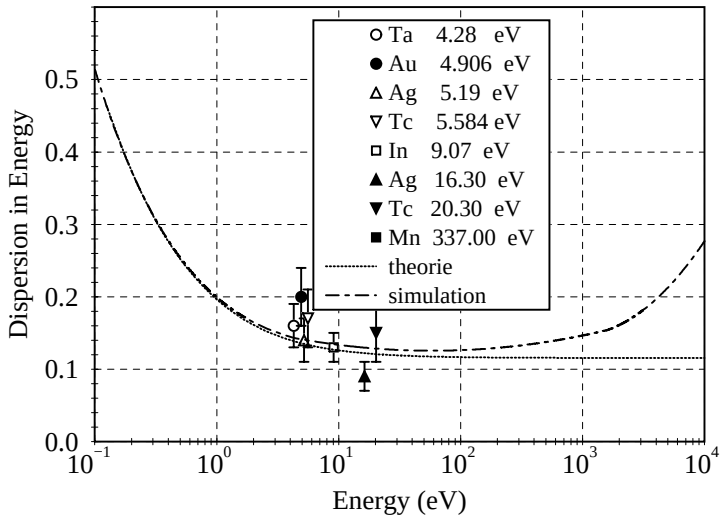

Figure 5.10: Dispersion in the Energy-Time relation. The continuous line refers to the theoretical value [42], and the dotted line to the simulation. All the data are for energies below 10 keV. On the experimental points, the errors are estimations of the width of the resonances from the measurements with the CeF_3 detector and the PM.

5.3.1 Systematic Errors of the Monte Carlo

The main systematic error contributions to the calculation of the neutron flux come from:

FLUKA Simulation

The simulation of the spallation process in *FLUKA* and the neutron transport down to 19.6 MeV for which the major sources of uncertainties can be summarized as follows:

- Cross sections (mostly reaction cross sections) for protons and neutrons in the energy range of interest (20 MeV – 3 GeV): The RMS deviation between the cross section adopted in FLUKA and available experimental data for lead is below 10%. The error introduced in the calculations is significantly smaller in the bulk of the cascade since at the energies of TARC almost all protons interact inelastically before being ranged out by ionization losses.

- Neutron production model: The model used in FLUKA for the description of nuclear interactions has been extensively benchmarked against several sets of experimental data. Double differential data about neutron production in lead are available for energies from 20 MeV to 3 GeV. The predicted double differential spectra agree with the experimental data within a factor two and often much better over the full range of energy and angles. The resulting agreement on angle integrated spectra which are likely to be most relevant for TARC is typically within 10-20% over most of energy spectra. The total neutron multiplicity can be estimated to be predicted with errors not exceeding 10%. These errors are significantly reduced in a thick target cascade due to a significant averaging among different energies and to overall constraints (like energy conservation).

Lead Cross Section

The simulation of neutron physics in lead below 19.6 MeV (mainly uncertainties in neutron cross sections for lead, anisotropy at high energy, etc.). This contribution is estimated to be of the order of 10%.

The Effect of Impurities in Lead

With the *TARC* simulation code, we studied the effect of the various impurities contained in the lead, on the neutron flux. Four different lead qualities were considered: TARC lead of purity 99.999% and purity of 99.99%, 99.985% and 99.987%. For the TARC lead, we use the measured concentrations, for the others we change the concentration for all the elements for which the vendor gives the concentration and for the others which are not known we keep the same concentrations as for TARC.

We find that within a distance of 1.5 meter from the center of the lead assembly, the average change in fluence over the entire neutron energy range is smaller than 10% for qualities 99.99% and 99.985%. For quality 99.97% the decrease in flux below 5 eV reaches 30% (Fig. 5.11).

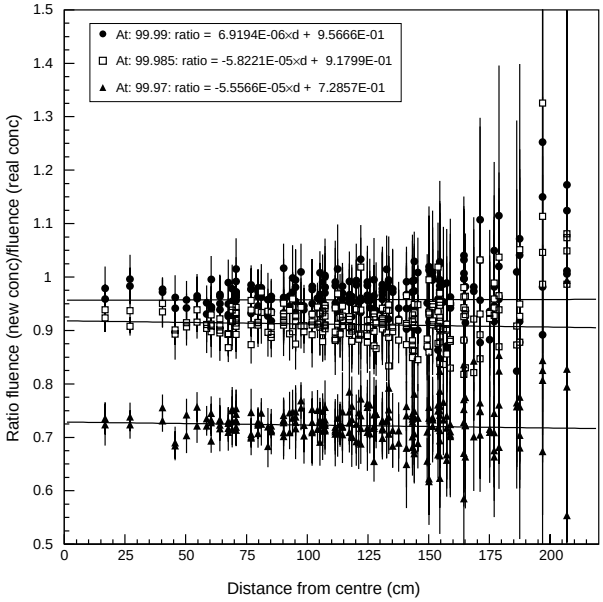

Figure 5.11: Variation of the ratio of neutron fluence in TARC lead to neutron fluence in lead with different impurity contents as a function of distance to the center of the lead assembly, as obtained from *Monte Carlo* simulation. The neutron fluence is considered in the energy range from 1.0 eV to 5.0 eV.

In order to assess the systematic error contribution from the uncertainty in the impurity content of the TARC lead, we have run the simulation with concentrations modified in the following way:

- all concentrations increased by 2 standard deviations $C = C + 2\sigma_c$;
- all concentrations decreased by 2 standard deviations $C = C - 2\sigma_c$.

Then we computed the fluence ratio between the two cases Fig. 5.12. The change of fluence is small, negligible above 1 eV, it reaches 6% at thermal neutron energy. This implies that the

effect, on the TARC neutron fluence measurement, of the uncertainty in the impurity concentration in the TARC lead is negligible, over the whole energy range investigated by TARC.

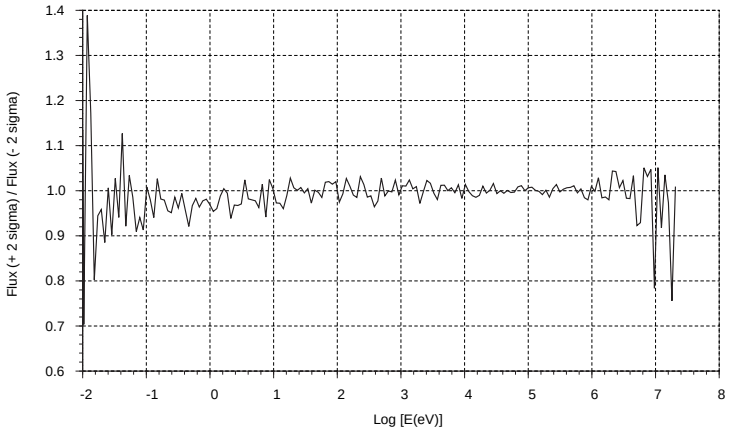

Figure 5.12: Ratio of neutron fluences obtained with modified concentrations of all impurities by ± 2 standard deviations with respect to TARC nominal concentrations, in the simulation.

In order to study more specifically the effect of silver, we have run the simulation for a silver concentration increased by a factor 10, $C(\mathrm{Ag}) = 37.8\ ppm$. The ratio of fluences with the increased Ag concentration to the normal TARC concentration shows no effects down to neutron energies of 50 eV. A spectacular effect is found, as expected below the main silver resonance of 5.2 eV, where the fluence drops by 20% (Fig. 5.13). This allows to quantify the effect of silver. A variation of the silver concentration by 2 standard deviation, implies a maximum flux change by 0.6%, well, below the main other sources of systematic errors.

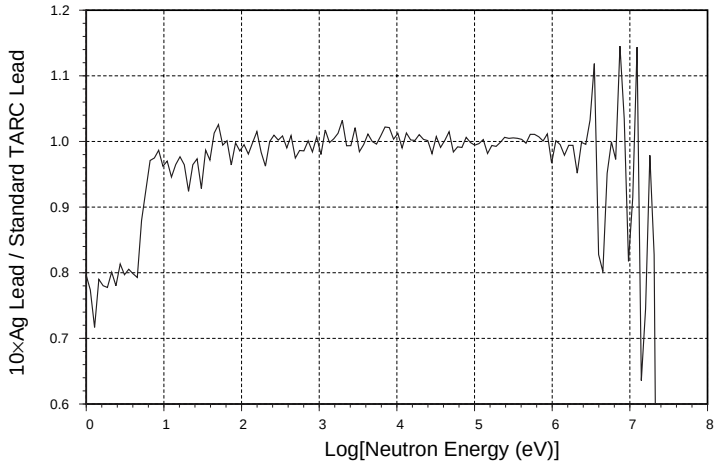

Figure 5.13: Ratio of neutron fluences obtained from *TARC Monte Carlo*, with modified silver concentration by a factor 10 with respect to the TARC nominal value.

We conclude that the error coming form the uncertainty in impurity concentrations in the TARC lead is safely negligible. The total systematic uncertainty in the flux calculation, over the neutron energy range covered by TARC, from thermal neutrons to a few MeV, even though hard to pin down precisely, we estimate not larger than 20%. A systematic analysis of all the cross section data is needed to be more precise on this point.

5.3.2 Technical Checks of the Monte Carlo Quality

A number of technical checks were performed to ensure that the Monte Carlo calculation was free of technical flaws:

Continuity Between FLUKA and EA Monte Carlo Code

The flux calculated in the FLUKA step was extended to the EA Monte Carlo code energy range ($\leq$ 19.6 MeV) and the continuity of the flux between the two simulation programs was checked.

Comparison Between Various Flux Calculation Methods

A study was made to ensure that the flux calculation does not depend on the method used to perform the calculation. In particular, it was checked that adding, in the simulation, a 1 cm thick layer of lead at each end of the instrumented block ($15 \times 15 \times 15\ cm^3$) does not induce distortions in the neutron flux distribution in the energy range of interest (thermal to few MeV neutrons). This lead layer randomizes the energy distribution of neutrons which otherwise would go through the hole without interacting, thereby producing spikes in the neutron flux energy distribution.

This is clearly illustrated in Fig. 5.14, where we compare the ratio of the neutron fluence in one instrumented block ($15 \times 15 \times 15\ cm^3$) relative to the one in the entire instrumented hole ($15 \times 15\ cm^2$ in cross section and 300 cm in length) for which no additional lead is needed. We find the that distortion is negligible in the energy range between thermal neutrons and a few MeV.

The Effect of Neutron Capture in Flux

We used the simulation to investigate further the behavior of neutrons in lead. For instance, we switched off the neutron capture process in the simulation and observe the modification of the neutron fluence (Fig. 5.15). We found that indeed, in lead, the effect of captures are relatively small, down to neutron energies of 1 eV. For instance, the neutron fluence $dF/d\ln E$, which is

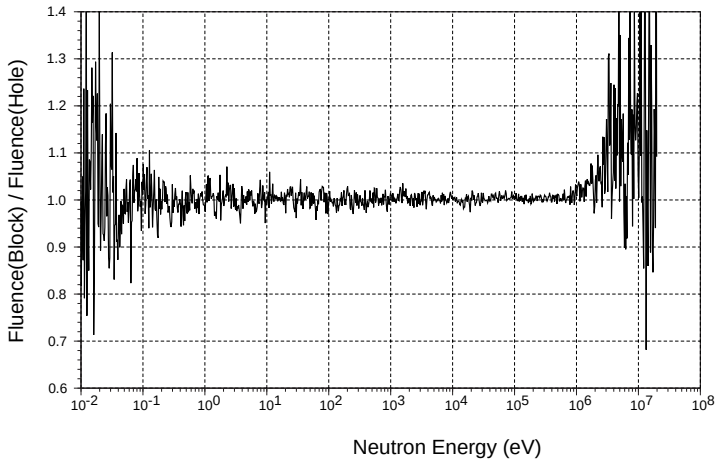

Figure 5.14: Ratio of the neutron fluence in one instrumented block (hole 10, block 11) with the addition of 1 cm of lead at each end of the hole relative to that of an entire instrumented hole (hole 10, z = + 7.5 cm) for incident protons of 3.5 GeV/c.

equal $E \times dF/dE$, decreases only by a factor of 10 from 1 MeV to 1 eV, while if we switched off lead captures, this factor is reduced to 5. This remaining decrease in fluence is due in part to the fact that the lead volume is not infinite, and also to a diffusion effect well accounted in the Fermi age theory.

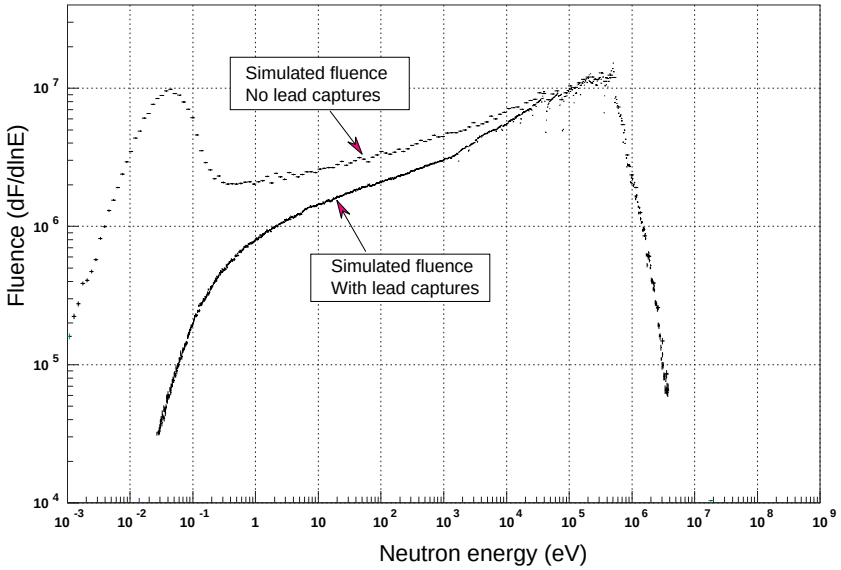

Figure 5.15: Comparison of the neutron fluence in hole number 10, with and without neutron captures in lead.

Comparison Between Flux from 2.5 GeV/c and 3.5 GeV/c

It has always been taken for granted that the ratio of neutron fluences produced by protons of different energies is independent of neutron energy. We have verified, using our simulation that this is indeed the case, at least in the neutron energy range between thermal and a few MeV (Fig. 5.16). These systematic checks, together with many more trivial checks allowed us to develop both confidence in the results obtained, but also gave us a good understanding of the detailed neutron behavior in lead, which is one the main objects of the TARC study.

5.4 Neutron Flux Measurements

The neutron fluence is the quantity that characterize the performance of the ARC effect and the neutronics of the lead volume. For these reasons, several detectors/techniques have been used in *TARC* to measure the neutron fluence (Fig. 5.17). These detectors fall into the following broad categories:

- Low energy ($E_n \leq 50\ keV$) using the Energy-Time relation, like the ^{6}Li/^{233}U silicon detectors performed by the French groups and ^{3}He scintillation counter from the Greek groups.

- Low energy activation, for integral or measurements at specific energies like the Thermoluminescence and the Activation foils, by the Greek groups.

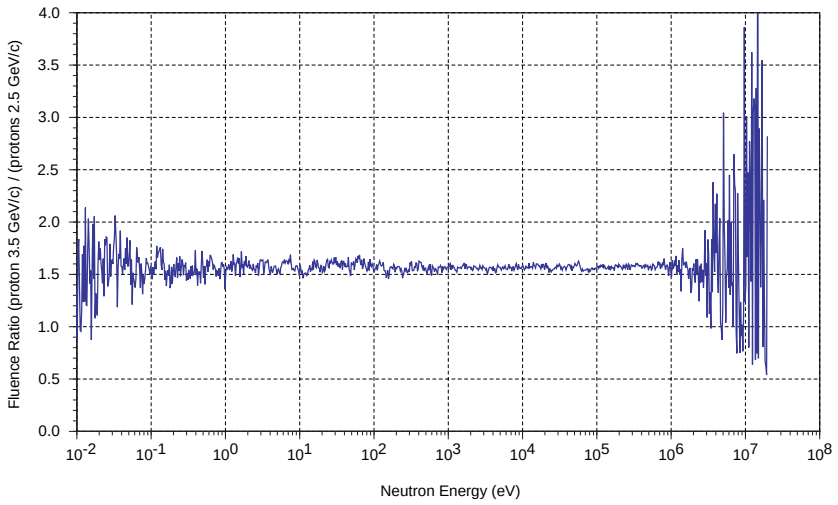

Figure 5.16: Ratio of fluences produced by 3.5 and 2.5 GeV/c protons in TARC *Monte Carlo*, as a function of neutron energy (hole 10, z=+7.5 cm). (Compare with Fig. 5.19)

- High energy ($10\ keV \leq E_n \leq 2\ MeV$) with ^{3}He ionization counters, performed by the Spanish groups.

- High energy neutron integral measurements with activation methods, with the use of Lexan detectors with fission measurements in ^{232}Th by the Greek groups, and the threshold reactions $^{12}\mathrm{C}(n,2n)^{11}\mathrm{C}$ ($E_n > 22\ MeV$) and $^{12}\mathrm{C}(n,3n)^{10}\mathrm{C}$ ($E_n > 34\ MeV$), performed by the French groups.

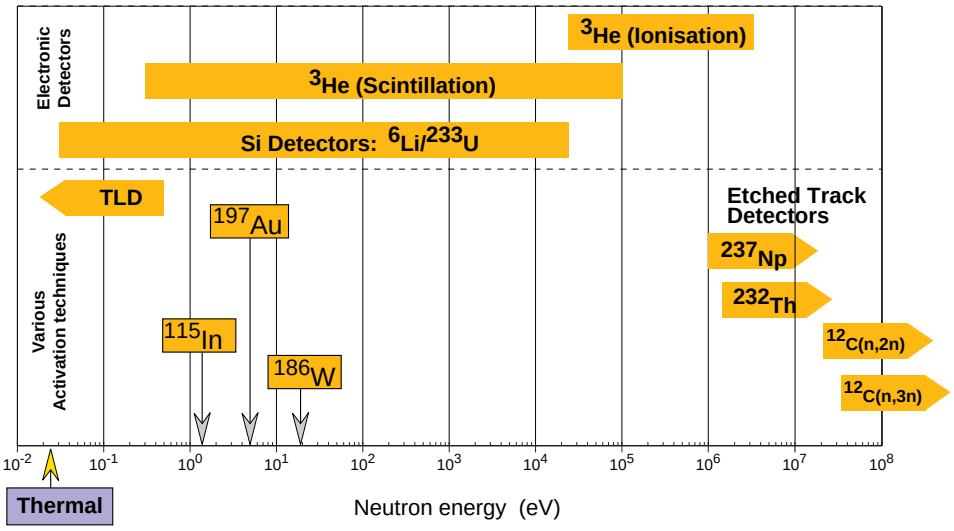

Figure 5.17: Illustration of the energy ranges covered by the different detector techniques used in TARC to measure neutron fluence.

5.4.1 ^{6}Li, ^{238}U Counters

One of the detectors for measuring the neutron in the low energy range ($E_n < 50\ keV$) using the Energy-Time relation, was the ^{6}Li/^{233}U silicon detector. The neutron fluence was measured, using the exothermic reactions $^6\mathrm{Li}(n,T)\alpha$ or $^{233}\mathrm{U}(n,\mathrm{fission})$. The ionizing particles of these reactions, were detected using Si detectors. Provided that the relative cross sections $\sigma(E)$ of these reactions is well known, from the number of events we can extract the neutron flux.

Description

The two Si detectors [43] ($10 \times 10 \times 0.3\ mm^3$) were enclosed in a common lead box ($10 \times 15 \times 20\ mm^3$) facing respectively a ^{6}Li ($100\ \mu g/cm^2$ ^{6}LiF converter layer) and a ^{238}U ($200\ \mu g/cm^2$ converter layer) target separated by a $0.1\ mm$ thick sheet of lead (Fig. 5.18). Each Si junction (surface of $10 \times 10\ mm^2$ and thickness $300\ \mu m$) detects the ionizing products (α and t) of the neutron induced reaction

$$n + {}^6\mathrm{Li} \rightarrow \alpha + t + 4.78\ MeV$$

or fission fragments (FF) from ^{238}U fissions ($Q = 180\ MeV$). Two thin foil targets of $1 \times 1\ cm^2$ separated by a $0.1mm$ foil of lead, were inserted between the two Silicon detectors. The ^{6}Li was made of a 95% ^{6}LiF layer of either $50\ \mu g/cm^2$ or $100\ \mu g/cm^2$ deposited on a $50\ \mu g/cm^2$ polyethylene backing. The ^{233}U target of $200\ \mu g/cm^2$ is pure ^{233}U electro-deposited on a $200\ \mu m$ thick aluminum foil.

This small detection device is enclosed in a lead box. The external size was of $20 \times 37 \times 12\ mm^3$, which was itself enclosed in a stainless steel cylinder of $25\ mm$ diameter. Vacuum was established by external pumping trough a small tube. Between the magnets and the silicon detectors, two diaphragms select the trajectories by rejecting those with too large angles with respect to the perpendicular direction to the Si detector plane. The α-decay of ^{238}U ($t_{1/2} \sim 1.59 \times 10^5\ yr$) provides an absolute calibration of the detector efficiency. This detector ensemble allows us to measure, at the same position and at the same time, the neutron fluence with two different nuclear reactions having different cross sections and sensitivities to the background. The error on the detector efficiency is 6%. The detector thickness is small enough that it does not perturb the fluence significantly. Flash ADC's were used to record time and amplitude of signals generated by alpha's (α), tritons (T) and fission fragments (FF) all clearly distinguished from the observed backgrounds.

Data Analysis

The measured event rate, $n(t)$, in Δt bins can be written as:

$$\begin{aligned} n(t)\Delta t &= \varepsilon N_{\mathrm{at.}}\ \Delta t \int \phi(E,t)\sigma(E)dE \\ &= \varepsilon N_{\mathrm{at.}} \Delta\Phi(t) \int C(E,t)\sigma(E)dE \end{aligned} \tag{5.3}$$

where ε is the detector efficiency, $N_{\mathrm{at.}}$ is the number of atoms in the target, $C(E,t)$ is a normalized function describing the E dispersion at time t obtained from the data, $\sigma(E)$ is the ^{6}Li (n,t) or ^{238}U (n,f) cross section, $\Phi(E,t)$ is the neutron fluence, $\Delta\Phi(t)$ is the differential fluence corresponding to all neutrons detected at time t, in the interval Δt. Eq. 5.3 is obtained using the relation (Eq. 2.67 on page 24) and the calculation of $\sigma_{\mathrm{eff}} \equiv \int C(E,t)\sigma(E)dE$ with the *JENDL-3.2* cross section database.

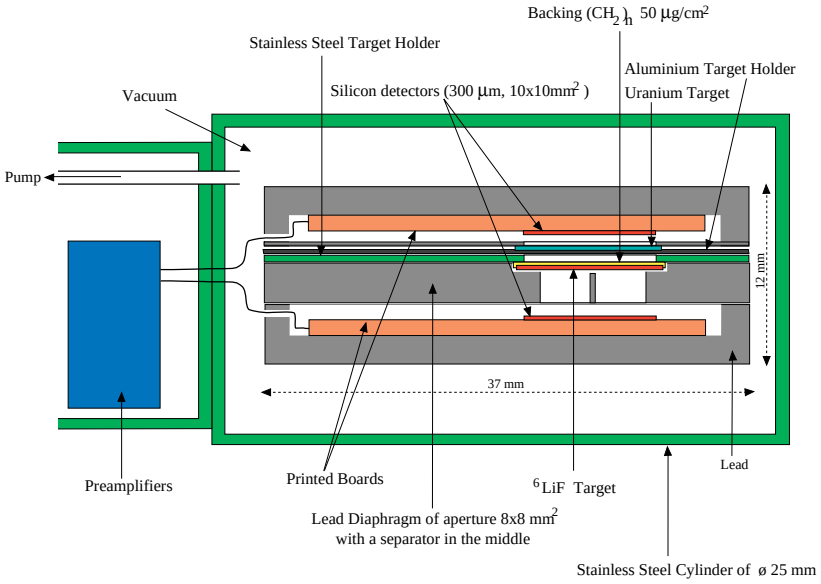

Figure 5.18: Schematic of the Si-detector ensemble showing both the ^{238}U and the ^{6}LiF targets.

We did not measure the neutron energy by summing the triton and α energies detected in coincidence, due to the limited energy resolution, poor statistics and the important random coincidences background. Therefore the $n + ^6$ Li reactions were identified by α or T detection, and no direct neutron energy measurement has been made.

In total, 69 positions were measured [43], providing a detailed map of the neutron fluence evolution throughout the entire lead volume. Typical results are shown in Fig. 5.18, in hole number 10, 45 cm from the beam axis at the position $Z = +7.5$ cm (Fig. 1). The total systematic error on the fluence measurement is 14% below 100 eV and reaches 16% at 1 keV.

While most of the measurements have been made using a proton beam of 3.5 GeV/c, few measurements have been made at 2.5 GeV/c. The associated fluence energy spectra for both beam energies are compared. As expected, these fluences are proportional to each other, in the measured energy range. This is illustrated in Fig. 5.19 and leads to the measured ratio

$$R = \left\langle \frac{\Phi_{3.5\ GeV/c}(E)}{\Phi_{2.5\ GeV/c}(E)} \right\rangle = 1.44 \pm 0.05 \qquad (5.4)$$

This ratio is not too far of the expected value coming from the ratio of beam kinetic energies $R_{kinetic} = 1.58$, if the number of primary spallation neutrons is proportional to the proton kinetic energy.

5.4.2 ^{3}He Detector in the Scintillation Mode

Description of the Counter

The scintillation light[1] produced in a mixture of

$$^3\text{He} \quad (1 \times 10^5\ Pa)$$
$$\text{Xe} \quad (1.18 \times 10^5\ Pa) \quad \text{and}$$
$$^4\text{He} \quad (2.75 \times 10^5\ Pa)$$

[1] on average 13 photoelectrons per neutron capture on ^{3}He

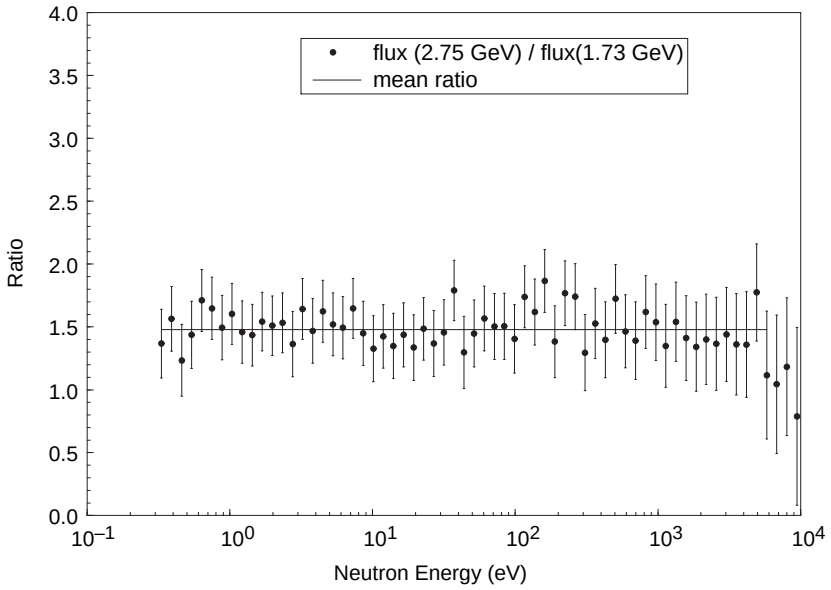

Figure 5.19: Ratio of differential fluences obtained with the two beam momenta 3.5 GeV/c and 2.5 GeV/c.

by the reaction

$$n + {}^3\mathrm{He} \rightarrow p + T \quad (\text{Q-value of} + 764\ keV)$$

was detected by a phototube, after having been wave shifted to 340 nm in order to go through the quartz window, which was separating the chamber from the photocathode [44]. A Flash ADC was used to record signals from the phototube working in the current integration mode. As in the case of the ^{6}Li/^{233}U detectors, the Energy-Time relation and the known cross section for

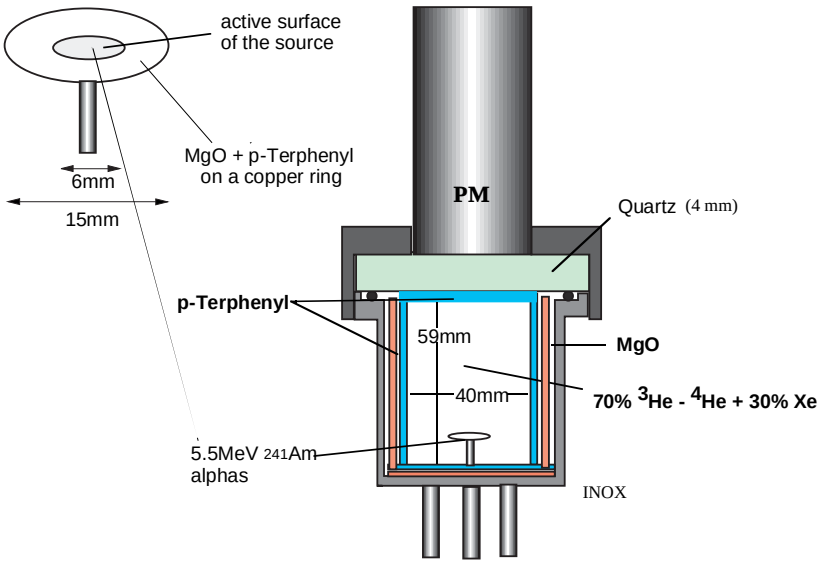

Figure 5.20: ^{3}He scintillation counter layout

the reaction ^{3}He (n,p)^{3}H were used to transform the measured time evolution of the interaction rate into a neutron fluence measurement as a function of neutron energy.

During the slowing down process of charged particles, through ionization loss inside the ^{3}He gas, photons were emitted with intensity proportional to the energy deposited in the gas. The photons were emitted in the atomic de-excitation and recombination processes, following the electromagnetic interactions with the electrons of the gas atoms. In order to increase the scintillation light output, a mixture of ^{3}He 90% with Xe 10% was used. Xe produces light at 172 nm and is also used as a wavelength shifter that shifts part of the ^{3}He scintillation photons from 62 nm to 172 nm. Finally, a layer of p-terphenyl was deposited on a highly reflecting coating of MgO on the inner walls and on the base of the chamber.

The ^{3}He scintillation chamber (Fig. 5.20) is cylindrical, made from stainless steel, with inner diameter of 40 mm and length of 59 mm. A quartz window 4 mm thick was used to connect the photomultiplier with the chamber.

At room temperature p-terphenyl evaporates and introduces an impurity in the gas, quenching the photon emission. Thus, an ^{241}Am α-source 5.5 MeV was placed inside the chamber for the continuous calibrating of the gas efficiency.

Measurements

There were two sets of measurements, for the two different proton momentum 3.5 GeV/c and 2.5 GeV/c. For each position an extra measurement was made, using a mixture of 1.18 bar Xe, 2.75 bar ^{4}He for background calculation. These background measurements have been normalized to the same proton beam intensity and subsequently subtracted from the spectra.

The signal of the photomultiplier (PM) was directed to a 200 MHz, PM amplifier and then to an 8-bit ICARUS FADC with a sampling rate of 100 ns. Each measurement of at 3.5 GeV/c was carried out at three different PM voltages 450, 500 and 550 V (to ensure that there is no saturation of the signal at very short times). At 2.5 GeV/c the voltages used were 500, 550 and 600 V. This difference is due to the smaller signal we had at 2.5 GeV/c. The voltages we used were in the linearity region of the photomultiplier. In order to reduce the photomultiplier gain. Since the light output from the chamber, saturates at the nominal photomultiplier high voltage (850 V), for a beam shot intensity of more than 3×10^7 protons.

An example for a typical run at 2.5 GeV can be seen in Figures 5.21,5.22. The mean signal is calculated from the accepted pulses (those with intensity inside the valid limits).

The efficiency of the detector was continuously monitored by observing the photopeak produced by 5.5 MeV αlpha's from an ^{241}Am source. This detector covers a neutron energy range from 0.3 eV up to about 50 keV, over which the systematic uncertainty on the neutron fluence measurement varies from 0.1% up to 55% at 50 keV.

Neutron Fluence Calculation

The ^{3}He (n,p)^{3}H reactions per energy are proportional to the neutron fluence

$$N_{\text{events}}(E) = \sigma(E) \times \Phi(E) \times N_{\text{atoms}} \tag{5.5}$$

where $N_{\text{events}}(E)$ are the number of reactions in the chamber volume as a function of the incident neutron energy, $\sigma(E)$ is the cross section of the (n,p) reaction on ^{3}He, $\Phi(E)$ is the neutron fluence and N_{atoms} is the ^{3}He atoms inside the chamber. The FADC is giving the number of events, as a function of time of every FADC channel. The time is then converted to the kinetic energy of the neutrons using the energy-time relation (see § 2.9 on page 23)

For a given binning in energy (100 equal lethargy bins from 10^{-2} up to 10^5), every energy bin corresponds to a time bin, which is calculated with the Energy-Time relation. The contents

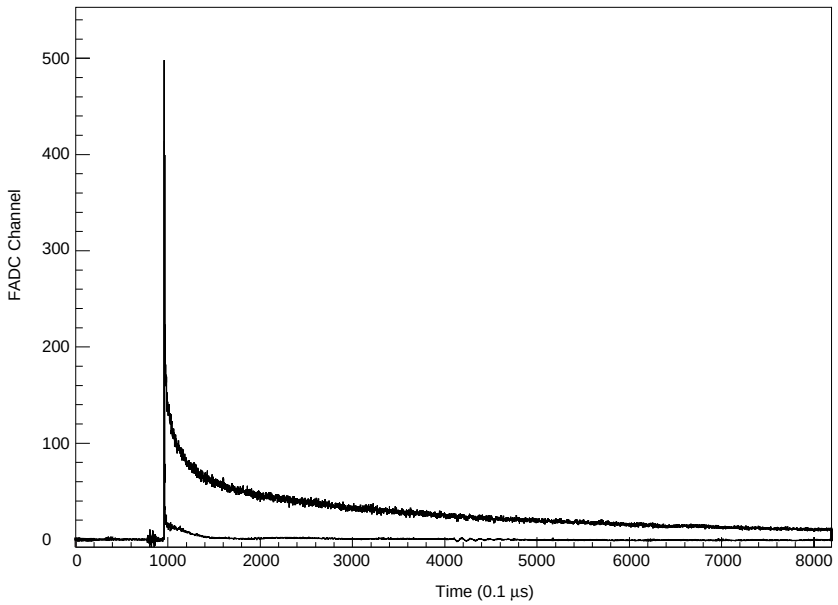

Figure 5.21: Mean signal ^{3}He upper curve, and background ^{4}He lower curve, for 100 ns binning for hole 10, +7.5,500 V at 2.5 GeV/c

of this time bin in the data spectrum (100 ns binning), are added and converted, using the calibration factor of the FADC for the given PM voltage, to the number of events.

Typical results are shown in Fig. 6.13 and 6.14 on page 112, where the neutron fluence $\Phi(E) = dN(E)/dE$ per energy bin is plotted as a function of the energy, for hole 1 at +7.5 cm. The main sources of errors was the uncertainty of the proton beam, and the FADC calibration.

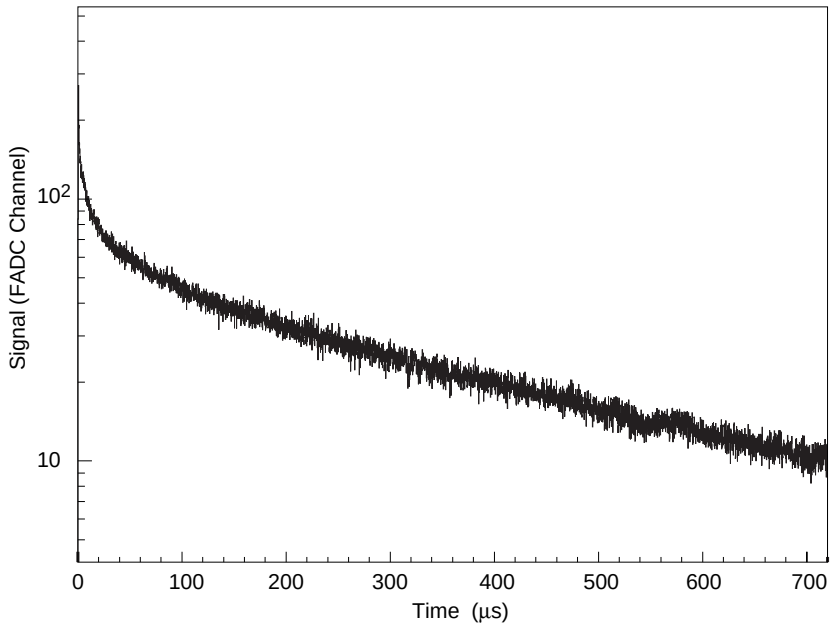

Figure 5.22: ^{3}He signal minus background (^{4}He) for 100 ns binning for hole 10, +7.5,500 V at 2.5 GeV/c

Resulting in a total contribution of less than 13.7%.

5.4.3 Thermoluminescence Detectors

Thermoluminescence detectors [45] provide an integral measurement of the low energy neutron fluence ($E_n < 0.5\ eV$). The thermoluminescence (TL) technique for radiation measurements involves two steps. In the first step, the TL detector is exposed to the radiation and the absorbed energy remains stored in the detector, via electron trapping in long lived metastable states. In the second step, the material is heated and the electrons are released from their trapping levels and recombine with holes; during this procedure, light is emitted, whose intensity is proportional to the stored energy.

The application of TL in dosimetry is based on the fact, that the TL intensity is directly proportional to the amount of the incident radiation. Therefore, after the calibration of the TL detectors, with a known amount of radiation, the measured TL glow-peaks become a measure of the unknown amount of the incident radiation.

The basic model of TL assumes that the ionizing radiation produces free electrons and holes, and some of these are trapped in local, discrete energy levels within the forbidden band. Usually, the shallower level is called a trap and the deeper level recombination center. The electrons remain trapped until the appropriate energy is given to free them. In the case of TL, this energy is given by heating the material. As the material is heated, the electrons are thermally stimulated to escape from the trapping centers into the conduction band and then, to recombine with trapped carriers of opposite sign in the recombination center, giving rise to a TL photon. The probability per second for the release of an electron increases proportional to the temperature and it is given by $S\,e^{-E/kT}$. $E\ (eV)$ is the activation energy, $S\ (sec^{-1})$ is the frequency factor, k the BOLTZMANN constant, and T the absolute temperature in ^oK. As the temperature is raised, the recombination rate increases at first as more trapped electrons are released. Then, after reaching a maximum, it drops as the traps are depleted. The result is a characteristic glow-peak whose intensity as a function of a linearly $T = T_o + \beta T$ increasing temperature is given by

$$I(T) = n_o\, S\, e^{-\frac{E}{kT}} e^{\left(-\frac{S}{\beta}\int_{T_o}^{T} e^{-E/kT}\, dT\right)} \tag{5.6}$$

where n_o is the concentration of trapped electrons, T_o is the starting temperature and β the heating rate K/s. Eq. 5.6 is used for the fitting of the experimental glow-peaks. A real TL curve consists of several overlapping single glow-peaks.

Thermoluminescence Dosimetry

The commonly used TL detector, for neutron radiation is the $LiF : Mg, Ti$. The main contribution to the TL after thermal neutron irradiation, comes from the α-particles and tritons produced from the $^6\mathrm{Li}(n,T)\alpha$ reactions. For mixed gamma-neutron fields, pairs of ^{6}LiF and ^{7}LiF are used, where the ^{6}Li is very sensitive to neutrons while the ^{7}Li is not. Both, have the same sensitivity to gammas.

Use of Cadmium Cover

To discriminate the thermal contribution, another pair of crystals is used covered with Cd. Cd due to its high resonance at $0.55eV$, is a perfect high-pass filter for neutron. Detailed estimates have shown that for an adequate attenuation of the thermal neutrons, the cadmium foil should

be at least 0.76 mm thick and preferably 1.0 mm. In this way, the contribution from neutrons with energies below 0.55 eV can be evaluated.

Exposure in Lead

The ^{7}LiF : Mg, Ti and ^{6}LiF : Mg, Ti detectors, before their use, were annealed at 400^o C for 1 hr and 100^o C for 2 hrs. The detector setup is shown in Fig. 5.23. Two pairs of crystals ^{6}LiF and ^{7}LiF were placed inside two lead cups, where the one pair had extra Cd cover on both sides. The two cups where placed inside a lead barrel and placed inside the holes of the $TARC$ lead block. The measurements were performed with the *Harshaw 3500* manual TLD reader. The maximum readout temperature was 350^o C and the heating rate used was 10^o C/sec.

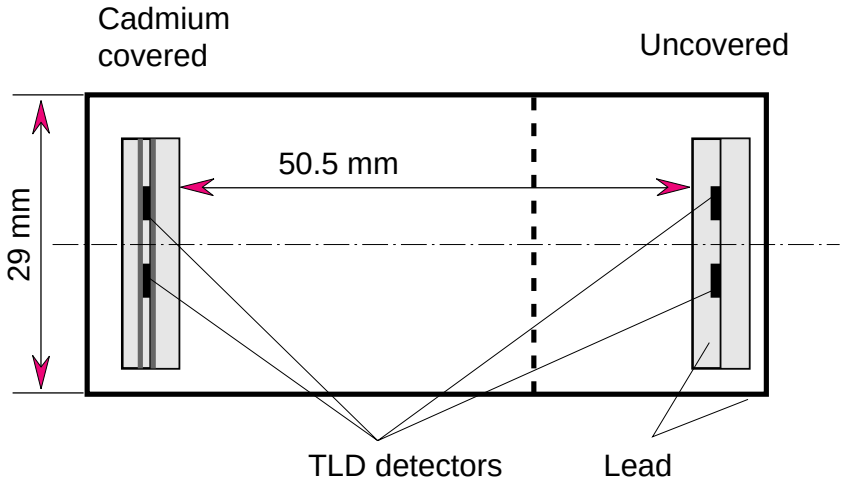

Figure 5.23: TLD detector setup

The glow-curve shapes, obtained from the readout annealing, are shown in Fig. 5.24. It is observed that the glow-curve shapes of the two detectors are completely altered, due to the different rearrangement of the individual glow-peak intensities. In this case, it is clear that the integral of ^{7}LiF is not comparable to the integral of ^{6}LiF.

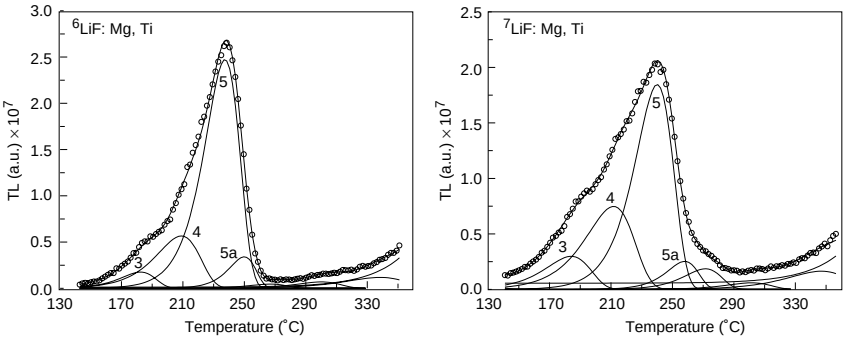

Figure 5.24: Glow-curve shapes of ^{6}LiF:Mg,Ti (left) and ^{7}LiF:Mg,Ti (right) after their normal annealing at 400^{o}C for one hour and 100^{o}C for two hours and post irradiation annealing at 80^{o}C for one hour. The test dose was 13.8 mSv from ^{60}Co gamma rays.

Usually, the measure of TL is taken to be the integral of TL between some channels defined from the beginning of the glow-peak 4 up to the end of glow peak 5. However, it is evident

that integral of glow-peaks 4+5 is not appropriate to be taken as a measure for the TL. For this reason a glow-curve deconvolution procedure was applied, which overcomes successfully the problems appearing when integrating in the simple way.

Calibration

The transformation of the TL signals into neutron fluence needs the proper calibration of the ^{6}LiF-^{7}LiF pairs with a fluence of thermal neutrons. The thermal neutron source used for the calibration was the subcritical nuclear reactor of the Nuclear Physics Laboratory of the University of Thessaloniki, Greece.

Five ^{6}LiF-^{7}LiF pairs uncovered and Cadmium covered were exposed in the nuclear reactor to a fluence of $(1.08 \pm 0.04) \times 10^6$ thermal neutrons per cm^2 per min. From these measurements a calibration line was obtained. The slope of this line is the calibration factor which was found to be $(12.4 \pm 0.5) \times 10^{-3}$ TL counts per neutron.

The gamma doses are evaluated from the TL signal of ^{7}LiF detectors. The detectors were calibrated with a known exposure from a ^{60}Co gamma source in the CERN calibration room. The calibration exposure was 1.386 10^{-2} Sv. The gamma calibration factors for ^{7}LiF were for normal annealing 2.337 $10^7 \pm 6.13$ 10^5 TL counts per Sv and for Readout anneal 4.16 $10^7 \pm 2.26$ 10^6 TL counts per Sv.

Thermal Neutron Fluences

Due to the relatively small dimensions of the LiF crystals ($3.1 \times 3.1 \times 0.89$ mm^3) and the large ^{6}Li (n,T) cross section the detector is opaque to neutrons with energies below 0.5 eV. Since the detection efficiency is approximating the unity, using this implementation we can measure the integrated neutron fluence for energies below the cut-off threshold of Cd 0.5 eV. The thermal neutron fluence as a function of the radial distance from the center of the lead block are shown in Fig. 5.25. The errors in neutron fluence are as high as $15 - 20\%$.

5.4.4 High Energy Neutrons (10 keV to 2 MeV) with ^{3}He Ionization Counters

As, already explained in previous sections the low energy range is the most important for the long-lived fission fragments transmutation. Neutron energies up to 10 keV are covered by several detectors, mainly the ^{3}He scintillation counter and the(LiF,^{233}U)-Si detector. However, the beginning of life of neutrons takes place in the high-energy region where the competition between the capture resonances and the elastic and inelastic collisions and the multiplicative (n,2n) reactions, will determine the available flux at low energies. In addition, the knowledge of the neutron flux in the region of the spallation cascade, dominated by the high-energy neutrons, is very important for the design of the spallation target, one major item of any ADS design. The energy range above 1 MeV is covered partially, in an integrated way, by ^{237}Np and ^{232}Th based fission counters, but the main detector providing at $TARC$ the energy spectrum in this region is the ^{3}He ionization chamber.

This counter use the same

$$n + {}^3\mathrm{He} \rightarrow p + {}^3\mathrm{H} + \mathrm{Q} \qquad \text{where Q=764 } keV \tag{5.7}$$

reaction as the ^{3}He scintillation counters, but measure the ionization charge deposited by the outgoing proton and triton in the chamber gas mixture (^{3}He 4 10^5 Pa, ^{40}Ar 2 10^5 Pa and CH_4 0.4 10^5 Pa). They are of the *Culter-Shalev* type [46] with the addition of guard electrodes

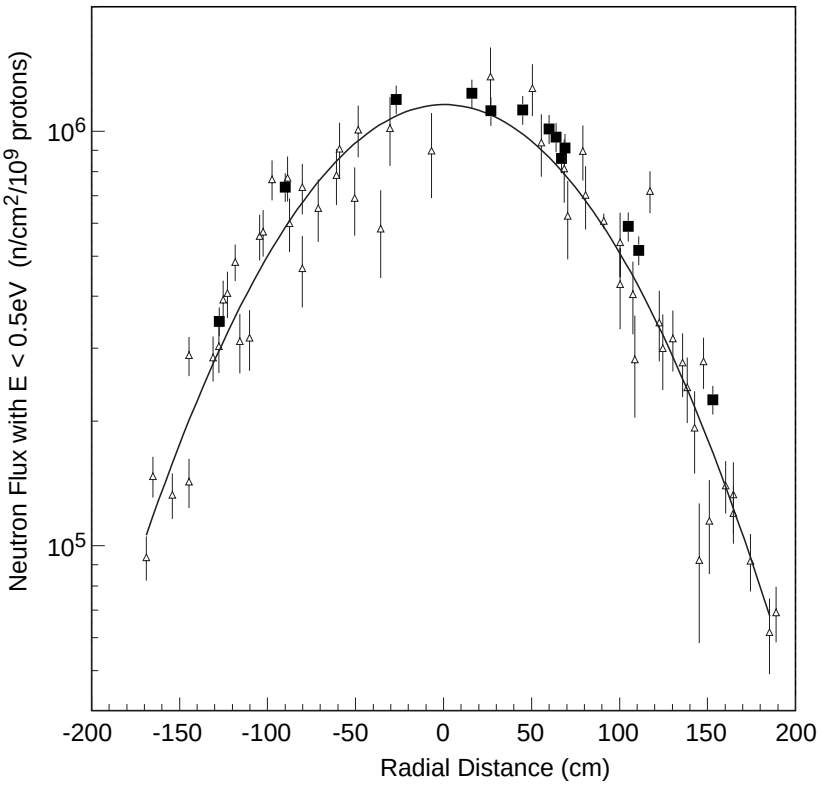

Figure 5.25: Thermal neutron fluence ($E < 0.5\ eV$) as a function of the radial distance in the Lead block. The line is an eye guide connecting the experimental points. The black points are Monte Carlo points.

and proportional wires allowing precise definition of the fiducial volume in which the p and t tracks are fully contained. They extend neutron fluence measurements from 20 keV to 2 MeV.

Description of the Counter

Fig. 5.26 shows the transverse view of the counter. The container is a stainless steel (304L) cylinder, 0.8 mm thick, with an external diameter of 57.9 mm, capable of holding a pressure $> 15\ bars$. The length of 140 mm, defining a total internal volume of $\approx 330\ cm^3$ was chosen to have a sensitive volume giving a maximum counting rate of a few kHz and representing a small perturbation to the gradual slowing down of neutrons in lead since the ^{3}He has very large neutron capture cross section at low and intermediate energies.

Elements of the Detector Response to Neutrons

As already mentioned, the main reaction between the neutrons and the gas contained in the ^{3}He counter, producing the signals collected, is the (n,p) reaction $n + ^3\mathrm{He} \rightarrow p + ^3\mathrm{H}$. The kinetic energy contained in the p and the ^{3}H, is in very good approximation equal to the neutron energy plus the 764 keV of the Q of the reaction. The signal collected is proportional to this sum of kinetic energies, and the neutron energy can easily be computed from the observed signal amplitude. The (n,p) reaction has a high cross section at low energies that decreases with the energy, with a $1/v$ law Fig. 5.28. As a first consequence, low-energy neutrons have

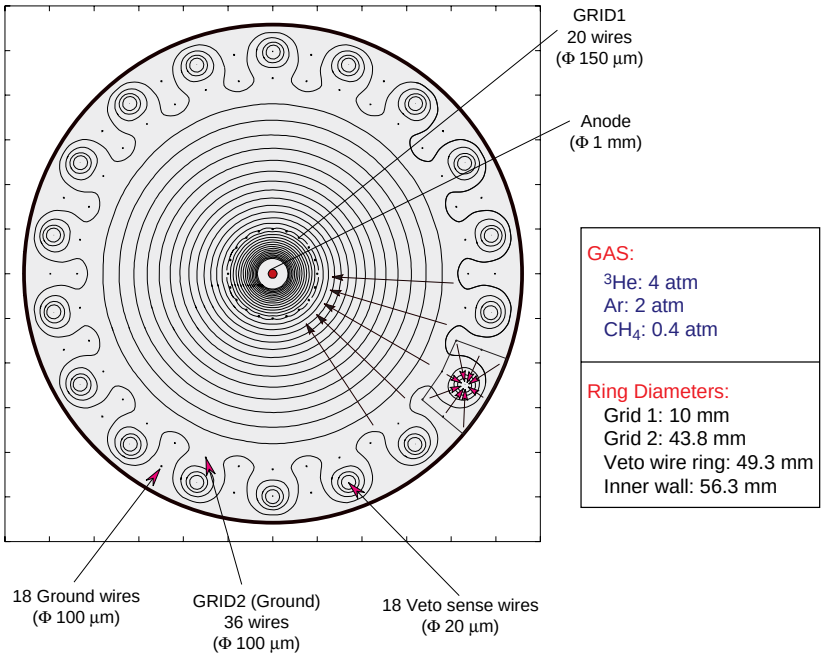

Figure 5.26: Transverse view of the ^{3}He ionization detector

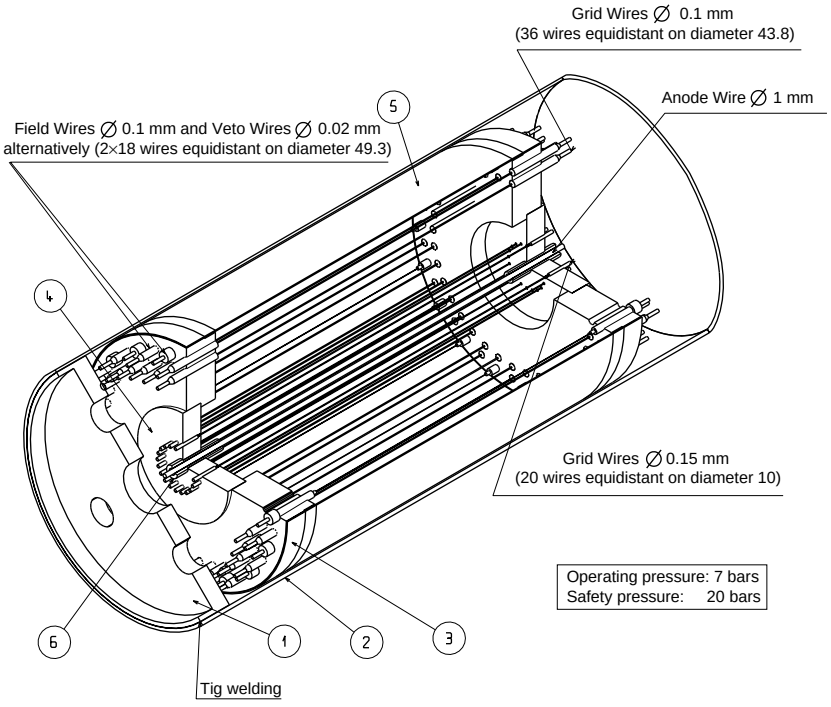

Figure 5.27: 3D scheme of the ^{3}He ionization detector

a high probability of producing signals in the counter, with a strong peak in the amplitude spectrum at 764 keV, corresponding to the thermal and epithermal neutrons. On the other

hand, the counter is nearly transparent to fast neutrons[2], the efficiency is smaller, and there are nearly no shelf-shielding effects in this case. As a second consequence, as the energy increases new processes have a larger relative importance in the production of the observed signals. The recoil nuclei from elastic collisions of neutrons with progressively heavier nuclei contained in the counter gas, are the main alternative source of signals in the region below 10 MeV. The amplitude distribution of the signals, produced by neutrons of a fixed energy through any of these processes, is to a first approximation (isotropic approximation), a flat distribution from zero to the maximum energy. This maximum energy is a fraction, $4A/(1+A)^2$, of the neutron energy. In reality, at neutron energies close to or higher than 1 MeV, the elastic scattering with nuclei, including ^{3}He, is not completely isotropic and this anisotropy distorts the flatness of the energy distribution of the recoil nuclei. The presence of these components in the detector response at high energies makes impossible a direct determination of the neutron energy from the collected signal on an event-by-event basis. However, in principle it is always possible to compute the neutron energy spectra from the amplitude spectra of the collected signals by a deconvolution procedure. This procedure requires knowing precisely, the detector response to monoenergetic neutron beams of all the energies in the range of interest. In addition, if the total amount of non-(n,p) reactions is sufficiently small, the use of a corrected (n,p) detector efficiency allows one to extract the neutron energy spectra in a simpler and more direct way.

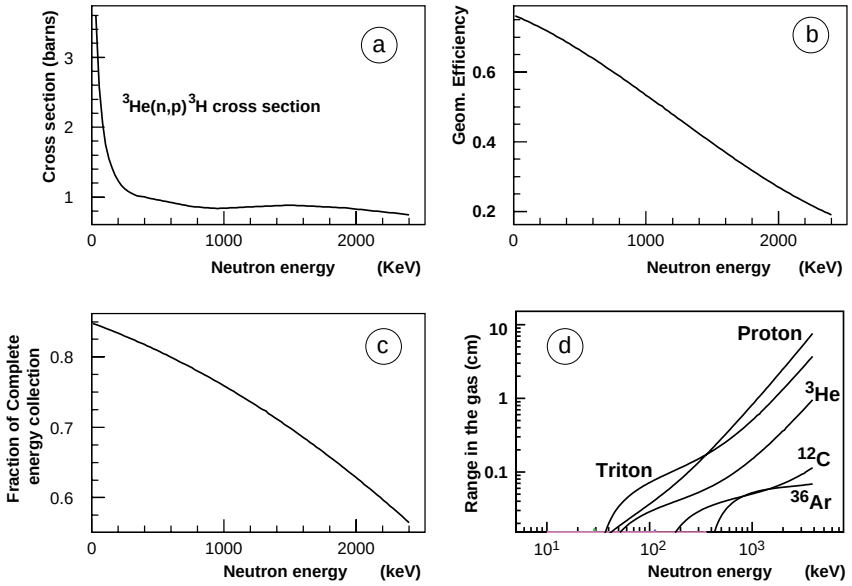

Figure 5.28: Factors of the (n,p) peak efficiency calculation in the quasi-transparent approximation.

TARC Experimental Data

The beam used in the slow extraction mode, mainly at a momentum of 2.5 GeV/c, contains 20% of protons separated from pions 60%, muons and electrons 20% by time of flight measurements. Only beam particles with a four-fold coincidence in the scintillation hodoscope were accepted. The estimated accidental background is $\leq 1.6\%$.

[2]When a detector is placed inside a neutron field, then the presence of the detector is altering the field. So, the detector must be either small in size or made up from materials with low total cross section for neutrons.

The counters with typical energy resolution of 6% FWHM at the thermal neutron peak were tested with neutron sources (^{252}Cf and ^{241}Am/Li and calibrated with monoenergetic neutrons at the *CEN Bordeaux Van de Graaff*. A detailed detector simulation was developed adjusting the fiducial volume limit by fitting the calibration data. The effect of neutron elastic scattering on hydrogen and ^{3}He nuclei was estimated to be acceptably small ($< 20\%$) for the neutron energy range considered. Fluence energy spectra were obtained from the recorded anode signal, of the amplitude histogram by deconvolution, taking into account the detector response function. The typical fluence uncertainty is 16 to 18%, of which $\approx 15\%$ comes from the calibration and 10% from the deconvolution process. There has been in total more than 400 runs covering 15 positions in the lead volume.

Chapter 6

Neutron Flux with Activation Foils

Standard isotopes like Gold (^{197}Au), Indium (^{115}In), and Tungsten (^{186}W), exhibit a very strong and isolated resonance (Fig. 6.1, 6.2), which is several orders of magnitude larger than the other resonances of the isotope. These elements, can be used as neutron "filters" for the neutron energy where the main resonance is located. Hence, they can be used, for measuring the neutron flux at specific energies (the main resonance energy) or even to measure the neutron cross sections of other elements. It is a simple technique, that we used as a complement of the other fluence measurements. Moreover it provides a good test for the activation procedure.

6.1 Triple Foil Activation

The triple foil activation as standard technique [47, 48, 49] was proposed as an additional test in the determination of the neutron fluence at specific energies, to very strong and isolated capture resonance, ie. ^{197}Au (4.9 eV), ^{186}W (18.8 eV) and ^{115}In (1.457 eV) Fig. 6.1,6.2. The method

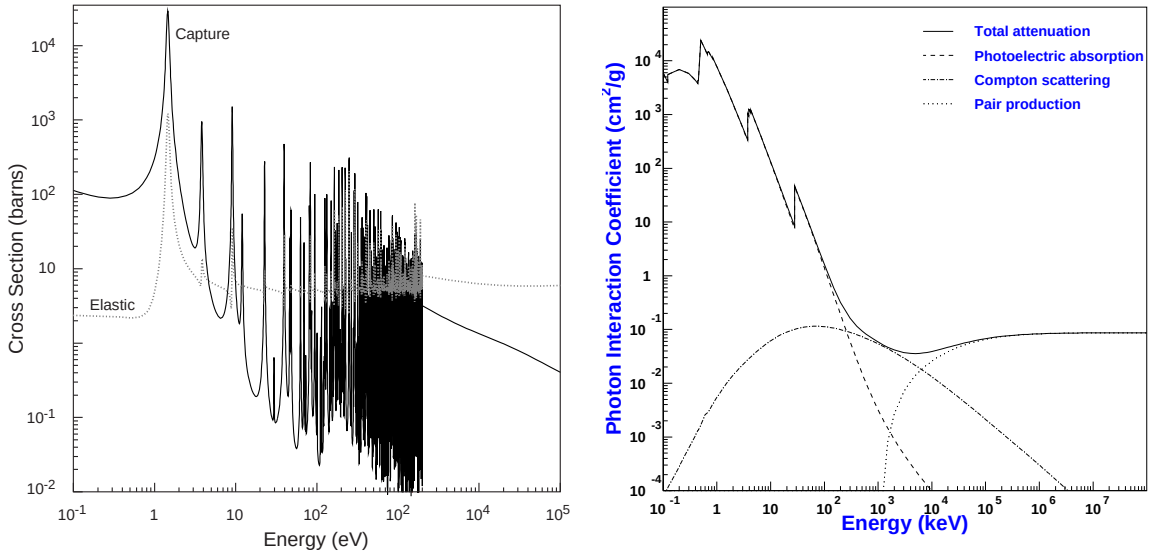

(a) Indium

Figure 6.1: Indium (*JENDL-3.2*) capture and elastic cross section, and photon interaction coefficients.

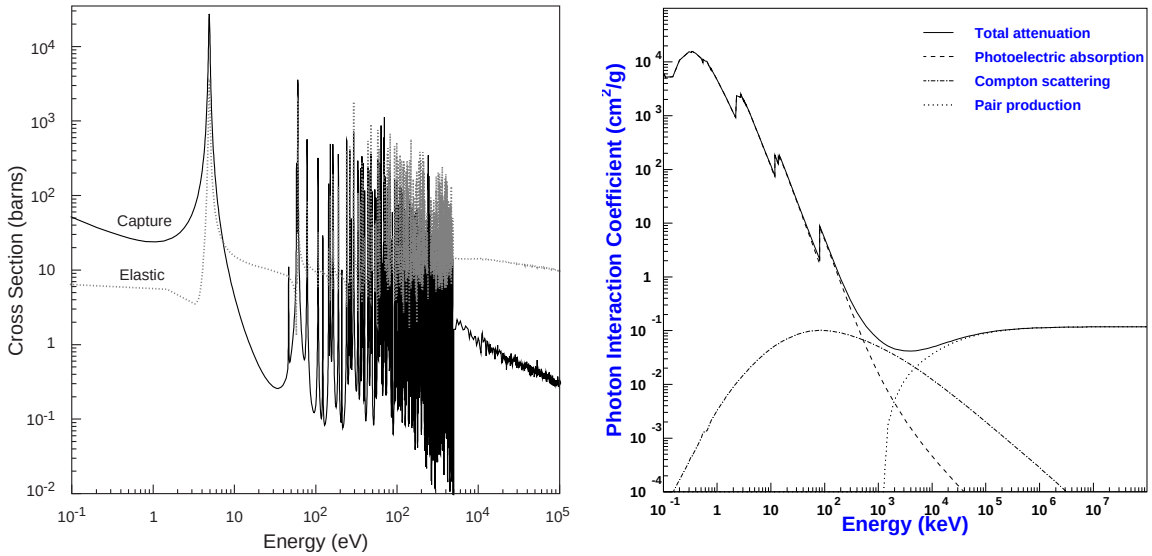

(b) Gold

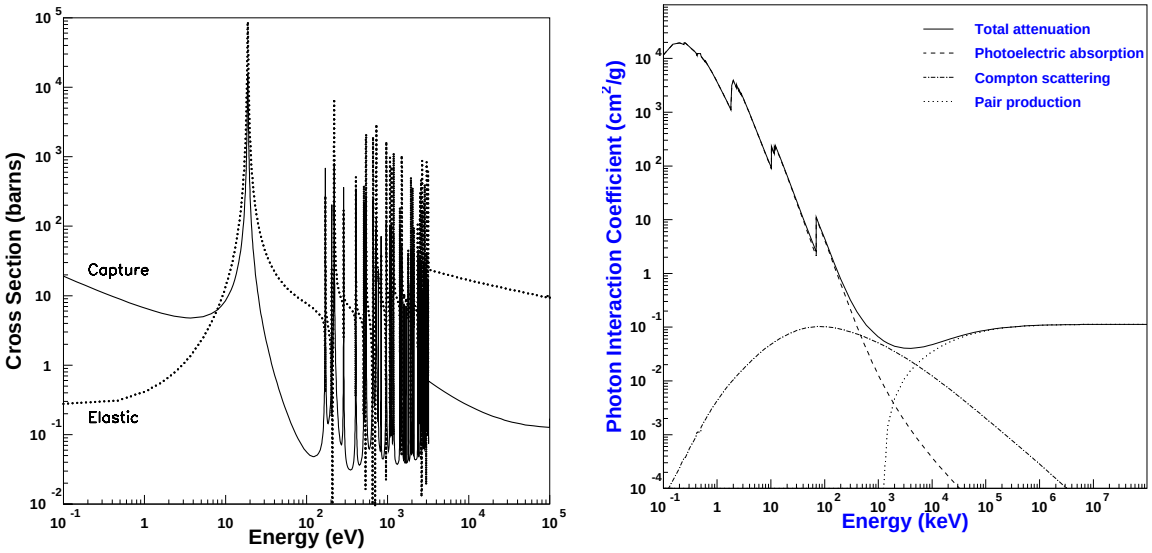

(c) Tungsten

Figure 6.2: Gold (*JEF-2.2*) and Tungsten (*ENDF-B/VI*) capture and elastic cross section, and photon interaction coefficients.

utilizes a foil sandwiched by two other foils of the same material and thickness Fig. 6.3, and is used to measure activities induced only by the resonances. The two outer layers predominantly absorb neutrons with energies at the main resonance. Their thickness is chosen such as to absorb $\geq$ 80-90% in this energy region. The inner layer is activated as strongly as the outer ones by the $1/v$ part (where v is the neutron velocity) of the absorption cross section and the minor resonances at higher energies.

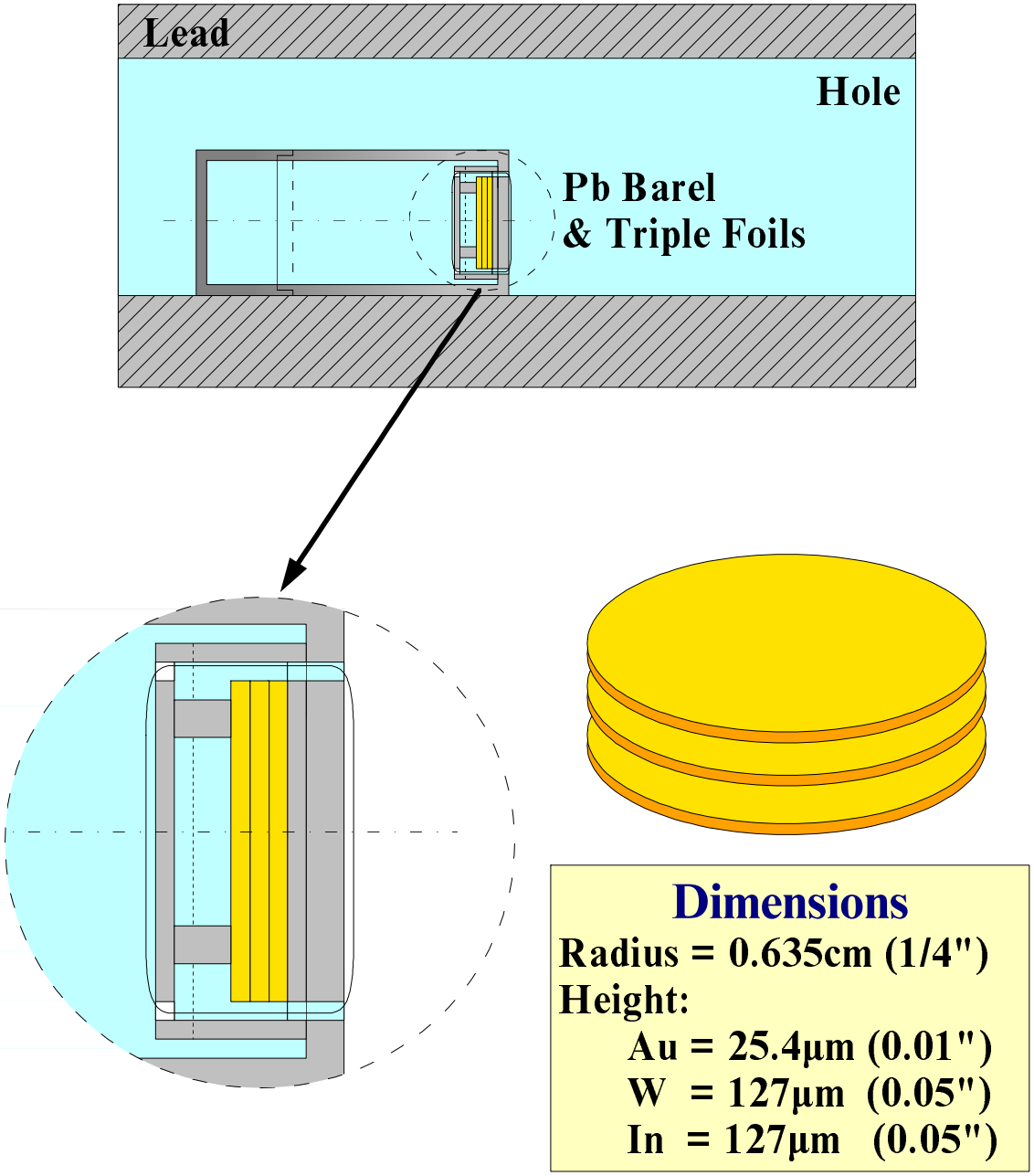

Figure 6.3: Triple foils geometry. The lead barrel was used for the correct placing of the foil sandwich inside the hole.

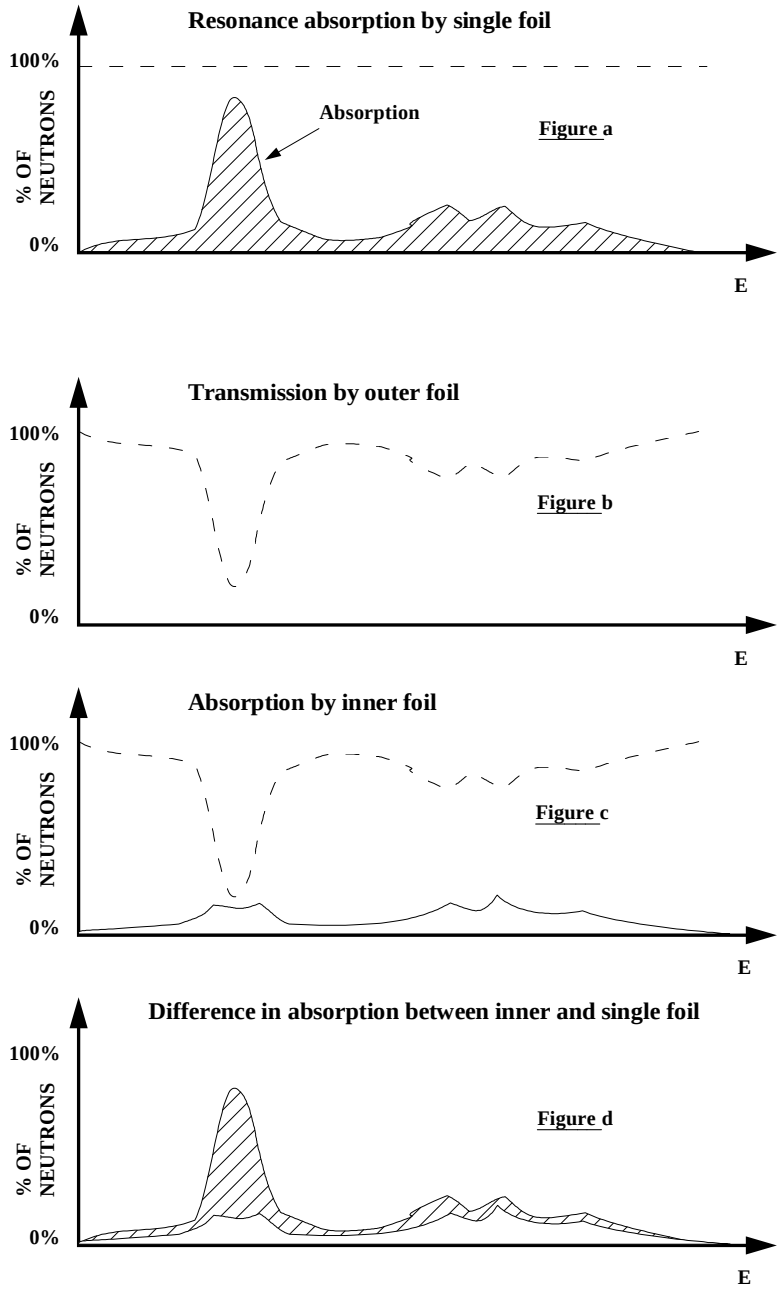

Figure 6.4: Self absorption method for enhancing resonance fluence. The dashed horizontal line of **a** indicates the neutron energy spectrum (which for purpose of illustration, we assume to be constant). The solid line shows the percentage of neutrons being absorbed by the foil. (**a** indicates what occurs in either of the outer foils). The fraction of fluence transmitted by the outer foil is shown in **b** and the same fraction is shown in **c** as the fluence impinging on the inner foil. The inner foil is exposed to a reduced fluence, especially in the main resonance region. Hence, it absorbs a smaller fraction, as it is shown with the solid line in **c**. The amount by which it is reduced is the shaded area in **d**.

If the foils are so thin that the self-absorption is negligible (except at the resonance energy region), the fraction of difference in activation between an outer and inner layer is from the contribution of the main resonance. In order to determine the difference $A_{out} - A_{in}$ (difference of the activity of an outer foil to that of the inner foil) as accurately as possible, the ratio A_{out}/A_{in} must be as large as possible.

Fig. 6.4 illustrates the general principle of this method. The dashed horizontal line of Fig. 6.4a indicates the neutron energy spectrum (which for purposes of illustration, we assume to be constant). The solid line shows the percentage of neutrons being absorbed by the foil (**a** indicates what occurs in either of the outer foils). The fraction of fluence transmitted by the outer foil is shown in Fig. 6.4b and the same fraction is shown in Fig. 6.4c as the fluence impinging on the inner foil. The inner foil is exposed to a reduced fluence especially in the main resonance region and absorbs a smaller fraction as shown by the solid line in Fig. 6.4c. The amount by which it is reduced is the shaded area in Fig. 6.4d. Fig. 6.9a,b shows the histogram of captures on Outer and Inner foil from a *Monte Carlo* simulation of a triple *Gold* foil. From the difference Outer-Inner Fig. 6.9c, we can see clearly, the contribution of the main resonance. By subtracting the mean activity S

$$S = \frac{A_1 + A_3}{2} \tag{6.1}$$

of the outer foils from the inner one, we get the activity A

$$A = S - A_2 \tag{6.2}$$

only due to the main resonance.

6.1.1 Determination of Neutron Fluence

If we neglect the neutron scatterings in the foil (in the energy region of interest, near the main resonance where $\sigma_{abs} \sim \sigma_{total}$) the activation of a single foil, in a monoenergetic isotropic neutron field $\Phi(E)$ is given by (see § 2.5 on page 14)

$$\begin{aligned} C(E) &= \frac{\Phi(E)}{2}\,\phi_0(\mu_\alpha(E)\delta) \\ \phi_0(\mu_\alpha\delta) &= 1 - 2\int_0^1 te^{-\frac{\mu_\alpha\delta}{t}}dt \simeq \frac{2\mu_\alpha\delta}{1+2\mu_\alpha\delta} \end{aligned} \tag{6.3}$$

where $\delta = \rho d$ (g/cm^2) is the foil thickness, ρ (g/cm^3) is the foil density, d (cm) is the foil height, $\mu_\alpha(E) = \Sigma_a\rho$ (cm^2/g) the absorption coefficient, and Σ_a the macroscopic absorption cross section.

By integration of Eq. 6.3, we get the total activation of the foil. If we assume that the fluence $\Phi(E) \approx const.$ varies slowly in the region of the main resonance, then the activity of a single foil due to the resonance A_{res} will be

$$A_{res} = \lambda\frac{\Phi_{res}}{2}\int_{E_1}^{E_2}\phi_0(\mu_\alpha(E)\delta)dE \tag{6.4}$$

where λ is the radioactive decay constant.

In the case of the triple foils, we can calculate the activity of the inner foil as the difference a foil with double thickness from a single foil, with the assumption that all the neutrons fall only from one side

$$C_{in} = \frac{\Phi}{2}\left[\phi_0(2\mu_\alpha\delta) - \phi_0(\mu_\alpha\delta)\right] \tag{6.5}$$

The total activity of the triple foil sandwich, if we considered as a single foil with triple thickness, is given by

$$C_{in} + 2C_{out} = \frac{\Phi}{2}\phi_0(3\mu_\alpha\delta) \tag{6.6}$$

If we integrate over the energy region of the main resonance and create the difference of the activities of the inner foils from the outer, we get

$$\begin{aligned} A_{res} &= \lambda\frac{\Phi_{res}}{4}\int_{E_1}^{E_2}[\phi_0(3\mu_\alpha\delta) - 3\phi_0(2\mu_\alpha\delta) + 3\phi_0(\mu_\alpha\delta)]\,dE \\ &= \lambda\frac{\Phi_{res}}{4}f_r \end{aligned} \tag{6.7}$$

with

$$f_r = \int_{E_1}^{E_2}[\phi_0(3\mu_\alpha\delta) - 3\phi_0(2\mu_\alpha\delta) + 3\phi_0(\mu_\alpha\delta)]\,dE. \tag{6.8}$$

So, the fluence Φ_{res} in resonance region per eV will be

$$\Phi_{res} = \frac{4A_{res}}{\lambda f_r} \tag{6.9}$$

6.1.2 Measurements and Data Analysis

Material	Purity	d (mm)	R (mm)	E_{res} (eV)	σ_{peak} (b)	Γ (eV)
Indium	99.99334	0.127	6.35	1.46	29230	0.083
Gold	99.9936	0.025	6.35	4.906	27405	0.1502
Tungsten	99.9729	0.127	6.35	18.81	15426	0.369

Table 6.1: Foil properties (d is the thickness, R is the radius, E_{res} the energy of the resonance, σ_{peak} the cross section at the resonance and Γ the width of the resonance).

In *TARC* we have used 3 types of foils; In, Au and W with properties which are shown on Table 6.1. We have chosen, these three elements, because of the strong and isolated resonances they have, and they are considered to be standard materials for these kinds of activations. For each of these three elements, a sandwich of them was put in a small lead cap well fixed to one side of a lead barrel Fig. 6.3. This barrels were pushed to various positions inside the Lead assembly of the *TARC* experiment. After, being irradiated for a specific period of time, the foils were transfered to the *GeLi* detector for analysis. In each foil we were interested in the γ-lines resulted from the de-excitation, after the capture of neutrons. More specific:

Indium, in natural-abundance has two stable isotopes, ^{113}In (4.29%) and ^{115}In (95.71%). The activation cross section, we are interested in, is the capture of ^{115}In to the metastable states. The reaction (n,γ) leads to one ground state ^{116}In with resonance integral $I = 40\ b$ and half life $T_{1/2} = 14.1\ sec$ and two metastable states ^{116m}In and ^{116m_2}In with equal resonance integral of $I = 81\ b$ and half life $T_{1/2} = 54.29\ min$ for the first metastable and $T_{1/2} = 2.18\ sec$ for the second. ^{116m_2}In with its short half life immediately drops to ^{116m}In. While the decay from the ^{116}In ground state proceeds directly into the ^{116}Sn ground state, the isomeric states decay into excited states of ^{116}Sn [50]. Several gammas are emitted (Fig. 6.5) in their de-excitation, from these gammas we have used the followings:

Energy (keV)	%	μ_γ (cm^2/g)	Abs. (%)
1097.29	56.2	0.0540	0.49
1293.59	84.4	0.0496	0.46

both of them are coming from the two metastable states of Indium.

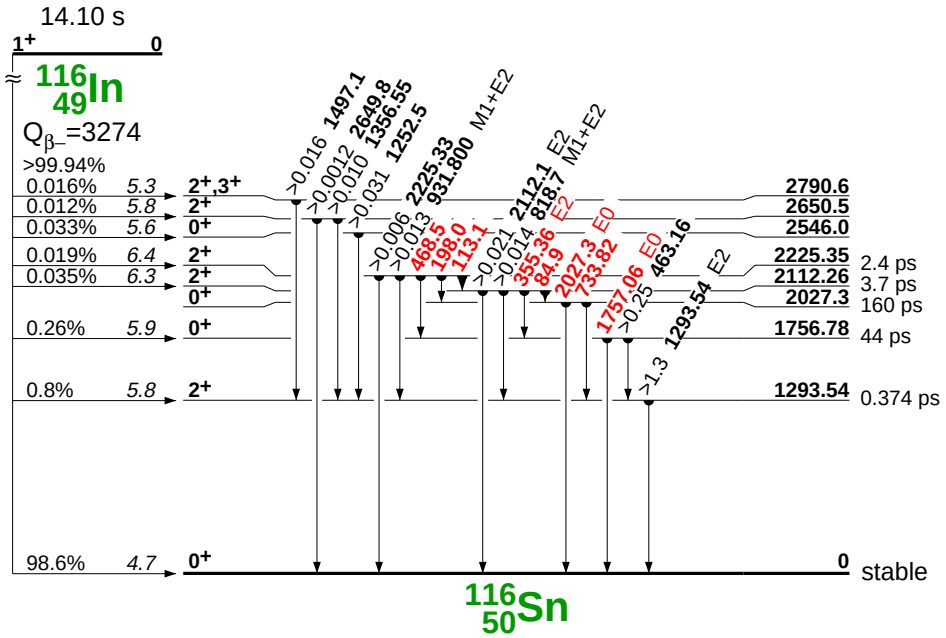

Figure 6.5: ^{116}Sn transition levels.

Gold has only one stable isotope ^{197}Au. The capture reaction of gold goes to ^{198}Au ground state with probability 99.95% and a 0.05% goes to the metastable state. The ground state emits only one gamma 411.804 keV (95.5%) Fig. 6.6, with a half life of $T_{1/2} = 2.69517$ $days$. With a total attenuation coefficient of $\mu_\gamma = 0.192 cm^2/g$ the abs.=0.9% of the gammas is lost. Gold, after the neutron capture it proceeds directly to ^{198}Hg [50]. Because of all of the above, gold is one of the best probes, and the easiest to handle.

Tungsten, the natural-abundance has five stable isotopes, ^{180}W (0.12%), ^{182}W (26.5%), ^{183}W (14.3%), ^{184}W (30.6%) and ^{186}W (28.4%). Here, we are interested in the (n,γ) reaction of ^{186}W isotope. By capturing one neutron it becomes ^{187}W which emits several gammas, with a half life of $T_{1/2} = 23.72$ $hours$ [50]. The gammas we used are given from the following table (Fig. 6.7):

Energy (keV)	%	μ_γ (cm^2/g)	Abs. (%)
618.335	6.07 %	0.107	2.5
685.744	26.4 %	0.097	2.3
772.89	3.98 %	0.085	2.0

Where, μ_γ is the total attenuation coefficient of the gammas in the foil material. The average probability that a γ-ray escapes a foil of thickness δ , which has been homogeneously activated is

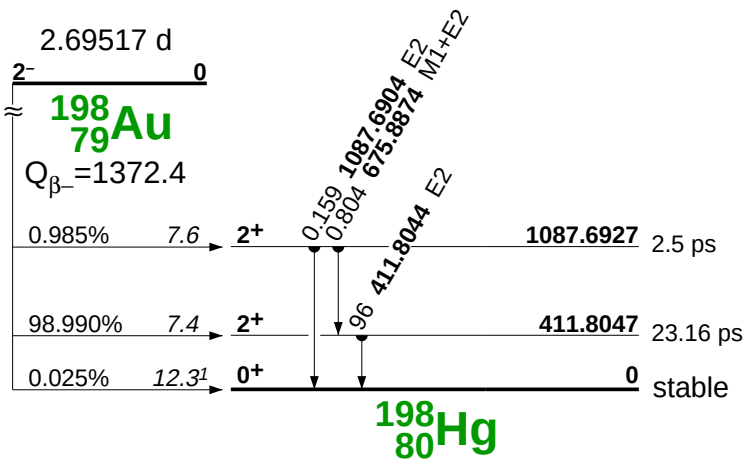

Figure 6.6: ^{198}Hg transition levels.

$\phi_0(\mu_\gamma\delta)/2\mu_\gamma\delta$. The total absorption coefficient has been used here, because Compton-scattered γ-rays suffer an energy loss and thus, can no longer be detected if a window discriminator is used.

The *triple foils* where placed in various positions (different radius from center), to create a fluence map of the entire lead block. During the irradiation, the activated samples are also decaying. Thus, we have two competing processes that determine the absolute value of the radioactivity of the sample at any point in time. The rate of change in N (the total number of radioactive nuclei) is the difference between the rate of activation R and the rate of decay:

$$\frac{dN}{dt} = R - \lambda N \tag{6.10}$$

where, λ is the decay constant for the isotope of interest, and R the rate of produced activated nuclei by capture. For this reason, we introduce the *effective* number of protons as the number of protons that would have produced the same number of radioactive nuclei at the end of irradiation, if they all came in one shot. If we are activating R atoms in each proton bunch, then at the end of the i-th bunch, the total number of atoms will be

$$N_i = R\,\Delta t - \lambda\, N_{i-1}\,\Delta t \tag{6.11}$$

where, N_i is the number of activated atoms in the i-th bunch, λ the decay constant, and Δt is the time interval between the two bunches which is smaller than the half life of the activated isotope. The solution of this equation is

$$N_n = n\,R\,\Delta t\,\cdot \sum_{i=0}^{n} [-\lambda\,\Delta t]^i \tag{6.12}$$

Since the number of activated nuclei, is proportional to the number of initial protons, then the *effective* number of protons P_{eff}, will be

$$P_{eff} = P \cdot \sum_{i=0}^{n} [-\lambda\,\Delta t]^i \tag{6.13}$$

where, P is the number of proton in each bunch. In the tables 6.2, 6.3, 6.4, is given the effective number of protons, for each irradiation.

At the end of the irradiation the foil sandwich was removed from the lead block and transferred to the GeLi Counter. The samples were counted and analyzed with the help of Inter Technique Gamma Spectrum analysis program. (For calibration of the GeLi detector see § 7.1.1 on page 113

The activity is further normalized for a common time (the end of irradiation), for surface of 1 cm^2 and for 10^9 effective number of protons. Then, we calculated the values of S and A from Eq. 6.1, 6.2. From the value of A, we can extract the fluence Φ_{res} per eV to the energy region near the main resonance (Eq. 6.9). The value of f_r (Eq. 6.8) can be calculated either analytically, by doing a Breit-Wigner fit on the main resonance or by evaluation with the use of cross section databases. In the following table we have shown the values of f_r (Eq. 6.8) for an integral range of 20Γ (Γ is the FWHM) around the resonance region ($E_1 = E_r - 10\Gamma$ and $E_2 = E_r + 10\Gamma$), and also the value we have taken from *Monte Carlo*. In the theoretical model we have not taken into account the effect of elastic scattering of a neutron in the foil for the In and Au (Eq. 6.3), since the elastic cross section is several orders of magnitude below the capture cross section, in the region of the main resonance Fig. 6.1, 6.2. In the case of *Tungsten*, what is also important, is the effect of the elastic scattering, since the scattering cross section has a peak at the resonance energy near 90.000b, 5 times larger than the capture. Because of the small height of the foils the effect of the neutrons coming from the sides of the foil can be safely neglected. The following table shows the analytic calculation of the value of f_r and the value from *Monte Carlo* simulation.

Element	f_r	MC f_r
^{116m}In	0.34	0.38
^{198}Au	0.34	0.33
^{187}W	0.50	0.53

In the case of *Indium*, we used as a lower limit of the integration $E_C = 0.55eV$ and not the $E_1 = E_r - 10\Gamma$ since the main resonance is very near to the thermal region, and the thermal contribution becomes important.

Tables 6.2, 6.3, 6.4 show the position in which the triple foils were placed, the mean normalized activity S in Bq (Eq.6.1) for 10^9 *effective* protons, the difference A in Bq (Eq.6.2) and the Flux Φ_{res} in $10^3\, n/cm^{-2}eV^{-1}$ for 10^9 protons for the energy of resonance E_r. The errors include only the statistical and the systematical errors from the γ measurements.

6.1.3 Monte Carlo Simulation

The *Monte Carlo* simulation was carried out in three steps:

1. With the FLUKA [5] program, spallation neutrons were created from a proton beam that collides on the Lead target. These neutrons were traced, until they reach a kinetic energy below 20 MeV or exit from the edges of the block.

2. With the TARC Monte Carlo, the *fluka* neutrons (from previous step) are traced in the Lead block geometry and logged into DST's (Data Summary Tape) when they cross specific targets (virtual blocks that surrounds each hole).

3. For every triple-foil position (block) a sandwich target was placed at the same position (as in the experiment). We traced down the neutrons for the block's DST file and collected

Run	Hole	Z (cm)	Eff. Protons	S (Bq)	A (Bq)	Φ $(10^3 n/cm^2 eV)$
760	3	-22.5	2.749E+12	61.678±0.972	14.150±1.422	552±55
195	3	-22.5	3.51E+11	58.583±0.954	14.069±1.411	555±55
760	3	7.5	2.749E+12	61.610±0.922	14.853±1.362	583±53
760	3	67.5	2.749E+12	41.653±0.675	9.839±0.985	386±38
760	6	-112.5	2.749E+12	17.429±0.269	5.152±0.848	202±33
760	6	-67.5	2.749E+12	35.197±0.533	10.100±0.762	396±29
760	6	7.5	2.749E+12	48.231±0.769	10.866±1.131	426±44
760	6	37.5	2.749E+12	43.900±0.677	13.138±0.965	424±36
195	6	37.5	3.51E+11	39.967±0.649	10.818±0.936	515±37
760	12	7.5	2.749E+12	26.680±0.405	7.088±0.590	278±23
760	12	112.5	2.749E+12	9.544±0.151	2.492±0.218	97±8
195	12	112.5	3.51E+11	9.315±0.168	2.878±0.239	112±9

Table 6.2: Position of In foils.

Run	Hole	Z (cm)	Eff. Protons	S (Bq)	A (Bq)	Φ $(10^3 n/cm^2 eV)$
183	3	-22.5	6.766E+12	0.339±0.005	0.067±0.007	216±22
800-2	3	7.5	2.362E+13	0.325±0.005	0.078±0.006	252±19
183	3	7.5	6.766E+12	0.339±0.005	0.078±0.007	252±22
183	3	67.5	6.766E+12	0.229±0.003	0.050±0.005	161±16
183	6	-112.5	6.766E+12	0.094±0.001	0.022±0.002	71±6
183	6	-67.5	6.766E+12	0.187±0.003	0.043±0.004	138±12
183	6	7.5	6.766E+12	0.254±0.004	0.068±0.005	219±16
183	6	37.5	6.766E+12	0.230±0.003	0.053±0.005	171±16
183	12	7.5	6.766E+12	0.143±0.002	0.031±0.003	100±9
183	12	112.5	6.766E+12	0.048±0.001	0.013±0.001	42±3

Table 6.3: Position of Au foils.

all the capture events done by the foils. The last procedure is repeated several times until a sufficient number of events was collected.

Because of the small size of the foils, several modifications had to be done to the *Monte Carlo* code. Gold foil had a thickness of $25\mu m$ which is near to the accuracy of single precision numbers used by the *Monte Carlo* code. In order to avoid this systematic error, the code had to be changed to double precision. To improve statistics we doubled the radius of each foil, which means 4 times larger surface. In order to speed up the process, we have created miniDSTs for a small empty volume placed in the same position as the foils. This volume was big enough to include the biggest of triple foils. A first run was made with this empty volume to collect all the neutrons passing through. Then with the use of this miniDST for every position, we have run the *Monte Carlo* simulation for each triple foil, taking special care of neutrons which they were passing the volume more than one time. If one of these neutrons was captured in one of the foils, then in all the subsequent crossings, this neutron was discarded. With the use of miniDSTs we have speed up the process by a factor of 3.

Run	Hole	Z (cm)	Eff. Protons	S (Bq)	A (Bq)	Φ $(10^3 n/cm^2 eV)$
544-6	2	7.5	1.272E+13	0.481±0.005	0.128±0.007	94±5
755	3	-22.5	1.788E+13	0.558±0.007	0.128±0.010	103±8
189	3	-22.5	4.E+12	0.545±0.007	0.140±0.011	94±7
755	3	7.5	1.788E+13	0.574±0.006	0.149±0.010	109±7
189	3	7.5	4.E+12	0.552±0.007	0.155±0.011	114±8
755	3	67.5	1.788E+13	0.391±0.005	0.102±0.007	67±5
189	3	67.5	4.E+12	0.371±0.005	0.091±0.008	75±5
755	6	-112.5	1.788E+13	0.156±0.002	0.042±0.003	30±2
189	6	-112.5	4.E+12	0.155±0.002	0.042±0.003	30±2
755	6	-67.5	1.788E+13	0.316±0.004	0.087±0.005	64±3
189	6	-67.5	4.E+12	0.316±0.004	0.081±0.006	59±4
755	6	7.5	1.788E+13	0.440±0.005	0.109±0.008	80±5
189	6	7.5	4.E+12	0.414±0.005	0.108±0.008	79±5
755	6	37.5	1.788E+13	0.386±0.005	0.101±0.007	63±5
189	6	37.5	4.E+12	0.372±0.005	0.086±0.007	74±5
544-6	12	7.5	1.272E+13	0.276±0.003	0.066±0.005	45±2
755	12	7.5	1.788E+13	0.240±0.003	0.062±0.004	48±3
189	12	7.5	4.E+12	0.225±0.003	0.057±0.004	42±2
755	12	112.5	1.788E+13	0.080±0.001	0.021±0.002	15±1
189	12	112.5	4.E+12	0.078±0.001	0.019±0.002	14±1

Table 6.4: Position of W foils.

The Monte Carlo gave us the number of captures for every foil and isotope. We calculated the activity with the following formula

$$A_{mc} = \frac{\lambda C N_o}{\pi R^2}$$

where, A_{mc} is the activity of the foil, λ is the decay constant of the isotope, C the number of captures on the foil, N_o is a normalization factor depending on the number of runs and R is the radius of the foil. From this point, we followed the same procedure as in the experimental data, to calculate S and A. In the *Monte Carlo* we have also the possibility, to extract the actual fluence at the foil position. This can be done, by placing an 'empty' vacuum foil and counting the neutrons that cross this empty volume. We know that the number of neutrons that cross a cylindrical volume with negligible thickness from both sides is $\Phi/2$. Results of Monte Carlo runs are shown in tables 6.5, 6.6, 6.7. The activities and fluences were normalized to 10^9 effective number of protons including only the statistical errors.

6.1.4 Conclusions

The precision of this method, is limited by the uncertainty on neutron capture cross sections $\sim 15\%$, except for Tungsten where large discrepancies were found between different cross section data libraries Fig. 6.8 (*JENDL-3.2* [47] and *ENDF-B/VI*). Data were collected at 14 positions Tables 6.2, 6.3, 6.4 for each of the three elements, to provide an independent fluence measurement, at energies within the range of the two previous electronic detectors. For Tungsten, our measurements were clearly best described by *ENDF-B/VI*. Typical measurements using

Hole	Z (cm)	S (Bq)	A (Bq)	Φ ($10^3 n/cm^2 eV$)
2	7.5	53.084±0.586	14.779±0.917	618±7
3	-22.5	69.097±1.393	19.176±2.178	622±7
3	7.5	70.666±0.690	16.866±1.096	686±9
3	22.5	73.982±1.441	19.457±2.267	732±8
3	67.5	76.248±0.782	19.854±1.231	491±7
6	-112.5	69.827±1.213	19.963±1.890	191±1
6	-67.5	71.481±0.694	17.911±1.097	404±5
6	7.5	50.538±0.622	13.324±0.978	519±8
6	22.5	18.151±0.153	5.472±0.237	569±7
6	37.5	39.449±0.408	11.198±0.636	507±6
10	7.5	54.042±0.675	14.471±1.059	599±9
12	7.5	53.872±0.615	16.418±0.951	274±3
12	37.5	49.142±0.544	13.585±0.851	260±2
12	112.5	62.240±0.836	17.857±1.302	124±1

Table 6.5: MC position of In foils.

3.57 GeV/c protons are shown in Fig. 6.12, in excellent agreement with those from ^{6}Li/^{233}U and ^{3}He scintillation detectors Fig. 6.13 and 6.14.

One important parameter is the fraction A/S (the activation of the resonance over the average activation of the outer foils). This is independent from most of our systematic errors: the foil position, efficiency of the GeLi detector, self absorption of gammas, beam calibration, the effective number of protons, the activation time, the absolute value of the neutron flux, and the radius of the foils. This factor is sensitive to the shape of the neutron flux, and the cross section database. Moreover, it depends very weakly in the uncertainty of the thickness of the foils. This A/S fraction from the *TARC* experiment and the *TARC Monte Carlo* simulation is about 10% above the experimental values. Possible causes of the difference are wrong impurities, error in cross section database, or a different temperature than 293^{o}K used for the analysis, so the Doppler broadening of the resonances in important.

Hole	Z (cm)	S (Bq)	A (Bq)	Φ $(10^3 n/cm^2 eV)$
2	7.5	0.229±0.009	0.056±0.011	192±4
3	-22.5	0.367±0.012	0.088±0.014	262±5
3	7.5	0.372±0.013	0.080±0.015	276±5
3	22.5	0.355±0.012	0.105±0.013	264±5
3	67.5	0.272±0.011	0.075±0.013	205±4
6	-112.5	0.089±0.003	0.017±0.003	73±1
6	-67.5	0.187±0.007	0.040±0.008	153±3
6	7.5	0.286±0.012	0.073±0.014	224±5
6	22.5	0.272±0.010	0.063±0.012	221±4
6	37.5	0.250±0.009	0.071±0.011	196±4
10	7.5	0.319±0.014	0.074±0.017	246±6
12	7.5	0.147±0.004	0.038±0.005	123±2
12	37.5	0.131±0.004	0.034±0.004	103±1
12	112.5	0.050±0.001	0.015±0.002	41±0

Table 6.6: MC position of Au foils.

Hole	Z (cm)	S (Bq)	A (Bq)	Φ $(10^3 n/cm^2 eV)$
2	7.5	0.345±0.021	0.044±0.024	67±2
3	-22.5	0.487±0.052	0.138±0.059	97±3
3	7.5	0.517±0.026	0.119±0.030	98±3
3	22.5	0.575±0.057	0.078±0.065	95±3
3	67.5	0.573±0.030	0.158±0.034	68±2
6	-112.5	0.502±0.046	0.120±0.052	27±0
6	-67.5	0.550±0.027	0.184±0.030	50±1
6	7.5	0.387±0.024	0.095±0.027	70±2
6	22.5	0.138±0.006	0.032±0.007	74±2
6	37.5	0.275±0.015	0.092±0.017	70±2
10	7.5	0.405±0.026	0.123±0.029	86±3
12	7.5	0.395±0.023	0.101±0.026	45±1
12	37.5	0.383±0.021	0.125±0.024	34±1
12	112.5	0.482±0.033	0.151±0.037	13±0

Table 6.7: MC position of W foils.

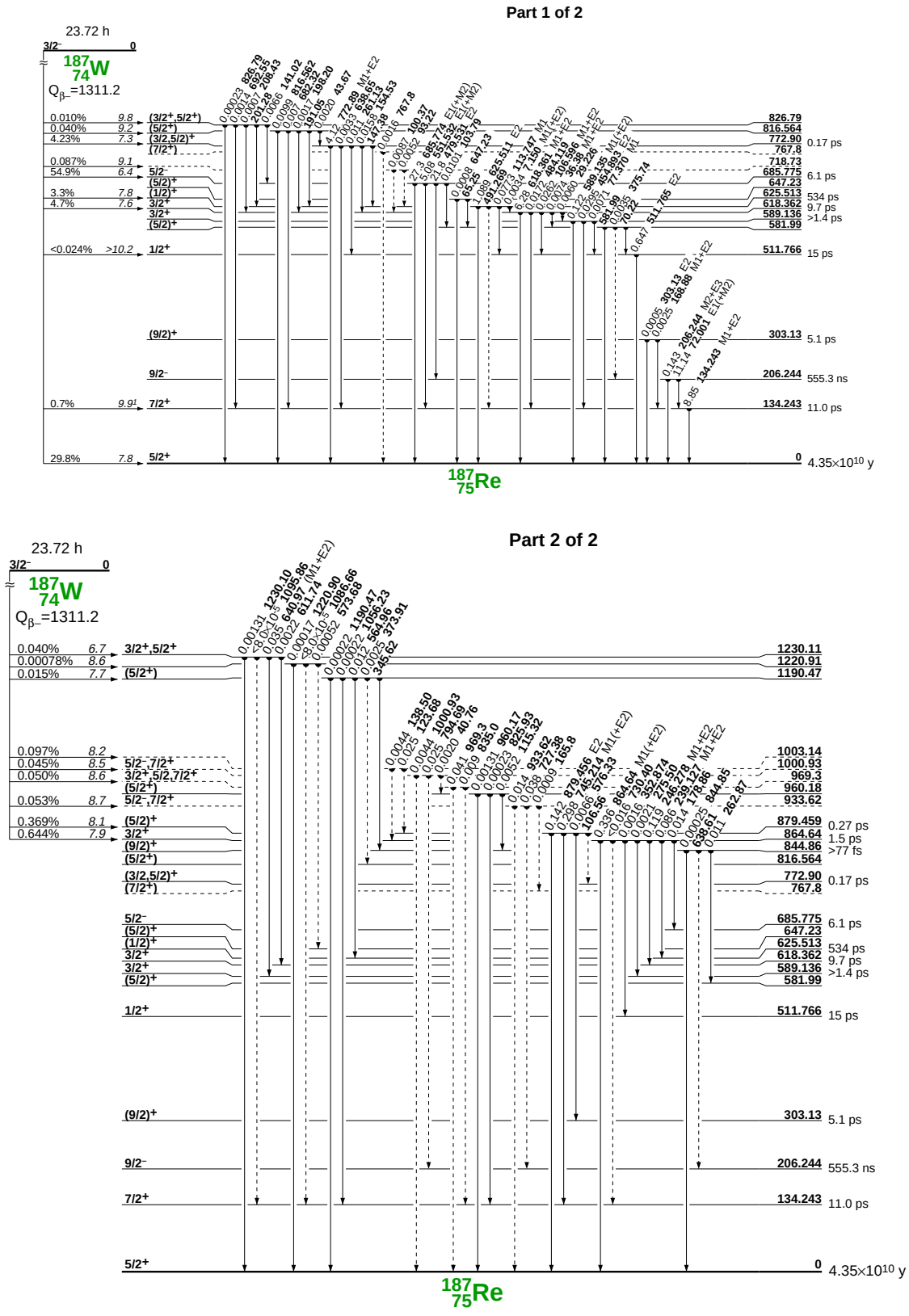

Figure 6.7: ^{187}Re transition levels.

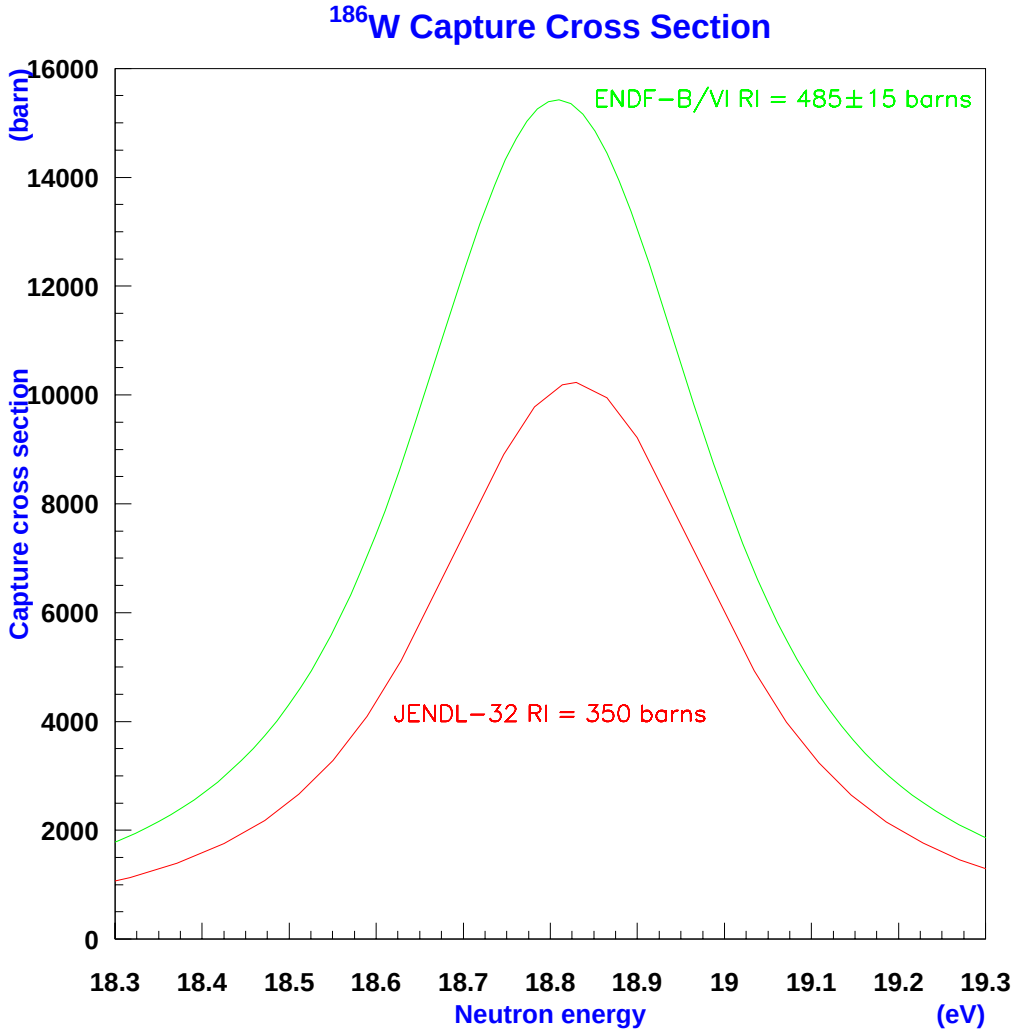

Figure 6.8: Main resonance of ^{186}W, from *ENDF-B/VI* and *JENDL-3.2* cross section databases, where the difference of 40% in the cross section is evident. Difference which is reflected into the number of captures.

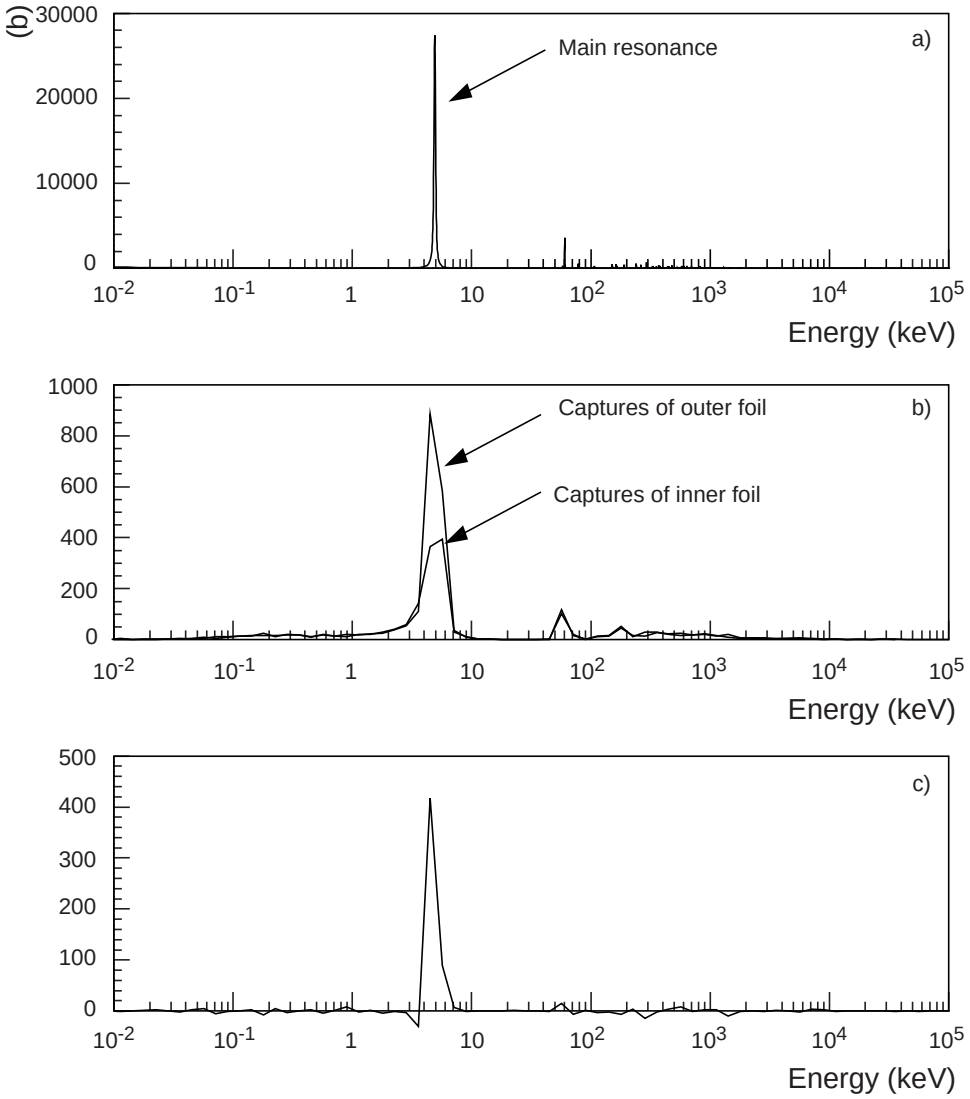

Figure 6.9: a) Capture cross section of Gold, b) histogram of captures on an Outer and an Inner foil, c) the difference Outer-Inner in the number of captures.

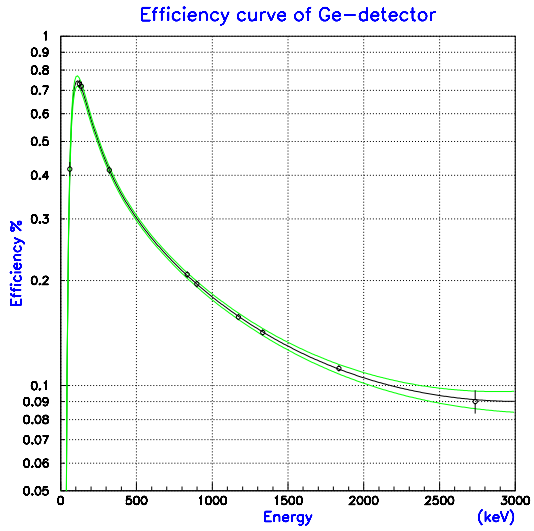

(a) GeLi efficiency

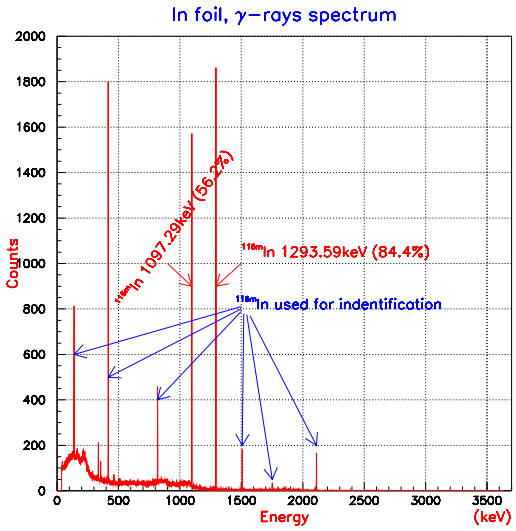

(b) Indium

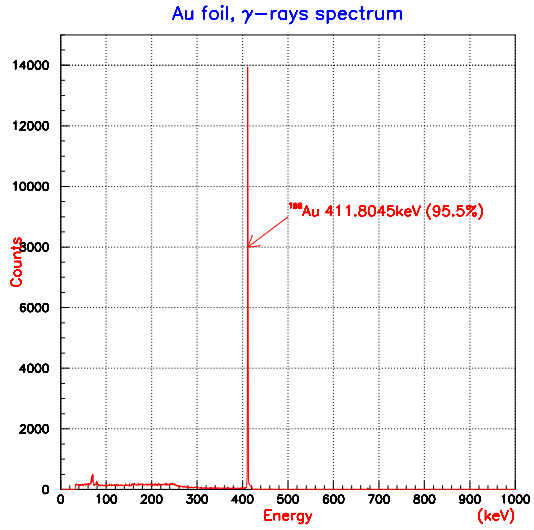

(c) Gold

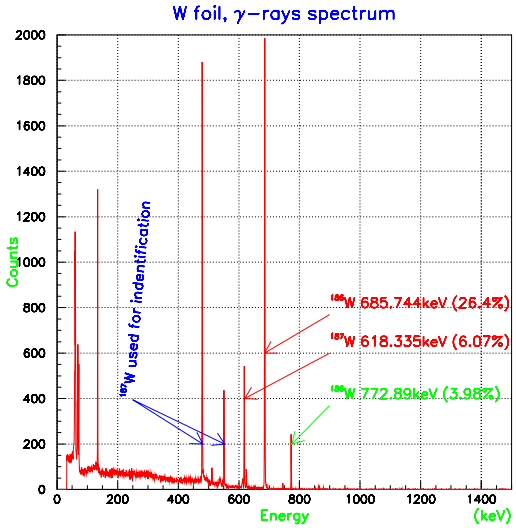

(d) Tungsten

Figure 6.10: a)Efficiency versus energy of Ge detector, b) γ spectrum from an In foil (Run 760, Hole=3, Z=+7.5cm), c) Gold, d) Tungsten

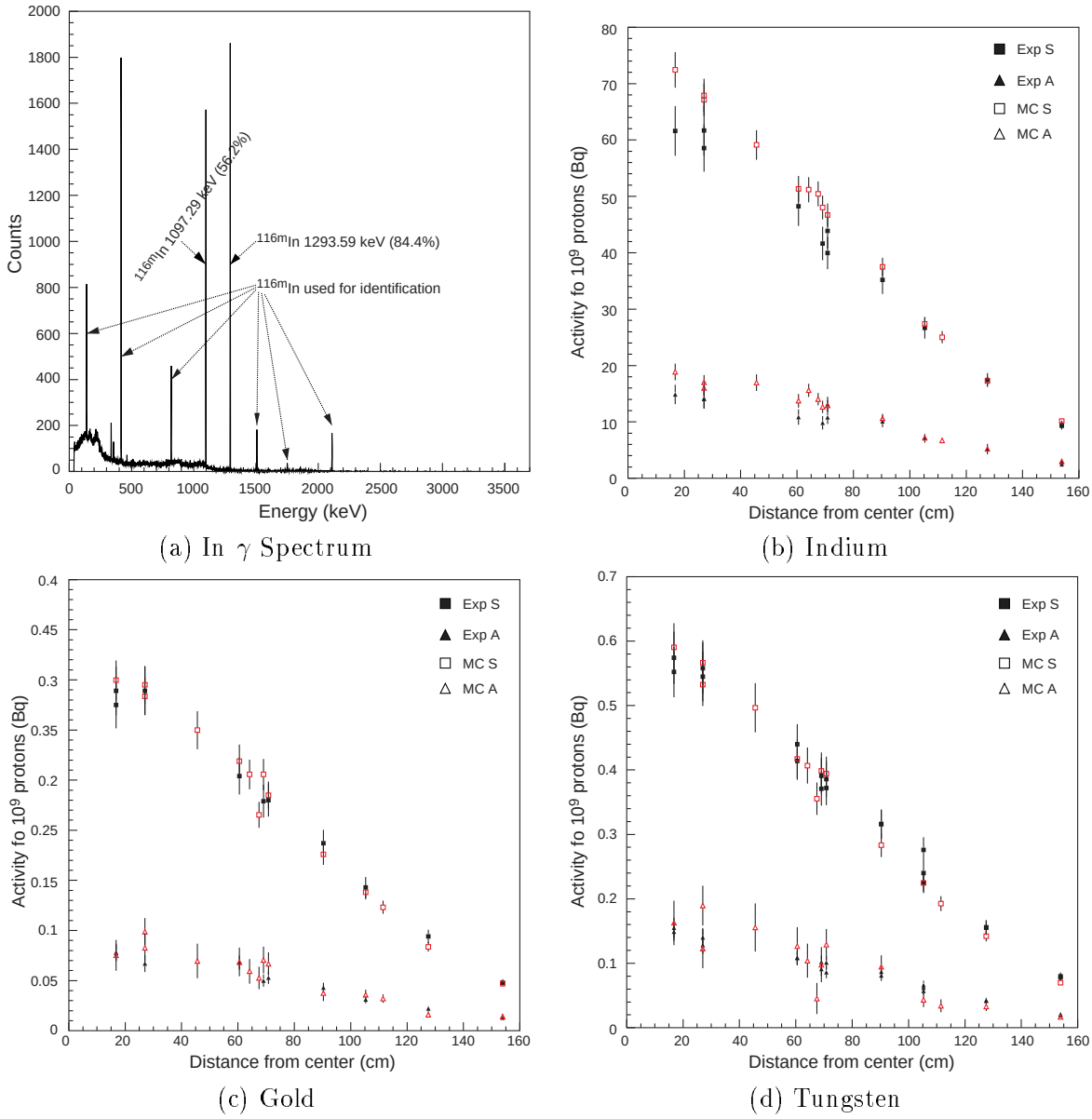

(a) In γ Spectrum

(b) Indium

(c) Gold

(d) Tungsten

Figure 6.11: γ spectrum of Indium and the activities versus distance for the 3 isotopes. Where S is the mean activity of the outer foils, and A is the resonance activity. *Exp* is for the experiment and *MC* for the Monte Carlo Simulation.

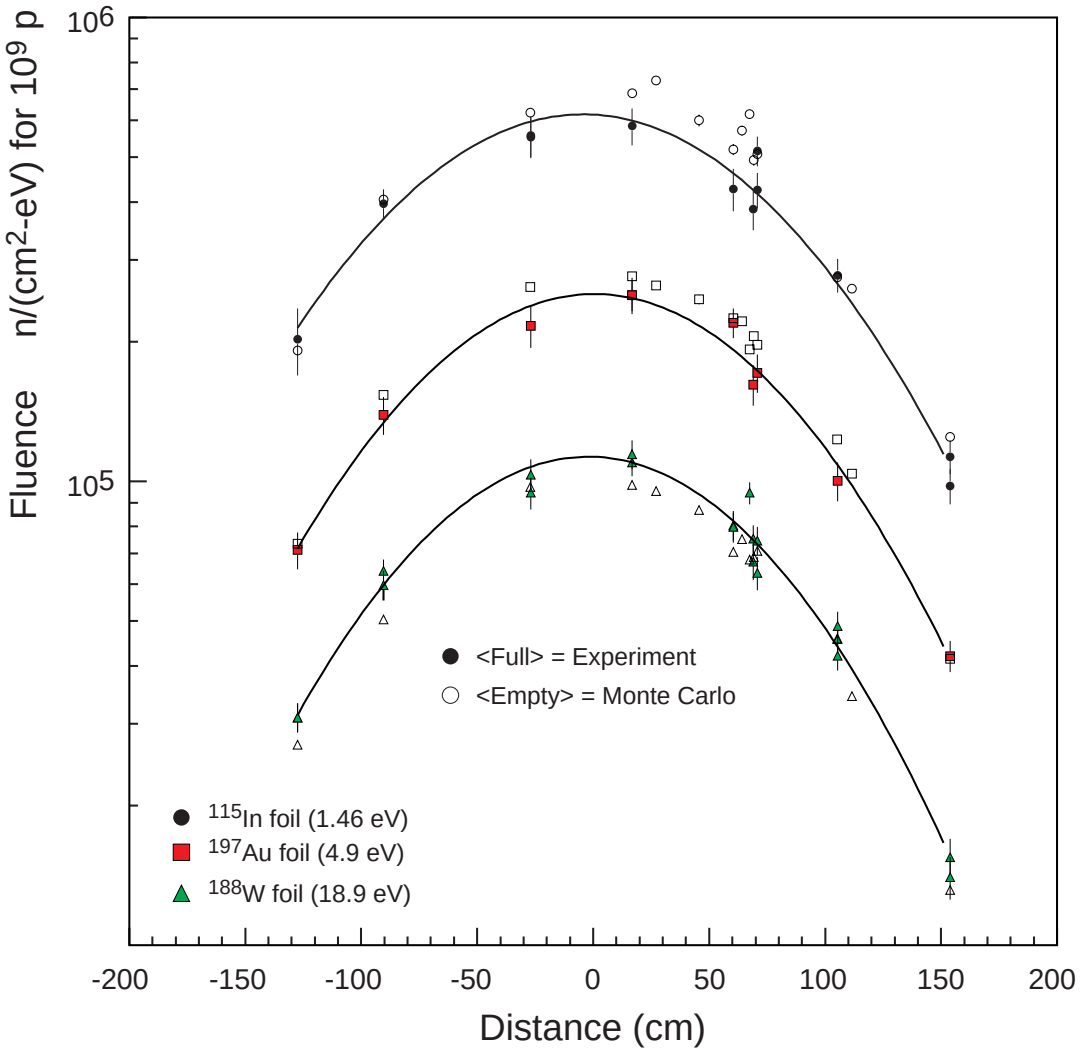

Figure 6.12: Fluence per eV at main resonance of the activation foils.

6.2 Conclusions on Neutron Fluence Measurements

Several techniques have been used Fig. 5.17 on page 77 in *TARC* to measure the neutron fluences over the desired energy range from thermal to MeV neutrons.

In summary, we have obtained a large coherent set of neutron fluence measurements, with redundant methods especially in the energy range below 10 keV where we want to use the *ARC* method. We verified that $dn/d\ln E$ decreases very slowly with neutron energy, only by one order of magnitude in the neutron energy range from 10 keV to 1 eV. This is the first important element in our demonstration of the *ARC* effect.

An example of *TARC* fluence measurements is shown on Fig. 6.13, 6.14. The energies 1.46, 4.96 and 18.9 eV have been chosen because at these energies Indium, Gold and Tungsten exhibit strong resonances in their neutron absorption cross section, and are used by the activation foils. The energy of 480 eV is of particular interest, since it is the energy of the ^{98}Mo capture resonance.

At low energies, below 10 keV and up to a radius of 1.5 meters, the neutron fluence, has a spherical symmetry and behaves approximately as a point-like source, even though the neutron production through the spallation process is neither point-like nor isotropic. This is of course precisely what is expected from the small elastic collision length in lead an also from the fact that the lead volume is sufficiently large (near the diffusion length) that edge effects do not constrain the shape of the neutron cloud.

The comprehensive ensemble of measurements constitutes a very precise validation of the innovative simulation developed by the *TARC* collaboration. Moreover, these neutron fluence measurements provide a check of the complete chain of processes from neutron production by spallation to neutron transport until capture or escape from the lead assembly. If we assume that neutron transport is known with good accuracy ($\approx 10\%$ see § of § 5.1 on page 63), then our measurements provide a check on the spallation process. We can note that the number of neutrons produced and transported down to 19.4 MeV is found to be 98 for a proton of 3.5 GeV/c momentum.

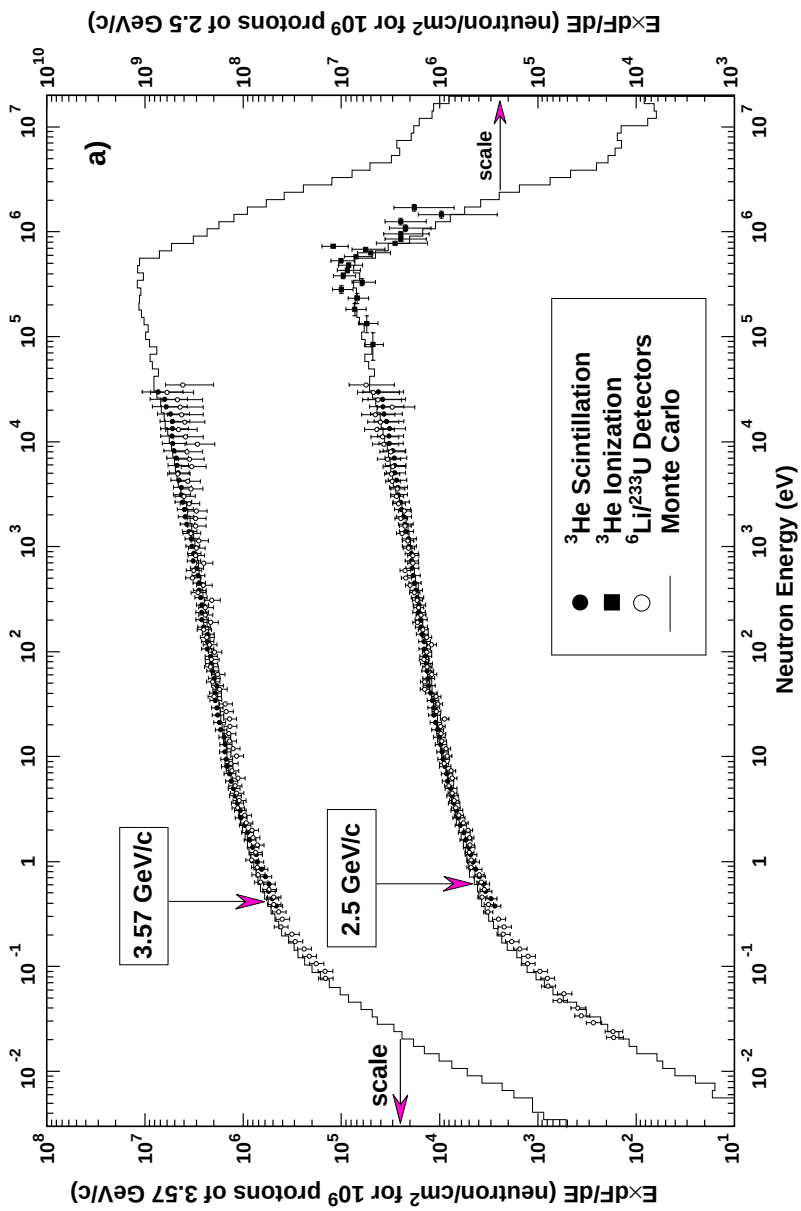

Figure 6.13: Example of $TARC$ measurements of the neutron fluence. $E\ dn/dE$ is shown as a function of neutron energy, for 2.5 and 3.5 GeV/c protons in hole number 10 ($Z = +7.5\ cm$, at a distance of 45.6 cm from the center of the lead volume). The Monte Carlo predictions are shown as histograms. The data are from $^6Li/^{233}U$ detectors (open circles), ^3He in the scintillation mode (full circles) and ^3He in the ionization mode (full squares);

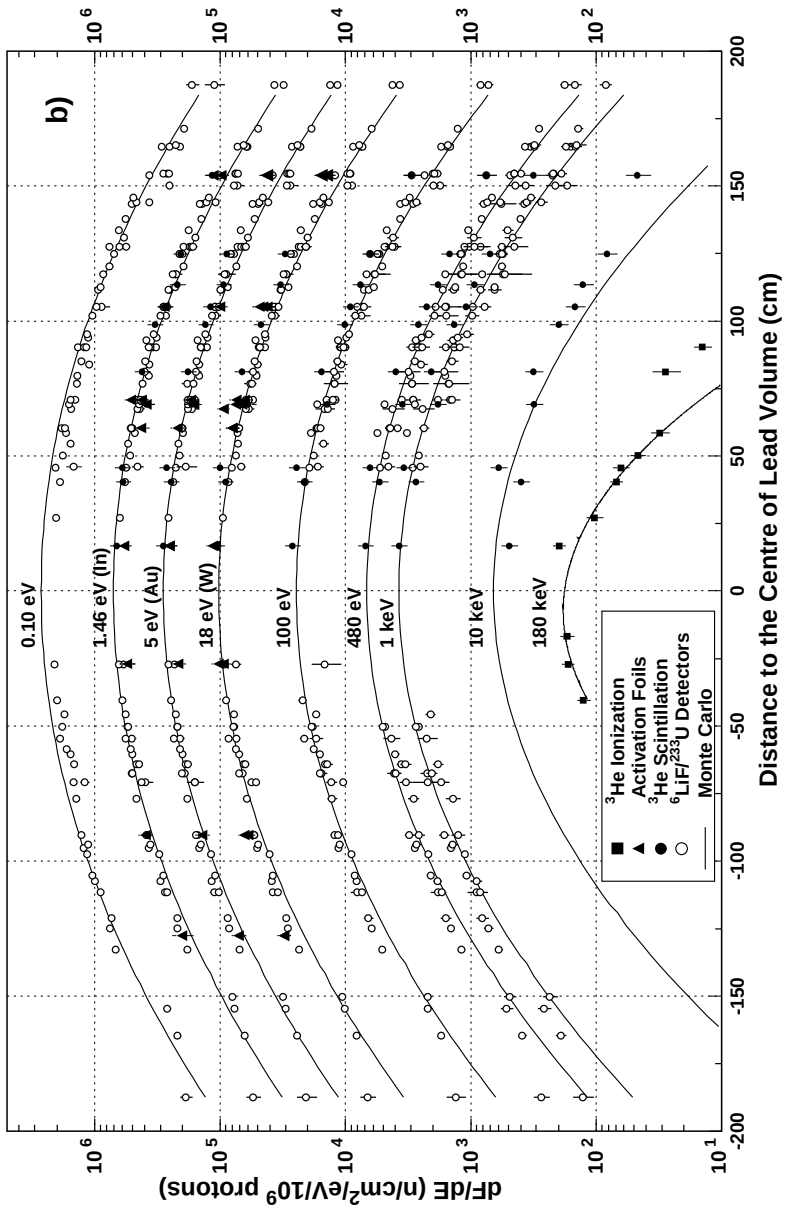

Figure 6.14: Variation of the neutron fluence as a function of distance from the center of the lead volume (the minus sign indicates negative Z positions). dn/dE is shown for a few selected energy bins. The Monte Carlo predictions are shown as lines obtained from a Gaussian fit to Monte Carlo points. The data are shown with the same convention as in part **a.** Data from triple foil activation are shown as full triangles.

Chapter 7

Measurements of Transmutation Rates

7.1 Capture Rates on ^{232}Th and ^{238}U

This section describes in detail the procedure used for collecting and analyzing the data to measure the neutron capture rate on ^{232}Th and ^{238}U, two reactions important for the Thorium cycle and the Uranium cycle related to the ADS, using lead as coolant and moderator. Both set of samples were irradiated in the *TARC* experiment and analyzed using the method of *delayed* γ *spectroscopy* (DGS), with the use of a *HPGe* detector. Several samples of pure ^{232}Th were irradiated and of depleted ^{238}U with 400 *ppm* of ^{235}U.

7.1.1 HPGe Detector

The HPGe-detector is a p-type coaxial device, which is very precise and it is able to measure the energy of the detected photons. The fraction of the incident photons which are totally absorbed is of the order of 40%, with a resolution close to 1 keV in a range from 500 eV to more than 2 MeV. In order to estimate the production (or transmutation rates) of an isotope, one must evaluate the number of photons on the characteristics lines of the produced isotope. This number of photons is traditionally obtained from the analysis of single-photon energy spectra. The energy is divided into bins corresponding the ADC bins, and the number of counts corresponding to each ADC value is represented as a histogram. The histogram always shows a typical shape with a set of very narrow peaks, corresponding to the energies of the decay photons, and a continuous spectrum that includes the signals corresponding to photons which, after colliding with the HPGe crystal, deposit only part of their energy and then escape (Compton). The second component for the continuum is the noise of the electronic chain. Finally there is also an environmental background from the external radioactivity in the area, with peaks and continuous component.

7.1.2 Peak Analysis

The analysis of these energy spectra consists of the identification of the different observed lines with the known peaks of the spectrum and the evaluation of the number of signal events in each peak after background subtraction.

The method used in the present analysis, is described in Ref. [51], where an automatic search of the peaks is performed, with the identification of the single or doublets of lines inside

the peak. A constrained fit of one or more Gaussian plus one polynomial to the peak and the surrounding channels, providing the number of photons on each line inside the peak. If the maximum height of the Gaussian fit is greater than the average value of σ (standard deviation of the Gaussian fit) then the analysis program marks the window that has a peak.

The assessment of the background noise under a peak is calculated using the GALTON curve, which assumes a linear behavior of the background inside the region of interest. We can calculate, the background from the area of a trapezoid defined from the average content of the first channels and the last ones. In our case, we were using the 3 first and 3 last channels of the peak that it was identified. If Y_a is the average of the 3 first channels of the peak, and Y_b of the 3 last channels, and the channel content of channel k is Y_k. The background area is $\sum_a^b F_k$, where

$$F_k = Y_b + (Y_a - Y_b)\frac{\sum_a^k Y_k}{\sum_a^b Y_k} \tag{7.1}$$

F_k is the background level in channel k, and a and b are the first and last channels of the peak.

Then the net area S_n of the peak is given by

$$S_n = S_b - F_d \tag{7.2}$$

where, S_b the gross area $S_b = \sum_a^b Y_k$, and F_d the background area under the peak. The error in the estimation of the net area is

$$Error\% = 100 \times \frac{\sqrt{S_n + 2F_d}}{S_n} \tag{7.3}$$

After having determined the peak, a searching is performed in the nuclide database to determine the element that has a disintegration level that produces γ rays with the window energy. From the net area of the peak, the specific activity A_m at measurement time is extracted with the help of the following formula

$$A_m = \frac{S_n}{t_a} \times \frac{100}{\varepsilon} \times \frac{100}{R_{db}} \times \frac{1}{m} \times k\, D_m \tag{7.4}$$

where, A_m is the activity of a peak at measurement time per mass unit, S_n the net area of peak which is the gross area minus the background, t_a the acquisition live time, ε the efficiency in percents for the peak energy, R_{db} the branching ratio in percents of the considered peak, m the mass of the sample, k the conversion factor for the unit that the operator wants, $D_m = \frac{\lambda t_r}{1-e^{-\lambda t_r}}$ decay factor during the measurement, with λ the decay constant of the nuclide and t_r the real time of acquisition in seconds.

Figures 7.2, 7.8 shows the typical γ-ray spectrum for the ^{232}Th and ^{238}U foils, the γ-lines used for calculating the activity, and the identification lines, which were used as a cross checking.

7.1.3 Efficiency and Calibration of the Germanium Detector

The standard source for calibration is ^{152}Eu, a multi energy γ-emitter which covers fairly well the range from 122 keV to 1408 keV. The source used had an activity of 43.4 kBq with 5% overall uncertainty within confidence level of 99.5%. The source comes from Amersham Buchler, Germany, and follows the regulations for ISO (International Organization for Standardization) classification. ^{133}Ba, ^{241}Am sources were also used in the calibration of the Ge detector for cross checking with the ^{152}Eu source.

Successive measurements in the detector were made at a distance of D =10cm between the irradiated sample the Ge crystal. The distance was chosen to be large enough in order to reduce pile-ups, and to approximate better the geometry of a point like-source.

After finding the position of the main peaks using the γ-peak-finding algorithm described in the previous section, a fit was made by an automatic procedure, to obtain the relation between channel and energy for each run. The 10 most intense peaks were selected to make the final calibration. Finally the theoretical energies are least-squares fitted to a quadratic function of the channel number:

$$Energy(keV) = A_i + B_i \times Channel + C_i \times (Channel)^2 \tag{7.5}$$

To compute the efficiency for each peak of each source we proceeded as follows: for each peak i of each source the efficiency was calculated as Q_i, the weighted average of the Q_{ji} from the different runs j of the same source

$$\overline{Q_i} = \frac{1}{\sum_j \frac{1}{\sigma_j^2}} \times \sum_j \frac{Q_{ij}}{\sigma_j^2} \tag{7.6}$$

where

$$Q_{ij} = \frac{\overline{N_j}}{A_j(1 - DT_j)(t_{DAQ})_j \; Br_i} \tag{7.7}$$

where, A_j is the computed activity, DT_j is the dead time, t_{DAQ} the total DAQ time of the run j, and Br_i the branching ratio of line i.

The error for the factors Q_{ij} has been computed as the quadratic sum of the following independent contributions: the error in the number of counts, the error in the activity (the dominant contribution), and the error in the dead time. The error in the average factor Q_i has been computed in the same way as the error computed for the average number of counts. The total error in the efficiency, for each line, has been obtained by adding quadratically the error on the branching ratio.

The efficiency curve is shown in Fig. 7.1, where a fit of 5^{th} order polynomial is used

$$\varepsilon = \exp\left[a + b \times \ln E + c \times (\ln E)^2 + d \times (\ln E)^3 + e \times (\ln E)^4 + f \times (\ln E)^5\right] \tag{7.8}$$

Table 7.1 shows the values of the factors a, b, c, d, e and f of the polynomial fit. We estimate also, that the error in the position uncertainty of the sample in both vertical and horizontal position is of the order of 1 mm. The solid angle introduces an extra error of the order of 2.1% for the distance of 10cm. This error has a direct effect on the uncertainty in the measured efficiency.

Factor	Value	Error
a	$-2.8364067667\ 10^{2}$	-9.8029644779
b	$2.3005105100\ 10^{2}$	7.3810266237
c	$-7.3998136912\ 10^{1}$	-1.5446121205
d	$1.1821399514\ 10^{1}$	$1.0064726272\ 10^{-1}$
e	$-9.4057587484\ 10^{-1}$	0
f	$2.9808004794\ 10^{-2}$	0

Table 7.1: The polynomial factors used for the fit to the efficiency curve. Note that the error was fitted with a 3^{rd} order polynomial.

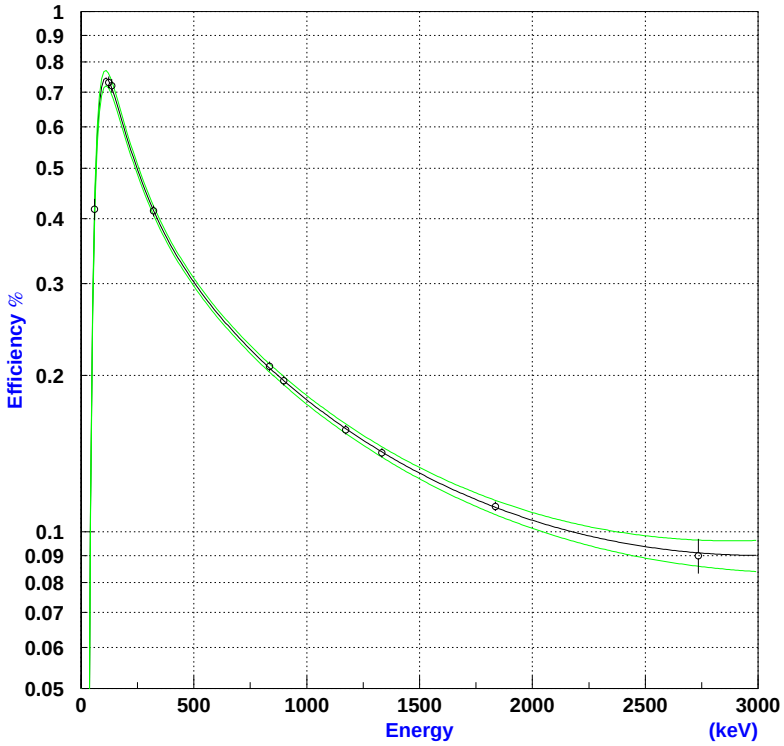

Figure 7.1: Efficiency versus the energy of the Ge-detector. Also the 5^{th} order fitting polynomial is shown.

7.1.4 Corrections

Efficiency correction

The measured efficiency is calibrated with a point-like naked ^{152}Eu source. Since the samples were extended we had to correct the efficiency with the following factors.

- a geometrical factor due to the solid angle difference from punctual to extended source
- gamma-ray absorption within the sample itself.

For these reasons, I have wrote a small program emitting randomly (isotropic in space), the gammas of interest and calculating the probability of reaching the Ge detector. Also taking into account the total attenuation of the gammas inside the sample. With this program, the ratio of the extended source over the punctual one for the standard foils used (Radius=6.35 mm), was estimated, to be of the order of $\sim$ 1.004. Resulting in a negligible correction of the efficiency of 0.4%, compared with the total error of the absolute calibration with the ^{152}Eu source. The total attenuation factor μ of the gammas was taken from BNL, and it is shown on the figures 7.4, 7.10.

Angular Correlation

Previous works, [52] and [53], about the decay of ^{233}Pa suggests coincidence between the transition of 86.814keV and 103.971keV with the 311.9keV (Fig. 7.3).

The probability of emission of a gamma depends in general on the nuclear spin axis and the direction of the emission. If two or more gammas are emitted close in time, there is a probability that they reach the detector at the same time. The detector will register this as a single gamma and the contribution to the peak of interest will be missing. If γ_1 and γ_2 are close in time, separated with an angle θ, the relative probability to find the two gammas within a solid angle $d\theta$ is $W(\theta)d\theta$

$$W(\theta) = 1 + A_2 P_2(\cos\theta) + A_4 P_4(\cos\theta) \tag{7.9}$$

where, P are the Legendre polynomials, and A_x are the F-coefficients [54]. The coefficients depends on the initial and final spin state and the multipole orders with mixing ratio and can be evaluated for all the theoretical cases (Table 7.2).

The relative difference between the number of counts with and without angular correlation correction is,

$$\frac{\Delta N}{N_{311.9}} \approx \Omega W(0^o) \tag{7.10}$$

where Ω is the solid angle from the sample to the detector depending on the configuration. For a cylindrical detector we have

$$\Omega = 2\pi \times \left(1 - \frac{D}{\sqrt{D^2 + R^2}}\right) \tag{7.11}$$

where, D is the distance of the detector with the measure position, R is the radius of the detector. For all cases (different positions, and gamma correlations) the ratio $\frac{\Delta N}{N_{311.9}}$ was always

Correlation (keV)	A_2	A_4
86.814-311.9	-0.005844	0
103.971-311.9	0.008168	0

Table 7.2: Calculated correlation coefficients

smaller than 6×10^{-4}, small enough that can be safely neglected.

Dead Time and Pile-up

The *Inter-gamma* analysis program, calculates automatically the account for Dead time and Pile-up effects. The data print out indicates counting time as an "elapsed time" and a "real elapsed time". The former is corrected for dead time and pile-up effects and used in calculations. The ratio is of order $0.3 - 1.0\%$.

7.2 ^{232}Th Capture Rate

When a Thorium sample is exposed to a neutron flux, nuclear reactions occur which produce ^{233}U with the following scheme,

$$^{232}\mathrm{Th} \xrightarrow{(n,\gamma)} {}^{233}\mathrm{Th} \xrightarrow{\beta^-(22.3\ min)} {}^{233}\mathrm{Pa} \xrightarrow{\beta^-(27\ d)} {}^{233}\mathrm{U}$$

^{233}Th has a half-life of $\lambda_1 = 22.3\ min$ and decays by β-emission to ^{233}Pa with half-life of $\lambda_2 = 27\ days$ which in turn is a β-emitter. We can see that the disintegration of one ^{233}Th atom gives rise to one ^{233}Pa atom, which implies that the production rate, of ^{233}Pa must be equal to the activity of ^{233}Th (Fig. 7.5). This is true since the neutron field where the samples were exposed had a low neutron fluence. Hence, we can easily neglect the captures on ^{233}Th and ^{233}U. Thus, it is more convenient to measure the transmutation rate of ^{233}Pa since the larger half-life 27 *days* of ^{233}Pa compared to the 22.3 *min* of ^{233}Th, results in smaller uncertainty in time (activation, transport and gamma counting), and consequently in the activity.

We call $n_1(t)$ and $n_2(t)$ the number of ^{233}Th and ^{233}Pa atoms respectively, and λ_1, λ_2 their decay constants. Hence,

$$R(t) = \lambda_1 n_1(t) \tag{7.12}$$

where $R(t)$ is the rate of produced isotopes of ^{233}Pa. A complete description of our system, follows from

$$dn_1(t) = -\lambda_1 n_1(t)dt \tag{7.13}$$

and

$$dn_2(t) = R(t)dt - \lambda_2 n_2(t)dt \tag{7.14}$$

By integration of the above equation we can find the solution for ^{233}Th

$$n_1(t) = n_1(0)e^{-\lambda_1 t} \tag{7.15}$$

and for ^{233}Pa

$$n_2(t) = \frac{\lambda_1}{\lambda_2 - \lambda_1} n_1(0)\left(e^{-\lambda_1 t} - e^{-\lambda_2 t}\right) + n_2(0)e^{-\lambda_2 t} \tag{7.16}$$

By counting the dominant transition of 311.98 keV of ^{233}U Fig. 7.3 the number of captures on ^{232}Th can be extracted (Fig. 7.6). This transition has a branching ratio of 38.63% with an uncertainty of 5.6% [50]. The total attenuation coefficient, is shown in Fig. 7.4, and for the γ-lines of interest is $\mu_\gamma = 0.11\ cm^2/g$, resulting in an absorption of 1.1% of the gammas with this energy[1]. We are using the total absorption coefficient since Compton-scattered γ-rays suffer an energy loss and thus can no longer be detected if a window discriminator is used. Except from the main transition of 311.98 keV several other transition were used for cross checking, and all of them gave consistent results within 3%.

7.2.1 Sample Information and Irradiation

We used eight ^{232}Th samples which were provided by Reactor Experiments Inc. having a good homogeneity. All the samples were placed in various position in the lead volume, and irradiated in the same run 767 (Table 7.4). They all have a cylindrical shape and equal dimensions. It should be noted that the small variations in mass (less than 10%) are due to the small dimensions of the foils. Hence, an uncertainty in the radius of less than 0.5 mm results to a change in the weight of 14%. This set of foils were irradiated during the run 767 (Table 7.4). This run was

Shape	Purity	Thickness	Diameter	Mass
Cylindrical	99.85%	88.9 μm	12.7 mm	132 mg

Table 7.3: Characteristics of the first batch of ^{232}Th samples

[1]The Average probability that a γ-ray escapes a foil of thickness δ is $\phi_0(\mu_\gamma\delta)/2\mu_\gamma\delta$.

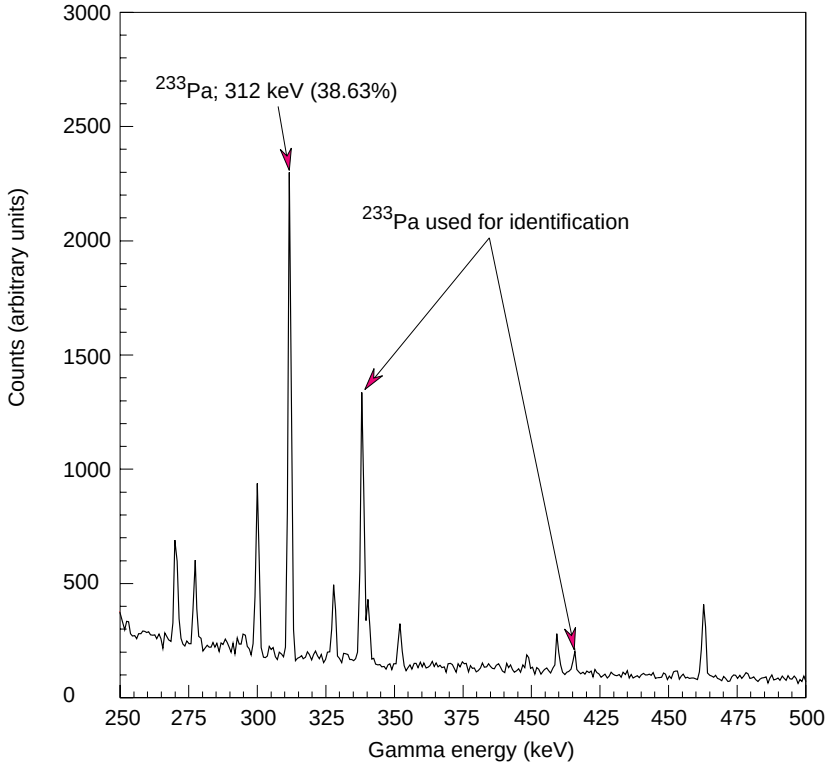

Figure 7.2: ^{233}U γ-ray spectrum, as it was measured from the Ge-detector.

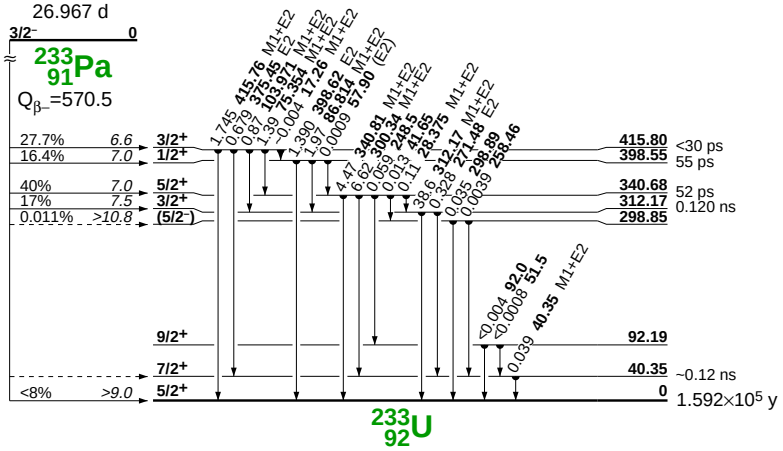

Figure 7.3: ^{233}U transition levels.

Run	Duration	Protons
767	8.5 hours	$2.141\ 10^{13} \pm 0.107\ 10^{13}$

Table 7.4: Irradiation time and number of protons

chosen because of the long irradiation time all the ^{233}Th (with the short half-life of 22.3 *min*) will eventually fall to ^{233}Pa. The foils were placed in various position in the lead block Table

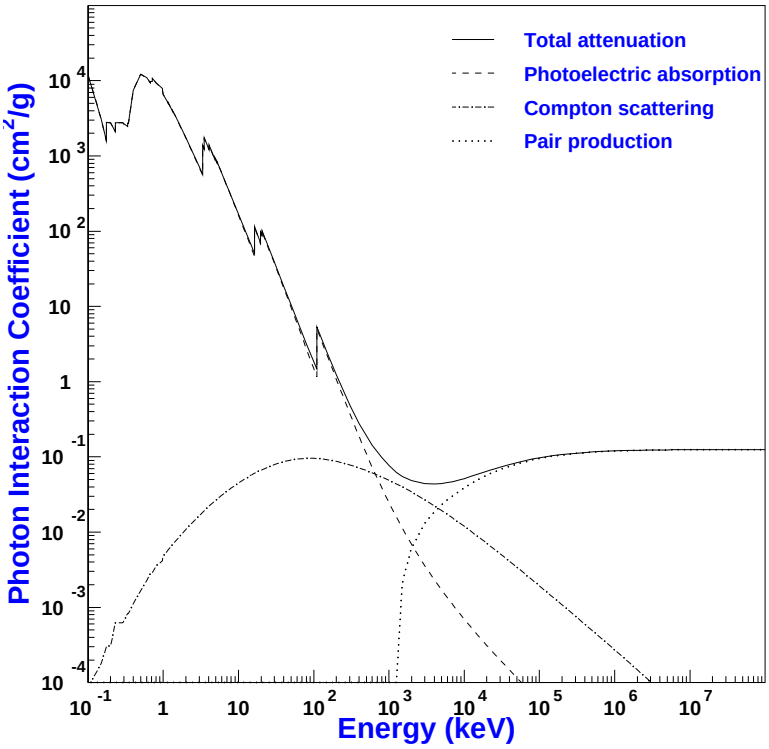

Figure 7.4: Photon Interaction Coefficients of Thorium

7.5. At the end of the irradiation the foils were removed and transfered to the Ge-detector. The samples were counted and analyzed with the help of the *Inter Technique Gamma Spectrum* analysis program. Furthermore all the results, on the foils activity was renormalized to 10^9 initial protons. The transmutation rate is represented here as the mass (g) of the produced

Hole	Block	Z(cm)	R (Bq)	P $(g/g)10^9p$
1	12	22.5	97.0±6.4	$3.7\ 10^{-17}\pm2.4\ 10^{-18}$
2	13	37.5	202.9±10.4	$7.7\ 10^{-17}\pm3.9\ 10^{-18}$
3	12	22.5	338.8±14.8	$1.3\ 10^{-16}\pm5.6\ 10^{-18}$
3	14	52.5	277.1±12.3	$1.0\ 10^{-16}\pm4.7\ 10^{-18}$
6	12	22.5	238.3±11.0	$9.0\ 10^{-17}\pm4.2\ 10^{-18}$
7	12	22.5	165.6±7.9	$6.3\ 10^{-17}\pm3.0\ 10^{-18}$
8	12	22.5	100.0±7.7	$3.8\ 10^{-17}\pm3.0\ 10^{-18}$
9	11	7.5	28.6±4.1	$1.0\ 10^{-17}\pm1.6\ 10^{-18}$

Table 7.5: ^{232}Th foil positions, Run=767, Protons=$2.141 \cdot 10^{13}$. Where Bq is the activity of the foil and g/g is the mass of the produced ^{233}U over the initial mass of the ^{232}Th foil.

element over the mass of the initial one, and it is calculated using the following expression

$$P = \frac{R \cdot T_{1/2} \cdot A}{\ln 2 \cdot N_A \cdot m_f} \tag{7.17}$$

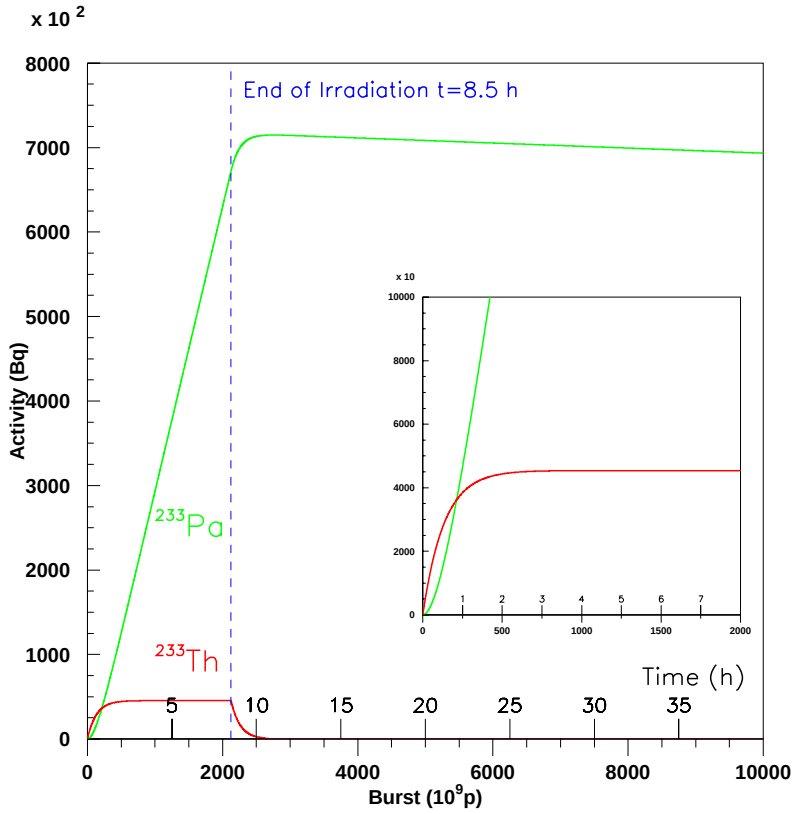

Figure 7.5: Simulated activity of ^{233}Th and ^{233}Pa, for Hole 3, Z=+15cm, as a function of the number of proton bursts. Each burst has 10^9 protons.

where, P is the production rate (g/g) grams of the produced element over the initial, R is the normalized activity of the foil in (Bq), $T_{1/2}$ is the half-life of the measured element, A is the Atomic Weight, N_A is the Avogadro Number $6.023 \cdot 10^{23}$, and m_f is the mass of the foil. Fig. 7.6 shows the transmutation rate of ^{232}Th and the relevant Monte Carlo simulation for various positions.

7.3 ^{238}U Capture Rate

As in the case of ^{232}Th, we have measured also the transmutation rate of ^{238}U when it is exposed to a neutron flux, from the following reaction

$$^{238}\mathrm{U} \xrightarrow{(n,\gamma)} {}^{239}\mathrm{U} \xrightarrow{\beta^-(23.5min)} {}^{239}\mathrm{Np} \xrightarrow{\beta^-(2.35d)} {}^{239}\mathrm{Pu}$$

^{239}U has a half-life of 23.5 min and decays by β-emission to ^{239}Np with half-life of 2.35 $days$ which in turn is a β-emitter. We can see that the disintegration of one ^{239}U atom gives rise to one ^{239}Np atom, which implies that the production rate, of ^{239}Np must be equal to the activity of ^{239}U (Fig. 7.7). This is true since the neutron field, where the samples were exposed had low neutron fluence, and we can easily neglect the captures on ^{239}U and ^{239}Np. Thus, it is more convenient to use the delayed gammas of ^{239}Pu, since the half-life of ^{239}Np (2.35 d) is larger than the half-life of ^{239}U (23.5 min) which consequently results in smaller time measurement errors.

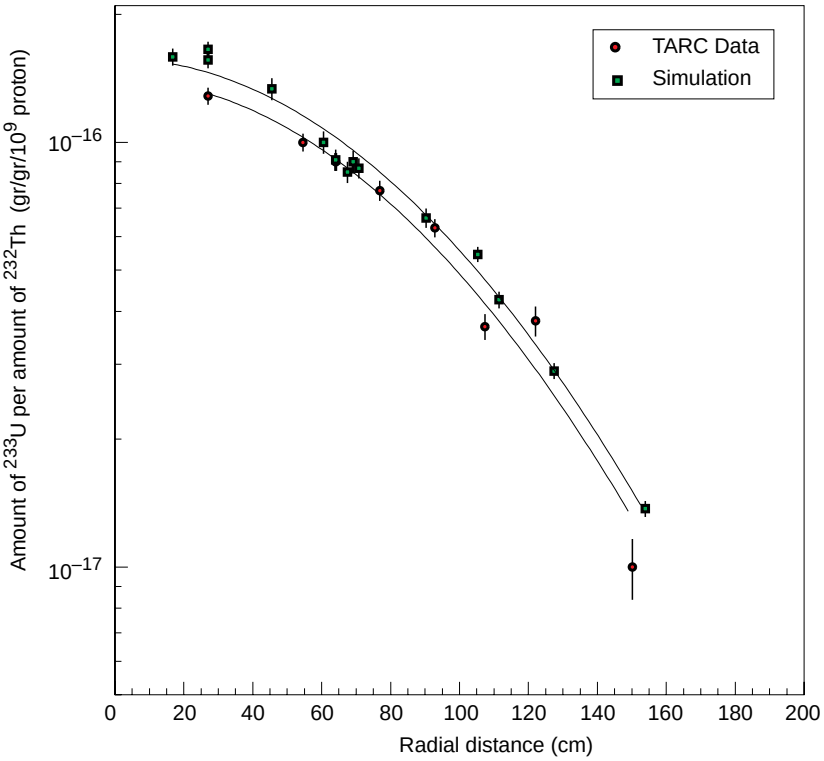

Figure 7.6: Production rate of ^{233}U. Experimental data and Monte Carlo simulation versus the distance from the center of the Lead block. The lines are eye-guides created using a Gaussian fit on the experimental data.

The dominant transition levels of ^{239}Pu are given in the Table 7.6, which are the most direct from all the gammas that are emitted during the de-excitation of ^{239}Pu [50] (Fig. 7.9). Except

Energy (keV)	Branching ratio (%)	Attenuation μ_γ (cm^2/g)	Absorption (%)
228.18	11.46	0.11	2.6
277.6	6.8	0.11	2.6

Table 7.6: Transition levels of ^{239}Pu, used for measuring the activity of the ^{238}U samples.

from the two transitions of 277.6 keV and 228.18 keV several other transitions were also used for cross checking. All of them gave consistent results within 3%.

7.3.1 Sample Information and Irradiation

We used, five ^{238}U samples depleted to 400 ppm of ^{235}U. They were provided by Reactor Experiments Inc. having a good homogeneity. They all have a cylindrical shape and equal dimensions. This set of foils were irradiated during the same run 767 as in the case of the first

Shape	Purity	Thickness	Diameter	Mass
Cylindrical	99.23%	127 μm	12.7 mm	290 mg

Table 7.7: Characteristics of the ^{238}U samples.

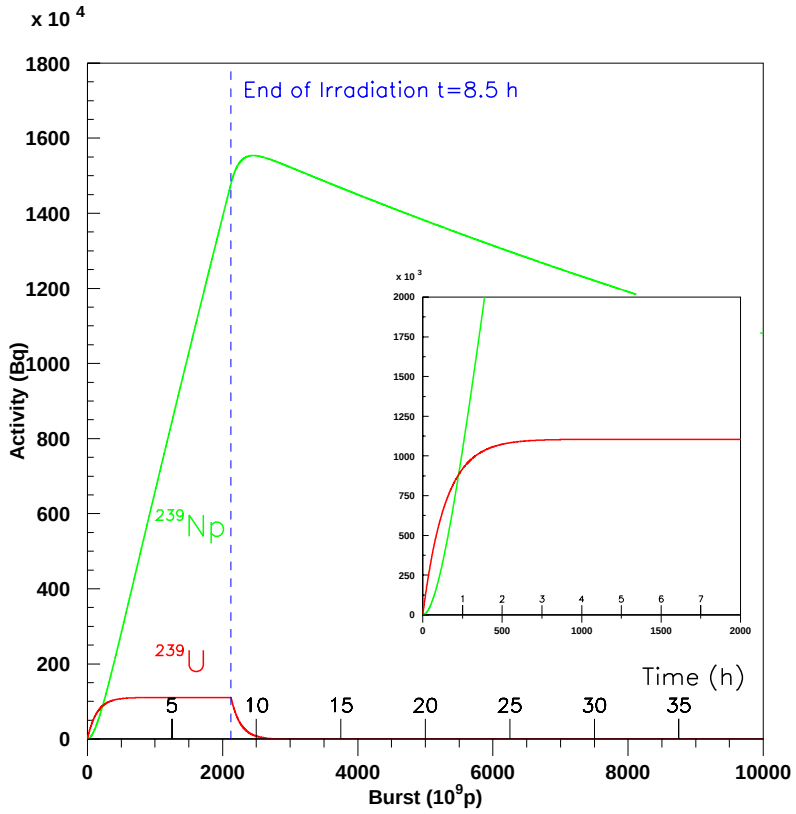

Figure 7.7: Simulated activity of ^{239}U and ^{239}Np, for Hole 3, Z=+15cm, as a function of the number of proton bursts. Each burst has 10^9 protons.

batch of ^{232}Th measurements Table 7.4. This run was chosen because of the long irradiation time all the ^{239}U (with the short half-life of 23.5 min) will eventually fall to ^{239}Np. The foils were placed in various position in the lead block Table 7.8. At the end of the irradiation the foils were removed and transfered to the Ge-detector. The samples were counted, analyzed and renormalized to an activity that corresponds to 10^9 initial protons, exactly with the same way as described previously for the ^{232}Th samples. Fig. 7.11 shows the (g/g) production ratio of ^{239}Pu as a function of the distance placed in the lead volume. The results are normalized for 10^9 initial protons of 3.5 GeV/c.

Hole	Block	Z(cm)	R (Bq)	P $(g/g)10^9p$
1	9	-22.5	2762±66	$5.510^{-17}\pm1.310^{-18}$
3	9	-22.5	7825±248	$1.610^{-16}\pm5.010^{-18}$
3	7	-52.5	6787±187	$1.310^{-16}\pm3.710^{-18}$
6	9	-22.5	5734±173	$1.110^{-16}\pm3.410^{-18}$
7	9	-22.5	3887±119	$7.710^{-17}\pm2.410^{-18}$

Table 7.8: ^{238}U foil positions, Run=767, Protons=$2.141 \cdot 10^{13}$. Where Bq is the activity of the foil and g/g is the mass of the produced ^{239}Pu over the initial mass of the ^{238}U foil.

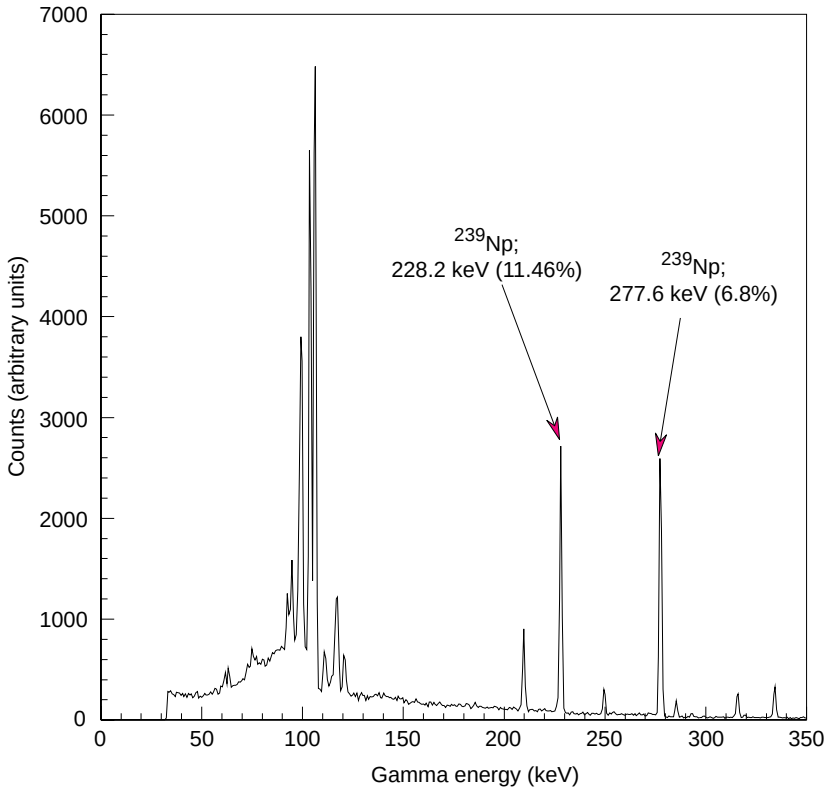

Figure 7.8: ^{239}Pu γ-ray spectrum, as it was measured from the Ge-detector.

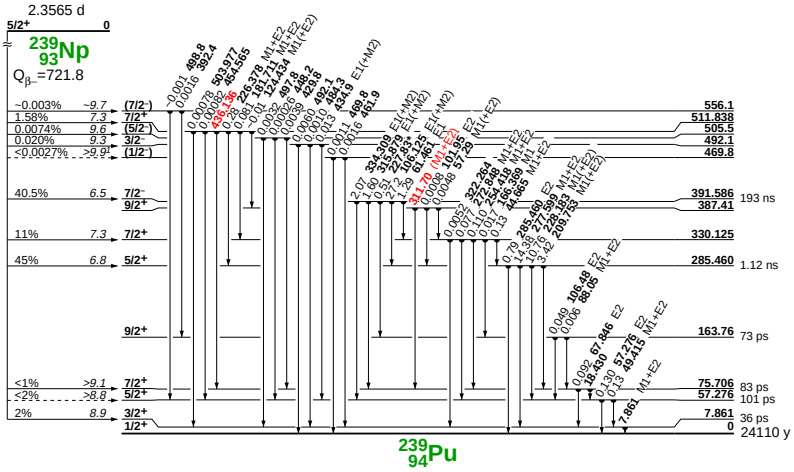

Figure 7.9: ^{239}Pu transition levels.

7.4 Monte Carlo Simulation

The *Monte Carlo* simulation was carried out the same way as in the triple foils (see § 6.1.3 on page 99). The initial proton beam and the spallation products were simulated using the FLUKA [5] high energy inter-cascade code. The produced neutrons were tracked down to $20MeV$, the upper limit where the neutron databases are available. Above this energy, only nuclear cascade

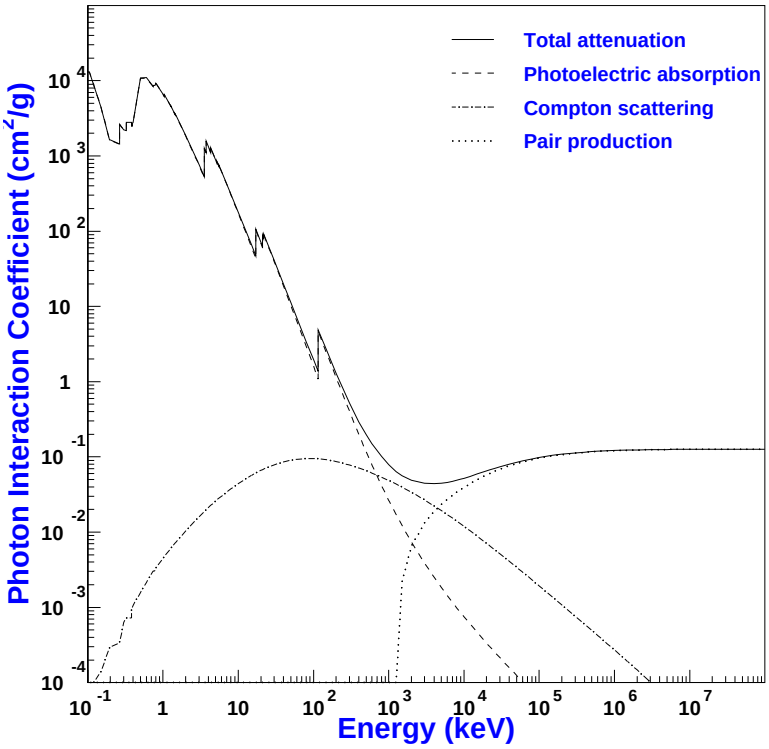

Figure 7.10: Photon Interaction Coefficients of Uranium

models exist.

The next step was through the TARC Monte Carlo, program. The program was able to handle all the interaction channels (n, x) by sampling from the available neutron data bases, and also the secondary neutrons from reactions (n,xn) or fission. The program was using also the exact geometry of the lead block, the support materials (I-beams, etc.), and the surrounding concrete walls. Each neutron was traced down until it was absorbed, by some material. During the transport, when a neutron was crossing some specific volumes, the position, velocity and time were recorded in a DST file for further processing. This specific volumes were imaginary regions, surrounding the detector (foil) position, including several cm of Lead in all directions.

The last step was, simple runs for each specific volume where the foils were placed, using only the geometry of the foil and the surrounding lead.

Several tricks were used, to increase the statistics, ie. making the foil surface bigger, and re-using the original neutrons many times, but always with different random numbers.

The total error from a Monte Carlo simulation is something difficult to extract. The only reliable way is by launching several runs using different initial random seeds. The error then, is the RMS of the different results.

7.5 Errors

There are several sources of errors, where the most important are the followings

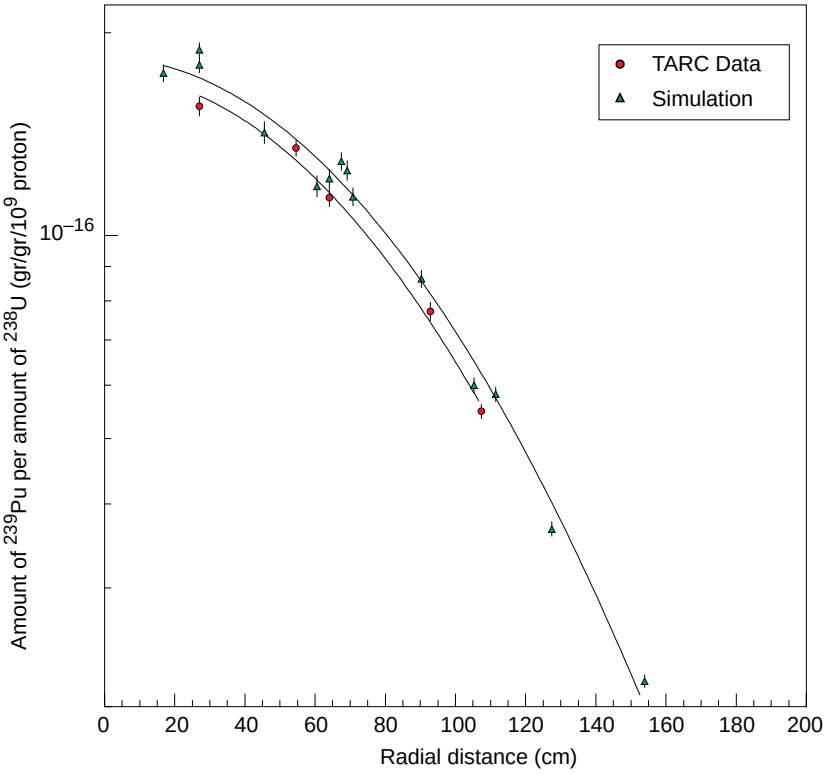

Figure 7.11: Production rate of ^{239}Pu. Experimental data and Monte Carlo simulation versus the distance from the center of the Lead block. The lines are eye-guides created using a Gaussian fit on the experimental data.

- We estimate that the uncertainty in the foil position inside the hole is less than 1 cm, which results to an error of less than 1% in the number of captures and consequently in the estimation of the transmutation rates.
- The error induced from the calibration of the Ge-detector and the estimation of the foil activity is less than 3%.
- The cross section error according to *ENDF-B/VI* is 6.5% for ^{232}Th and 7.1% for ^{238}U. The error in the determination of the beam intensity is less than 7%.
- Also we have an uncertainty of less than 2 min in time difference, between the end of irradiation and the counting of the foils. This is negligible if compared with the half-lives of the measured isotopes.

Thus, the total systematic error is estimated to be in the case of the transmutation of ^{232}Th less than 9% and in the case of ^{238}U less than 10%.

7.6 Fissions in ^{232}Th, ^{235}U, ^{238}U, ^{237}Np and ^{239}Pu

Fission measurements were performed in the *TARC* experiment for ^{235}U, ^{nat}U, ^{239}Pu and ^{237}Np, with the use of Lexan etched track detectors. From these measurements we were able to determine the fission rate spatial distributions of several isotopes, and also the determine the integral

neutron fluence at high energy ($E > 1.4\ MeV$) from fission on ^{232}Th, since it experience a step like behavior in the fission cross section.

Neutron fluences were measured in various positions in the *TARC* lead assembly using the above fissionable materials in close contact with Lexan track-etch detectors, which can detect the produced fission fragments.

Lexan as well as CR-39 type detectors had also been used for this type of measurements in the 1994 experiment (see App B *FEAT*) Lexan was found the best-suited material for use as an integral fission fragment counter since it is as efficient as CR-39 in detecting fission fragments while it does not see any alpha particles hitting it [55].

7.6.1 Measuring System

Solid state nuclear track detectors (SSNTD), provide a convenient method for registering ionizing charged particles. The properties of materials to be used as SSNTD, their registration efficiencies for various particles as well as the required experimental tools and procedures are well established [56]. When a heavy ionizing charged particle, like a fission fragment, hits the surface of a track-etch detector a latent track is produced. The tracks left from passing particles are only made visible upon etching in a strong base solution. These tracks are then examined using standard optical transmission microscopy[57]. In most applications, tracks are counted and classified manually in order to obtain a high degree of counting precision.

The first step in the procedure, after the track-etch detectors were exposed to radiation, is the chemical treatment. The Lexan type detector foils were placed in a NaOH solution of molarity $6\,N$ at 55^oC for a period of two hours. The chemical treatment parameters were chosen after a study of the size and number of holes observed on Lexan detectors irradiated with fission fragments from calibrated ^{252}Cf sources, in order to achieve the best possible detection efficiency [55].

The next step is the scanning of each detector foil with a fully automated optical microscope. The microscope consists of the illumination system, a stage and a CCD camera, which takes the picture through a magnifying lens and sends it to a computer using a special video card. The microscope has two step motors to control the movement of the stage from frame to frame automatically, and one step motor to control the focus of the optical system. The whole process is computer controlled with specially developed programs.

Each detector foil was scanned in frames of $0.360 \times 0.566\ mm^2$ and analyzed with a track recognition program which performs an analysis of each frame counting the objects found on the pictures and which, according to predefined selection criteria, can be assigned to tracks made on the detector by alpha particles or fission fragments [58]. The analysis of each foil was performed for a large number of frames and results with very good statistics (statistical errors $< 2\%$). Fig. 7.12 shows, a typical frequency distribution of the number of tracks per frame, found from the analysis program, by scanning 100 frames of a detector.

Method

Two kinds of foils were studied: CR-39 (manufactured by Pershore Moulding Ltd) and Lexan (provided by General Electric Plastics). Their main difference was that the latter (Lexan) registers only fission fragments, and it is insensitive in α-radiation. The CR-39 registers both kinds of particles.

The overall task is to count, identify and classify the recorded tracks, given their digital image obtained through a microscope. On an obtained image a track is defined as an object with specific properties, such as gray levels, size, shape, etc., which satisfies certain constraints

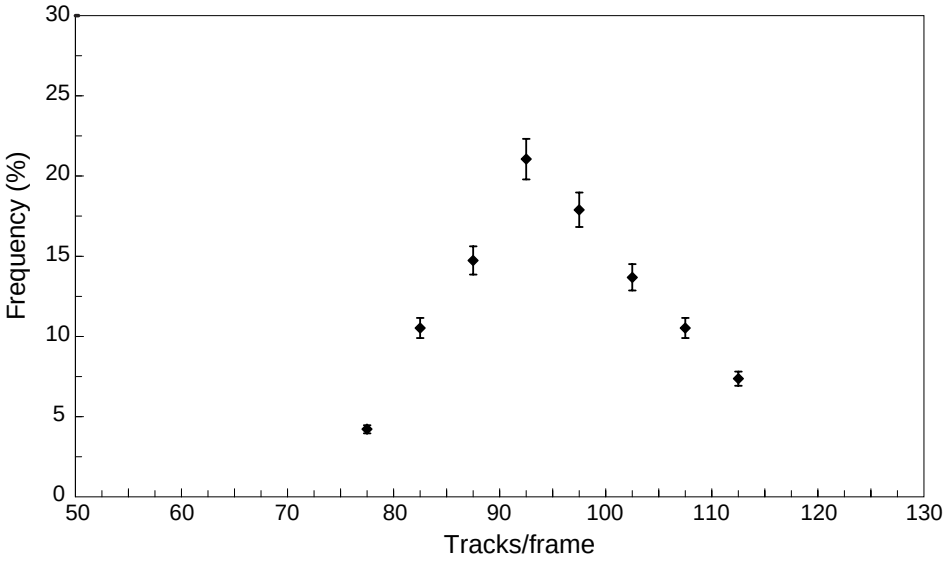

Figure 7.12: Frequency distribution of tracks/frame.

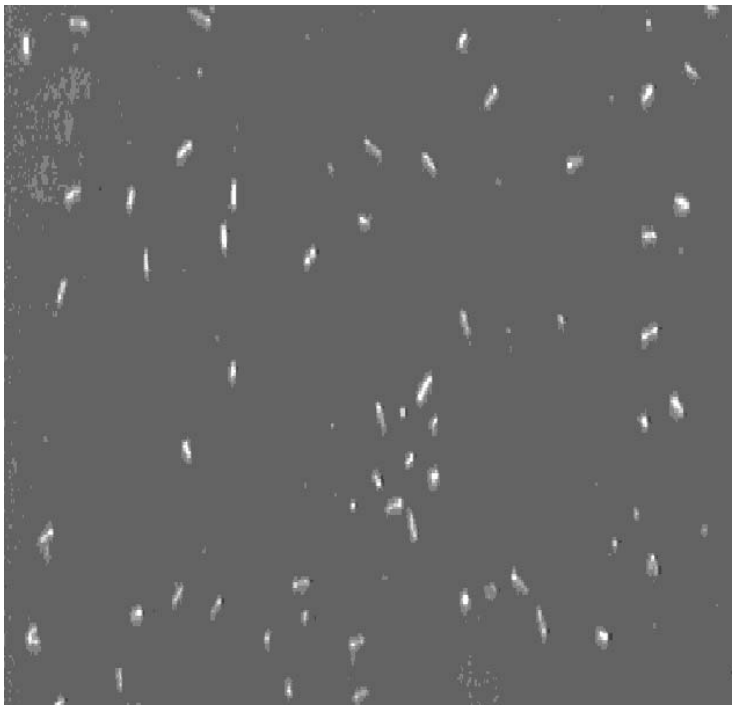

Figure 7.13: Fission fragment tracks as seen in a frame of Lexan detector

in shape, size, intensity, position, etc. The process of defining such objects is known as feature detection or segmentation [59]. There are three major classes of segmentation methods:

1. Threshold techniques.
2. Computation of derivatives.
3. Template matching.

Algorithms using threshold techniques are the easiest to implement, but they have serious performance drawbacks. The main drawback is, their limited ability to localize precisely the boundaries of the regions of interest, in particular in cases of noisy images. Template techniques, especially in their simplest forms, depend on the size of the objects to be extracted. Improved methods that overcome this disadvantage require an excessive computing effort.

For these type of measurements, the most adequate feature is the step edge, defined as an abrupt change of the gray level. Hence it corresponds to a maximum in the first derivative of the image, which can in general be precisely located by determining the zero crossing of the second derivative. In real life images however, noise may cause ambiguities in the selection of the proper zero crossing, hence a smoothing preprocessing of the image is required. A Gaussian function provides one of the best smoothing

$$g(x,y) = \frac{1}{\sqrt{2\pi}\sigma}\, e^{-\frac{x^2+y^2}{2\sigma^2}} \tag{7.18}$$

The input image $I(x,y)$ is convoluted with the Gaussian, and then the second derivative is calculated. The output image $O(x,y)$ is given by:

$$\begin{aligned} O(x,y) &= \nabla^2 \left[I(x,y) \otimes g(x,y) \right] \\ &= -\nabla^2 \int_{-\infty}^{\infty} \int_{-\infty}^{\infty} I(x',y') \times g(x'-x, y'-y)\, dx'dy' \\ &= \left[-\nabla^2 g(x,y) \right] \otimes I(x,y) \end{aligned} \tag{7.19}$$

Therefore, the whole operation can be performed by the convolution of the input image with the function

$$\nabla^2 g(x,y) = \frac{1}{\sqrt{2\pi}\sigma^5}(x^2+y^2-2\sigma^2)\; e^{-\frac{x^2+y^2}{2\sigma^2}} \tag{7.20}$$

The above function represents a band-pass filter whose center frequency depends on σ. A plot of that function for the one-dimensional case is shown in Fig. 7.14. High σ values reduce the locality of the filter and thus the noise by smoothing the image, where smaller values of σ give fine details in gray-level changes, with increased noise sensitivity.

The main variables that describe the performance of the counting system are:

Efficiency of track finding: the system has an efficiency of 98%. This means that the 98% of all the manually identified tracks were labeled as such also by the system.

Background acceptance: that is the identification of non track areas as tracks. The system is counting 3% more tracks than those identified manually, which belong to background noise.

To study further the performance of the track recognition system, the Lexan foils were exposed for a determined period to a calibrated radioactive source. We used a ^{252}Cf source,

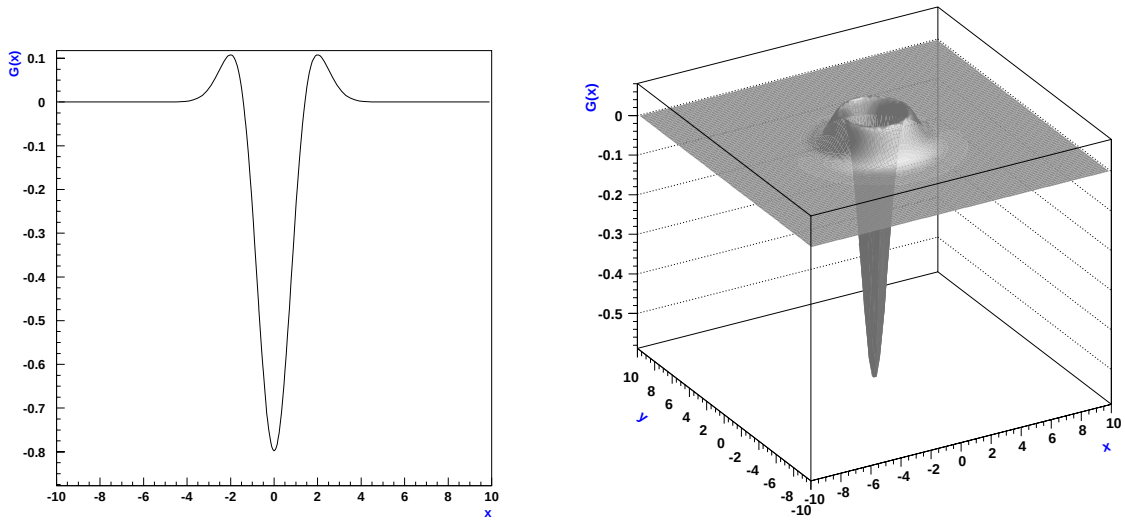

(a) (b)

Figure 7.14: The band pass filter used in the track selection algorithm for the (a) one-dimensional case, and for the (b) three-dimensional case. The plots corresponds for $\sigma = 1$.

where the lexan foils were exposed to it by direct contact for minimal losses. Exposures of various time durations were executed. All the exposed foils were subsequently etched together for 2h in a NaOH 6N solution at a temperature of 55°C. After a proper cleaning of the etched foils, the samples were ready for microscope observation. The microscope used for this observation was connected to a CCD camera that obtained images of the optical fields and transferred them to an image frame grabber of a PC computer. The camera used was a high resolution (512×512), low light sensitive (0.3 Lux), 1/3" CCD one, with an incorporated automatic iris facility, which allowed a constant image intensity level, independent of the lighting conditions. The track counting program was executed for each image counting the numbers of tracks, and thus evaluating the track density on each Lexan foil. Fig. 7.15 shows the measured track density as a function of the exposure time of the Lexan sample to the radioactive source. On the same plot a line is drawn representing the expected track density as a function of the exposure time. The experimental points show an excellent linear behavior up to the highest track densities where the measurements deviates from linearity. Even if this deviation is attributed solely to the performance of the track recognition system, it is still proven that the track counting is precise for track densities up to $60,000\ tracks/cm^2$.

7.6.2 Experimental Procedure

Track-etch detectors can be applied to a neutron field using a foil of a fissionable material (converter), in close contact with the detector, which can generate fission fragments. In this way fission, fragments produced by the converter are registered in the detector and the neutron fluence through the detector can be measured.

The converters of the fissionable material were sandwiched very tightly between two Lexan detectors inside a small plastic envelope. The fissionable material was in contact with the surface of one Lexan foil. The other foil was in contact with the support of the fissionable material and

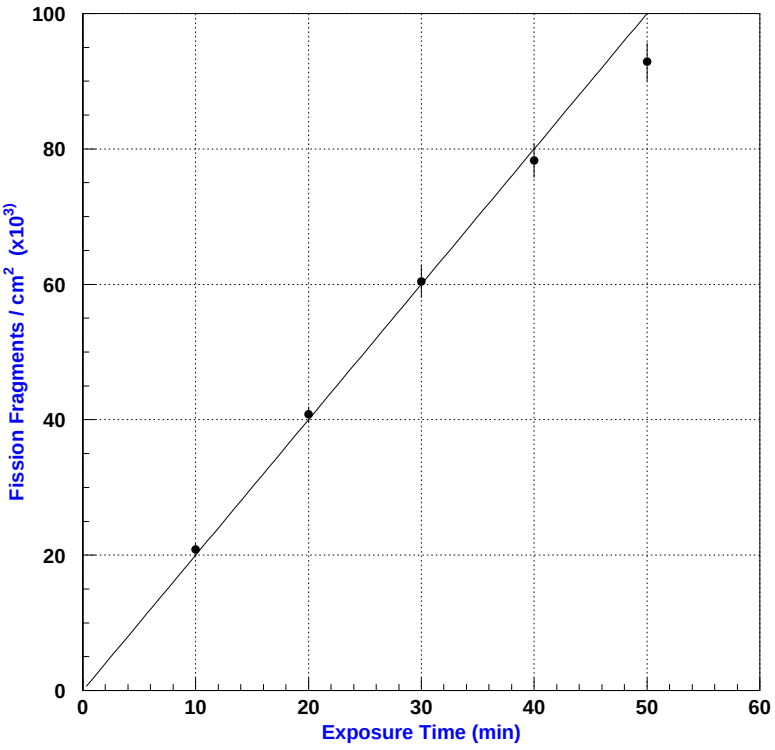

Figure 7.15: Measured track densities on a Lexan foil as a function of the exposure time to a ^{252}Cf calibrated source. The straight line drawn represents the expected track density to be observed on the foils, for the given geometry and intensity of the source.

was therefore not hit by fission fragments. This was done to avoid the relative movement of the various detector components and to reduce the air gap between the converter and the Lexan. The positioning in the holes of the lead assembly was done at the beginning by placing each sample inside a lead barrel (2 cm diameter, 6 cm long). It was found, however, that this method was cumbersome and resulted in large positioning errors (of the order of 1 cm^2). In later exposures the samples were fixed very accurately on pure aluminum strips, this were inserted in the hole. This proved to be a fast, very accurate (2 mm) and fully proof method. The Lexan detectors were developed, measured and analyzed in the way described in the previous section.

The parameters used in the track recognition program and the efficiency of the method ($78\% \pm 2\%$) were calculated from a systematic study of a large number of frames using Lexan foils irradiated with a calibrated ^{252}Cf fission fragment source.

The background was estimated by scanning the Lexan surface that was not in contact with the fissionable material and had exactly the same chemical treatment. For the beam intensity the final figures obtained from the analysis of the data collected during the runs, which include

[2]Some fission cross sections like ^{237}Np (Fig. C.6 on page 170) and ^{232}Th (Fig. C.2 on page 166) are sensitive to high neutron energies. The spatial distribution of neutrons with energies near the MeV region, strongly depends on the distance from the interaction point, and the neutron flux drops very quickly for large distances. Thus, for these elements it is important to know precisely the distance. While for other measurements which are based on thermal, and epithermal neutrons, the accuracy of the distance is not important.

beam transformer saturation corrections and single shots, were used.

The data are presented in fissions per μgr of the fissionable material of the converter for a beam intensity of 10^9 protons incident to the lead target calculated from the fission fragment measurements using the equation:

$$\frac{\text{fissions}}{\mu gr} = \frac{\text{fission fragments}/cm^2}{\text{surface density}(\mu gr/cm^2)} \tag{7.21}$$

All measurements have been corrected for the efficiency of the method. Each parameter used in the analysis has been studied in many different ways, e.g. the minimum and maximum number of pixels that define an object, etc. The quantity of the fissionable material of the converters was measured first by weight during the manufacturing of the converters, then whenever applicable, by the emission of alpha particles measured with CR-39 track etched detectors, or gas proportional counters. An overall error of 5% was estimated for mass measurements. For the U-natural, the abundance (0.72%) of ^{235}U was checked by gamma-spectroscopy (lines: 185.9 keV and 63.3 keV from ^{234}Th). For the ^{235}U source which is actually a mixture of ^{235}U and ^{234}U, the mass of the ^{235}U in the source was found using the value of *disintegrations/min* given by the source manufacturer and our measurement of the source activity by alpha spectroscopy, which gave a ratio of 1.2 for the activities A(^{235}U)/A(^{234}U). All methods gave consistent values within their statistical errors. By exposing many times at the same position the total error of the method, including errors in positioning, beam fluctuations, and statistical errors, were estimated to be 7%. From the systematic study of the efficiency of the method, it was found that for frame densities larger than 150 $ff/frame$ (fission fragments/frame), a correction of 1.27% must be applied to the measured mean values. This was caused from the overlapping of tracks in the edges. In addition, for all detectors with densities smaller than 8 $ff/frame$, the systematic error was estimated to be 15% because of the larger contribution of the background.

7.6.3 Results

a. Fission measurements

Figures 7.16, 7.17, 7.18, 7.19, 7.20 shows the fissions per μgr of converter material for all the holes, for 10^9 protons ($fissions/\mu gr/10^9\ protons$), calculated using equation Eq. 7.21, as a function of the radial distance from the center of the lead block. The negative radial distances correspond to the negative z co-ordinates within the hole.

In addition, the data for ^{232}Th are presented in Fig. 7.22 as a function of the position Z within the hole. The figure demonstrates, that significant intensity exists only in hole 3 and for $-50\ cm \leq z \leq 50\ cm$. Hence, indicating that the intensity of the fast neutrons (with $E > 1.4\ MeV$) presents a peak at about $z = 16.5\ cm$ (in hole 3) and falls rapidly (faster in the backward direction compared to the forward direction).

The fission cross section of ^{232}Th is negligible for neutrons with energies $E < 1.4\ MeV$ but becomes significant for neutrons with higher energies Fig. 7.23 (Fig. C.2. This makes the ^{232}Th a good probe to measure the integral neutron fluence for energies above 1.4 MeV.

b. Fast neutron fluence determination with ^{232}Th

The fissions per μgr of material is given by the expression:

$$\frac{\text{fissions}}{\mu gr} = \frac{N_{\text{AV}}}{A_{\text{Th}}} \int_0^\infty \Phi(E)\,\sigma(E)\,dE \tag{7.22}$$

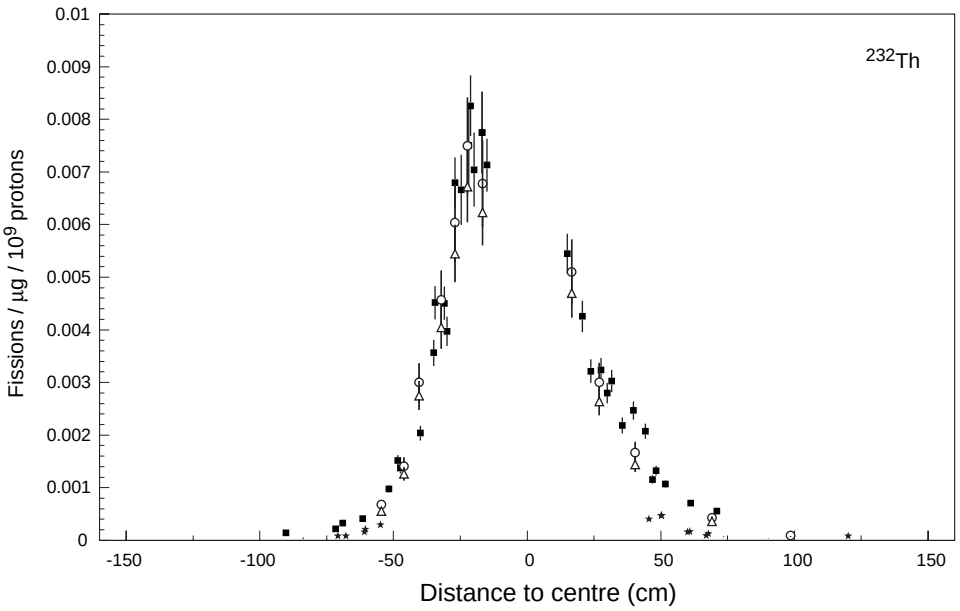

Figure 7.16: Measurement of fissions rates in ^{232}Th as a function of distance from the center of the lead volume, in hole 3 (black squares), in other holes (stars) and comparison with the EET Monte Carlo simulation using ENDF-B/VI (open circles) and using a step function cross section (0.27b) (open triangles).

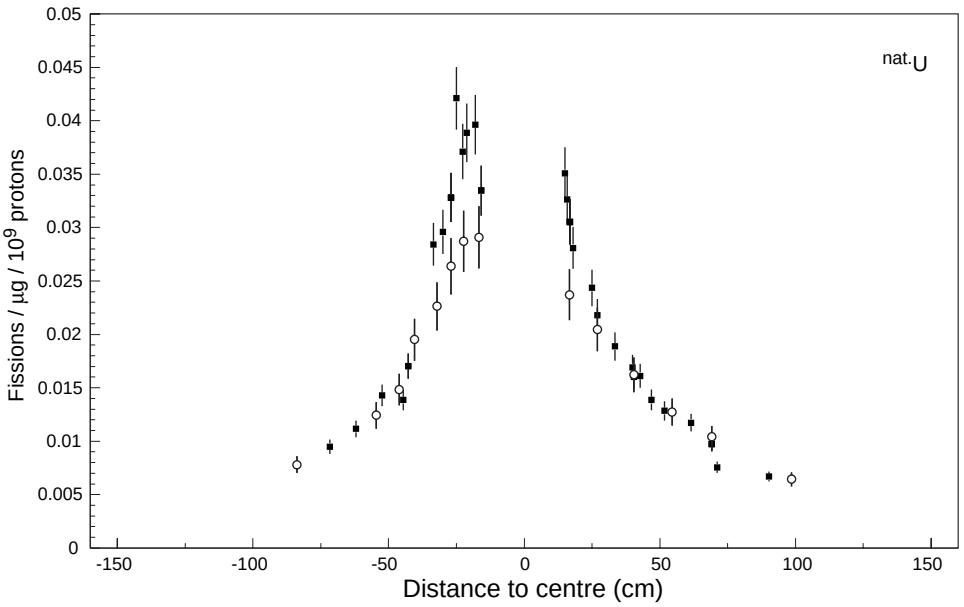

Figure 7.17: Measurement of fissions rates in ^{nat}U as a function of distance from the center of the lead volume, in hole 3 (black squares) and comparison with the Monte Carlo simulation (open circles).

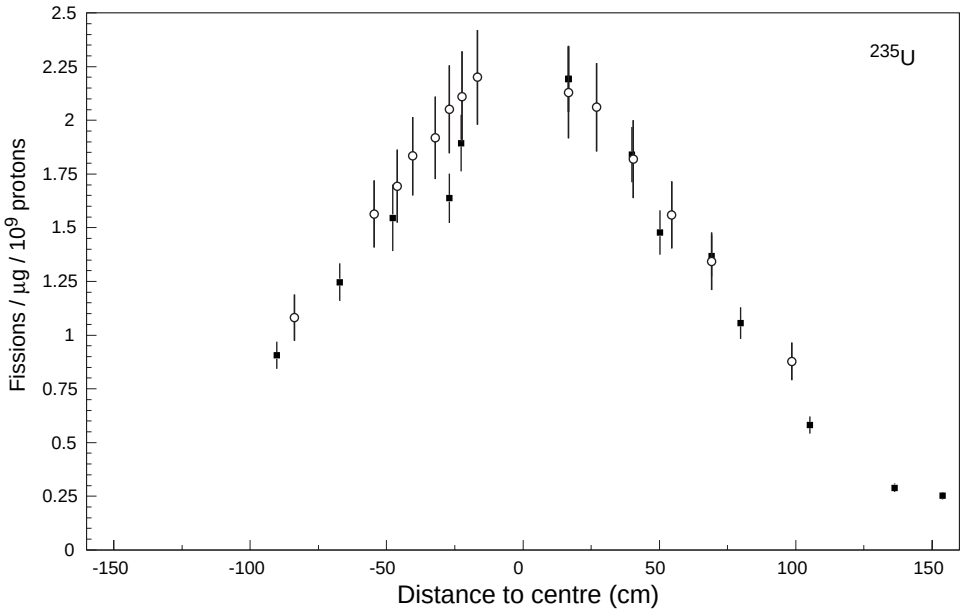

Figure 7.18: Measurement of fissions rates in ^{235}U as a function of distance from the center of the lead volume, in hole 3 (black squares) and comparison with the Monte Carlo simulation (open circles).

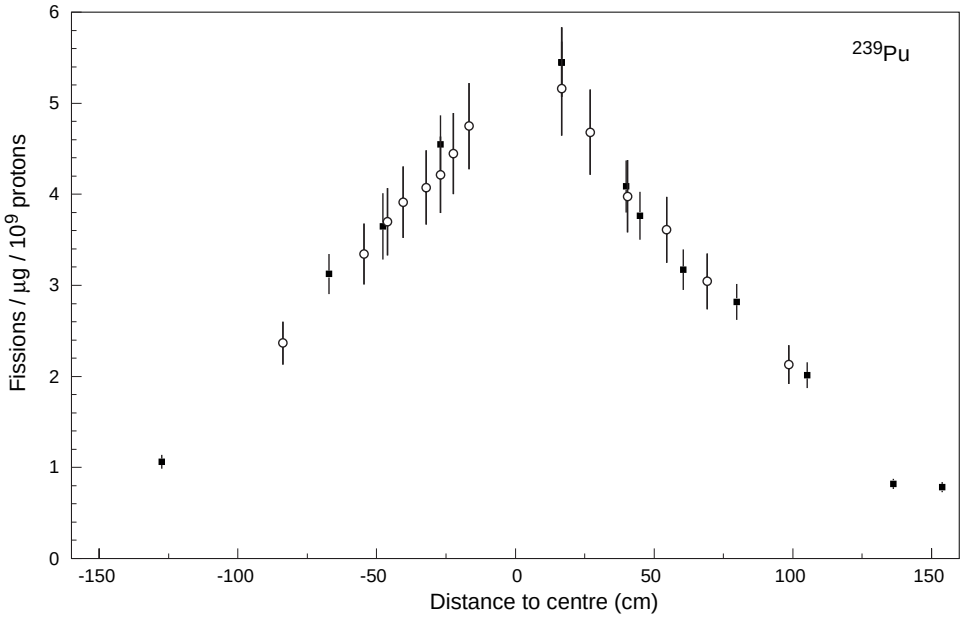

Figure 7.19: Measurement of fissions rates in ^{239}Pu as a function of distance from the center of the lead volume, in hole 3 (black squares) and comparison with the Monte Carlo simulation (open circles).

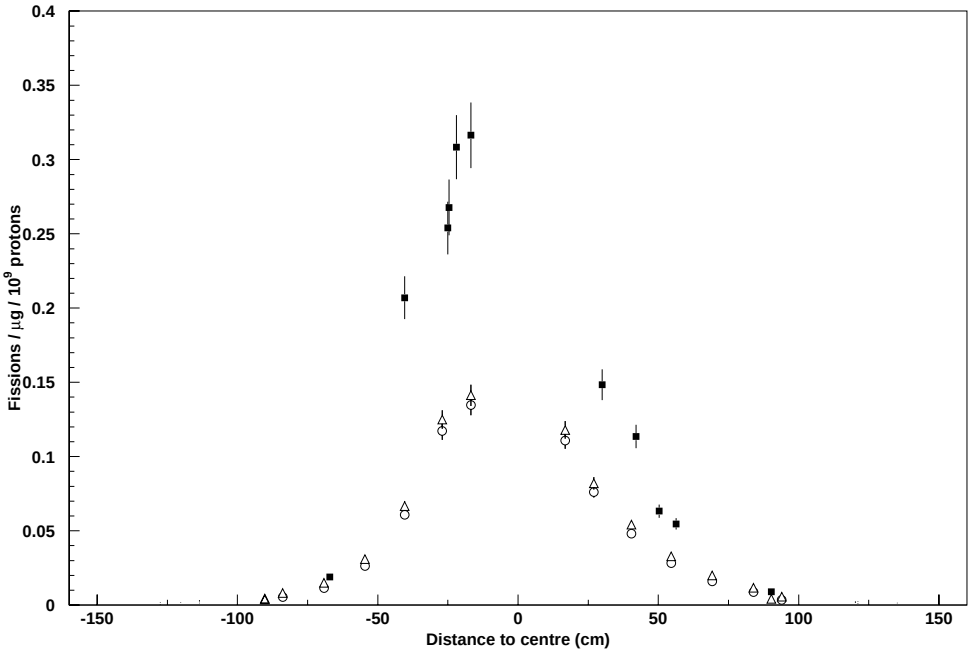

Figure 7.20: Measurement of fissions rates in ^{237}Np as a function of distance from the center of the lead volume, in hole 3 (black squares) and comparison with the Monte Carlo simulation using *ENDF-B/VI* (open circles), and with the *JENDL-3.2* (open triangles).

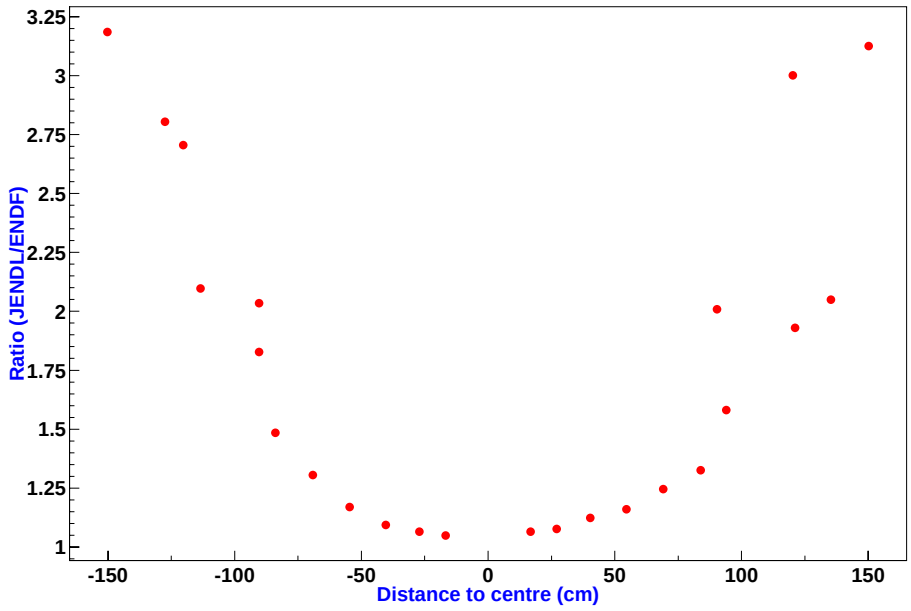

Figure 7.21: Ratio of the simulation using the *JENDL-3.2* and *ENDF-B/VI* database. At small distances (below 50cm) where the neutron spectrum is more hard the difference in the two databases is of the order of 10%. At larger distances where the neutrons are more thermalised the difference is increasing up to a factor of 3.

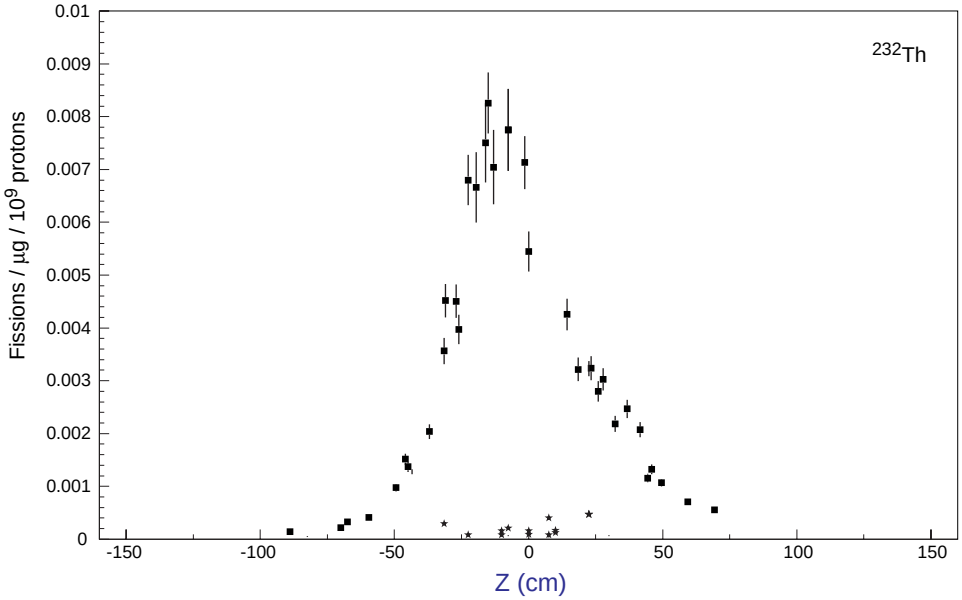

Figure 7.22: Measurement of fissions rates in ^{232}Th as a function of position along the Z axis in hole 3, (full squares) and in other holes (stars).

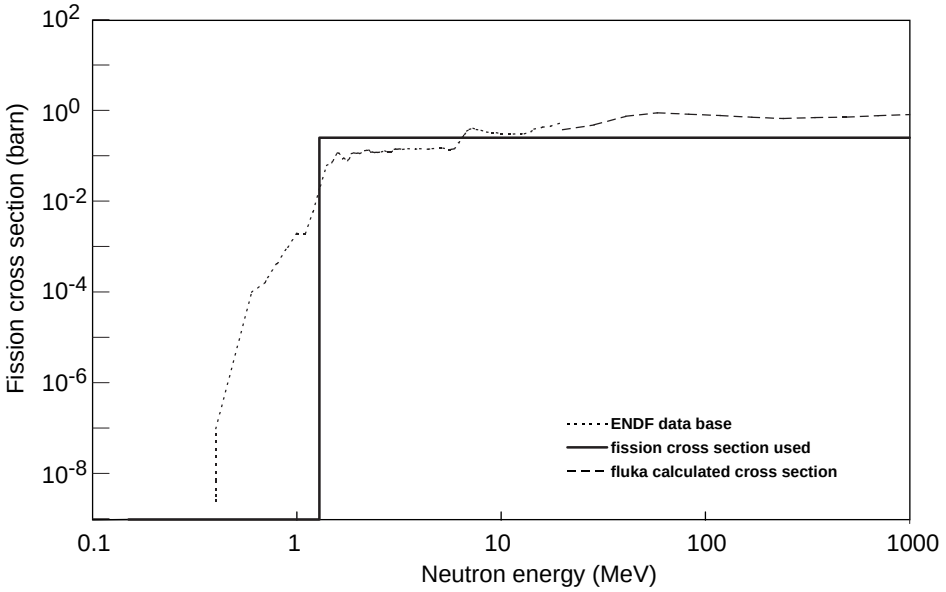

Figure 7.23: ^{232}Th fission cross section from various sources as indicated.

where $N_{\rm AV}$ the Avogadro constant and $A_{\rm Th}$ the atomic weight of the thorium isotope (in gr). In the case of ^{232}Th converter the majority (e.g. $> 96\%$ and $> 98\%$ at $z = 7.5\ cm$ in holes 10 and 3, respectively) of fissions have been produced by fast neutrons with energy $E > 1.4\ MeV$ and Eq. 7.22 now becomes:

$$\frac{\text{fissions}}{\mu gr} \sim \frac{N_{\rm AV}}{A_{\rm Th}} \int_{1.4\ MeV}^{\infty} \Phi(E)\,\sigma(E)\,dE \tag{7.23}$$

There are two possible ways to estimate the integral neutron fluence for energies above $1.4\ MeV$ which is given by the integral: (a) To assume a constant average fission cross section for $E > 1.4\ MeV$ and to calculate the above integral from Eq. 7.23 using the measured fissions per μgr and (b) to use the $\Phi(E)$ for $E > 1.4\ MeV$ as calculated from the *Monte Carlo* simulation program as a model to determine from Eq. 7.22 the fissions per μgr, and to normalize the fluence values calculated from this model using the ratio (measured fissions per μgr)/(calculated fissions per μg).

The average fission cross section needed in the first method was calculated by weighting the neutron energy spectrum with the fission cross section. The neutron energy spectrum was calculated using the TARC Monte Carlo simulation program for energies up to 20 MeV and the FLUKA program for higher energies. The fission cross section for ^{232}Th was taken from the *ENDF-B/VI* database for neutrons with energies up to $20MeV$ and from nuclear models used by the FLUKA program for higher energies Fig. 7.23.

The average fission cross section was estimated to be $\overline{\sigma}_{\rm f} = 0.277 \pm 7\%\ b$ in hole 3 at $z = 7.5\ cm$. This average cross section value is expected to become different at other positions in the *TARC* assembly because of the different neutron energy spectrum. However this difference, as calculated for the hole 10 at $z = 7.5\ cm$, is less than 5%. Thus, an average fission cross section of $0.271 \pm 10\%\ b$ for all positions was used and the fluence of neutrons with energy $E > 1.4\ MeV$ (neutrons $(E > 1.4\ MeV)/cm^2/10^9\ pr$) was calculated from Eq. 7.23 using this value and the measured fissions per μgr. The results are presented in Fig. 7.24 for hole 3.

In hole 10 at $z = 7.5\ cm$ the corresponding fluence was calculated to be $(0.52 \pm 0.06)\ 10^6$ using the first method and $(0.52 \pm 0.08)\ 10^6$ (neutrons $(E > 1.4\ MeV)/cm^2/10^9\ protons$) using the second method (arrow in Fig. 7.25).

c. Monte Carlo calculations

The *Monte Carlo* calculations of the lexan type detectors was carried out almost in the same way as in the triple foils (see § 6.1.3 on page 99). In the beginning, the spallation neutron source was created with FLUKA [5] program, simulating the CERN-PS proton beam and the hadronic interactions. The neutrons were transported by *FLUKA* code until they reached a kinetic energy below 19.6 MeV. The transport of the neutrons, was continued with the use of *TARC Monte Carlo* using the complete geometry of the installation. The program was recording the neutrons in a DST (Data Summary Tape), when during their transport they were crossing specific targets, imaginary blocks surrounding each hole.

In the last step, a reduced geometry containing only the block and the geometry of the lexan detector, was simulated using as input the neutrons from the DST, of the block where the detector was located. The geometry of the Lexan detector, was made as sandwich of the two cylindrical lexan foils where in between it was placed the support material and the converter. Because of the relatively small fission cross sections (Figures C.4, C.5, C.7, C.6 and C.2 on page 166) special tricks were used to increase the statistics. For example, in the case of ^{237}Np, where the fission cross section is very small, the experimental results showed (Fig. 7.20) that for 10^9 protons, that the fission events are of the order of 0.1 $fiss/\mu g$. In each simulation run, we were using 30,000 initial protons, which corresponds to 3×10^{-6} fission events. The simulation

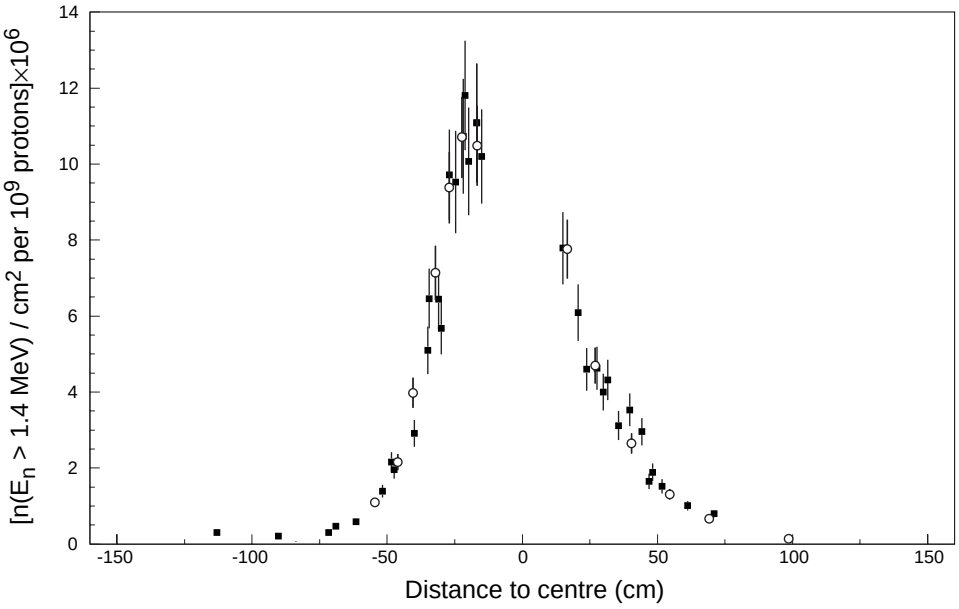

Figure 7.24: Distribution of neutron fluence (full squares) as a function of distance from the center of the lead volume and comparison with Monte Carlo simulation (open circles).

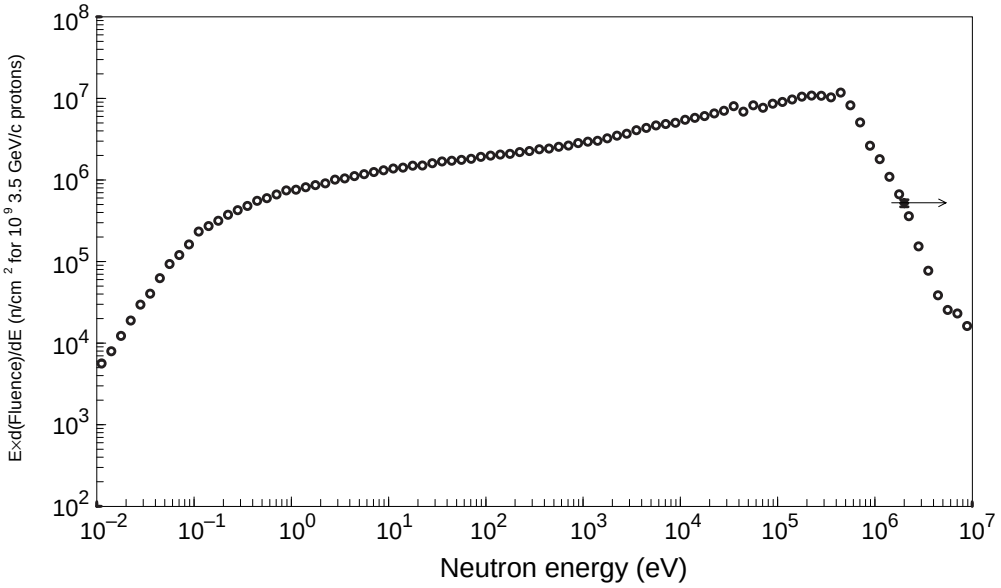

Figure 7.25: Energy dependence of the neutron fluence at hole 10, $z = +7.5\ cm$ (MC) compared to our integral estimation (black square) for 3.5 GeV/c protons.

time of 30,000 protons, starting from the DST in the block, is around $1-2$ minutes. Using the real thickness of the sample, to collect a single fission event we need a 200 days run, time unreasonable for a simulation. In the beginning we thought of increasing the dimensions of the converter, (surface and thickness), since the fission cross section is so small and no self-shielding exists. The simulation gave, for most of the converters, a good agreement with the experiment, except in the case of ^{237}Np, where a factor of 2 difference existed between experiment and simulation, with both *JENDL-3.2* and *ENDF-B/VI* libraries. A careful study of the ^{237}Np cross section, showed that by increasing the thickness of the sample, the self-shielding of the capture reactions becomes important. The capture cross section of ^{237}Np (Fig. C.6 on page 170), in the resonance region is on average 4 orders of magnitude greater than the fission. The only way for overcoming this problem, was to use the real thickness, but instead of counting the fission events, to sum the probability of having a fission reaction when a neutron was passing through the converter.

$$R = \frac{\sum [1 - e^{-\sigma_f(E)\,\frac{N_A}{A}\,\rho\, l(E)}]}{m} \tag{7.24}$$

where R is the sum of probabilities for having a fission reaction, $\sigma_f(E)$ the fission cross section at energy E, N_A the AVOGADRO number, A the atomic weight of the element, ρ the density, $l(E)$ the neutron path inside the converter with energy E, and m the mass of the sample. The method used, is a variation of the track length estimator technique (see § 3.8.2 on page 40) for measuring the neutron fluence. Where in this case, the probability of a certain reaction is recorded, as a function of the distance the neutron traveled in the sample, instead of the actual distance.

Since, now we are interested in probabilities and not number of events, a single run of 30,000 protons is enough to give a good estimation of the fission events.

The figures 7.16, 7.18, 7.17, 7.19, and 7.20 show the number of fissions per μgr of converter material for 10^9 protons ($fiss/\mu gr/10^9\,pr$), both from simulation and experiment. The error in *Monte Carlo* points was calculated as the RMS deviation from several runs using different initial seeds for the random numbers, and it is of the order of 10%. The *TARC* Monte Carlo simulation code takes into account neutrons with energy $E_n < 20\ MeV$. However there is a contribution of neutrons with higher energies ($E_n > 20\ MeV$) which is ignored. This contribution was found using FLUKA and is of the order of 12% and 10% of the neutrons with energy $1.4\ MeV < E_n < 20\ MeV$, at $z = 7.5\ cm$ in holes 3 and 10, respectively. The absence of neutrons with energies $E_{>}20\ MeV$ in Monte Carlo code is not important for most converters, where the majority of interactions are due to low energy neutrons, but it is important in the case of ^{232}Th and ^{237}Np. Thus the simulated data for ^{232}Th and ^{237}Np converters are underestimated.

For ^{232}Th the average fission cross section of 0.27 b for neutrons with energy $E > 1.4\ MeV$ (Fig. C.2 on page 166) used for the fluence measurements of neutrons with $E > 1.4\ MeV$, as well as the cross sections of *ENDF-B/VI* database were used for comparison Fig. 7.16. Both gave compatible results although the Monte Carlo predicted data, using the ENDF database are underestimated.

For ^{235}U, ^{239}Pu and ^{237}Np the *ENDF-B/VI* database was used while in the case of ^{nat}U which is a mixture of ^{238}U (99.28%) and ^{235}U (0.72%) the fission cross sections were calculated using the above percentages and the fission cross sections of ^{238}U and ^{235}U from the *ENDF-B/VI* database. In the case of ^{237}Np (Fig. C.6 on page 170) the cross sections in existing databases present a significant difference indicating large inaccuracies in ^{237}Np fission cross sections which can partially explain the difference between the Monte Carlo calculated and the measured data of Fig. 7.20. Fig. 7.21 shows the ratio from the simulation of ^{237}Np, with the use of the two different databases *JENDL-3.2* and *ENDF-B/VI*. The ratio in small distances is of the order of

10% since the neutron spectrum is more hard, and the neutron databases are almost identical for neutron energies above 100 keV. At larger distances, where the neutron spectrum is more thermalised the ratio is increasing to a factor of 3.

7.6.4 Conclusions

Lexan type track-etch detectors were used to measure fission fragments, and consequently fissions, produced in five converters ^{239}Pu, ^{235}U, ^{237}Np, ^{232}Th and ^{nat}U placed in different positions within the *TARC* experimental assembly. The measurements are in agreement with the relative Monte Carlo calculations using the TARC Monte Carlo simulation code. Using the fission measurements, the fission rate of each converter, as a function of the radial distance from the center of the experimental assembly, was also calculated. Lexan is an integral fission fragment detector. It measures fission fragments produced in the converter by the whole energy spectrum of neutrons incident on the converter. In cases of ^{232}Th, where the fission cross sections experiences a step-like behavior Fig. 7.23, an estimation can be made for the neutron flux, from the number of fissions, assuming that the cross section is constant above the threshold value $\sigma_f(E) = \overline{\sigma}$. Therefore, the number of reactions will be

$$\begin{aligned} Fissions &= \int_{E_{thres}}^{\infty} \sigma(E)\Phi(E)dE \\ &= \overline{\sigma}\int_{E_{thres}}^{\infty} \Phi(E)dE \\ &= \overline{\sigma}N_{int} \end{aligned} \tag{7.25}$$

where N_{int} is the integrated neutron fluence above the threshold value. The correct way to calculate the $\overline{\sigma}$ is to weight it with the neutron spectrum

$$\overline{\sigma} = \frac{\int_{E_{thres}}^{\infty} \sigma(E)\Phi(E)dE}{\int_{E_{thres}}^{\infty} \Phi(E)dE} \tag{7.26}$$

The shape of the neutron spectrum, in the high-energy domain (above MeV), strongly depends on the distance from the spallation source. Therefore, it is difficult to make an accurate estimation of the mean cross section $\overline{\sigma}$, more over to measure neutron fluences from fission measurements.

We find also in particular with the fission measurements in ^{232}Th that the spatial distribution of the high energy component of the neutron fluence shows a significant forward-backward asymmetry and dies away quickly (within 50 cm from the center of the cascade) which is a very useful practical consideration for the design of the *Energy Amplifier* where fast neutron damage in structural materials must be minimized.

Sample	Converter	mass ($\mu gr/cm^2$)
1	^{nat}U	856 ± 43
2	^{nat}U	856 ± 43
3	^{nat}U	856 ± 43
4	^{nat}U	856 ± 43
5	^{nat}U	856 ± 43
6	^{nat}U	830 ± 42
7	^{nat}U	935 ± 47
8	^{nat}U	952 ± 48
9	^{nat}U	951 ± 48
10	^{232}Th	1025 ± 51
11	^{235}U	22.5 ± 1.1
12	^{237}Np	10.1 ± 0.5
13	^{239}Pu	7.5 ± 0.4

Table 7.9: Converters used for LEXAN measurements, (Aug. - Sep 1996 , runs 742-1446), Etched in 6 N NaOH at 55^oC for 2 hours. The detectors were counted in frames of 360×566 $\mu m^2 = 0,002038$ cm^2

Run number	Total protons	Run number	Total protons
743	4.178×10^{11}	803	1.054×10^{12}
745	2.258×10^{13}	806	1.012×10^{12}
750	2.156×10^{11}	808-811	1.687×10^{13}
753	7.704×10^{11}	869	1.651×10^{12}
755	2.060×10^{13}	875	1.600×10^{12}
758	3.694×10^{9}	879	9.830×10^{11}
759	2.005×10^{12}	879-884	1.375×10^{13}
758-759	2.008×10^{12}	1301	1.180×10^{12}
761	2.324×10^{12}	1303	6.570×10^{12}
767	2.155×10^{13}	1308	4.630×10^{12}
780	8.776×10^{12}	1308-12	2.74×10^{13}
781	9.838×10^{12}	1319	3.56×10^{12}
780-781	1.792×10^{13}	1319-25	3.177×10^{13}
801	2.311×10^{13}	1443-46	8.278×10^{12}
802	1.576×10^{12}	801-802	2.468×10^{13}

Table 7.10: List of runs and proton intensities.

Hole	z $[cm]$	D $[cm]$	$ff/frame$	$ff/\mu g/10^9 pr$
6	-67.5	90.3	64.9	1.540
3	-45.3	47.7	232.3	2.390
3	-22.5	27.0	45.0	2.783
3	-17.0	32.6	66.4	3.220
11	-3.5	67.2	158.2	2.119
3	7.5	16.8	31.7	3.620
3	7.5	16.8	83.3	3.768
3	7.5	16.8	95.3	3.792
12	7.5	105.3	48.2	0.988
10	22.5	50.3	87.0	2.512
3	37.0	39.9	66.4	3.128
10	66.0	79.9	60.2	1.796
3	67.5	69.1	10.5	2.327
12	112.5	153.9	78.9	0.429
10	128.7	136.3	90.1	0.492

Table 7.11: ^{235}U measurements

Hole	z $[cm]$	D $[cm]$	$ff/frame$	$ff/\mu g/10^9 pr$
3	7.5	16.8	15.28	5.964
3	7.5	16.8	67.85	5.417
3	7.5	16.8	70.77	4.971
3	37.0	39.9	49.14	4.086
10	0.0	45.0	71.59	3.765
6	7.5	60.5	75.68	3.172
10	66.0	79.9	55.32	2.820
12	7.5	105.3	18.43	2.013
10	128.7	136.3	85	0.820
12	112.5	153.9	21.61	0.783
3	-22.5	27.0	22.59	4.550
6	-112.5	127.5	110.70	1.062
3	-45.3	47.7	201	3.649
11	-3.5	67.1	132.2	3.125

Table 7.12: ^{239}Pu measurements

Hole	z $[cm]$	D $[cm]$	$ff/frame$	$ff/\mu g/10^9 pr$
3	-112.5	113.5	3.01	0.212
3	-89.0	90.3	2.04	0.144
3	-70.0	71.6	9.81	0.220
3	-67.5	69.1	4.67	0.329
3	-59.6	61.5	18.51	0.415
3	-49.5	51.7	43.41	0.973
3	-46.0	48.4	21.47	1.513
3	-45.0	47.4	61.18	1.372
3	-37.0	39.9	81.71	2.036
3	-31.5	34.9	97.79	3.565
10	-31.5	54.9	7.38	0.269
3	-31.0	34.4	101.00	4.516
3	-27.0	30.9	100.70	4.504
3	-26.0	30.0	115.80	3.974
11	-22.5	70.8	3.70	0.072
3	-22.5	27.0	96.50	6.799
3	-19.5	24.6	161.80	6.663
3	-16.0	21.9	171.60	7.506
3	-15.0	21.2	117.20	8.257
3	-13.0	19.8	171.00	7.042
11	-10.0	67.8	3.73	0.072
5	-10.0	60.8	7.59	0.147
3	-7.5	16.8	110.00	7.750
3	-7.5	16.8	204.80	7.714
6	-7.5	60.5	6.57	0.187
9	-7.5	150.2	2.09	0.060
3	-1.4	15.1	101.20	7.130
3	0.0	15.0	121.80	5.447
11	0.0	67.1	4.29	0.083
5	0.0	60.0	7.58	0.147
10	7.5	45.6	14.85	0.370
7	7.5	90.3	1.05	0.031
8	7.5	120.2	1.49	0.044
8	7.5	120.2	2.54	0.076

Table 7.14: ^{232}Th measurements

Hole	z $[cm]$	D $[cm]$	$ff/frame$	$ff/\mu g/10^9 pr$
3	-70.0	71.6	57.88	9.49
6	-67.5	90.3	20.92	6.84
3	-60.3	62.1	68.05	11.15
3	-50.2	52.4	87.17	14.29
3	-42.0	44.6	17.93	13.86
3	-40.0	42.7	103.10	16.90
3	-40.0	42.7	22.20	17.16
11	-30.2	73.6	39.98	8.53
3	-30.0	33.5	44.83	28.43
3	-26.0	30.0	38.27	29.58
3	-22.5	27.0	18.71	34.03
3	-22.5	27.0	9.24	32.57
3	-22.5	27.0	32.28	31.84
11	-22.5	70.8	44.51	9.50
6	-22.0	63.9	48.20	10.29
3	-20.0	25.0	66.38	42.10
3	-17.0	22.7	48.02	37.12
11	-16.0	69.0	47.01	10.03
3	-15.0	21.2	50.29	38.87
6	-10.4	60.9	59.03	12.60
3	-10.0	18.0	62.49	39.64
11	-10.0	67.8	49.90	10.65
3	-5.0	15.8	54.78	34.75
3	-5.0	15.8	41.65	32.20
10	0.0	45.0	21.92	10.41
10	0.0	45.0	22.29	10.26
10	0.0	45.0	23.23	10.69
3	0.0	15.0	55.32	35.09
11	0.0	67.1	44.33	9.46
6	0.0	60.0	66.41	14.17
10	0.0	45.0	121.60	10.59
3	5.0	15.8	51.45	32.63
3	7.5	16.8	16.52	30.05
3	7.5	16.8	9.70	34.19

Table 7.16: ^{nat}U measurements

Hole	z $[cm]$	D $[cm]$	$ff/frame$	$ff/\mu g/10^9 pr$
3	-19.5	24.6	77.2	0.268
3	-16.0	21.9	83.6	0.308
3	-7.5	16.8	109.6	0.316
11	-2.0	67.1	9.6	0.019
7	7.5	90.3	3.0	0.009
10	22.5	50.3	23.0	0.063
3	26.0	30.0	58.9	0.148
3	39.3	42.1	16.1	0.113
3	54.3	56.3	24.1	0.055

Table 7.17: ^{237}Np measurements

Chapter 8

Conclusions of TARC and Perspectives

8.1 Conclusions

The *TARC* experiment, represents the first attempt towards a transmutation device, using the *ARC* method within a large volume of pure lead. The produced spallations neutrons, created by the PS proton beam interacting with the lead, were isolethargically slowed down to energies where the elements to be transmuted experience large resonances, with this way we are increasing the probability of being absorbed by the isotope which was introduced like an impurity in the block.

With the *TARC* experiment we have obtained a large coherent set of neutron fluence data over 8 orders of magnitude in neutron energies (from thermal to 2 MeV). In the energy region below 10 keV this was done with three different detector techniques, each with an absolute precision to the order of 15%. The spatial distribution of the neutron fluence within the lead volume has been mapped in detail over distances up to 1.9 meters from the center.

Furthermore, the technique of triple foils was used for measuring the neutron fluence at specific energies. The foils were made of isotopes that experience a strong and isolated resonance at some specific energy. Three types of foils have been used Gold, Indium and Tungsten. All of them gave consistent results with the other fluence measurements and the Monte Carlo simulation. In the case of ^{186}W the neutron databases *ENDF-B/VI* and *JENDL-3.2* represent a difference of 38% in the main resonance. Clearly our results (Fig. 6.8 on page 105) are best described by the *ENDF-B/VI* library.

One of the goals for TARC was to validate, the inovative simulation neutron transport code developed in the framework of Energy Amplifier. This code was especially optimised to decrease the computation time, by effectively using all the available computing resources and also, by optimising the use of lead as the main element in the simulation. Moreover, to improve the statistics for the detectors simulation, we decided to factorise the problem of simulation the TARC experiment, into three discrete steps. First was the hadronic interaction step, where the proton beam comming from the CERN-PS interacts with the lead volume, and produces neutrons by spallation. For the simulation of the high energy cascade and the transport of neutron down to energies of 19.6 MeV where nuclear data bases exists, we have used the well established code FLUKA[5], with the accurate geometry of the whole assembly. The second step, was the transport of all the neutrons produced by the FLUKA down to thermal energies in the complete geometry of the lead target and the surrounding room, logging into a Data Summary

File the position, direction and time of the neutrons that they were crossing imaginary volumes of Lead ($15 \times 15 \times 15\ cm^3$) around the instrumentation holes. The dimension of these volumes was selected under MC simlulation checks, that it doesn't distort the neutron fluence. Finally the last step, was the simulation of the detectors inside this imaginary volume where the DST files were created.

The unique and comprehensive ensemble of measurements, taken under well controlled conditions, constitutes a very precise validation of the innovative simulation developed by the *TARC* Collaboration and the spallation mechanism of FLUKA for different proton energies. More over, practical schemes for the transmutation of LLFF and for the incineration of Actinides were studied. These data will be extremely useful for benchmarking any new simulations needed for the development to future nuclear systems and for related systems as for the disposal of nuclear waste.

The simulation validated by *TARC* was then used to predict the transmutation rate for the example of ^{99}Tc, in the lead volume outside the *Energy Amplifier* core, where the neutron fluence is quasi isolethragic, as in *TARC*. A simple calculation predicts that 1 GW_{th} EA, after a burnup of 100 $GW_{th} \times$ d/t and with an initial load of 270 kg of ^{99}Tc uniformly diluted in lead, the fraction of 16.5% of ^{99}Tc is transmuted [4]. This corresponds to a transmutation rate of 0.85 kg/$TW_{th} \times$ h. Similarly for ^{129}I a burning rate of 1 kg/$TW_{th} \times$ h was achieved.

Thin foils of ^{232}Th and ^{239}U were placed inside the lead volume. They were irradiated in a long run of 8.5 hours an analysed with the use of a *Ge* detector, measuring the delayed gammas. The experimental measurements and the relative simulation of the transmutation of ^{232}Th and ^{239}U (see § 7.1 on page 113) showed, that we can produce the fertile ^{233}U and ^{239}Pu, to quantities up to $10^{-16}\ g/g$ for a 10^9 initial proton. In the case where the EA is loaded with 5 tons of ^{232}Th, with a proton beam of 10 mA, it will be able to produce 2.7 kg/day of the fissile element. However, in the case of possible dilution of the material to be transmuted in the lead, these *TARC* results require only temperature corrections.

Finally, fission measurements were also performed with the use of lexan foils. The fisionable material was mounted on a lexan foil. The fission fragments leaves tracks during their passage through the lexan foils. These tracks are visible with an optical microscope after the proper chemical treatment. From the counting of the tracks, the number of fissions per μg can be obtained. The fission measurements were well reproduced with the simulation, except in the case of ^{237}Np, where a discrepancy was found. There are several reasons that can partially explain this difference. Among them the most important is the difference in the two databases *ENDF-B/VI* and *JENDL-3.2* in the resonance region, and the fact that the neutrons with energies above 20 MeV are ignored by the Monte Carlo code.

The fission rate for ^{239}Pu of $5 ff/\mu g$ per 10^9 initial protons, gives a fission rate of $2\ 10^{-15}\ g/g$ comparable with the production of ^{239}Pu through the breeding process in the ^{238}U fuel cycle. Validating the necessary conditions for the equilibrium of the Uranium cycle.

Moreover, the understanding of the physics related to the exploitation of a high energy proton beam as an intense source of spallation neutrons and the unique features of "free" neutron diffusion in a high Z medium of very high transparency, both arising from the *TARC* experiment, have led to the concept and design of world-wide unique neutron source at CERN, the Time-Of-Flight (TOF).

8.2 Medical Applications

The domain of applications of the ARC method of enhancement of neutron captures is very vast. One of the promising applications using the ARC method is the production of (short-lived) isotopes for medical use. Radionuclides are extensively used for medical applications as "tracing" elements, i.e. they are directly detectable within the patient under study because of their spontaneous radioactive decays. In order to minimize the integrated radiotoxicity, the half-life of the chosen tracing isotope should be very short, ideally not much longer than the examination time. Consequently, its utilization is limited to a period of a few half-lives from activation. Another field of application of growing interest for radionuclides is (cancer) therapy, for which significantly larger than those used in diagnostics are required. Most of these isotopes must have a relatively short half-life, since they are generally injected or implanted in the patient's body. Today the main sources of supply for these isotopes are nuclear reactors or particle accelerators irradiating a suitable target with a charged particle beam.

The TARC collaboration using the ARC principle has designed a device (activator) [60], with a relatively modest cost and dimensions are intended to promote "local" production of short-lived radio-isotopes, thus eliminating costly, swift transportation and the consequent need of larger initial inventories. This is made possible by the high efficiency of the neutron capture, which results from the ARC method, utilizing a relatively modest neutron generator.

This method of radioisotope production is intended to be a competitive alternative to reactor-driven, neutron capture activation. Moreover, several isotopes that are difficult to produce by activation in the (usually thermal) neutron flux of an ordinary reactor can be produced using the broad energy spectrum. The spectrum of the neutrons in the activator is extending up to high energies. It is especially designed to make use of the large values of the cross sections in correspondence of resonances. This is the case for instance in the production of ^{99m}Tc from ^{99}Mo, widely used in medicine and which is nowadays chemically extracted from the fission fragments of spent nuclear fuel. Incidentally, the total amount of additional, useless radioactive substances, which have to be produced and handled in association with a given amount of this wanted radionuclide is also greatly reduced.

8.3 High Resolution Cross Section Measurements

The experimental determination of neutron cross sections, elastic and inelastic across the whole Mendeleiev Table has always been of primary importance in Nuclear Physics. Many of the salient features of nuclear levels can be determined from the resonant structure of such cross sections and of their decay schemes. These cross sections have many different channels and exhibit a complex phenomenology with very many resonances over a very wide energy spectrum, extending from a fraction of eV to many MeV of neutron kinetic energy.

In addition to such a primary interest, recent developments at CERN and elsewhere have raised the practical need for better known cross sections aimed specifically at the design and understanding of the behavior of ADS. In such devices, a charged particle beam is used to produce intense neutron fluxes.

These practical studies make massive use of Monte Carlo techniques in order to predict the ADS behavior in a variety of possible configurations and running conditions. The relatively high energies involved require that not only neutron capture and fission, but also a large variety of channels, like for instance (n,2n), (n,3n), (n,np), etc. should be taken into consideration. The presence of a high-energy cascade implies extending the exploration to higher energies (several hundreds of MeV). The design of innovative ADS for incineration of nuclear waste, energy

production (EA) and radio-isotope activation for medical applications, as well as many other subjects in Nuclear Physics, requires knowledge, as complete and as precise as possible, of cross sections for neutron induced process.

A fundamental pre-requisite of any computing method is the availability of reliable cross section data for many channels and at the appropriate energies. Unfortunately, the available Compilation Databases (*ENDF-B/VI,JENDL-3.2*, *JEF-2.2* and *BROND-2*) in general based on a mix of experimental measurements and of theoretical prejudices; present many "holes" and substantial differences amongst them, most likely due to the different fitting procedures used and the reliance on different theoretical models. They cannot be considered today as a totally reliable basis for planning in detail for instance the EA prototype. Indeed, while the Thorium and Uranium related cross sections are relatively well known, there are sometimes gigantic differences between the databases, when it comes to Americium and Curium, or more generally to higher Actinides.

As a result of the studies reported in the Ref.[61, 62], was proposed at CERN-PS a neutron time of flight facility (n_TOF), delivering a maximum proton intensity of 3×10^{13} *ppp* at a kinetic energy of 24 GeV. The CERN-n_TOF facility allows the study systematically and with excellent resolution of neutron cross sections of almost any element using targets of modest mass (even few milligrams), as needed for unstable or otherwise expensive materials. This facility uses as a neutron production mechanism the spallation neutrons produced by the high kinetic protons interacting with a block of lead, like in the *TARC*. The existing tunnels at CERN can provide a flight path of 200m.

8.3.1 The Neutron Source

The spallation mechanism [61, 62] is a remarkably powerful source of neutrons: in an infinite lead spallation target, one 24 GeV proton can produce as many as 760 neutrons. The CERN-PS[33] accelerator is capable of accelerating up to 3×10^{13} *ppp* resulting to as many as 2×10^{16} neutrons at each pulse. This prolific source can be concentrated in short time pulses which are typically of the order of about 7 ns RMS length, offering the added feature of a tremendous potential accuracy in the time of flight (TOF) determination of the neutron energy. The rich initial source strength offers a flux of $2.8 \times 10^5/L^2(km)$ $n/cm^2/pulse$ at a measuring station located a distance L (Fig. 8.1).

The energy resolution can be further optimized with the use of Hydrogenic layer (H_2O or Polyethylene). When the neutrons are colliding with the Hydrogen atoms, they rapidly lose their kinetic energy reflected by their velocity, while their time remains the same. So in the Eq. 2.69 on page 24 $\lambda = v(t)\, t$ the velocity v is dramatically reduced, resulting to smaller values of λ and also to $\Delta\lambda$ (Fig. 8.2).

8.3.2 The Spallation Target

An overall optimization of the layout made of a lead spallation target of length h, radius R followed by a water moderator of thickness W has been performed for the neutron emission angle of 16^o from the proton beam direction, as set by the configuration of Ref.[61]. As a resolution of the general trade-off between neutron flux and $\Delta\lambda$ resolution, the parameters $h = 40\ cm$, $R = 40\ cm$ and $W = 5\ cm$, are chosen.

Detailed calculations show that the power dissipation in the target gives rise to an increased temperature and requires therefore a cooling. In fact, about half of the 2 kW "initial phase" beam power will dissipate into the block and will require an air-cooling (closed circuit). The

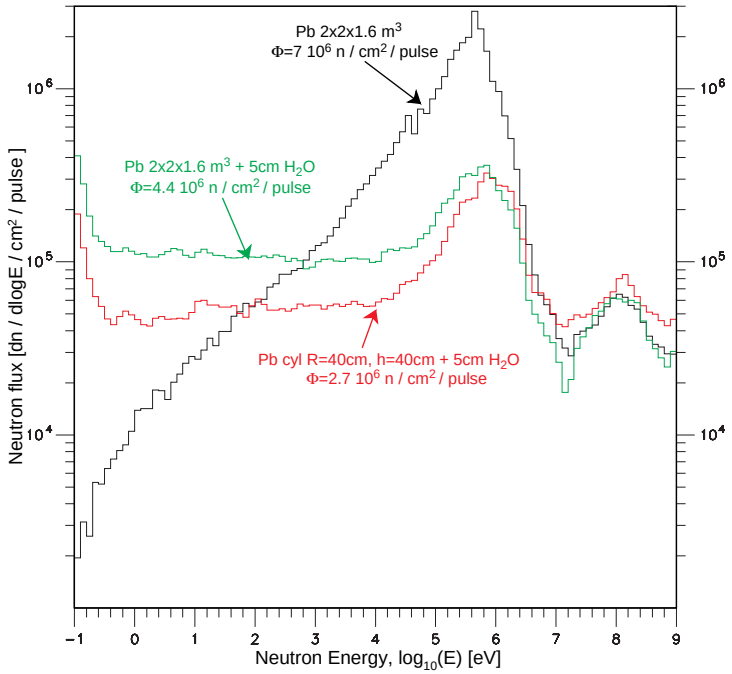

Figure 8.1: Neutron energy spectrum for various lead target configurations, with and without a 5cm water moderator. The TOF path is 200m.

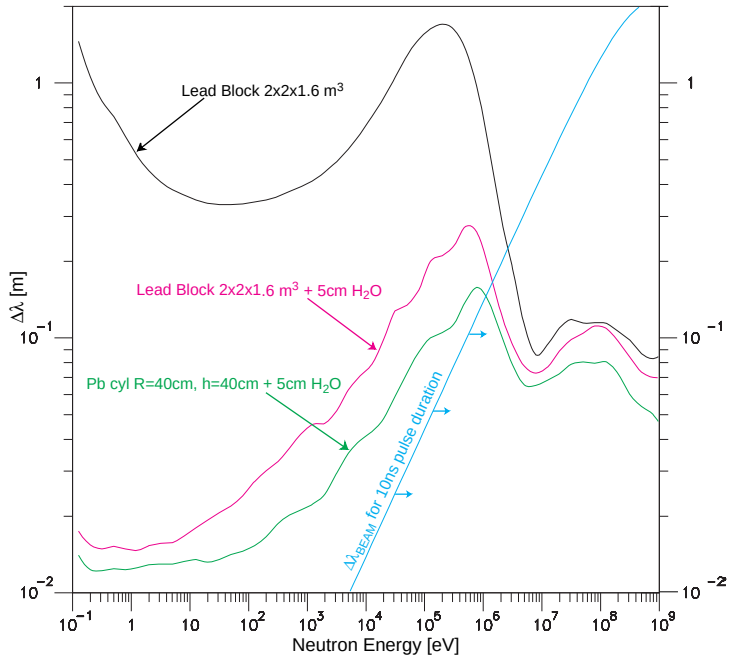

Figure 8.2: The uncertainty in the path $\Delta\lambda$ as a function of the neutron energy for various target configurations. The reflected $\Delta\lambda$ uncertainty due to the CERN-PS pulse duration is also shown.

temperature in the center will reach 60^oC.

8.3.3 Experiments

The uniqueness of n_TOF lies in the availability of a very high neutron flux, of a broad energy range, exceeding eight orders of magnitude and of a unprecendeted energy resolution. These novel features provide great potential for modern experimentation with neutrons, exploiting new ideas in nuclear ADS technology While also covering new ground in the fields of nuclear physics, nuclear astrophysics and nuclear medicine. It's high-energy resolution and event rates allow practically all resonances to be resolved. Moreover, permitting the systematic study of all relevant neutron induced reactions, in the energy interval between 1eV to above 250MeV, of almost any nuclide using targets of very modest mass (few milligrams). Important, for radioactive or expensive materials such as transuranics and medium to long-lived fission fragments. The fact that teams from all over Europe are participating in the n_TOF project, renders the sophisticated measuring techniques from various physics domains, the accelerator, and infrastructure of CERN accessible to the European nuclear data community. Thus, making the n_TOF project, a European challenge.

For the above reasons a vast variety of experiments/measurements has been proposed[63] to take place at the n_TOF facility, which can be subdivided into the following categories.

- Neutron reactions for stellar nucleosynthesis. Exploration of the reactions that are related with the *s-process*, *r-process*, *p-process*[1] used in the stars, and supernova creation scenarios.
- Improvement of the statistical model.
- Neutron cross sections for cornerstone applications (fusion, fission reactors, ADS for nuclear waste transmutation and medical radio-isotope production).
- Reactions used as probe for basic nuclear physics; *nucleon-nucleon* interactions: neutron-neutron scattering, neutron-proton Bremsstrahlung, meson production in neutron-proton scattering, neutron-nucleus scattering.
- Fission reactions as a probe of nuclear matter, studying the vibrational resonances in ^{232}Th, and ^{234}U
- Investigation of the fundamental nuclear properties of the neutron: neutron-electron scattering length, the electric polarizability,

[1]The proton rich nucleus are produced by (γ, n) process, the measurement of (n, γ) cross section for proton rich nucleus permit to explain the process by detailed balance [64].

Appendix A

Main Features of the "Energy Amplifier"

The *Energy Amplifier* [1] (EA) is the result of a "cross-fertilization" between the technology of modern accelerators and the one of Nuclear Electricity Production. In contrast with an ordinary reactor, in the *Energy Amplifier* the energy is produced in the form of heat, as the result of nuclear cascades, rather than of self supported chain reactions. Nuclear cascades are initiated by relativistic protons produced by a small but efficient accelerator. The basic physics and the conceptual design of the EA are comprehensively illustrated in the references [1, 65]. The underlying physical principles of *Energy Amplification* have been demonstrated in the *FEAT* experiment performed at CERN [66].

The general layout of the EA is shown in Fig. A.1. The choice of fast rather than thermal neutrons, is motivated by the higher attainable power density and the larger burning efficiency, for the higher Actinides. The nominal thermal power has been set to $1500\,MW$. The coolant medium is molten natural *Lead*, operated in analogy with Fast Breeders (Sodium cooled) "models" at a maximum temperature of $600 - 700^{o}C$. Because of the high boiling temperature of Lead ($1743^{o}C$ at n.p.t) and the negative void coefficient of the *Energy Amplifier*, even higher temperatures may be considered, provided the fuel and the rest of the hardware are adequately designed.

The most relevant feature of the *Energy Amplifier* design is the possibility of using natural convection alone to remove all the heat produced inside the core. Convection cooling has been widely used in "swimming pool" reactors at small power levels. This very safe method can be also applied to the very large power of the EA, because of the unique properties of Lead such as, high density, large dilatation coefficient and large heat capacity. Elimination of all pumps in the primary loop is an important simplification and a contribution towards safety, since unlike pumps, convection cannot fail. In the convective mode, a very large mass of liquid Lead ($\approx 10\,000$ *tons*), with an associated exceedingly large heat capacity[1] moves very slowly ($\leq 2.0\,m/s$ inside the core, about 1/3 of such speed elsewhere). Hence, transferring the heat from the top of the core to the heat exchangers located some 20 meters above and returning at a lower temperature ($\Delta T \approx -200^{o}C$) from the heat exchangers to the bottom of the core.

The geometry of the EA main vessel is therefore relatively slim (6.0m diameter) and very tall (30m). This relatively slender geometry enhances the uniformity of the flow of the liquid

[1]The heat capacity of liquid Lead at constant pressure is about $0.14\,\mathrm{Joule/gram}/^{o}C$. For an effective mass of $\approx 10^{4}$ tons $= 10^{10}$ grams and a power of $1.5\,GWatt$ (full EA power), the temperature rise is of the order of $1.0^{o}C/s$. The mass flowing through the core for $\Delta T \approx 200^{o}C$ is $53.6\,tons/sec$, corresponding to some 1.5 minutes of full power to heat up the half of the coolant in the *cold* loop, in case the heat exchangers were to fail completely.

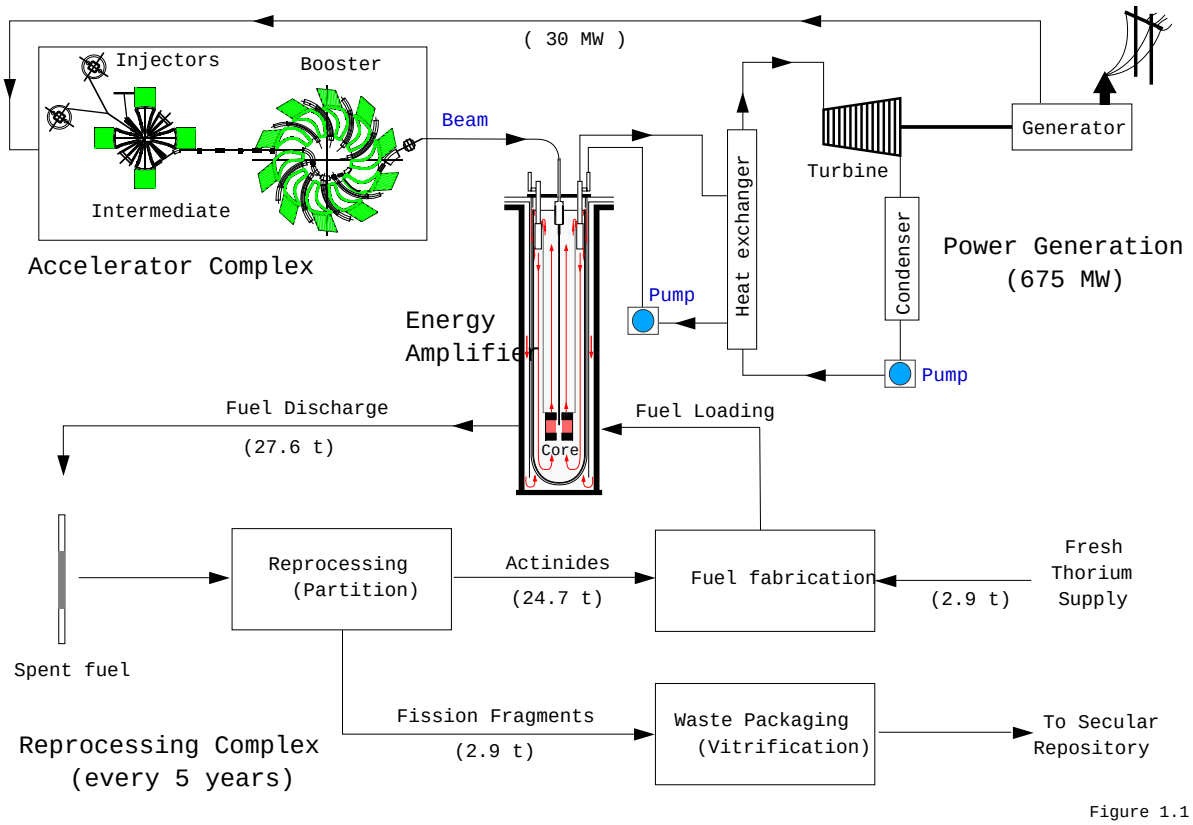

Figure A.1: General layout of the *Energy Amplifier*.

Lead and of the natural circulation for heat removal. The vessel is housed below floor level, in a robust cylindrical silo geometry lined with thick concrete which acts also as ultimate container for the liquid Lead in case of highly hypothetical rupture of the main vessel. The Reactor Vessel Air-Cooling System (RVACS), is located in the space between the main vessel and the concrete. This system is completely passive and based on convection and radiation heat transfer. In case of a thermal overheating, the significant dilatation of the molten Lead will raise the level of the liquid which (see Fig. A.2) activates the RVACS cooling, stops the proton beam by flooding an appropriate emergency beam stopper (EBDV) and scrams the EA at a lower multiplication coefficient $k \leq 0.90$. The whole vessel is supported at the top by anti-seismic absorbers.

The fuel is made of mixed oxides, for which considerable experience exists. More advanced designs have suggested the use of metallic fuels or carbides. These fuels are possible candidates for the EA. The choice of the chemical composition of the fuel is strongly related to the one of the fuel preprocessing method.

A relative novelty of the EA, when compared to ordinary Pressurized Water Reactors (PRWs), is the large concentration of ThO_2 in the fuel and the corresponding production of a small but relevant amount of Protactinium. A liquid separation method called THOREX has been developed and tested on small irradiated ThO_2 fuel samples. The extrapolation from the widely used PUREX process to THOREX, is rather straightforward.

The average power density in the fuel has been conservatively set to be $\rho = 55\ Watt/gr - oxide$, namely about 1/2 the customary level of LMFBR[2] (ALMR, MONJOU and EFR). The

[2]This choice is motivated by the relative novelty of the "all-convective" approach and the relative scarce

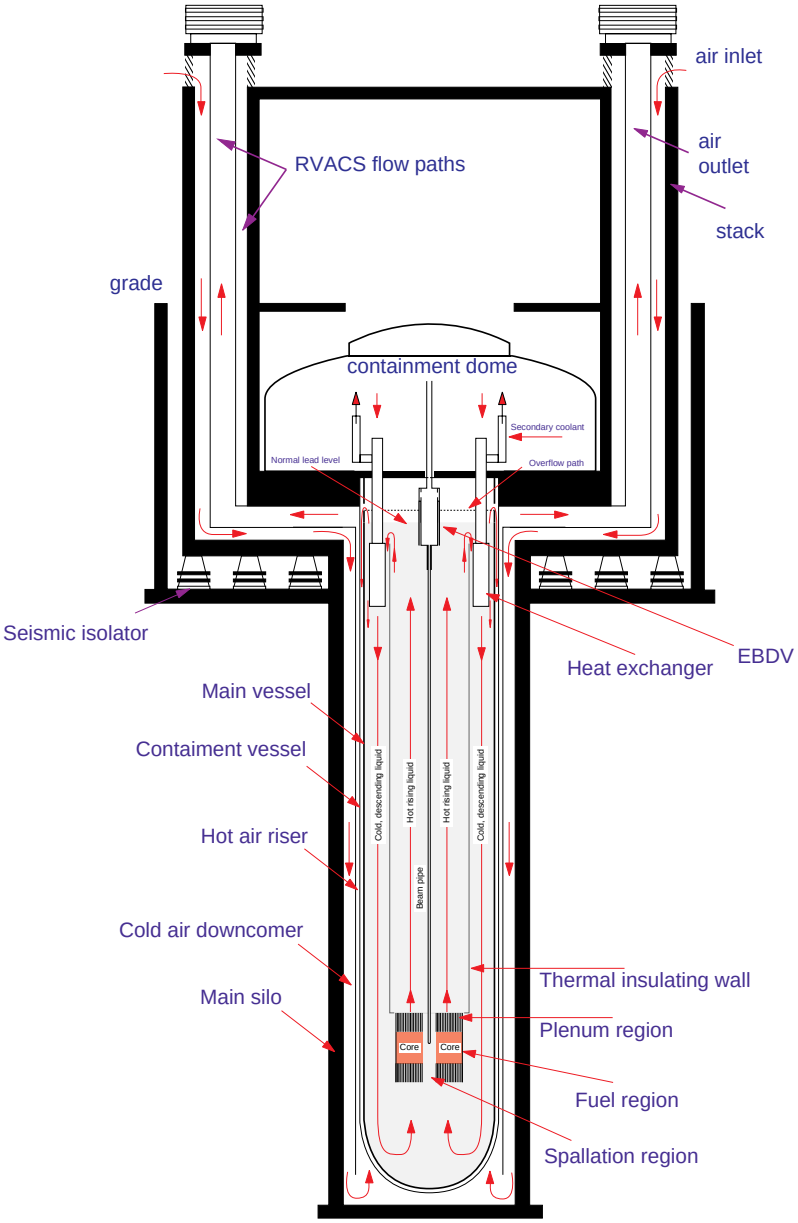

Figure A.2: Core of the *Energy Amplifier* unit.

nominal power of $1500\,MW_{th}$ requires then 27.3 tons of mixed fuel oxide. The fuel dwelling time is set to be 5 years equivalent at full power. The average fuel burn-up is then 100 GWatt day/ton-oxide. Since the fissile fuel is internally regenerated inside the bulk of the Thorium fuel, the properties of the fuel are far more constant than in the case of a PWR.

Normally the EA is well away from criticality at all times ($0.95 \leq k \leq 0.98$), there are no control bars (except the scram devices) and the power produced is directly controlled by the injected beam current. The accelerator is a synchronous cyclotron with an accelerated continuous current of $10 - 20\,mA$ and kinetic energy of 1.0 GeV. It makes use of warm magnets ($B_{max} = 1.8\,Tesla$ over $5\,cm$ magnet gap) and RF-cavities. The accelerator can be housed

experience with ThO_2, when compared with UO_2.

outside the containment region. The nominal external power provided by the beam is $P_{ext} = 12.5\,MW$, corresponding to a gain $G = P_{EA}/P_{ext} = 120$ (to be compared with $G = 40$ for Magnetic Fusion MF).

Therefore, in the case of the EA, the external power source is about 1/3 of the one assumed for MF for a given power production[3]. The heat flux extracted by the Lead coolant from the fuel pins, is on the average $100\,W/cm^2 = 1\,MW/m^2$, a factor 2-3 larger than the one of the first wall of MF[4]. The peak power density in the beam window, is of comparable magnitude, namely $113\,W/cm^2 = 1.13\,MW/m^2$, but much smaller than the one of the divertor of MF ($5.0 - 10\,MW/m^2$).

A.1 The Advantages of the EA

The EA is becoming a serious candidate because of it's reasonable cost, and it's capability to produce clean Nuclear Energy in the near future, for the following main reasons:

1. The technology is mature and an EA can be constructed sensibly and quickly within the present state of the art. There are precisely three specific and well defined components which must be realized with a reasonable extrapolation of present technologies, namely:
   (a) The accelerator;
   (b) The energy producing tank;
   (c) The fuel fabrication and preprocessing.
2. The EA fulfill the main new missions of Fusion [67], with respect to ordinary Nuclear Energy, namely:
   (a) Minimize the quantity of nuclear waste for Geologic Storage ("waste" less radioactive than coal ashes after a reasonable cool-down period);
   (b) Elimination of the "Criticality" and "Melt-down" accidents;
   (c) A better use of primary element for the fuel which is burnt at the theoretical efficiency, namely $\approx$ 200 times more effectively than PWR (the never fulfilled goal of Fast Breeders);
   (d) It permits the use of Thorium and therefore, the development of a Plutonium-less nuclear energy.
3. The EA can be a natural, safer substitute for present electricity producing nuclear energy, at the end of the currently operating reactors and for the new installations in the developing countries. Neither Fusion nor renewable energies will be ready on time to replace the amount of power produced by the present generation of Reactors (6% of the world consumption). Replacement of nuclear with fossil fuels will represent a serious increase of the Carbon Dioxide emissions. Incidentally, we remark that the new generation of thermal PWRs although they introduce significant improvements on the questions of safety

[3]The indicated powers are the ones actually given respectively to the plasma or to the spallation source. The transformation of electric power (mains) to neutral beam or radio frequency heating for MF have expected efficiencies (30-50%) which are rather close to the one of the EA accelerator (43%). Hence, the factor 3 in favor of the EA vs. the MF is also roughly valid, if one compares the re-circulated fractions of produced electrical energy.

[4]It is of course much easier to cool the pins immersed inside the molten lead than the first wall of MF facing the burning plasma. Note that the power density for the EA fuel is about 1/2 of the one in operation with Superphenix and MONJOU.

(better containment and cooling of decay heat), they leave the problems of the long lived waste, and of the Geological Repository untouched. In particular they keep producing vast quantities of Plutonium, which nobody wants because it represents a considerable risk.

4. In an intermediate, overlapping phase of a hypothetical PWR to EA transition, it is possible also to clean up the huge amount of "waste" produced by present day Nuclear Power [68], thus introducing an alternative to the Geologic Storage for the presently accumulated waste (Plutonium). This is a point of great concern (see for instance the law Curien in France) and which is not solved with MF. The "waste", if burnt in an EA, produces about 30% of the energy of the initial burning in the PWR. Preliminary economical considerations [69] show that Plutonium incineration when compared to direct geological disposal, is not only environmentally more acceptable, but also an economically profitable alternative.

5. Any new energy source must be cost competitive with standard fossil sources, namely Oil, Natural Gas and Coal. The energy cost from EA has been estimated to a first order and found significantly lower than conventional sources.

6. The EA can be used to eliminate effectively the military grade Plutonium from the stockpile of bomb-grade Plutonium from Military Arsenals [68]. The amount which needs to be eliminated is about 100 tons ($> 20\,000$ warheads), out of a total of about 300 tons, of which about 180 tons are still in warheads. The energy stored in 100 tons of military Plutonium corresponds to 1400 millions of barrels of oil.

Appendix B

The FEAT Experiment

A **F**irst **E**nergy **A**mplifier **T**est (FEAT [3]) was created to verify the basic principle of the *Energy Amplifier*. The experiment was consisted of a sub-critical arrangement made of natural Uranium and water moderator which was exposed to a low intensity ($\approx 10^9 ppp$) proton beam from CERN-PS at several kinetic energies from 600 MeV to 2.75 GeV. The energy delivered by the hadronic cascade, induced by the beam in the device, has been measured by the temperature rise of small sampling blocks of Uranium, and also by counting the fissions in thin probe foils of natural Uranium. These blocks were located in several different positions inside the device. A typical $G \approx 30$ was found in reasonable agreement with calculations, where G is the ratio of the energy produced in the device to the energy delivered by the beam.

B.1 Description

The *FEAT* experiment showed that it is possible to "amplify" the energy deposition of a high-energy cascade to such an extent as to potentially recover the energy of the incident beam and to make a considerable net energy gain. With the experimental conditions, the energy produced by the cascade has been typically some thirty times the one delivered by the beam.

In a proton, induced cascade one can distinguish two qualitative and successive physical regimes: (1) a spallation driven, high-energy phase and (2) a neutron driven, fission dominated regime. When the energy of the cascade products falls below several MeV, ionization losses bring particles rapidly to rest, with the exception of neutrons which continue down to thermal energies.

Neutrons from the first phase, are acting as "source" for the second phase. The first phase, was explored with calorimeters, since it is rather complicated and the relevant cross sections are often poorly known, it can be approximately parameterized with the help of phenomenological models and *Monte Carlo* calculations [5]. Which are sufficiently detailed to give a first order agreement with the experimental measurements.

In the second phase (for neutron energies below $20 MeV$, where almost a complete set of cross sections exists) the main physical process is a diffusive process of neutrons, which gradually loose energy by collisions and they are multiplied by fission and (n,2n) reactions. This phenomenology resembles the one of Nuclear Reactors. However, because the *Energy Amplifier* is not critical, there are some differences: in a Reactor the fluence distribution inside the volume is determined essentially by the boundaries [70], in the *Energy Amplifier* the location and geometry of the initial cascade acting as the neutron source, is dominant. A simple analytic theory based on diffusion theory has been developed [71]. The neutron source excites a superposition of ortho-

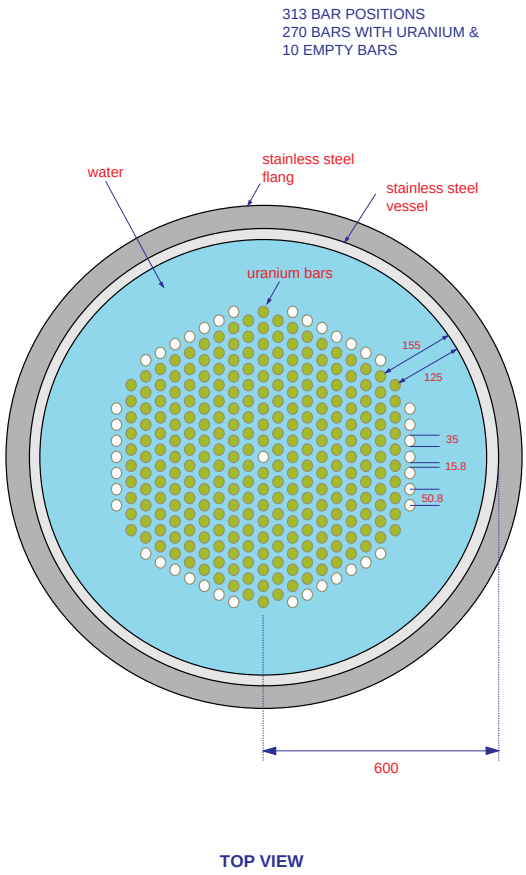

Figure B.1: Top view of the subcritical assembly. Distances are in mm.

normal modes of the "bulking" equation representing the neutron fluence, of which only the fundamental mode is relevant to a Reactor Theory. Each of these modes has a different buckling parameter B_i and a different multiplication coefficient k_i. As a consequence, in the conditions of the *FEAT* experiment, in which the *microscopic multiplication coefficient* k_∞, defined as the average number of neutrons produced at each absorption in the fuel-moderator mixture, is $k_\infty < 1$, because

1. the spatial neutron fluence is expected to decay exponentially from the point of the source [72], rather than having the characteristic cosine distribution centered with respect to the volume as in a Critical Reactor [70]

2. for a proton pulse, sharp in time (δ-function), the neutron population decreases exponentially with a time constant which grows linearly with $1/(1 - k_{eff})$, where k_{eff} is the *effective multiplication coefficient*. The presence of such a second neutron driven phase is essential in order to achieve a large gain.

B.2 Experimental Results

The experimental setup is shown in Fig. B.1 and Fig. B.2. It was consisted of a sub-critical assembly made of natural Uranium rods, immersed in a stainless steel tank filled with ordinary de-mineralized water, which acted as moderator. The beam from CERN-PS was hitting a small

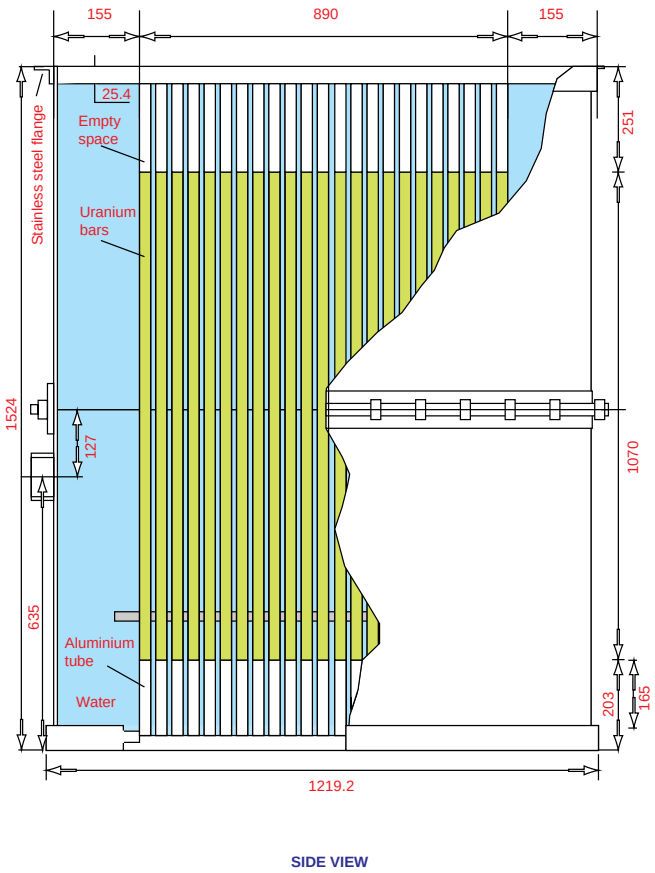

Figure B.2: Side view of the subcritical assembly.

target of depleted Uranium, that was located such as to approximately center, the source of spallation neutrons with respect to the device. The beam kinetic energy varied, in the interval from $600MeV$ up to $2.75GeV$. The proton beam intensity was typically of the order of $10^9 ppp$ on a $\leq 1.0cm$ radius focal spot, in the form of a sharp ($\leq 100ns$) fast extracted bunch.

The neutronic behavior of the assembly was calibrated, with the help of a 58 GBq neutron source ($Am - Be$) inserted in the center of the device. The neutron fluence was measured with Boron loaded counter. Comparing the source results with measurements using only water, the FEAT collaboration, found an effective multiplication coefficient for a point-like centered source, of $k = 0.915 \pm 0.010$. The result was in good agreement with *Monte Carlo* calculations which gave $k = 0.92$. The difference in the k factor is because the source was not point-like, and also that additional materials have been introduced, which did not exist in the *Monte Carlo* simulation. The calculated reduction is $\Delta k = -0.02$, which leads to an expected value for the beam configuration of $k = 0.895 \pm 0.010$.

In order to calculate the energetic gain G of the device, which is defined as the ratio between the energy produced in the device divided by the energy delivered by the beam, we must integrate the energy depositions sampled by the thermometers, over the full volume. Different methods were used in the counting of the energy deposition

1. thermometers;

2. fission measurements with Lexan foils;

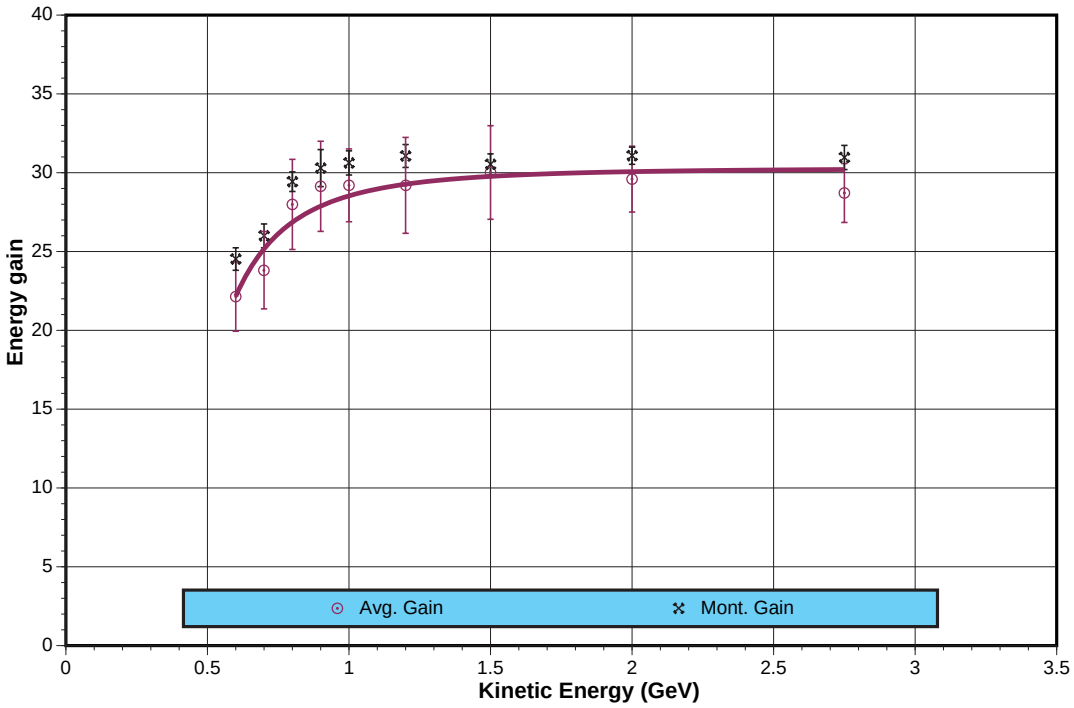

Figure B.3: Average energy gain G from various counters and *Monte Carlo* simulation, as a function of the mean energy of the proton beam in *FEAT* experiment. The continuous line is represents the fit of the data.

3. electronic counters.

All of the above methods gave an excellent agreement in the integrated values of G. Also they were found to be in satisfactory agreement with the relevant *Monte Carlo* calculations based on the FLUKA [5] for the energy cascade, complemented by the *Energy Amplifier Monte Carlo* code based on the *ENDF-B/VI* cross sections for the neutronic behavior. The gain G is essentially constant above a proton kinetic energy of 1 GeV and drops somewhat for lower values.

The expression that calculates the energy gain of a general *Energy Amplifier* system is the following

$$G = G_o/(1 - k_{eff}) \tag{B.1}$$

where, G_o relates the efficiency of the spallation regime and the well known $(1-k)$ factor, with the k as the effective multiplication coefficient, which is related to the neutron driven part of the cascade. Using $k = 0.895$, obtained from the source measurement, and the average gain for 1 GeV proton energy, $G = 29 \pm 2$ we find $G_o = 3.1 \pm 0.4$. We expect a gain of $G = 62 \pm 8$ with a somewhat larger device, resulting in a effective multiplication coefficient $k_{eff} \approx 0.95$, safely away from criticality.

Appendix C

Lead Data and Cross Section

C.1 Main Properties of Lead

The following are a compilation of some of the main physical and thermodynamical properties of Lead [73].

Symbol	**Pb**
Atomic number	82
Atomic weight	207.2
Density ($293\,^oK$)	11.336 g/cm^3
Melting point (^oK)	600.55
Boiling point (^oK)	2023.154 (1 atm)
Specific Heat (kJ/kgK)	0.1278
Thermal Conductivity (W/mK)	35.0

Table C.1: Lead physical data.

Nominal mass	*Accurate mass*	*% natural abundance*
^{204}Pb	203.973020	1.4
^{206}Pb	205.974440	24.1
^{207}Pb	206.975872	22.1
^{208}Pb	207.976627	52.4

Table C.2: Isotopic data for naturally occurring isotopes of Lead.

C.2 Cross Sections

The following cross sections are extracted from the *JENDL-3.2* database.

Reaction	$2200\,m/s$	I_{eff}	$14\,MeV$	$Fiss.Avg$
total	11.25		5.418	6.414
elastic	11.07		2.464	5.591
capture	$174.2\ 10^{-3}$	$142.6\ 10^{-3}$	$581.8\ 10^{-6}$	$2.745\ 10^{-9}$
inelastic			$429.4\ 10^{-3}$	$815.4\ 10^{-3}$
(n,2n)			2.525	$5.080\ 10^{-3}$
(n,3n)				$2.002\ 10^{-6}$
(n,na)		$21.27\ 10^{-6}$	$1.717\ 10^{-6}$	$749.8\ 10^{-12}$
(n,np)			$7.739\ 10^{-6}$	$21.55\ 10^{-9}$
(n,p)		$1.402\ 10^{-3}$	$755.6\ 10^{-6}$	$564.3\ 10^{-9}$
(n,a)		$2.369\ 10^{-3}$	$821.9\ 10^{-6}$	$451.8\ 10^{-9}$

Table C.3: Neutronic Information for Natural Lead (barns).

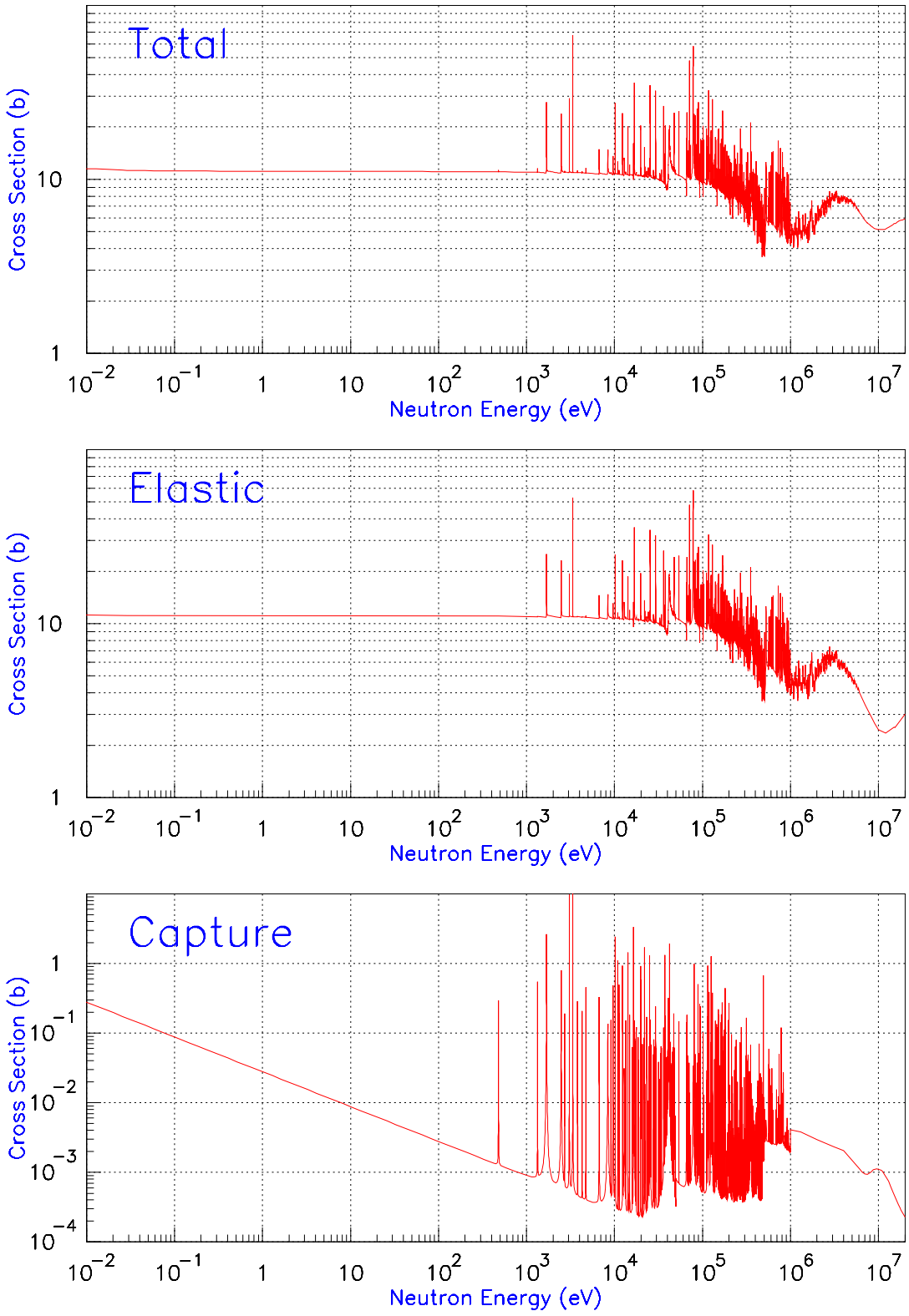

Figure C.1: Natural **Pb**, Total, Elastic and Capture cross sections, from *JENDL-3.2*

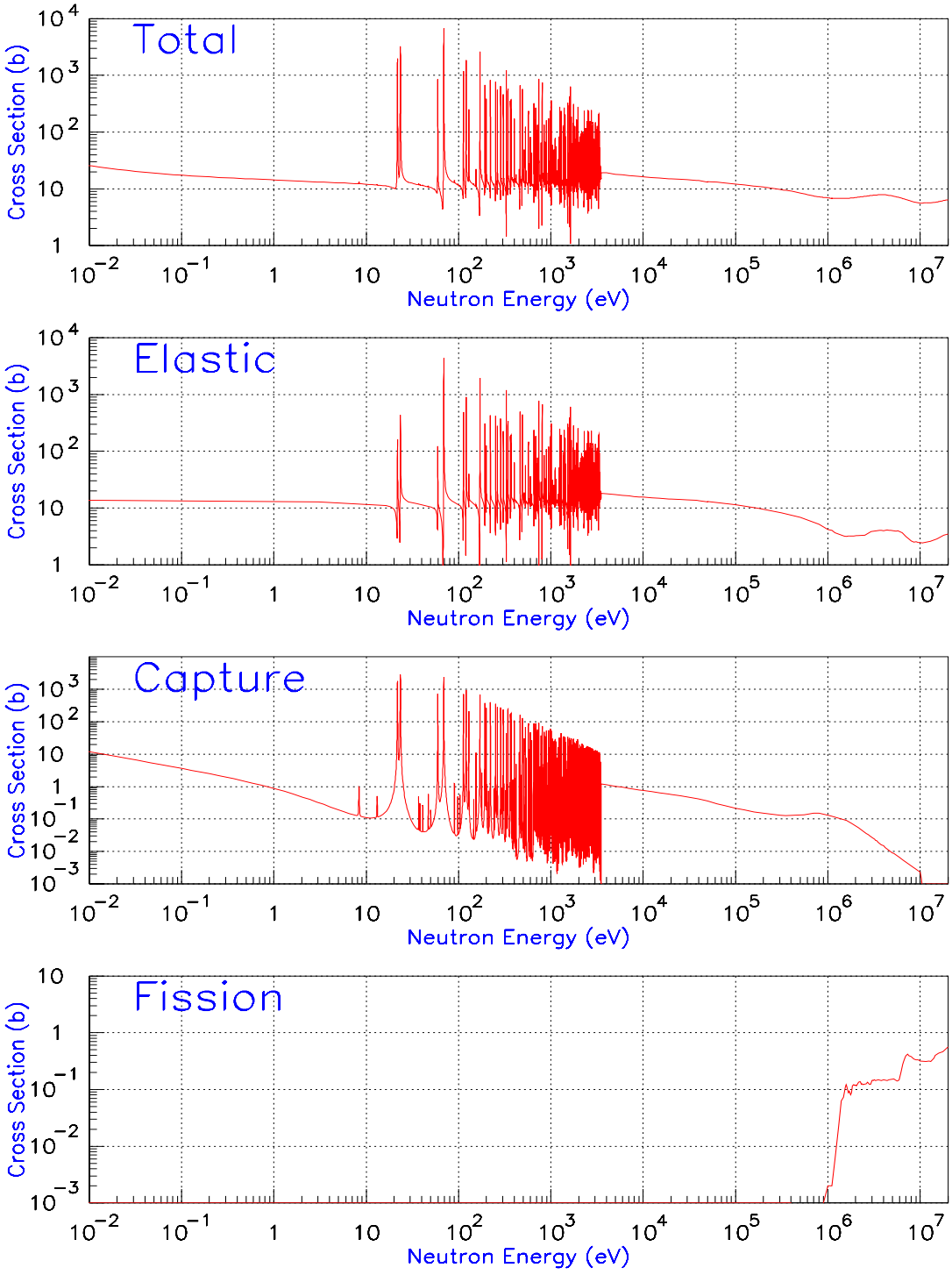

Figure C.2: ^{232}Th, Total, Elastic, Capture and Fission cross sections, from *JENDL-3.2*

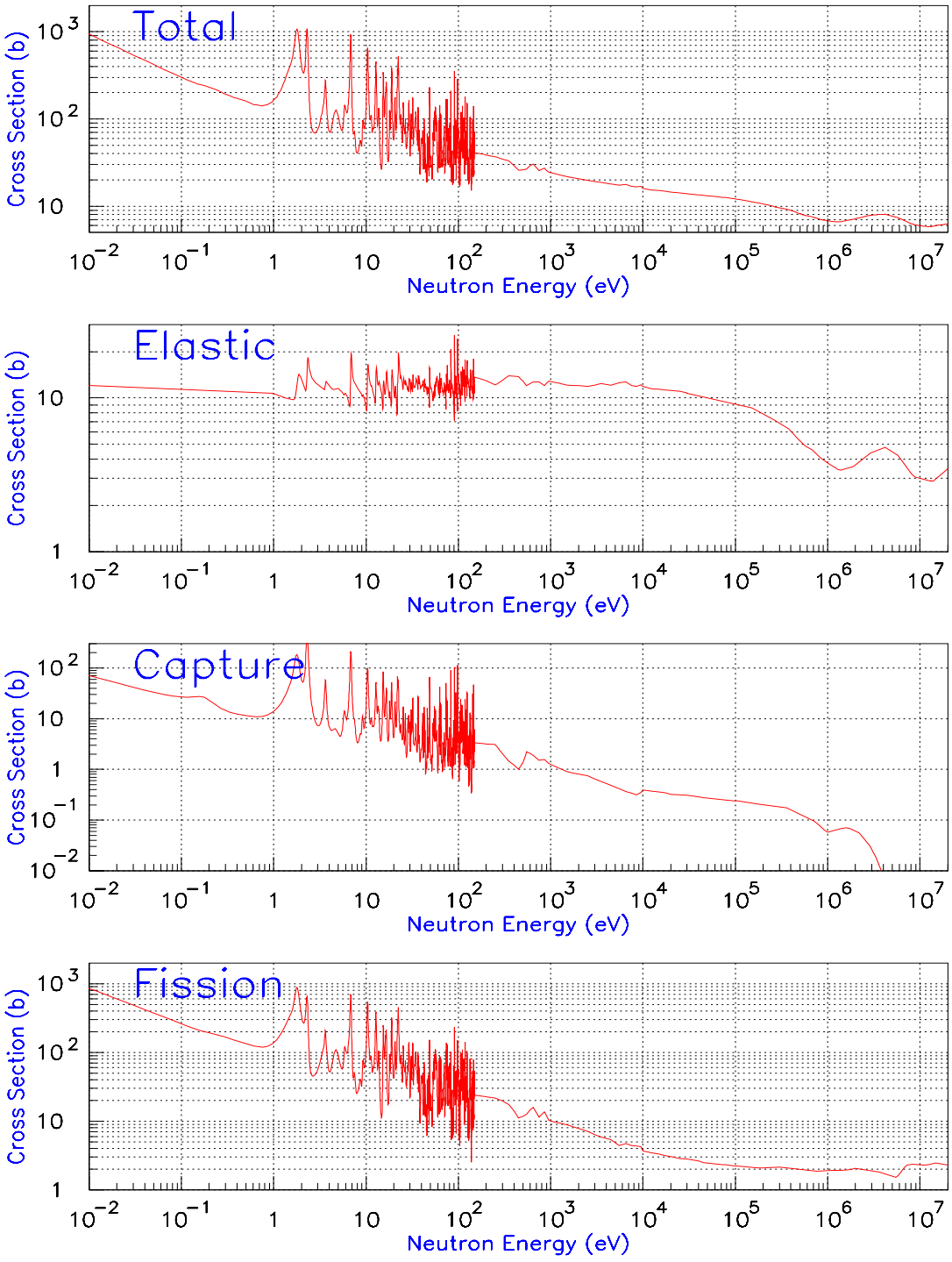

Figure C.3: ^{233}U, Total, Elastic, Capture and Fission cross sections, from *JENDL-3.2*

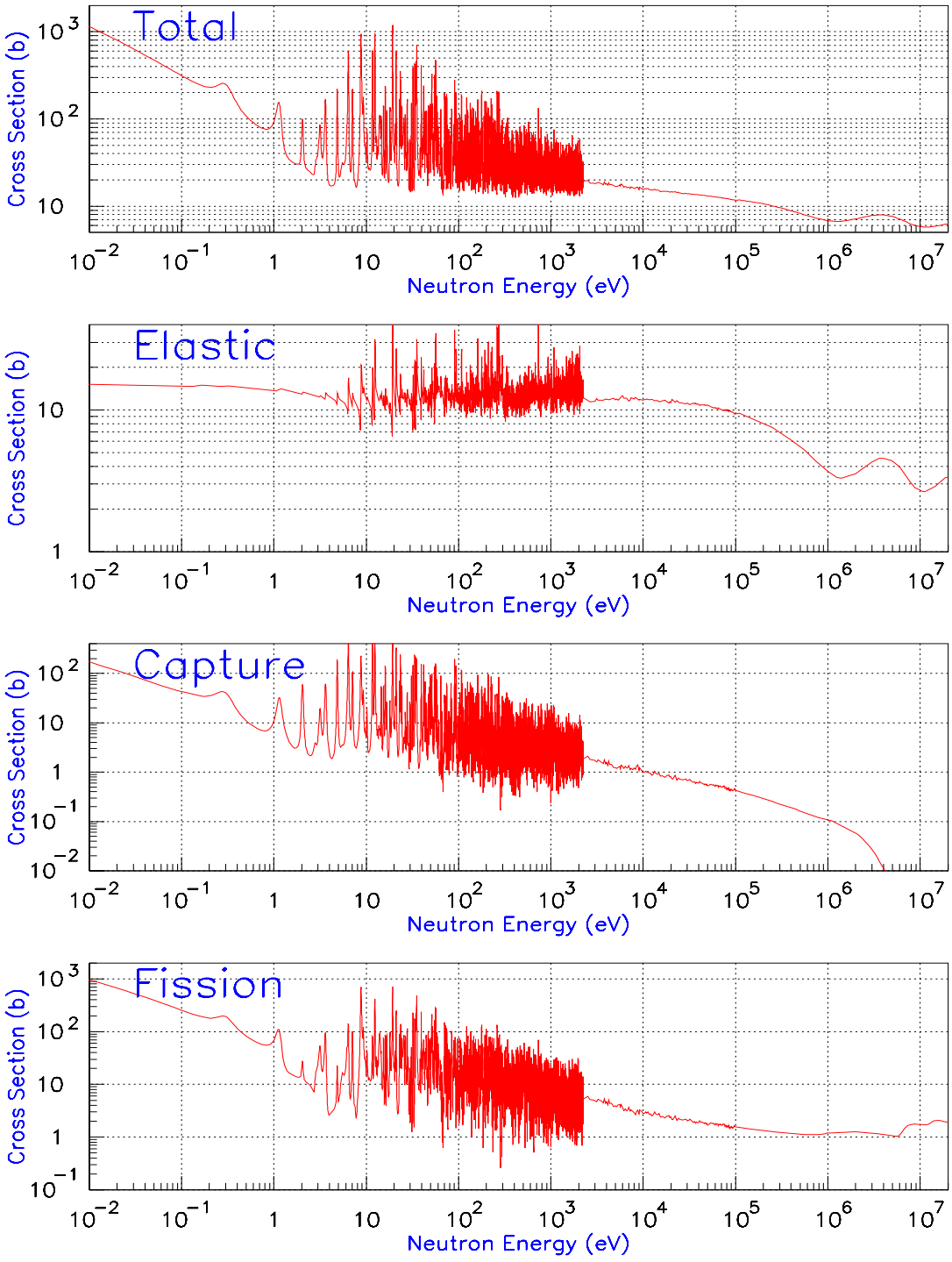

Figure C.4: ^{235}U, Total, Elastic, Capture and Fission cross sections, from *JEF-2.2*

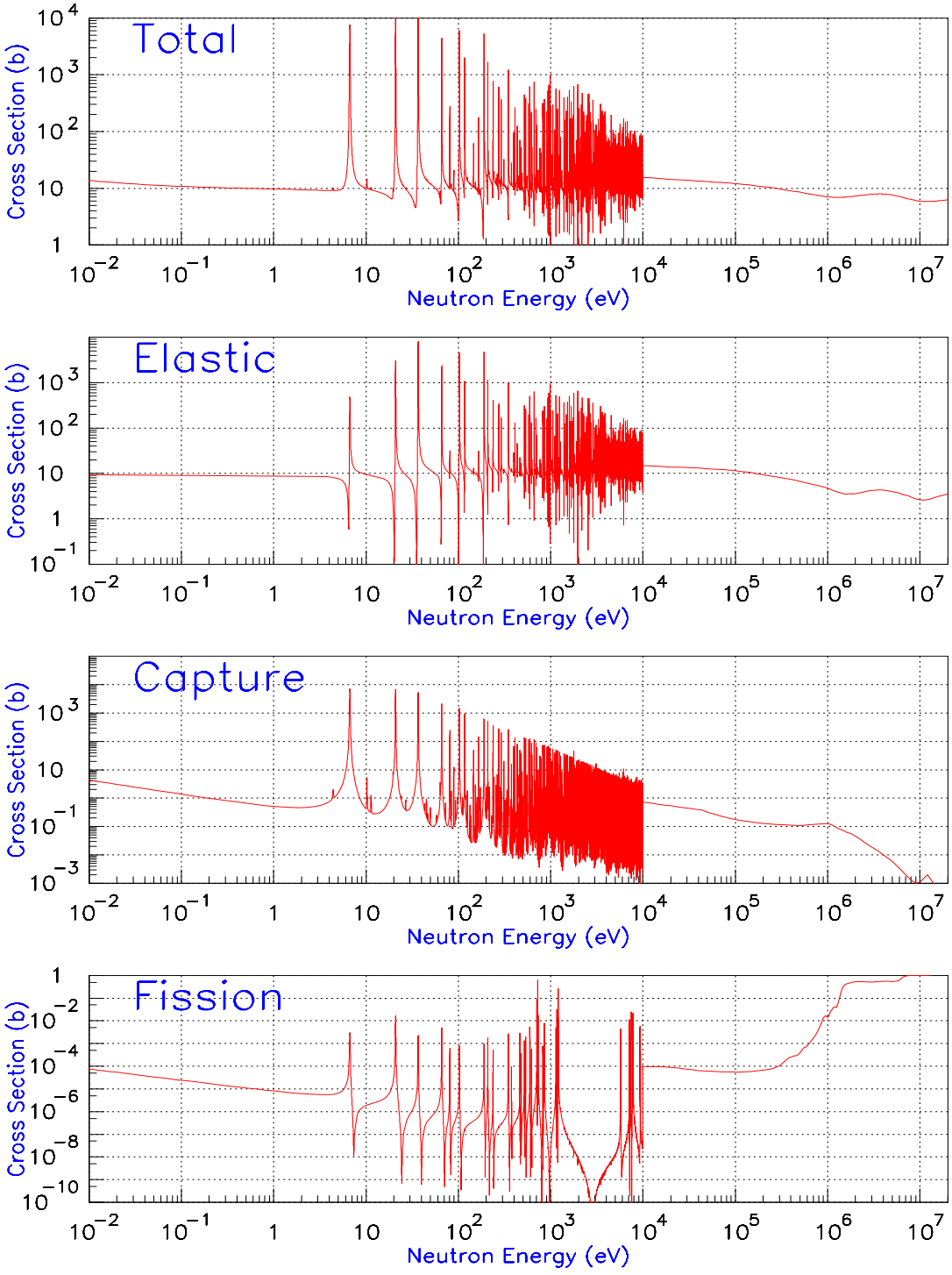

Figure C.5: ^{238}U, Total, Elastic, Capture and Fission cross sections, from *ENDF-B/VI*

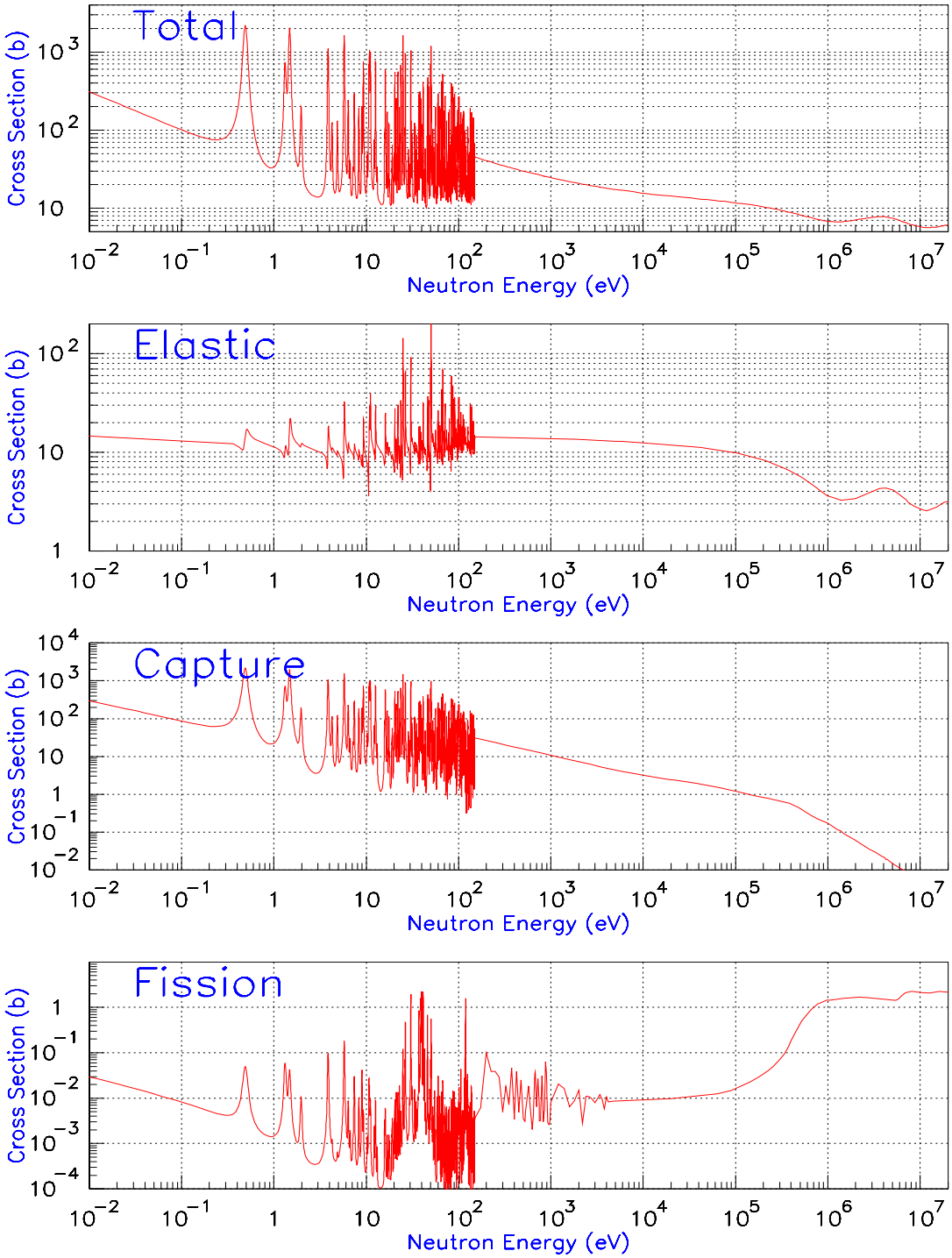

Figure C.6: ^{237}Np, Total, Elastic, Capture and Fission cross sections, from *ENDF-B/VI*

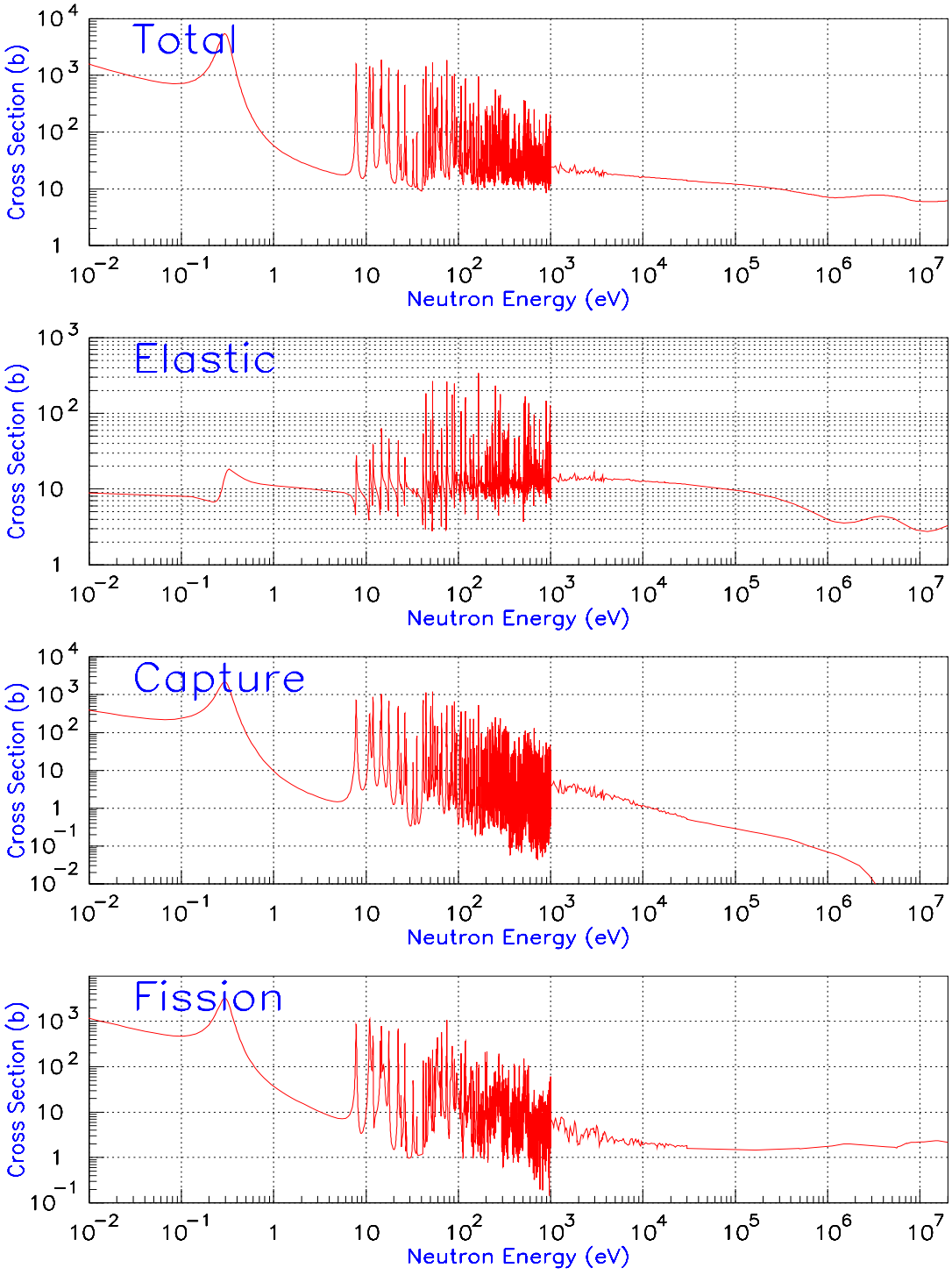

Figure C.7: ^{239}Pu, Total, Elastic, Capture and Fission cross sections, from *JEF-2.2*

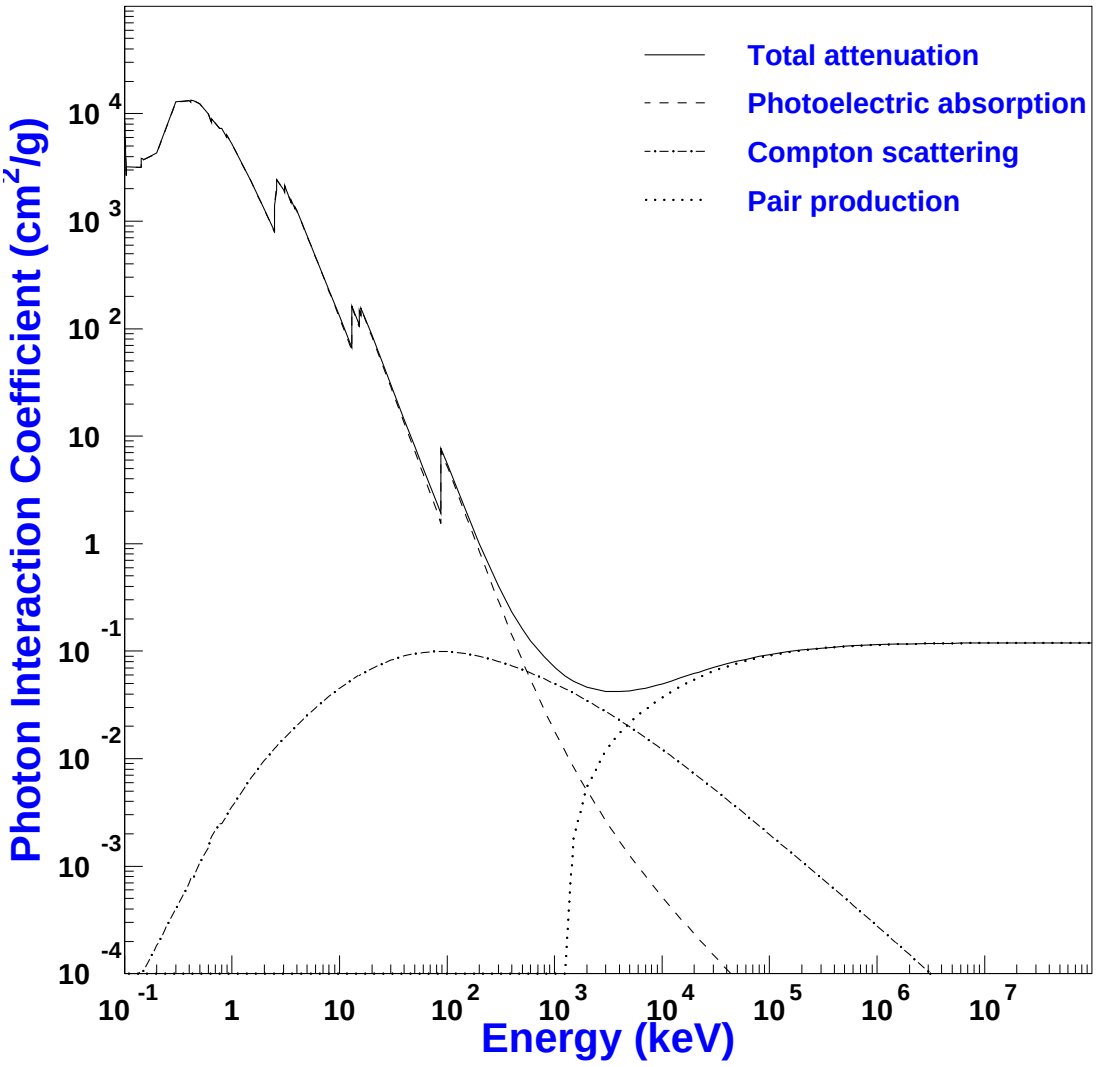

Figure C.8: Photon Interaction Coefficients of Lead

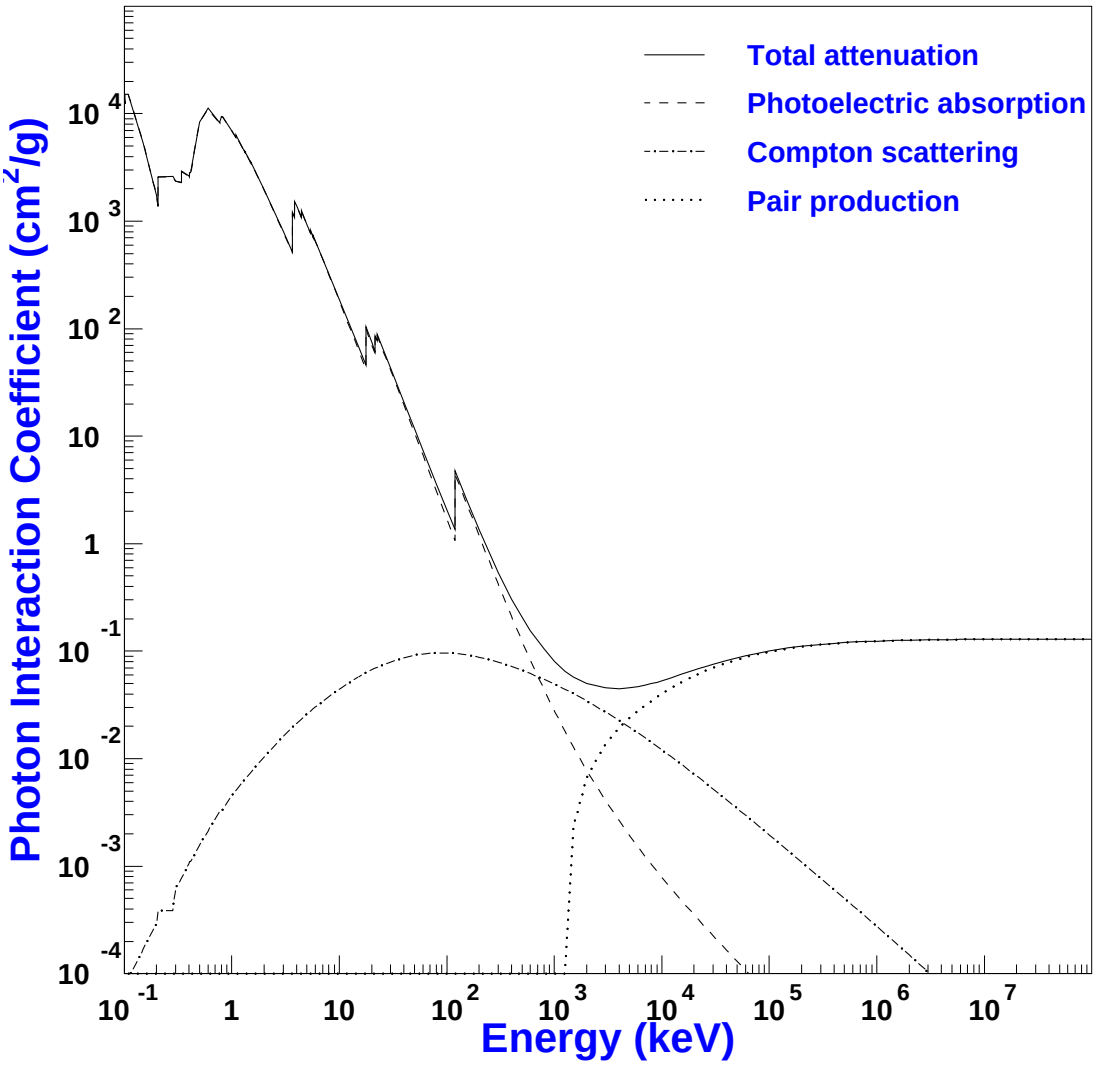

Figure C.9: Photon Interaction Coefficients of Neptunium

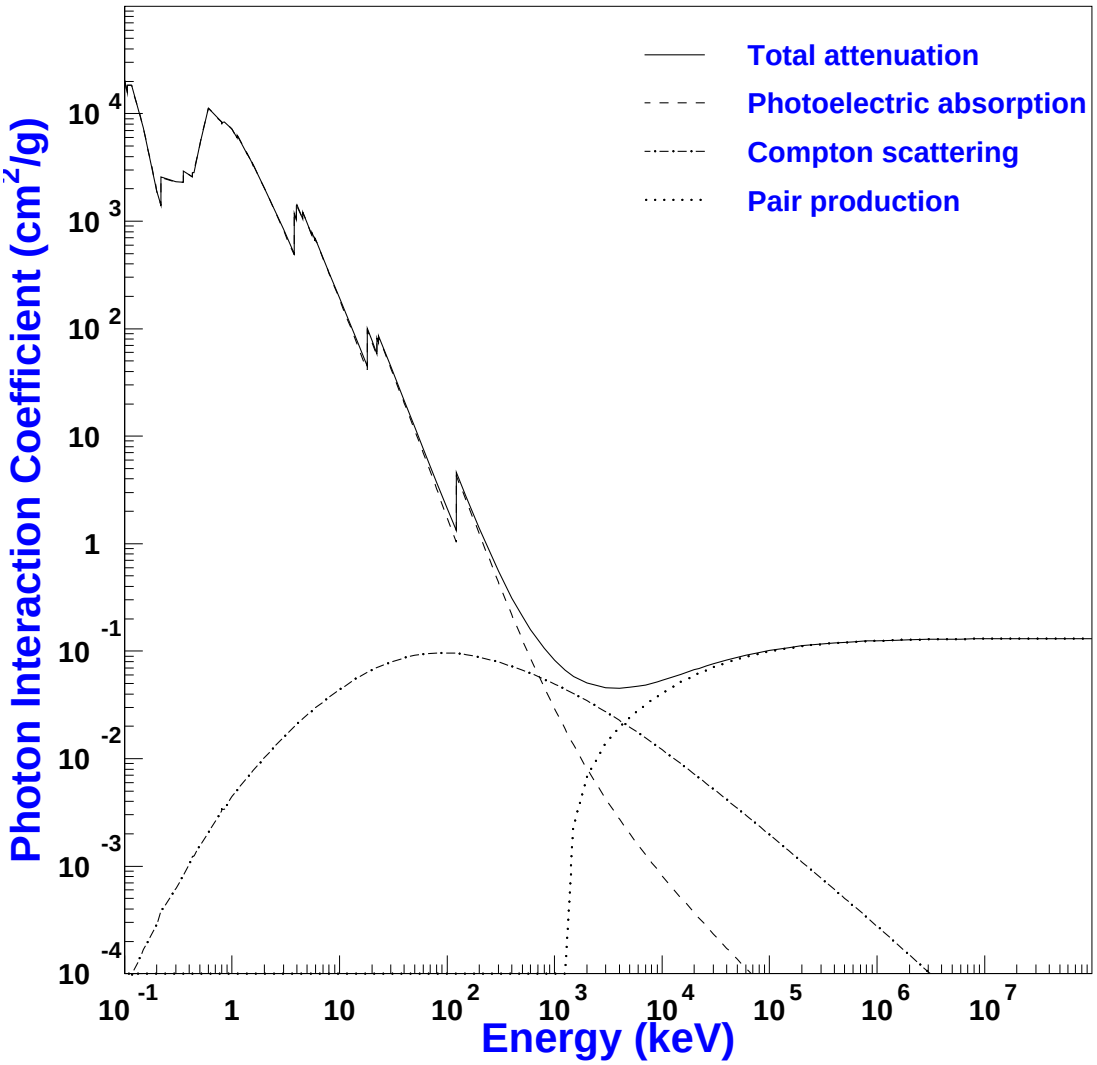

Figure C.10: Photon Interaction Coefficients of Plutonium

Appendix D

List of Symbols

A	mass number
$A\,[cm^{-2}\,sec^{-1}]$	activity
B_i	buckling parameter
$c\,[cm\,sec^{-1}]$	velocity of light
D, $D(E)\,[cm]$	diffusion coefficient
$E, E_n\,[eV]$ or $[MeV]$	neutron energy
$E_R\,[eV]$	resonance energy
$\mathbf{F}(\mathbf{r},\mathbf{\Omega},E)\,[cm^{-2}\,sec^{-1}\,steradian^{-1}\,eV^{-1}]$ $\mathbf{F}(\mathbf{r},\mathbf{\Omega},v)\,[cm^{-2}\,sec^{-1}\,steradian^{-1}]$	} differential neutron flux
$F(\mathbf{r},\mathbf{\Omega})\,[cm^{-2}\,sec^{-1}steradian^{-1}]$	vector flux
G	energetic gain
$J, \mathbf{J}\,[cm^{-2}\,sec^{-1}]$	neutron current density
$K\,[keV\,\mu s^2]$	factor in the Energy-Time correlation
$k\,[eV(^oK)^{-1}]$	BOLTZMANN'S constant
k_∞	microscopic multiplication coefficient
k_{eff}	effective multiplication coefficient
$L\,[cm]$	diffusion length
$L_s\,[cm]$	slowing-down length
$M\,[g]$	mass of scattering atom
$m, m_n\,[g]$	neutron mass
$N\,[cm^{-3}]$	number of atoms per cubic centimeter
N_{AV}	AVOGADRO number 6.022 $10^2 3$
$N(E)\,[MeV^{-1}]$	fission neutron spectrum
$n(\mathbf{r},\mathbf{\Omega},E)\,[cm^{-3}\,steradian^{-1}\,eV^{-1}]$	differential neutron density
$n(\mathbf{r},\mathbf{\Omega})\,[cm^{-3}\,steradian^{-1}]$	vector density
$n(\mathbf{r}), n\,[cm^{-3}]$	neutron density
$n(E)\,[cm^{-3}eV^{-1}]$	neutron density per unit energy
$p, p(E), p(u)$	resonance escape probability
$Q\,[sec^{-1}]$	source strength
$Q\,[MeV]$	reaction energy
$q(E)$ $q(u)$ } $[cm^{-3}\,sec^{-1}]$	slowing-down density at energy E (lethargy u)
$q_{th}(\mathbf{r})\,[cm^{-3}\,sec^{-1}]$	slowing-down density just above the thermal energy range

$R\,[cm]$	nuclear radius
T	time factor
$T\,[^oK]$	neutron temperature
$T_0\,[^oK]$	moderator temperature
$T_{1/2}\,[sec, min, h, d, y]$	half-life
$t_o\,[\mu s]$	time correction at Energy-Time relation
u	lethargy
$V\,[cm\,sec^{-1}]$	scattering atom velocity
$v\,[cm\,sec^{-1}]$	neutron velocity
$v_o\,[cm\,sec^{-1}]$	most probable velocity in a thermal neutron Maxwell spectrum with $T = 293.6^oK$
$v_T\,[cm\,sec^{-1}]$	most probable velocity in a thermal neutron Maxwell spectrum with temperature T
$\alpha\,[cm^2\,g^{-1}]$	β-ray absorption coefficient
$\alpha_o = \overline{v\Sigma_a}\,[sec^{-1}]$	absorption probability
$\Gamma\,[eV]$	total
$\Gamma_n\,[eV]$	neutron } width of a neutron resonance
$\Gamma_\gamma\,[eV]$	radiation
$\delta = \rho \cdot d\,[g\,cm^{-2}]$	surface mass loading
n	neutron yield per neutron absorbed in a fissionable material
$\lambda\,[sec^{-1}]$	radioactive decay constant
$\lambda\,[cm]$	mean free path
$\lambda_s\,[cm]$	scattering
$\lambda_a\,[cm]$	absorption } mean free path
$\lambda_{tr}\,[cm]$	transport
μ_t	total collision
μ_a	absorption
μ_{act}	activation } coefficient
μ_s	scattering
$[cm^2\,g^{-1}]$	
ξ	average logarithmic energy loss
$\xi\,\Sigma_s\,[cm^{-1}]$	slowing-down power
$\rho\,[g \cdot cm^{-3}]$	density
$\Sigma\,[cm^{-1}]$	macroscopic cross section (t=total, a=absorption, act=activation, s=scattering, tr=transport)
$\Sigma_a\,[cm^{-1}]$	average macroscopic absorption cross section for thermal neutrons
$\frac{\xi\Sigma_s}{\Sigma_a}$	moderation ratio
$\sigma\,[barns]$	microscopic cross section (t=total,a=absorption, act=activation, s=scattering, tr=transport, ne=non-elastic)
$\bar{\sigma}\,[barn]$	average cross section in a fission spectrum
$\Phi(r)$, $\Phi\,[cm^{-2}\,sec^{-1}]$	neutron flux
$\Phi(E)\,[cm^{-2}\,sec^{-1}\,eV^{-1}]$	neutron flux per unit energy interval
$\Phi_{th}\,[cm^{-2}\,sec^{-1}]$	thermal neutron flux
$\Phi_{epi}\,[cm^{-2}\,sec^{-1}]$	epithermal neutron flux per logarithmic energy unit
$\Phi_{iso}\,[cm^{-2}\,sec^{-1}]$	isolethargic neutron flux, neutrons per unit of lethargy equal to the Φ_{epi}
$\Phi_f\,[cm^{-2}\,sec^{-1}]$	fast neutron flux

List of Figures

List of Tables

Bibliography

[1] C. Rubbia et al, *"Conceptual Design of a Fast Neutron Operated High Power Energy Amplifier"*, CERN/AT/95-44 (ET), 29^{th} Sept. 1995

[2] C.D. Bowman Int. Conf. on Accelerator-Driven Transmutation Technologies and Applications, Las Vegas, NV, USA, Aug. 1994.

[3] S. Andriamonje et al, in *"Experimental Determination of the Energy Generated in Nuclear Cascades by a High Energy Beam"*, CERN/AT/94/45 (ET), 21^{st} Dec. 1994

[4] C. Rubbia *"Resonance Enhanched Neutron Captures for Element Activation and Waste Transmuation"*, CERN/LHC/97-04 (EET)

[5] A. Fassó et al, in *"Intermediate Energy Nuclear Data: Models and Codes"*, Proceedings of a Specialists Meeting, Issy les Moulineaux (France) 30 May – 1-June 1994, p.271, published by OECD, 1994 and references therein.
A.Fassó, A.Ferrari, J.Ranft, P.R.Sala, G.R.Stevenson and J.M.Zazula, Nuclear Instruments and Methods A, 332 459 (1993), also, CERN Divisional Report CERN/TIS-RP/93-2/PP (1993).

[6] W.C.Marcus *"The Average Number of Collisions in Moderation by Elastic Collision."* Nucl. Sci. Eng. **5**, 336 (1959)

[7] E.Fermi *"Neutron Physics"* AECD-2664 (1951), especially chap. VII: "The distribution of Slow Neutron in a Medium"

[8] S.Glasstone and M.C.Edlund *"The Elements of Nuclear Reactor Theory"* New York: D. Van Nostrand 1952

[9] R.E. Slovacek et al, *"$^{238}U\,(n,f)$ measurements below 100keV"* Nuclear Science and Engineering, 62:455-462,1977

[10] A. Ferrari and P.R.Sala *"The Physics of High Energy Reactions"* Workshop on Nuclear Reaction Data and Nuclear Reactors Physics, Design and Safety, May 1996

[11] C. Rubbia, *"An analytic approach to the energy amplifier"* CERN internal report, CERN/LHC 97-12 (EET), Geneva, 7 Dec. 1997

[12] J.F.Breismeister, MCNP^{TM} *"A general Monte Carlo N-particle transport code* Los Alamos National Laboratory report, LA-12625-M, Nov. 1993

[13] OECD/NEA Data Bank, Issy-Les-Moulineaux, Paris, France, 1994

[14] M. Cobo et al., *"Notes on the study of the most reliable neutron cross section data"*, CERN internal report, CERN/AT/ET 95-035, Geneva, 15 August 1995

[15] F. Carminati, *"Conversion of EAF 4.2 File for use by EET group"*, CERN internal report, CERN/LHC/EET 96-022, Geneva, 14th October 1996

[16] D.E. Cullen, *"The 1994 ENDF Pre-processing Codes (PRE-PRO 94)"* IAEA Nuclear Data Section, Vienna, IAEA-NDS-39 Rev. 8, January 1994.

[17] F. Carminati *"PROCESS: A cross section processing utility"*, CERN internal report, CERN/LHC/EET 96-005, Geneva, 16 January 1996

[18] F. Carminati, *"EET Code Collection User's Guide"*, 26th February, 1996.

[19] Audi et al. *"The 1995 update to the atomic mass evaluation"*, Nucl. Phys. A 595 (1995) 409-480

[20] I. Goulas and F. Carminati *"XSECT: Visualization of cross section data"*, CERN internal report, CERN/AT/EET 95-008, Geneva, 19 May 1995

[21] F. Carminati et al., *"TARC General Purpose Monte Carlo"*, CERN internal report CERN/LHC/EET 96-011, Geneva, 17th April, 1996.

[22] *"PAW Physics Analysis Workstation"*. CERN Program library Q121.

[23] V. Vlachoudis *"A faster response to the distance question in the neutron simulation code"* AUTH internal report, AUTH/EET/96-01

[24] F. Carminati et al. *"Modification of the neutron reaction sampling subroutine, FATE, for the EA Monte Carlo"* CERN internal report, CERN/LHC/EET-96-010, Geneva, 19 March 1996

[25] RSICC Peripheral Shielding Routine Collection, *"SAMMY-M2, A Code System for Multilevel R-Matrix Fits to Neutron Data Using Bayes Equations"* Oak Ridge National Laboratory, Feb. 1999

[26] Y. Kadi private communication.

[27] V.McLane, C.L.Dunford, P.F.Rose *"ENDF-102 Data Formats and Procedures for the Evaluated Nuclear Data File ENDF-6"* Cross Section Evaluation Working Group, National Nuclear Data Center, Brookhaven National Laboratory Upton, N.Y. 11973-5000

[28] S. Atzeni, Y. Kadi and C. Rubbia *"Statistical fluctuations in Monte Carlo simulation of the Energy Amplifier"* CERN internal report, CERN/LHC/97-011 (EET)

[29] S. Andriamonje et al, *"Experimental study of the phenomenology of spallation neutrons in a large Lead block."*, CERN/SPSLC 95-17, SPSLC/P291, 5th May 1995. Proposal to the Committee of European Union.

[30] I.Papadopoulos and K.Komnas, *"Simulation Concerning the Suitability of EMBECO as Base of the Experimental Setup"*, TARC Internal Note, December 1995.

[31] Britannia Refined Metals LTD, Gravescend, Kent, United Kingdom.

[32] M. Embid and J.P.Revol, *"Determination of the impurity content of the Lead Assembly for the TARC experiment"*, CERN/SPSLC/Internal Note 97-001

[33] R. Billinge, *"The CERN PS Complex: A Multipurpose Particle Source"*, Proc. of XIIth Intl. Conf. on High Energy Acc., 1983

[34] Bergoz Instrumentation, 01170, Crozet, France. (address Web: www.bergoz.com)

[35] J.P.Revol et al., *"Beam transformer Performance and Calibration for the TARC Experiment"*, CERN/ET/Internal Note in preparation.

[36] A.Abanades and E. Gonzalez *"The Data Acquisition System for the TARC Experiment"*, CERN/EET/ Internal Note 98-xx, January 20, 1998

[37] *"CASCADE User's Guide"*, CERN-ECP Division-FEX Group.

[38] Use the WWW link *"http://wwwinfo.cern.ch/ppp/cdr"* as an entry point for information on the CDR software.

[39] *"HBOOK Reference Manual"*, CERN Program Library Y250.

[40] *"mSQL relational database software" http://www.Hughes.com.au*

[41] L.E. Lazareva, E.L. Feinberg and F.L. Shapiro. *"Neutron spectrometry based on the measurement of the decelerating time of neutrons."*, J.Exptl. Theoret. Phys. (U.S.S.R), 29:381-383, 1955

[42] A. A. Bergman et al. Geneva International Conference on the Peaceful uses of Atomic Energy, pg.642 (1955)

[43] E. Belle et al. *"Neutron Flux Measurements with Silicon Detectors using* ^{6}LiF *and* ^{233}U *targets in the TARC experiment"*, CERN/ET/Internal Note 97-26

[44] A. Tzima et al. *"Neutron Flux Measurements in the TARC Experiment with the* ^{3}He *scintillation chamber"*, CERN/ET/Internal Note 97-27

[45] G. Kitis et al. *"Mapping of the Thermal Neutron Distribution in the Lead Block Assembly of the PS-211 Experiment using Thermoluminescence Detectors"*, CERN/ET/Internal Note 98-9

[46] S. Shalev and J. M. Culter, Nucl. Sci. Eng. 51, (1873) p.52

[47] V. Vlachoudis et al. *"Neutron Flux with Activation Foils in the TARC experiment"*, CERN/ET/Internal Note 98-8

[48] *"Neutron Activation Foils"*, Reactor Experiments Inc. 1965

[49] K.H.Beckurts and K.Wirtz 1964 *"Neutron Physics, The Sandwich method"*

[50] C.Michael Lederer and Virginia S.Shirley *"Table of Isotopes"* Seventh Edition

[51] M.A.Mariscotti *"A method for automatic identification of peaks in the presence of background and its application to spectrum analysis"*, Nucl. Instrum. Methods, 50, 309-320 (1967)

[52] J.E.Browne and R.Firestone, *"Table of radioactive isotopes"* Vol II

[53] J.E.Unik, *"Coincidence measurements in nuclear decay scheme studies"* (Thesis) UCRL-9105 (1960)

[54] Y.A.Ellis, *"Nuclear data sheets for A=233*"* Nuclear data sheets. (1978) pg. 259.

[55] A. Angelopoulos et al. *"Evaluation of Lexan and CR-39 foils for integral fission fragments measurements"* CERN/AT-ET, Internal Note 94/023

[56] S.A.Duranni and R.K.Bull *"Solid State Nuclear Track Detection."* Pergamont Press, Oxford (1987)

[57] G. Knoll et al. *"Radiation Detection and Measurement"* 1979

[58] P. Kokkas et al. *"An image processing system for track-etch detectors"* Radiation Measurements 26 (1996) 187/91

[59] A.Rosenfeld *"Computer vision: basic principles."* Proc. IEEE **76**, 863-868, 1988 Pergamont Press, Oxford (1987)

[60] C. Rubbia, *"Resonance enhanced neutron captures for element activation and waste transmutation"*, CERN/LHC/97-04 (EET)

[61] C. Rubbia et al., *"A high Resolution Spallation driven Facility at the CERN-PS to measure Neutron Cross Sections in the interval from 1 to 250 MeV"*, CERN/LHC/98-02 (EET), Geneva, May 30, 1998

[62] C. Rubbia et al., *"A high Resolution Spallation driven Facility at the CERN-PS to measure Neutron Cross Sections in the interval from 1 to 250 MeV; a relative Performance Assessment"*, CERN/LHC/98-02 (EET), Geneva, May 30, 1998

[63] S. Abramovich et al., *"Proposal for a Neutron Time of Flight Facility"* CERN/SPSC/99-8, Geneva, March 17, 1999

[64] F. Kaeppeler et al., *"Current Quests in Nuclear Astrophysics and Experimental Approaches"* Annu. Rev. Nucl. Sci. 1998. 48:175-251

[65] *"A High Gain Energy Amplifier Operated with Fast Neutrons"*, AIP Conference Proceedings 346, International Conference on Accelerator-Driven Transmutation Technologies and Applications, Las Vegas, July 1994.

[66] S. Andriamonje et al, *"For the experimental tests of the validity of the Energy Amplifier concept."* Physics Letters B 348 (1995) 697-706

[67] J. Raeder et al., *"Safety and Environmental Assessment of Fusion Power (SEAFP)"*, EUR-FU-BRU XII-217/95, June 1995

[68] C. Rubbia et al., *"A realistic Plutonium Elimination Scheme with Fast Energy Amplifiers and Thorium-Plutonium fuel"*, CERN/AT/95-53 (ET), 12^{th} Dec. 1995

[69] C. Roche and C. Rubbia, *"Some preliminary considerations on the Economical issues of the Energy Amplifier"*, CERN/AT/95-45 (ET), 29^{th} Oct. 1995

[70] S. Glastone, *"Principles of Nuclear Reactor Engineering"*, D. Van Nostrand Inc. (1955)

[71] C. Rubbia, *"An Analytic Approach to the* Energy Amplifier*"*, Internal Note, CERN/AT/ET/94-036.

[72] C. Rubbia, *"Why So Many Exponentials?"*, Internal Note, CERN/AT/ET/94-032

[73] Web Elements 2.0 Electronic Publications. Sheffield U.K.
http://www.shef.ac.uk/uni/academic/A-C/chem/web-elements/

Index